DEFORMATION AND FORCE CHARACTERISTICS OF LAMINATED PIEZOELECTRIC ACTUATORS

Sontipee Aimmanee

Dissertation submitted to the Faculty of the Virginia Polytechnic Institute and State University in partial fulfillment of the requirements for the degree of

Doctor of Philosophy
In
Engineering Mechanics

M.W. Hyer, Chair
R.C. Batra
M.R. Hajj
E.R. Johnson
S. Thangjitham

September 14, 2004
Blacksburg, VA

Keywords: Geometric Nonlinearities, Stability, Rayleigh-Ritz method, Laminated, Actuator, THUNDER, LIPCA, Finite-element method

DEFORMATION AND FORCE CHARACTERISTICS OF LAMINATED PIEZOELECTRIC ACTUATORS

Sontipee Aimmanee

Committee Chair: M.W. Hyer
Engineering Mechanics

ABSTRACT

This research discusses the mechanical characteristics of laminated piezoelectric actuators that are manufactured at an elevated temperature, to cure the adhesive bonding the layers together, or to cure the layers made of polymeric composite material, and then cooled to a service temperature. Mainly discussed are actuators that are composed of layers of passive materials and a layer of piezoelectric material. THUNDER (THin layer UNimorph ferroelectric DrivER and sensor) and LIPCA (LIghtweight Piezo-composite Curved Actuator) actuators, which consist of layers of metal, adhesive and piezoelectric material, and carbon-epoxy, glass-epoxy and piezoelectric material, respectively, are studied and investigated in detail to understand the thermal effects due to the elevated manufacturing temperature. Owing to the large out-of-plane deformations of the THUNDER actuators as a result of cooling to the service temperature, inclusion of geometric nonlinearities in the kinematic relations is taken into consideration for prediction of the thermally-induced deformations and residual stresses. The deformations and residual stresses are predicted by using a 23-term Rayleigh-Ritz approach and more rigorous, time-consuming, finite-element analyses performed with ABAQUS. The thermally-induced deformations of THUNDER actuators can result in multiple room-temperature manufactured shapes, whereas those of LIPCA actuators (LIPCA-C1 and LIPCA-C2) exhibit single room-temperature manufactured shape. Actuation responses of these actuators caused by a quasi-static electric

field applied to the piezoelectric layer are also studied with the Rayleigh-Ritz approach. It is shown that geometrical nonlinearities play an important role in the actuation responses, and these nonlinearities can be controlled by the choice of actuator geometry and the materials in the passive layers. In addition, blocking forces representing load-carrying capability of THUNDER and LIPCA actuators are determined. Support conditions and again geometrical nonlinearities are vital factor in load-resisting performances. Amongst the actuators considered, the actuated deflection and blocking forces are compared. Finally, based on the outcome of this study, new criteria for designing a new type of laminated piezoelectric actuators with improvement of performance characteristics are proposed.

DEDICATION

To my mother and my father,

whose love to me is never ended

ACKNOWLEDGEMENTS

During the course of my Ph.D. study, there are many people who have taught, supported, and assisted me. The one whom I must single out and acknowledge first is my own research advisor, Professor Michael W. Hyer. Without his intelligent guidance, consistent support, and opportunity and time given to me, this dissertation would never have existed. I also would like to thank Professors R. C. Batra, M. R. Hajj, E.R. Johnson, and S. Thangjitham for serving as the committee members and for providing their advice.

Additionally, I owe a debt of gratitude to all of my teachers from King Mongkut's University of Technology Thonburi, University of Delaware, and Virginia Polytechnic Institute and State University for valuable engineering knowledge. It is a great pleasure to learn from them.

Thanks are also due to all my officemates at Virginia Tech for nice academic and non-academic discussions. They are Drs. Tomoya Ochinero, Jaret Riddick, Marc Schultz, Ms. Gabriela Wolford, Ms. Miao Sun, and Mr. Majed Majeed. Besides this, thanks should go to all my Thai friends at Virginia Tech, particularly Drs. Siriroj Sirisukprasert, Surachet Kanprachar, Amnart Kanarat, Chawalit Jeenanunta, Mr. Songwut Hengprathanee, Mr. Boonyarit Intiyot, Ms. Rawee Suwandechochai, and Ms. Yodmanee Tepanon for their friendship.

Last but not least, I wish to acknowledge my lovely girlfriend, Ms. Pakinee Suwannajan. I cherish her love, support, and friendship given to me during all years long since we met.

TABLE OF CONTENTS

LIST OF TABLES

LIST OF FIGURES

Chapter 1

INTRODUCTION

1.1 Overview of Piezoelectricity

It has been over a decade since so-called “smart materials” first emerged to lead to technological innovations appearing in various fields such as aerospace, manufacturing, civil infrastructure systems, biomechanics, etc. The definition of a “smart material” is given in several publications: a few examples are given in references [1-3]. As defined in [1], a smart material is a non-biological material or material system having the following attributes: (i) a definite propose; (ii) a means and imperative to achieve that propose; and (iii) a biological pattern of functioning. Thus, to possess the above characteristics, the key functions of a smart material or structure are sensing and actuating. As stated in [2], the sensor part has ability to feedback thermal, electrical, and magnetic signals, like a human nervous system. The actuator part has the capability of changing shape, stiffness, position, natural frequency, damping, and/or other mechanical characteristics of the system in response to changes in temperature, electric field, and/or magnetic field analogous to a motor system in biological functions. Piezoelectric materials, magnetostrictive materials, shape memory alloys, electrorheological fluids, magnetorheological fluids, and optical fibers are examples of the smart materials in use today that accomplish these tasks. The work described herein is focused on piezoelectric materials.

Piezoelectric materials are materials that exhibit an interaction between electrical and mechanical response; namely they generate an electric charge when strained, the direct piezoelectric effect, and they deform (strain) when an electric field is applied, the

converse piezoelectric effect. The former phenomenon is a sensor property and the latter one is used for actuation purposes. The two piezoelectric effects are a physical property of acentric crystal materials, i.e., there is no center of symmetry in the elementary cell (unit cell) of the materials. In centric crystals, the center of positive and negative charge remains fixed when a force is applied because of the symmetry of the center. In acentric crystals, the centers of positive and negative charge are displaced by an applied force, and therefore, the crystal may possess “polarization” or net electric charges [4]. The polarization that is developed in a piezoelectric crystal is dependent on the orientation of the applied force. For example, the directional nature of the converse piezoelectric effect can be visualized by considering the effect of tensile stress on the two-dimensional hexagonal unit cell shown in Figure 1.1. In the unstressed unit cell illustrated in Figure 1.1(a), the center of positive charges coincides with the center of negative charges. When the unit cell is subjected to a tensile stress in the direction shown in Figure 1.1(b), the crystal deforms and the centers of positive and negative charges are separated. This results in the net polarization of the unit cell, i.e., piezoelectricity is observed. However, when the direction of the applied stress is

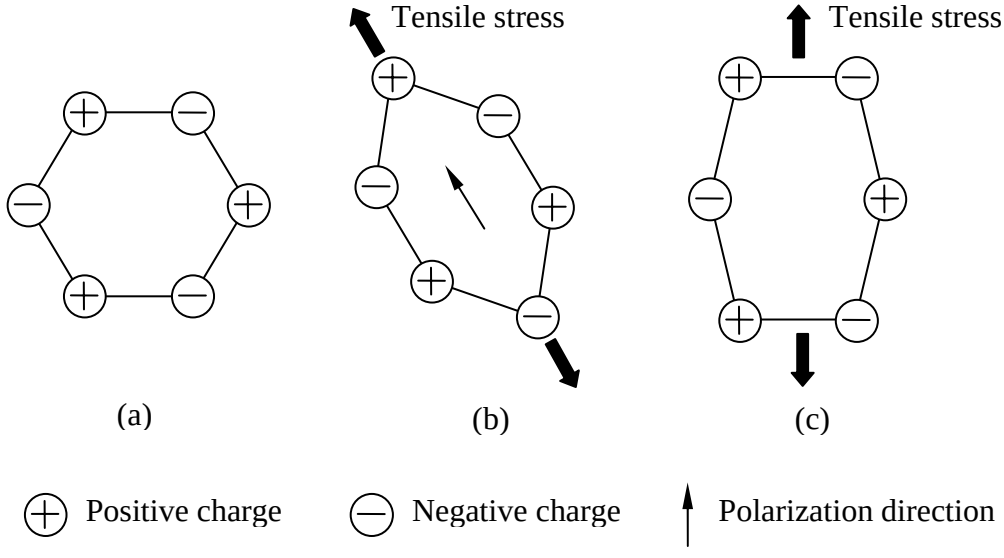

Figure 1.1: Directional Dependence of Piezoelectric Effect (after [4])

Indicated in Figure 1.1(c), the crystal deforms but the centers of positive and negative charges are not separated, i.e., no piezoelectricity is noticed.

Based on the possible symmetries of unit cells in nature, there are 32 crystal classes (or point groups). Out of these, 21 are acentric and thus piezoelectric. In 11 of the piezoelectric classes, a spontaneous polarization of the crystal structure is present in the absence of an applied stress or electric field. These 11 piezoelectric classes are so-called pyroelectric crystal classes, in which a net polarization change is induced by a change in temperature. In addition, certain pyroelectric crystals can switch the polarization direction by application of an opposite electric field; such crystals are also classified as ferroelectric crystals. The piezoelectric effects observed in ferroelectric crystals are much more noticeable than the effects in non-ferroelectric piezoelectric crystals. Normally, natural piezoelectric crystals such as single-crystal quartz exhibit the piezoelectric phenomenon, but their response is quite weak due to being non-ferroelectric. Furthermore, they are susceptible to moisture and chemical reactions in a typical atmosphere, as well as being more expensive to create. Therefore, polycrystalline ferroelectric ceramics such as $BaTiO_3$ and $Pb(Zr,Ti)O_3$ (Lead Zirconate Titanate, or PZT) have been produced to overcome these shortcomings.

The materials $BaTiO_3$ and PZT are composed of a mass of tiny crystallites. Above a specific temperature, called the Curie temperature (around $135\,°C$ and $350\,°C$ for $BaTiO_3$ and PZT, respectively), these crystallites have perovskite structure and exhibit cubic symmetry, which is centric or centrosymmetric, as shown in Figure 1.2(a). As a result, the materials don’t possess piezoelectric behavior. Below the Curie temperature, however, the crystallites take on tetragonal symmetry in which the positive charge from central the metal ion is biased toward one direction, as illustrated in Figure 1.2(b). Each elementary cell then has a built-in electric dipole, which may be reversed, and which also may be switched to certain allowed directions by the application of an electric field. These dipoles are not randomly oriented throughout the material. Neighboring dipoles align with each other to

form regions of local alignment known as Weiss domains. Within a domain, therefore, all the dipoles are aligned, giving a net dipole moment to the domain, and hence a net spontaneous polarization (dipole moment per unit volume). However, these domains are formed with random orientation in the material, so that no net overall polarization or piezoelectricity is observed in the bulk material. Piezoelectricity can be induced in the ferroelectric ceramics by a process of subjecting them to a strong electric field and elevated temperature (slightly lower than Curie temperature). This process is known as poling. During poling, the direction of spontaneous polarization within each domain is switched and nearly aligned with the applied field. This process makes the domains elongate in the direction of the poling field (poling axis). When the field is removed, most of the dipoles remain locked in the approximate alignment, so that the material will have a permanent residual (remanent) polarization and deformation after poling [4-6], as shown in Figure 1.3.

After the poling process is complete, an applied voltage lower than the poling voltage causes dimensional changes in the piezoceramic material due to movement of the ions within the unit cell, as long as the voltage is held. A voltage with the same polarity as the poling voltage (defined as positive field) generates more expansion along the poling

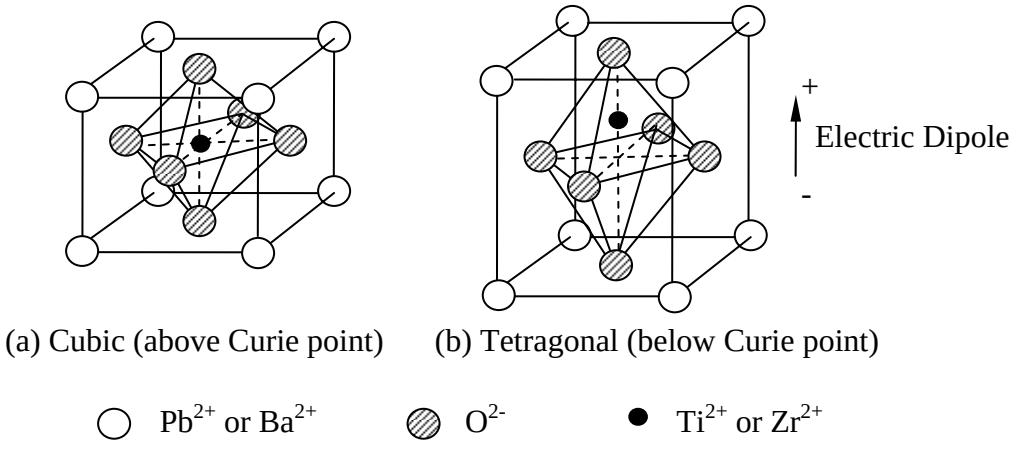

Figure 1.2: $BaTiO_3$ and PZT Unit Cell (after [5])

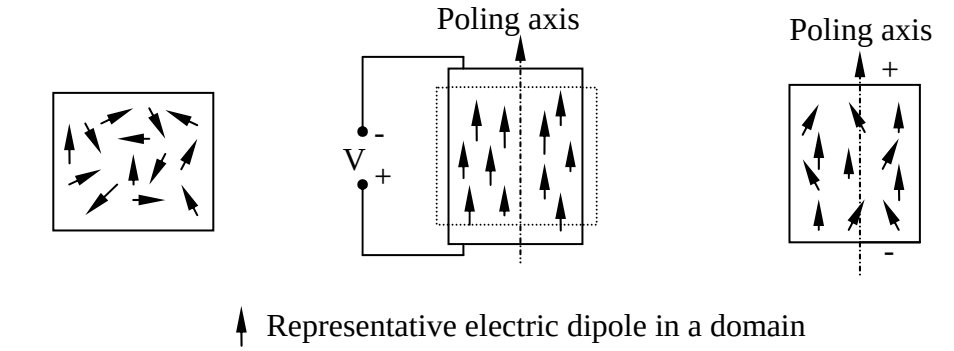

Figure 1.3: Effects of Poling

axis and contraction perpendicular to the poling direction. A voltage with the opposite polarity (negative field) has the opposite effect: contraction along the poling axis, and expansion perpendicular to the poling axis. In both cases, under the quasi-static field, the ceramic element returns to its poled dimension when the voltage is removed from the electrodes. These so-called converse effects are shown exaggerated in Figure 1.4. In either case, the applied voltage shouldn't be too high. When the voltage in the case of Figure 1.4(a) is applied higher than the coercive, or depoling, field of the piezoelectric element, the polarization is deteriorated and repoling process is needed to rebuild piezoelectric capability in the element. Moreover, when an extremely high field is applied to the element, electrical breakdown can occur, and eventually the piezoelectric function of the material is destroyed.

On the other hand, as illustrated in Figure 1.5, the direct effect can be obtained in the polarized piezoelectric element by applying forces to the material. A voltage with the same polarity as the poled element results from a compressive force applied parallel to the poling axis, or from a tensile force applied perpendicular to the poling axis. However, a tensile force applied along the poling direction or a compressive force applied perpendicular to the poling axis produces electrical charges against the original polarity of the material. Again, care must be taken when the force is applied as in the case of Figure

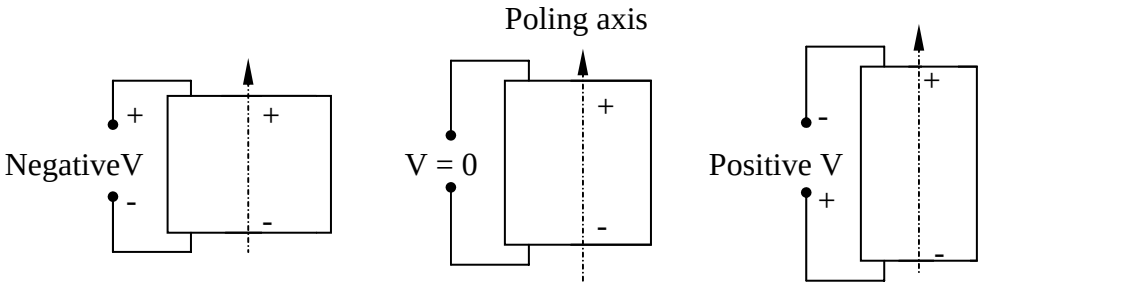

(a) Applied voltage of opposite polarity as poling voltage (b) No voltage (c) Applied voltage of same polarity as poling voltage

Figure 1.4: Piezoelectric Actions from Applied Voltages

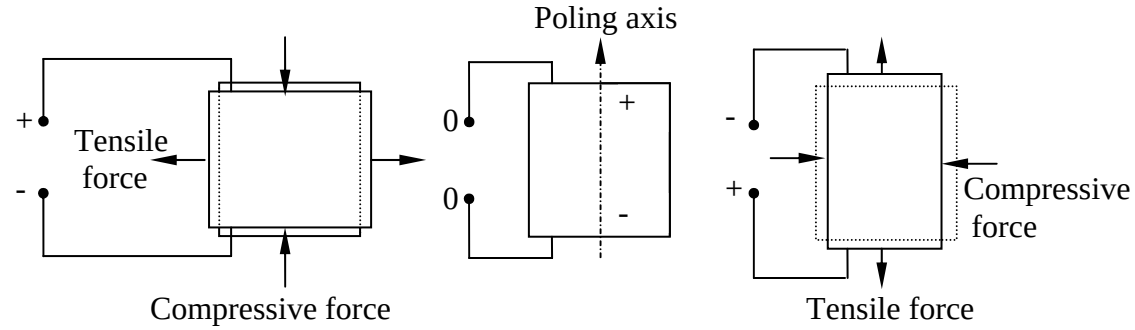

(a) Output voltage of same polarity as poled element (b) No applied force (c) Output voltage of opposite polarity as poled element

Figure 1.5: Piezoelectric Voltages from Applied Forces

1.5(a). A sufficiently strong force can switch the poled domain and weaken the piezoelectric effect.

The piezoelectric effects described above can be formulated as mathematical relations. When the applied field or force is not too large, the linear relationship between piezoelectric response and electrical or mechanical input is assumed. The linear piezoelectric effect has a tensor property that relates the generated polarization (or electrical charge) in response to an exerted mechanical stress. The property is a third-order tensor because it depends on the orientation of the second-order tensor applied stress to generate a

polarization vector, as depicted in Figure 1.1. In tensor notation, the direct piezoelectric effect is given by [4, 7]

$$P_i = d_{ijk}\sigma_{jk} \tag{1.1}$$

where $i, j,$ and k are indices of Cartesian axes running from $1-3$, d_{ijk} is the piezoelectric coefficient or piezoelectric modulus, σ_{jk} is the applied stress, and P_i is the polarization generated along the i-axis in response to the applied stress. In addition, because of the balance of linear momentum in the material, $\sigma_{jk} = \sigma_{kj}$, it follows from Equation (1.1) that the tensor d_{ijk} is symmetric in the last two indices, so Voigt's notation can be employed and Equation (1.1) can be expressed as

$$P_i = d_{ij}\sigma_j \tag{1.2}$$

where $i = 1-3$ and $j = 1-6$.

With the same repeated indices as defined above, the converse effect can also be modeled mathematically using Voigt's notation as

$$\varepsilon_j^E = d_{ij}E_i \tag{1.3}$$

where E_i is electric field and ε_j^E is strain induced by piezoelectricity.

The piezoelectric coefficients d_{ij} can have several components, depending on classes of symmetry of a crystal or piezoelectric material. It can be noted that, as seen from Figure 1.1 and Equation (1.2), some of components of d_{ij} can be zero. A poled ferroelectric ceramic is categorized in the class of 6mm and has been proven to have 3 independent piezoelectric moduli, namely d_{33}, d_{31}, and d_{15}, where index 3 indicates the poling direction. The longitudinal piezoelectric coefficient d_{33} relates the polarization developed along the poled axis to a stress applied in that same direction. The transverse piezoelectric coefficient d_{31} relates the polarization along the 3-axis to a stress applied in a perpendicular direction (1 direction). The shear piezoelectric coefficient d_{15} relates the polarization along the 1-axis to a shear stress applied in the 2-3 plane.

1.2 Unimorph and Bimorph Actuators

Although the piezoelectric coefficient of the ferroelectric ceramics is substantially higher than those of natural crystals, in some practical applications the amplification of the piezoelectric response is often required, especially for producing displacements by actuating the piezoelectric material. Examples of enhanced piezoelectric actuators include stacks, unimorphs, and bimorphs [5, 8]. A stack is made from several piezoelectric transducers connected mechanically in series and electrically in parallel. The stack illustrated in Figure 1.6 (a) uses piezoelectric coefficient d_{33} in actuation to create a displacement in the direction of stacking. The displacement of each transducer element adds to the total displacement. On the other hand, unimorph and bimorph actuators, shown in Figure 1.6 (b) and (c), are constructed in laminated cantilever beam or plate configurations. A unimorph is composed of a single layer of piezoelectric material with another layer of elastic material as a passive layer, whereas a bimorph is made from two layers of piezoelectric material with or without a passive layer. Both types of actuators utilize piezoelectric coefficient d_{31} to generate deformations parallel with the actuator's midplane that are unsymmetrical with respect to the actuator's mid-plane and thus induce more appreciable out-of-plane deflection through bending. Table 1.1 compares the performance characteristics of these actuators.

Table 1.1: Performance Characteristics Comparison of Various Transducers (After [8])

Transducer Type	Displacement Generated	Force Generated	Electro-Mechanical Energy Transfer	Resonant Frequency
Bulk PZT	Low	Medium	Medium	Medium
Stack	Medium	High	High	High
Unimorph/ Bimorph	High	Low	Low	Low

Due to their performance characteristics, the unimorph and bimorph usually are used for audio and ultrasonic alarm devices, relay motors, positioning devices, motion detectors, and instrumentation pick-up indicators. In order to properly design and implement this kind of transducer in a specific application, several mathematical models have been proposed during the past two decades. First, the model of integrating a piezoelectric layer with a passive substrate was developed in 1985 by Bailey and Hubbard [9]. However, their model was one-dimensional and took into account only uniform strain in both piezoelectric and passive layers, so it could not capture the bending strain in the transducers. In 1987, Crawley and de Luis derived the pin- force model, including flexural stiffness of the passive

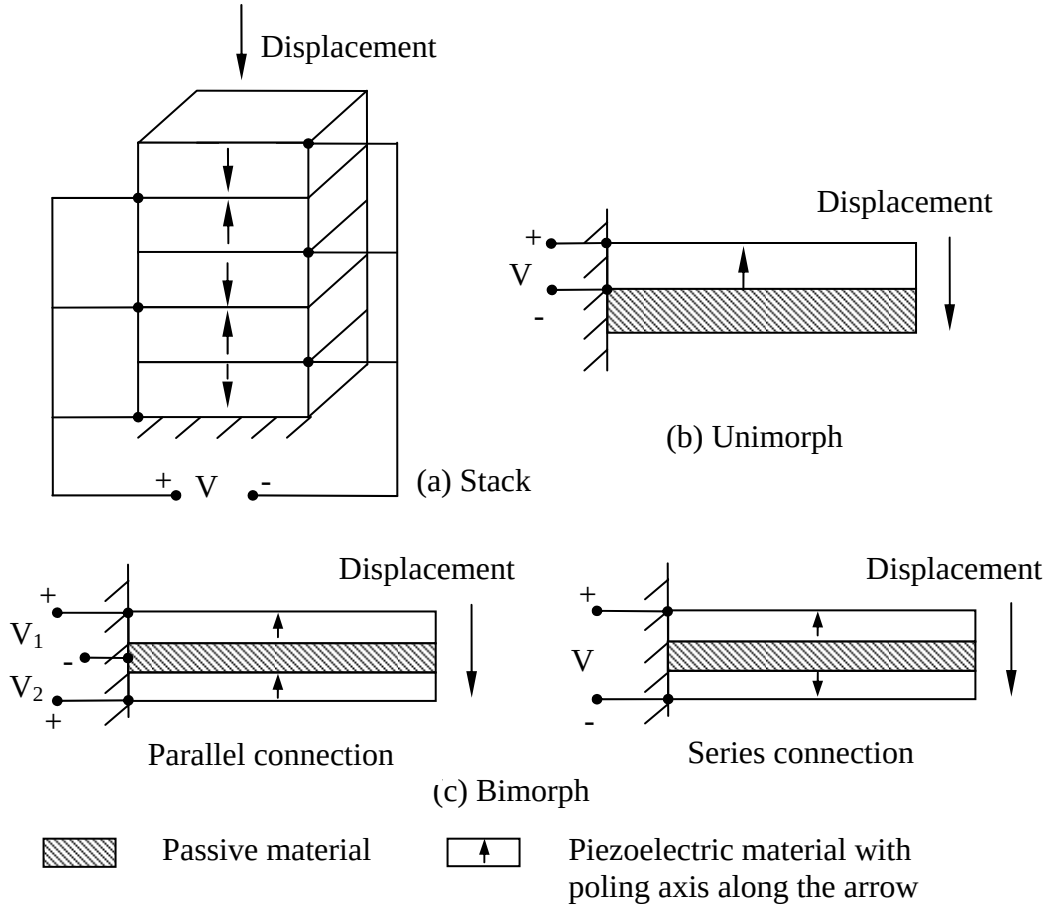

Figure 1.6: Displacement-Enhanced Piezoelectric Transducers

layer, which, therefore, acted as a beam [10]. However, the piezoelectric layer still had uniform strain distribution. Chaudhry and Rogers [11] proposed the enhanced pin-force model in 1994 by incorporating the bending stiffness of the active layer. Nonetheless, the piezoceramic layer was assumed to bend around its own neutral axis (at its geometric center) and actuation from the piezoceramic layer passed through the passive layer by two imaginary pins located at the edge of layer interface.

These models, even though they are simple and easy to use, have some limitations for certain thickness and stiffness ratios between the piezoceramic and passive layers. Thus, the more accurate model, so called the Euler-Bernoulli model, which is based on classical beam and plate theories, was put forward by Chaudhry and Rogers [11], Crawley et al. [12,13], Smits et. al. [14, 15], and Wang and Cross [16]. This model is equivalent to classical lamination theory for composite laminated beams and plates. Therefore, the model can accurately predict the strains and curvatures of unimorph and bimorph actuators throughout the actuators. However, since such models are based on geometrically linear theory, they are not able to capture the correct behavior of newer unimorph-type actuators like RAINBOW, THUNDER, and LIPCA, which possess geometrically nonlinear characteristics caused by the large deformations due to their elevated-temperature manufacturing process and subsequent cooling. These actuators are discussed next.

1.3 RAINBOW, THUNDER, and LIPCA Actuators

The models for unimorph and bimorph actuators discussed above were applied to actuators that were fabricated at room temperature or slightly above. The flexural motions of these actuators were limited either by the voltage limitations or the low tensile strain limit of the piezoceramic material. The notion of fabricating actuators so the piezoceramic material was in an initial state of compression was motivated by the desire to overcome the

latter limitation. An initial state of compression could be achieved by fabricating the actuator at an elevated temperature and using passive materials with thermoelastic properties that produced compression in the piezoceramic layer when cooled to the actuator service temperature. Unless the layer material properties were chosen properly, had the right thickness, and were located relative to the piezoceramic layer in a specific manner, fabrication at an elevated temperature and then cooling would result in an actuator with an initial curvature as well as initial stresses, much like a bimetallic strip. However, it was generally believed that the initial curvature enhanced the deflection characteristics, relative to a flat actuator, when the piezoceramic layer was activated. There has been some work on predicting the initial curved shapes and subsequent deflections due to activating the piezoceramic material. Nonetheless, there are still many issues that are not understood. To follow is a brief description of the three actuators mentioned above, namely RAINBOW [17-23], THUNDER [24-29, 49], and LIPCA [30-33].

1.3.1 Manufacturing Processes and General Characteristics of RAINBOW, THUNDER, and LIPCA

First developed by Haertling in 1990 [19], the RAINBOW actuator is composed of two different layers, specifically a reduced layer as an elastic passive layer and unreduced, or active, layer. A photo of a round RAINBOW actuator and a schematic cross-

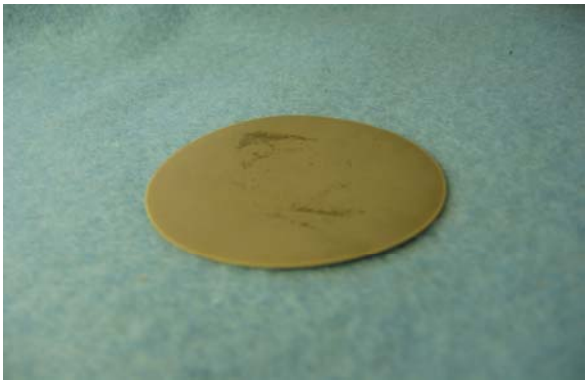

Figure 1.7: Photo of Round RAINBOW

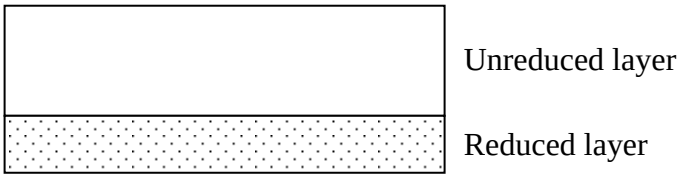

Figure 1.8: Cross-Section of RAINBOW Actuator

section of a RAINBOW actuator are illustrated in Figures 1.7 and 1.8, respectively. The actuator is manufactured by placing a standard flat piezoelectric material, such as PZT or PLZT ($(Pb,La)(Zr,Ti)O_3$), in wafer form on top of a carbon block. Then, the whole assembly is heated in a furnace to approximately 700-1,000 °C. This heating process is called a reduction process because the carbon oxidation at the ceramic-carbon interface takes the oxygen atoms from the PZT oxide ceramics. This, consequently, leaves the ceramic wafer with two distinctive layers, like the standard unimorph illustrated in Figure 1.6(b). The bottom layer is a cermet layer of lead, titanium oxide, or zirconium oxide, and the top layer is the intact PZT material. The thickness of the unreduced layer can be adjusted by altering the process temperature and the soaking time in the furnace. As a major effect, the reduced layer is no longer piezoelectrically active, but it is electrically conductive. Also as a result of the change in chemical component of the reduced layer from that of original PZT, a thermal expansion coefficient and elastic modulus mismatch between these two layers is generated. Specifically, there is a lack of symmetry of the layer thermoelastic properties with respect to the actuator's geometric midplane i.e., the actuator is an unsymmetric laminate [39]. Accordingly, the stiffness properties of the actuator are characterized by exhibiting bending-stretching coupling (*B* matrix) and thermally-induced effective moments. This lack of symmetry causes the residual stresses and the large out-of-plane deformation during cooling of the wafer to room temperature.

The THUNDER actuator, as seen in Figure 1.9, is another type of curved actuator, similar to RAINBOW. It was developed by the NASA Langley Research Center in

1994 [24] and now is manufactured and distributed by Face International Corporation [25]. However, unlike RAINBOW, which is a monolithic layered structure, THUNDER is composed of a PZT layer sandwiched between layers of metal, such as aluminum, stainless steel, beryllium, etc., all of which are bonded together in a flat condition with a polyimide adhesive that is cured approximately at 325 °C. A schematic cross-section of a THUNDER actuator is illustrated in Figure 1.10. The bottom layer serves as the backbone of the actuator and is used to attach the actuator to a structure. The very thin top layer, which is optional, is used for protecting the piezoceramic layer from direct exposure. All the layers are assembled in the desired order and thermally processed in an autoclave to produce the actuator. The temperature is raised to 320-325 °C at 5 °C/min with a full vacuum. Then, the autoclave is pressurized to 207 kPa for 30 min and cooled at a rate of 5 °C/min until the temperature reaches 200 °C [26]. After this, the vacuum is released and the actuator is allowed to cool to ambient temperature. Again, because the actuator is an unsymmetric laminate, residual stresses and large out-of-plane deformations develop, so the cooled, or manufactured, shape is not flat.

LIPCA is a recent variant of THUNDER introduced by Yoon, et al [30]. They put forward the idea of using fiber-reinforced composite materials as the passive layers in order to save weight without losing the capabilities for generating high force and large

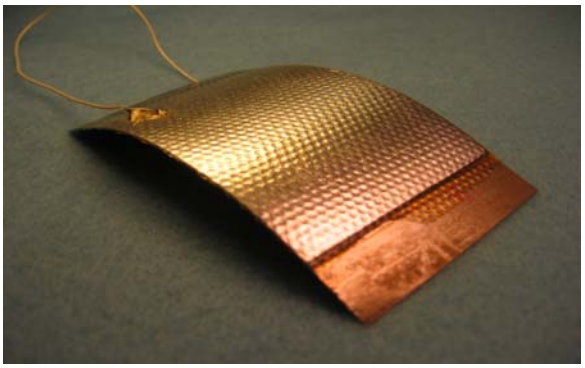

Figure 1.9: Photo of Rectangular THUNDER

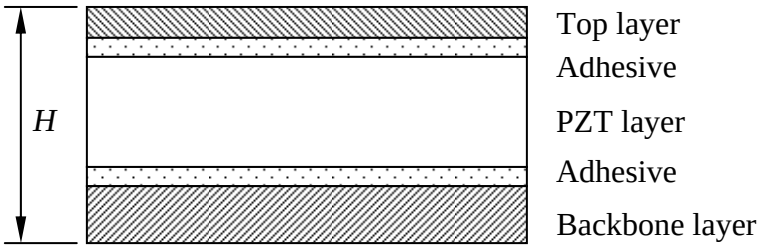

Figure 1.10: Cross-Section of THUNDER Actuator

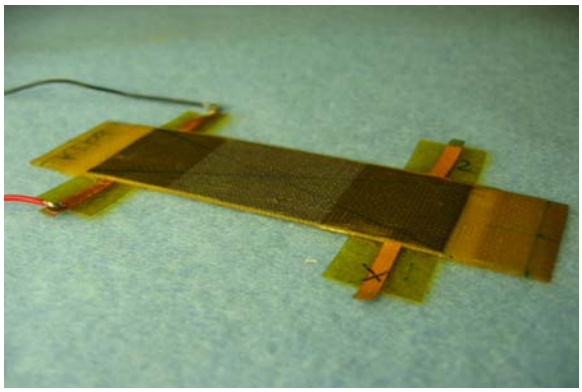

Figure 1.11: Photo of Rectangular LIPCA

displacement during electrical actuation. The main devices they have been developing are called LIPCA-C1 [30, 32], LIPCA-K [31], and LIPCA-C2 [33]. Figure 1.11 shows a photo of a LIPCA actuator. LIPCA-C1 consists of three different materials, namely a glass-epoxy layer, a piezoceramic wafer with electrode surfaces and silver pasted copper strip wires, and a carbon-epoxy prepreg layer. All of the materials are stacked in that order, from bottom to top, resulting in an unsymmetric laminate. Due to the epoxy resin prepreg material system, the actuator can be manufactured without adhesive. The stacked layers are vacuum bagged and cured at 177 °C for 2 hours in a cure oven. After removal from the flat mold, the device possesses residual stresses and curvatures.

LIPCA-K is very similar to LIPCA-C1 except Kevlar49-epoxy is used for the top layer instead of carbon-epoxy. It has been reported that LIPCA-K generates a larger manufactured curvature than LIPCA-C1. Nevertheless, the comparison of actuation responses between the two actuators has not been published. A schematic cross-section of LIPCA-C1 or LICA-K is illustrated in Figure 1.12.

Recently, Yoon, et al have introduced LIPCA-C2. The key objective of the LIPCA-C2 design is to place the neutral axis of the actuator laminate above the piezoelectric ceramic layer in order to produce compressive stresses in that layer. Based on the work of Barrett and Gross [34], Yoon and coworkers believe that the actuation displacement and force can be increased significantly by placing the ceramic layer on the compressive side of laminate at the service temperature. The actuator has five layers, namely glass-epoxy as a bottom layer, piezoceramic, glass-epoxy, carbon-epoxy, and again glass-epoxy as a top layer. Figure 1.13 shows a schematic cross-section of a LIPCA-C2 actuator. After hand lay-up, the stacked laminate is vacuum-bagged and cured at 177 °C for 2 hours in a cure oven. Experiments [33] have shown that a LIPCA-C2 beam generates twice as large a displacement as a LIPCA-C1 beam, for a simply-supported configuration.

It should be noted here that many performance tests of RAINBOW [18, 20, 23, 41, 42], THUNDER [26-28, 43-47], and LIPCA [30, 32-33, 47] actuators have been investigated and reported in the literature. Both quasi-static and dynamic actuated responses with either low or high applied electric field have been studied. Of interest are the maximum

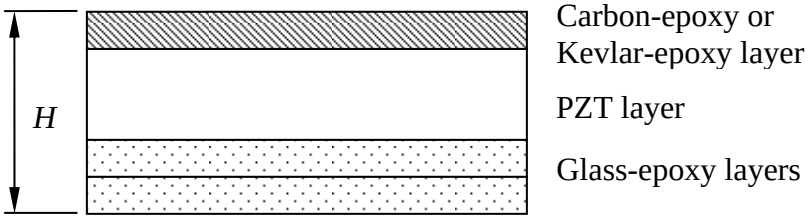

Figure 1.12: Cross-Section of LIPCA-C1 or LIPCA-K Actuator

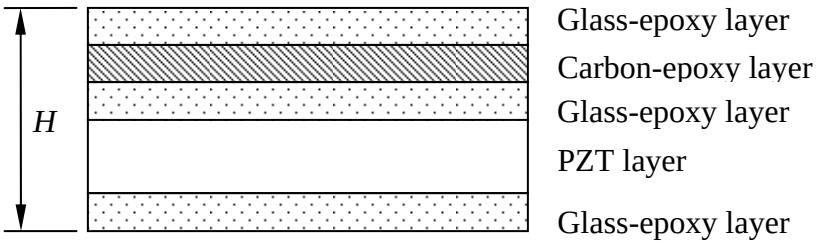

Figure 1.13: Cross-Section of LIPCA-C2 Actuator

deflections, the ability to move a load, i.e., a dead weight in most experiments reported, and the so-called blocking force, i.e., the force necessary to restrain the deflection of an actuator when an electric field is applied. However, some investigators have not paid enough attention to the effects of the boundary conditions on the test actuators. A clamped or fixed boundary condition may suppress the anticlastic curvature of the actuators dramatically, change the apparent stiffness of the actuators, and alter the actuated responses in an unaccounted for way, depending on the details of the clamping fixture, clamped position on the actuator, and how hard the actuators are clamped. Care also needs to be taken in the case of simply-supported boundary condition. This type of support has been simulated by using a knife edge, support jig, or a flat surface on which the actuator rests. Friction forces may be generated at points of contact at the supports and cause undesired effects on the actuated responses. Because of the variation in boundary conditions used in the laboratory to evaluate the performance of different actuators, it has been difficult to interpret and compare some of the reported results in the literature. Consequently, performance analyses of these newly-developed actuators with a range of boundary conditions should be carried out in order to evaluate actuator behavior due to a mechanical load and/or an applied electric field. The result would be specification of a set of boundary conditions which should then be used to design a standard performance test for actuators in order to obtain consistent experimental data and facilitate performance comparison among the actuators.

1.3.2 Previous Analysis and Mathematical Modeling

The modeling of round and rectangular RAINBOW actuators to determine the manufactured shapes and quasi-static-actuated shapes has been discussed by Jilani and Hyer [35-37], wherein RAINBOW actuators are modeled as a thin laminated plate subjected to a thermal load due to the manufacturing process and then are subjected to additive quasi-static electrical input. The energy-based Rayleigh-Ritz approach, which uses approximations to the three components of displacement, is employed to minimize the total potential energy of the actuator. Since the manufactured shape shows large out-of-plane deformation, the von Kármán assumption for nonlinear strain-displacement relations is utilized. All material properties are assumed to be uniform and independent of temperature. The actuation strains of the piezoelectric layer are assumed to vary linearly with applied electric field strength. Assumed displacement functions with 14, 35, and 81 unknown coefficients [37] are employed for round RAINBOW actuators. The analysis predicts that the manufactured shape would be dome-like or near-cylindrical. Which shape occurs is predicted to depend on the radius to total thickness ratio and also the thickness of the reduced layer relative to the unreduced layer. Additionally, for certain geometries for which the manufactured shape is near-cylindrical, there exists another possible near-cylindrical shape, i.e., multiple near-cylindrical shapes. The actuator can be snapped back and forth between these two shapes by applying moments on its edges.

Manufactured shape comparisons between the Rayleigh-Ritz approach and finite-element modeling with the commercial code ABAQUS for round RAINBOW actuators are also made by Jilani and Hyer [35-37] to verify the Rayleigh-Ritz approach. It is concluded that the 14-term approximation is not sufficient enough to achieve accurate deformations, but the 35- and 81-term approximations are in good agreement with finite-element results. The 35-term approximation is also used to predict actuated displacements, and they are found to vary almost linearly with applied voltage.

For rectangular RAINBOW actuators, a four-term approximation using the Rayleigh-Ritz approach is applied [36]. It has been shown there is a critical value of the ratio of actuator length to thickness that determines whether the manufactured out-of-plane shape is dome-like or near-cylindrical. In addition, there is a critical value of the ratio of the reduced layer thickness to total thickness which determines which shape will occur. Also, snap-through behavior between multiple near-cylindrical shapes can be observed when a snapping moment is applied on the edges of the actuator. Assuming the piezoceramic strain response varies linearly with applied electric field strength, the actuated displacement is investigated and revealed to be very nearly linear with applied field strength, like the case of the round RAINBOW actuator. Nonetheless, Jilani [35] has pointed out that there are some discrepancies in the curvature vs. cooling temperature relation between the four-term approximation and finite-element analyses from ABAQUS. Firstly, with the four-term approximation, the curvatures are uniform along the length and across the width of the actuator, but the result from ABAQUS shows the curvatures vary with position. Secondly, the four-term solution predicts the existence of a pitchfork bifurcation in the curvature vs. temperature relation, resulting in two stable solutions and one unstable solution, the stable solutions being the two near-cylindrical shapes. The ABAQUS finite-element results show no evidence of a pitchfork bifurcation. Instead one of stable paths runs smoothly over the entire domain of cooling temperature and the other stable path abruptly appears at a temperature without a connection with the former stable path. However, in general, fairly good correlations can be observed between the two theories when ignoring the bifurcation point problem. The net result is that both approaches predict that the character of the out-of-plane shape is dome-like or near-cylindrical, depending on the values of the above-mentioned thickness parameters.

A rectangular THUNDER actuator has been modeled by Hyer and Jilani [38] by employing the same energy-based Rayleigh-Ritz with four-term approximation approach as

used for rectangular RAINBOW. The similar conclusion can be drawn from the analysis from which multiple solutions for the THUNDER actuator shape and snap-through phenomenon between the solutions are obtained due to the geometrical nonlinearity nature of the problem. Again, the same bifurcation point disagreement probably would apply here, but it was not specifically mentioned in the reference.

Analyses of LIPCA have been done by Yoon, et al [30-33]. Most of the analyses employ linear classical laminated plate theory to predict curvatures and residual stresses caused by the manufacturing process. Some analysis is conducted by using geometrically nonlinear finite-element plate modeling [31]. Actuator central deflection differences of 6-7% between linear and nonlinear laminated plate models are reported. However, it must be noted that the considered cases are beam-like structures and, therefore, the nonlinearity may not exhibit any significant influence, as it would with a plate-like structure. Furthermore, according to the deformation plots resulting from the finite-element analyses in [31], the actuators develop considerable out-of-plane deformations and observable anticlastic curvatures despite their beam-like configuration. These characteristics suggest the necessity of employing the geometrically nonlinear plate theory to predict manufactured shapes of a LIPCA actuator in order to disclose interesting behavior of the actuator, especially possible multiple equilibrium shapes, snap-through phenomenon between the shapes, and critical bifurcation or limit points.

1.4 Objectives of This Research

In light of the literature review discussed above, it is clear that none of the mathematical models developed so far has been able to predict the manufactured shapes of these new unimorph-type rectangular actuators accurately. The manufactured-shape-prediction model utilized by Yoon and coworkers may not able to capture accurate out-of-plane deformations and residual thermal stresses for LIPCA actuators with other geometries

or with composite materials which require higher curing temperature because only a geometrically linear model has been presented. This is important since the cooled shapes and residual stresses can be keys to the behavior and performance of the actuators. The inclusion of geometric nonlinearities in the shape prediction of a THUNDER or RAINBOW rectangular actuator was considered by Hyer and Jilani. However, their Rayleigh-Ritz approach with a four-term displacement field approximation is too restrictive, especially because of the uniform curvature prediction and the prediction of bifurcation behavior that was not collaborated by finite-element analysis. Therefore, a more accurate model is warranted, and the development of such a model is one of the objectives here. Specifically, a more accurate Rayleigh-Ritz model is developed.

In addition, as mentioned, due to the inconsistency of the boundary conditions used by the investigators in the performance test of the actuators, a fair performance comparison among the actuators is difficult. Thus, by employing the to-be-developed mathematical model, the performance of different actuators with identical boundary condition can be predicted and compared. By studying the behavior and performance of the existing actuators in detail, an improvement of the actuators can then be proposed.

In summary, the objectives of this research are:

(1) To develop a more representative model to predict manufactured and actuated shapes of the newly-developed rectangular laminated piezoelectric actuators, such as THUNDER and LIPCA actuators

(2) To study the sensitivity of the cooled shapes and actuated deflections of existing actuator designs to material and geometric parameters

(2) To study the sensitivity of the blocking forces of existing actuator designs to material and geometric parameters.

1.5 Road Map to Subsequent Chapters

The next chapter discusses the improved Rayleigh-Ritz model developed to capture the manufactured and actuated shapes of a rectangular laminated actuator. The model is based on a 23-term approximation rather than the 4-term approximation of the previous work. The section which describes the 23-term Rayleigh-Ritz model is divided into two parts. The first part is for THUNDER-type actuators, which are composed of layers of isotropic materials. The second part is for LIPCA-type actuators, for which some layers are made of composite materials. In each part, the total potential energy, including the linear stress-strain relations for isotropic or composite materials, von Kármán nonlinear strain-displacement relations, and thermally-induced strain is formulated. The 23-term Rayleigh-Ritz approximation to the displacement fields is presented. The approximation takes into account inplane shear strains and twisting curvatures. Equilibrium conditions are obtained by extremizing the total potential energy. Stability of the equilibrium conditions is evaluated by investigating the second variation of the total potential energy. A geometrically nonlinear finite-element model utilizing ABAQUS is also developed to compare with the 23-term Rayleigh-Ritz approach. The extensions of the Rayleigh-Ritz model to include a tab region of the steel layer which is used for attaching a THUNDER actuator to a structure are discussed. In addition, the total potential energy is extended by including piezoelectrically-induced strains defined in Equation (1.3) into constitutive equations so as to predict the actuated shapes and displacement due to application of an electric field through the thickness of the piezoceramic layer. Finally, the inclusion in the total potential energy of mechanical work due to distributed edge moments and concentrated forces applied to actuators is put forward to characterize mechanical behavior and load-carrying capability of actuators.

In Chapter 3, numerical results for rectangular THUNDER actuator characteristics are presented. A THUNDER-type actuator is more preferably chosen to be a

calculation example rather than a RAINBOW actuator because of the variety of THUNDER actuators available in terms of size, geometry, and materials used, and their commercial availability, as illustrated in Figure 1.14, where the manufactured shape of actuators with a variety of shapes and sizes can be seen. In the Rayleigh-Ritz model the 23 equilibrium equations resulted from the first variation of the total potential energy developed in Chapter 2 are solved to obtain THUNDER actuator equilibrium shapes. Stability of the shapes is determined by investigating eigenvalues of the Hessian matrix generated from the second variation. The shapes of THUNDER actuators as a function of temperature relative to the manufacturing temperature are predicted, simulating the cool-down process. Manufactured shapes as a function of actuator geometry are also predicted. Validation of the equilibrium shapes computed from the Rayleigh-Ritz model is performed by comparing with the

Figure 1.14: Variety of THUNDER Available

ABAQUS model. The snap-through phenomenon between two manufactured shapes of a THUNDER actuator is discussed. Additionally, the effects of tabs on actuator shapes are investigated. At the end of this chapter, free actuation responses and blocking forces of

THUNDER actuators, namely, actuator authority, are calculated from the modified total potential energy expressions formulated in Chapter 2.

Chapters 4 and 5 consider rectangular LIPCA-C1 and LIPCA-C2 actuators, respectively. Analogous to Chapter 3, deformation and force characteristics of LIPCA-type actuators are evaluated by employing the Rayleigh-Ritz model with incorporation of composite material layers in the total potential energy. Manufactured configurations of LIPCA-C1 and LIPCA-C2 actuators as a function of their geometry are computed and checked for stability. Authorities of the actuators, i.e., free actuation response and blocking forces are calculated. Comparison of similarities and differences of the characteristics among LIPCA-C1, LIPCA-C2, and THUNDER actuators is presented and discussed.

Finally, in Chapter 6, conclusions of this research work are summarized. Exploiting geometrically nonlinear effects, design guidelines for laminated piezoelectric actuators are hypothesized and proposed. Recommendations for possible future work are specified.

Chapter 2

MODELING OF LAMINATED PIEZOELETRIC ACTUATORS: SHAPES, DEFORMATIONS, AND BLOCKING FORCES

2.1 Introduction

In this chapter, a discussion of the energy-based Rayleigh-Ritz model for predicting the deformation characteristics, including the manufactured shape, of rectangular THUNDER-type and LIPCA-type actuators is presented. Discussed are the key assumptions, the constitutive relations, the strain-displacement relations, including geometric nonlinearities, total potential energy, and variational methods. A model to predict manufactured shapes of THUNDER actuators with tabs is formulated. Extensions of the Rayleigh-Ritz model to embrace piezoelectrically-induced deformations and work done by external mechanical forces and moments are elaborated upon. Finite-element modeling using the commercial package ABAQUS, version 6.3, in order to compare with the Rayleigh-Ritz approach is also developed. A presentation of strategy to obtain multi-solutions in ABAQUS is given.

2.2 Problem Statement and Model Definition

As presented in Chapter 1 and illustrated in Figures 1.10, 1.12, and 1.13, laminated actuators are composed of a layer of active layer and several passive layers, all bonded together. A THUNDER actuator is manufactured by bonding together a layer of piezoceramic material and layers of metal with a polyimide adhesive. In contrast, with composite layers in a LIPCA actuator, fabrication is simpler, as adhesive layers are not

necessary since the polymer matrix provides the bond to the piezoceramic layer. At the first stage of manufacturing process, the initial room-temperature shape of an unbonded actuator laminate is flat. Then, the entire laminate is heated to cure the adhesive or the polymer matrix. After the adhesive or the polymer has been cured, the actuator in the curing temperature environment remains flat. When the actuator is cooled, out-of-plane deformations of the actuator develop due to the thermo-elastic property mismatches between the layers. Figure 2.1 shows schematic diagram of a rectangular laminated actuator during the cooling process. Consider the rectangular laminated actuator situated in an $x-y-z$ Cartesian coordinate system as illustrated in Figure 2.1(a). When flat at the curing temperature the laminate has inplane dimensions L_x by L_y. The total thickness of the actuator is *H*. The total numbers of layers is assumed to be *N*, which is equal to 5, 4, and 5 in the case of THUNDER, LIPCA-C1, and LIPCA-C2 actuators, respectively. The electrode layers on the piezoceramic layers in the LIPCA-C1 and LIPCA-C2 actuators are not included in the analyses. The location $z = 0$ is the geometric midsurface, here taken to be the reference surface. The lower and upper boundaries of layer 1, or the bottom layer, are located at $z = z_0 = -H/2$ and $z = z_1$, the boundaries of layer 2 at z_1 and z_2, and in general, the boundaries of the k^{th} layer at z_{k-1} and z_k. Figure 2.2 shows a general laminated actuator with the notations defined above.

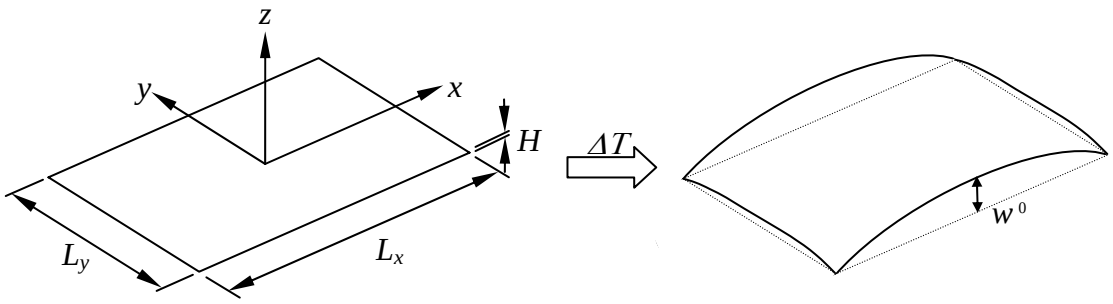

(a) Initial shape before cooling (b) Final shape after cooling

Figure 2.1: Initial and Cooled Shape and Coordinate System Used for Analysis

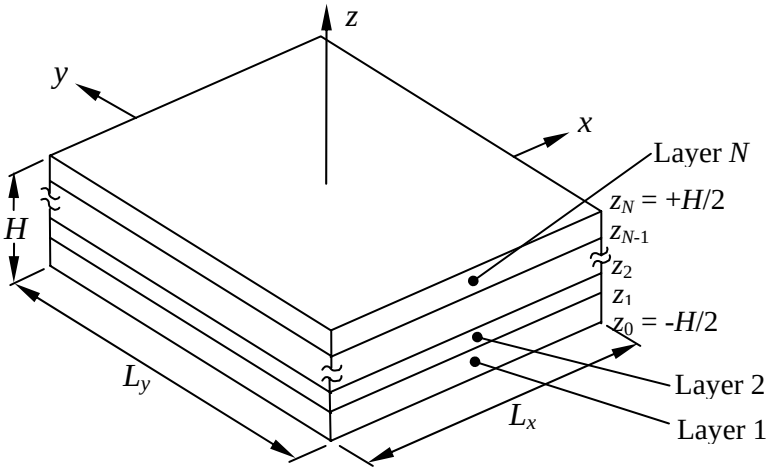

Figure 2.2: Laminated Actuator Notation

The actuator is considered a small thin layered plate, so the assumptions of classical laminated plate theory [39] are adopted. Foremost of these assumptions are: (1) a state of plane stress exists within each layer, and (2) the Kirchhoff hypothesis is valid. The plane-stress assumption allows the stress components σ_z, τ_{xz}, and τ_{yz} to be set to zero in the problem formulation. The Kirchhoff hypothesis states that the displacements in the $x-$ and $y-$directions vary linearly with the thickness coordinate, *z*, and the displacement in the $z-$direction is independent of the thickness coordinate. The net result is that the displacement of any point within the thickness of the laminate can be written in terms of the displacement of the reference surface and the $z-$coordinate of the point. Due to expected considerable out-of-plane deformation, w^o, the von Kármán approximation to Green-St. Venant strain measures is applied. Additionally, linear elastic isotropic temperature-independent material properties are assumed for each layer, including the piezoceramic layer, and the temperature changes are considered to be uniform, i.e., independent of the spatial coordinates.

2.2.1 Total Potential Energy for THUNDER-type Actuators

Based upon the plane-stress assumption, as stated above, the total potential energy of a cooled THUNDER-type actutator, Π, may be written as

$$\Pi = \frac{1}{2}\int_{-\frac{L_x}{2}}^{+\frac{L_x}{2}}\int_{-\frac{L_y}{2}}^{+\frac{L_y}{2}}\int_{-\frac{H}{2}}^{+\frac{H}{2}}\left(\left(\sigma_x - \sigma_x^T\right)\varepsilon_x + \left(\sigma_y - \sigma_y^T\right)\varepsilon_y + \tau_{xy}\gamma_{xy}\right)dxdydz \tag{2.1}$$

where integration is over the volume of the actuator. The strains in the energy expression are given by the Kirchhoff hypothesis as

$$\begin{aligned}\varepsilon_x &= \varepsilon_x^0 + z\kappa_x^0\\ \varepsilon_y &= \varepsilon_y^0 + z\kappa_y^0\\ \gamma_{xy} &= \gamma_{xy}^0 + z\kappa_{xy}^0\end{aligned} \tag{2.2}$$

The quantities ε_x^0, ε_y^0, γ_{xy}^0, and κ_x^0, κ_y^0, κ_{xy}^0 are the reference surface strains and curvatures, respectively. The reference surface quantities are functions of x and y. Including geometrically nonlinear effects, the reference surface strains are

$$\begin{aligned}\varepsilon_x^0 &= \frac{\partial u^0}{\partial x} + \underline{\frac{1}{2}\left(\frac{\partial w^0}{\partial x}\right)^2}\\ \varepsilon_y^0 &= \frac{\partial v^0}{\partial y} + \underline{\frac{1}{2}\left(\frac{\partial w^0}{\partial y}\right)^2}\\ \gamma_{xy}^0 &= \left(\frac{\partial u^0}{\partial y} + \frac{\partial v^0}{\partial x}\right) + \underline{\left(\frac{\partial w^0}{\partial x}\right)\left(\frac{\partial w^0}{\partial y}\right)}\end{aligned} \tag{2.3}$$

where u^0, v^0, and w^0 are the displacements of a point on reference surface in the x, y, and z directions, respectively. It should be pointed out that the underlined terms represent the von Kármán approximation to the full nonlinear strain-displacement relations. For classical linear plate theory, the underlined terms are not included. The reference surface curvatures are given by

$$\kappa_x^0 = -\frac{\partial^2 w^0}{\partial x^2}$$
$$\kappa_y^0 = -\frac{\partial^2 w^0}{\partial y^2} \tag{2.4}$$
$$\kappa_{xy}^0 = -2\frac{\partial^2 w^0}{\partial x \partial y}$$

For isotropic material behavior, the stress-strain relation for a given layer is

$$\sigma_x = Q\left(\varepsilon_x - \alpha\Delta T\right) + \nu Q\left(\varepsilon_y - \alpha\Delta T\right)$$
$$\sigma_y = \nu Q\left(\varepsilon_x - \alpha\Delta T\right) + Q\left(\varepsilon_y - \alpha\Delta T\right) \tag{2.5}$$
$$\tau_{xy} = \frac{1}{2}(1-\nu)Q\gamma_{xy}$$

or

$$\sigma_x = Q\varepsilon_x + \nu Q\varepsilon_y - \sigma^T$$
$$\sigma_y = \nu Q\varepsilon_x + Q\varepsilon_y - \sigma^T \tag{2.6}$$
$$\tau_{xy} = \frac{1}{2}(1-\nu)Q\gamma_{xy}$$

In the above

$$Q = \frac{E}{1-\nu^2} \text{ and } \sigma^T = (1+\nu)Q\alpha\Delta T \tag{2.7}$$

where E is the extensional modulus of the material and ν and α are the Poisson ratio and the coefficient of thermal expansion, respectively. The temperature change due to cooldown is given by ΔT. The quantity σ^T is primarily for notation but, physically, it is the hydrostatic-like stress induced in a fully restrained element of material subjected to temperature change ΔT.

If Equation (2.2) is substituted into Equation (2.1) and the results integrated through the thickness of the actuator, the total potential energy becomes

$$\Pi = \frac{1}{2}\int_{-\frac{L_x}{2}}^{+\frac{L_x}{2}}\int_{-\frac{L_y}{2}}^{+\frac{L_y}{2}}\{(N_x - \hat{N}^T\Delta T)\varepsilon_x^0 + (N_y - \hat{N}^T\Delta T)\varepsilon_y^0 + N_{xy}\gamma_{xy}^0 \tag{2.8}$$
$$+ (M_x - \hat{M}^T\Delta T)\kappa_x^0 + (M_y - \hat{M}^T\Delta T)\kappa_y^0 + M_{xy}\kappa_{xy}^0\}dxdy$$

In the above *N*s and *M*s are the force and moment resultants within the actuator and are given by

$$
\begin{aligned}
N_x &= \int_{-\frac{H}{2}}^{+\frac{H}{2}} \sigma_x dz = A\varepsilon_x^0 + A_\nu \varepsilon_y^0 + B\kappa_x^0 + B_\nu \kappa_y^0 - \hat{N}^T \Delta T \\
N_y &= \int_{-\frac{H}{2}}^{+\frac{H}{2}} \sigma_y dz = A_\nu \varepsilon_x^0 + A\varepsilon_y^0 + B_\nu \kappa_x^0 + B\kappa_y^0 - \hat{N}^T \Delta T \\
N_{xy} &= \int_{-\frac{H}{2}}^{+\frac{H}{2}} \tau_{xy} dz = \left(A - A_\nu\right)\gamma_{xy}^0 + \left(B - B_\nu\right)\kappa_{xy}^0 \\
M_x &= \int_{-\frac{H}{2}}^{+\frac{H}{2}} z\sigma_x dz = B\varepsilon_x^0 + B_\nu \varepsilon_y^0 + D\kappa_x^0 + D_\nu \kappa_y^0 - \hat{M}^T \Delta T \\
M_y &= \int_{-\frac{H}{2}}^{+\frac{H}{2}} z\sigma_y dz = B_\nu \varepsilon_x^0 + B\varepsilon_y^0 + D_\nu \kappa_x^0 + D\kappa_y^0 - \hat{M}^T \Delta T \\
M_{xy} &= \int_{-\frac{H}{2}}^{+\frac{H}{2}} z\tau_{xy} dz = \left(B - B_\nu\right)\gamma_{xy}^0 + \left(D - D_\nu\right)\kappa_{xy}^0
\end{aligned}
\tag{2.9}
$$

The quantities A, A_ν, B, B_ν, D, and D_ν are material properties that can be expressed in terms of the extensional modulus, Poisson ratio, and the interface locations of each layer as

$$
\begin{aligned}
A &= \sum_{k=1}^{N} \frac{E_k}{1-\nu_k^2}\left(z_k - z_{k-1}\right), & A_\nu &= \sum_{k=1}^{N} \frac{\nu_k E_k}{1-\nu_k^2}\left(z_k - z_{k-1}\right) \\
B &= \frac{1}{2}\sum_{k=1}^{N} \frac{E_k}{1-\nu_k^2}\left(z_k^2 - z_{k-1}^2\right), & B_\nu &= \frac{1}{2}\sum_{k=1}^{N} \frac{\nu_k E_k}{1-\nu_k^2}\left(z_k^2 - z_{k-1}^2\right) \\
D &= \frac{1}{3}\sum_{k=1}^{N} \frac{E_k}{1-\nu_k^2}\left(z_k^3 - z_{k-1}^3\right), & D_\nu &= \frac{1}{3}\sum_{k=1}^{N} \frac{\nu_k E_k}{1-\nu_k^2}\left(z_k^3 - z_{k-1}^3\right)
\end{aligned}
\tag{2.10}
$$

where the subscripts *k* on the material properties merely identify the material properties with the k^{th} layer. The quantities $\hat{N}^T$ and $\hat{M}^T$ are also material properties that involve, additionally, the coefficients of thermal expansion of each layer and are given by

$$
\hat{N}^T = \sum_{k=1}^{N} \frac{E_k \alpha_k}{1-\nu_k^2}\left(z_k - z_{k-1}\right), \qquad \hat{M}^T = \frac{1}{2}\sum_{k=1}^{N} \frac{E_k \alpha_k}{1-\nu_k^2}\left(z_k^2 - z_{k-1}^2\right) \tag{2.11}
$$

Physically, the *A*s describe the inplane stiffnesses of the layered actuator and the *D*s describe the bending stiffnesses. The *B*s are unique to layered materials. They are called the bending-stretching coupling terms, and they are also a measure of stiffness. The existence of the *B*s is one of the keys to the layered actuator deforming out-of-plane as it is cooled from the

processing temperature. The quantity $\hat{N}^T$ is the effective inplane force resultant due to a unit temperature change and $\hat{M}^T$ is the effective bending moment resultant, another key to the temperature-induced out-of-plane deformations.

2.2.2 Total Potential Energy for LIPCA-type Actuators

The total potential energy of a LIPCA-type actuator is somewhat different than that of a THUNDER-type actuator expressed in Equation (2.1). For composite materials, thermally-induced inplane shear effects are possible. Accordingly, using the Kirchhoff hypothesis of Equation (2.2), the total potential energy becomes

$$\Pi = \frac{1}{2}\int_{-\frac{L_x}{2}}^{+\frac{L_x}{2}}\int_{-\frac{L_y}{2}}^{+\frac{L_y}{2}}\int_{-\frac{H}{2}}^{+\frac{H}{2}}\left(\left(\sigma_x-\sigma_x^T\right)\left(\varepsilon_x^0+z\kappa_x^0\right)+\left(\sigma_y-\sigma_y^T\right)\left(\varepsilon_y^0+z\kappa_y^0\right)\right. \\ \left.+\left(\tau_{xy}-\tau_{xy}^T\right)\left(\gamma_{xy}^0+z\kappa_{xy}^0\right)\right)dxdydz \tag{2.12}$$

where, as before, using the von Kármán approximation of the geometric nonlinearities,

$$\varepsilon_x^0 = \frac{\partial u^0}{\partial x}+\frac{1}{2}\left(\frac{\partial w^0}{\partial x}\right)^2$$
$$\varepsilon_y^0 = \frac{\partial v^0}{\partial y}+\frac{1}{2}\left(\frac{\partial w^0}{\partial y}\right)^2 \tag{2.13}$$
$$\gamma_{xy}^0 = \left(\frac{\partial u^0}{\partial y}+\frac{\partial v^0}{\partial x}\right)+\left(\frac{\partial w^0}{\partial x}\right)\left(\frac{\partial w^0}{\partial y}\right)$$

and

$$\kappa_x^0 = -\frac{\partial^2 w^0}{\partial x^2}$$
$$\kappa_y^0 = -\frac{\partial^2 w^0}{\partial y^2} \tag{2.14}$$
$$\kappa_{xy}^0 = -2\frac{\partial^2 w^0}{\partial x \partial y}$$

As before, all the strains, curvatures, and deformations in Equations (2.13) and (2.14) are defined at the midplane (reference plane) of the LIPCA actuator so they are not a function of the coordinate variable *z*.

For composite materials, the plane-stress stress-strain relations for a given layer in the actuator coordinate system indicated in Figure 2.1 (a) are

$$\begin{Bmatrix} \sigma_x \\ \sigma_y \\ \tau_{xy} \end{Bmatrix} = \begin{bmatrix} \bar{Q}_{11} & \bar{Q}_{12} & \bar{Q}_{16} \\ \bar{Q}_{12} & \bar{Q}_{22} & \bar{Q}_{26} \\ \bar{Q}_{16} & \bar{Q}_{26} & \bar{Q}_{66} \end{bmatrix} \begin{Bmatrix} \varepsilon_x \\ \varepsilon_y \\ \gamma_{xy} \end{Bmatrix} - \begin{Bmatrix} \sigma_x^T \\ \sigma_y^T \\ \tau_{xy}^T \end{Bmatrix} \tag{2.15}$$

In the above, the $\bar{Q}_{ij}$ are the transformed reduced stiffnesses and are defined by

$$\begin{aligned}
\bar{Q}_{11} &= Q_{11}m^4 + 2\left(Q_{12} + 2Q_{66}\right)n^2m^2 + Q_{22}n^4 \\
\bar{Q}_{12} &= \left(Q_{11} + Q_{22} - 4Q_{66}\right)n^2m^2 + Q_{12}\left(n^4 + m^4\right) \\
\bar{Q}_{16} &= \left(Q_{11} - Q_{12} - 2Q_{66}\right)nm^3 + \left(Q_{12} - Q_{22} + 2Q_{66}\right)n^3m \\
\bar{Q}_{22} &= Q_{11}n^4 + 2\left(Q_{12} + 2Q_{66}\right)n^2m^2 + Q_{22}m^4 \\
\bar{Q}_{26} &= \left(Q_{11} - Q_{12} - 2Q_{66}\right)n^3m + \left(Q_{12} - Q_{22} + 2Q_{66}\right)nm^3 \\
\bar{Q}_{66} &= \left(Q_{11} + Q_{22} - 2Q_{12} - 2Q_{66}\right)n^2m^2 + Q_{66}\left(n^4 + m^4\right)
\end{aligned} \tag{2.16}$$

where $m = \cos\theta,\ \ n = \sin\theta$, in which θ is an angle between the actuator coordinate system and the fiber-direction of the composite material in the given layer. The Q_{ij} are the reduced stiffnesses and are functions of the engineering constants as follows:

$$\begin{aligned}
Q_{11} &= \frac{E_1}{1-\nu_{12}\nu_{21}} \\
Q_{12} &= \frac{\nu_{12}E_2}{1-\nu_{12}\nu_{21}} = \frac{\nu_{21}E_1}{1-\nu_{12}\nu_{21}} \\
Q_{22} &= \frac{E_2}{1-\nu_{12}\nu_{21}} \\
Q_{66} &= G_{12}
\end{aligned} \tag{2.17}$$

Here, E_1 and E_2 are inplane extensional modulus of the composite material in the fiber direction and transverse to the fiber direction, respectively. The property G_{12} is inplane shear modulus. In addition, ν_{12} and ν_{21} are major and minor Poisson's ratios, respectively,

which are related through the well-known reciprocity relation. The thermal-induced stresses (σ_x^T, σ_y^T, τ_{xy}^T) in Equations (2.12) and (2.15) are defined as

$$\begin{Bmatrix} \sigma_x^T \\ \sigma_y^T \\ \tau_{xy}^T \end{Bmatrix} = \begin{bmatrix} \bar{Q}_{11} & \bar{Q}_{12} & \bar{Q}_{16} \\ \bar{Q}_{12} & \bar{Q}_{22} & \bar{Q}_{26} \\ \bar{Q}_{16} & \bar{Q}_{26} & \bar{Q}_{66} \end{bmatrix} \begin{Bmatrix} \alpha_x \Delta T \\ \alpha_y \Delta T \\ \alpha_{xy} \Delta T \end{Bmatrix} \tag{2.18}$$

where the pertinent coefficients of thermal deformation in the actuator coordinate system are given as

$$\begin{Bmatrix} \alpha_x \\ \alpha_y \\ \alpha_{xy} \end{Bmatrix} = \begin{bmatrix} m^2 & n^2 \\ n^2 & m^2 \\ 2mn & -2mn \end{bmatrix} \begin{Bmatrix} \alpha_1 \\ \alpha_2 \end{Bmatrix} \tag{2.19}$$

and α_1 and α_2 are coefficients of thermal expansion of the composite material in the fiber direction and transverse to the fiber direction, respectively.

Integrating through the thickness of the LIPCA actuator, the total potential energy becomes

$$\begin{aligned} \Pi = \frac{1}{2} \int_{-\frac{L_x}{2}}^{+\frac{L_x}{2}} \int_{-\frac{L_y}{2}}^{+\frac{L_y}{2}} \{ & (N_x - \hat{N}_x^T \Delta T)\varepsilon_x^0 + (N_y - \hat{N}_y^T \Delta T)\varepsilon_y^0 + \left(N_{xy} - \hat{N}_{xy}^T \Delta T\right)\gamma_{xy}^0 \\ & + (M_x - \hat{M}_x^T \Delta T)\kappa_x^0 + (M_y - \hat{M}_y^T \Delta T)\kappa_y^0 + (M_{xy} - \hat{M}_{xy}^T \Delta T)\kappa_{xy}^0 \} dxdy \end{aligned} \tag{2.20}$$

where the force and moment resultants expressed in Equation (2.20) are defined as

$$\begin{Bmatrix} N_x \\ N_y \\ N_{xy} \\ M_x \\ M_y \\ M_{xy} \end{Bmatrix} = \begin{bmatrix} A_{11} & A_{12} & A_{16} & B_{11} & B_{12} & B_{16} \\ A_{12} & A_{22} & A_{26} & B_{12} & B_{22} & B_{26} \\ A_{16} & A_{26} & A_{66} & B_{16} & B_{26} & B_{66} \\ B_{11} & B_{12} & B_{16} & D_{11} & D_{12} & D_{16} \\ B_{12} & B_{22} & B_{26} & D_{12} & D_{22} & D_{26} \\ B_{16} & B_{26} & B_{66} & D_{16} & D_{26} & D_{66} \end{bmatrix} \begin{Bmatrix} \varepsilon_x^0 \\ \varepsilon_y^0 \\ \gamma_{xy}^0 \\ \kappa_x^0 \\ \kappa_y^0 \\ \kappa_{xy}^0 \end{Bmatrix} - \Delta T \begin{Bmatrix} \hat{N}_x^T \\ \hat{N}_y^T \\ \hat{N}_{xy}^T \\ \hat{M}_x^T \\ \hat{M}_y^T \\ \hat{M}_{xy}^T \end{Bmatrix} \tag{2.21}$$

where

$$
\begin{aligned}
A_{ij} &= \sum_{k=1}^{N} \bar{Q}_{ij_k} \left(z_k - z_{k-1} \right) \\
B_{ij} &= \frac{1}{2} \sum_{k=1}^{N} \bar{Q}_{ij_k} \left(z_k^2 - z_{k-1}^2 \right), \\
D_{ij} &= \frac{1}{3} \sum_{k=1}^{N} \bar{Q}_{ij_k} \left(z_k^3 - z_{k-1}^3 \right)
\end{aligned}
\tag{2.22}
$$

and

$$
\begin{aligned}
\hat{N}_x^T &= \sum_{k=1}^{N} \left(\bar{Q}_{11k} \alpha_{xk} + \bar{Q}_{12k} \alpha_{y_k} + \bar{Q}_{16k} \alpha_{xy_k} \right) \left(z_k - z_{k-1} \right) \\
\hat{N}_y^T &= \sum_{k=1}^{N} \left(\bar{Q}_{12k} \alpha_{xk} + \bar{Q}_{22k} \alpha_{y_k} + \bar{Q}_{26k} \alpha_{xy_k} \right) \left(z_k - z_{k-1} \right) \\
\hat{N}_{xy}^T &= \sum_{k=1}^{N} \left(\bar{Q}_{16k} \alpha_{xk} + \bar{Q}_{26k} \alpha_{y_k} + \bar{Q}_{66k} \alpha_{xy_k} \right) \left(z_k - z_{k-1} \right) \\
\hat{M}_x^T &= \frac{1}{2} \sum_{k=1}^{N} \left(\bar{Q}_{11k} \alpha_{xk} + \bar{Q}_{12k} \alpha_{y_k} + \bar{Q}_{16k} \alpha_{xy_k} \right) \left(z_k^2 - z_{k-1}^2 \right) \\
\hat{M}_y^T &= \frac{1}{2} \sum_{k=1}^{N} \left(\bar{Q}_{12k} \alpha_{xk} + \bar{Q}_{22k} \alpha_{y_k} + \bar{Q}_{26k} \alpha_{xy_k} \right) \left(z_k^2 - z_{k-1}^2 \right) \\
\hat{M}_{xy}^T &= \frac{1}{2} \sum_{k=1}^{N} \left(\bar{Q}_{16k} \alpha_{xk} + \bar{Q}_{26k} \alpha_{y_k} + \bar{Q}_{66k} \alpha_{xy_k} \right) \left(z_k^2 - z_{k-1}^2 \right)
\end{aligned}
\tag{2.23}
$$

Since only 0° or 90° fiber angles are used in the composite layers, and the piezoceramic layer is assumed to be isotropic in the LIPCA actuators, A_{16}, A_{26}, B_{16}, B_{26}, D_{16}, D_{26}, $\hat{N}_{xy}^T$, and $\hat{M}_{xy}^T$ are zero. Also, it should be noted that Equations (2.12)-(2.23) can be simplified to become Equation (2.1)-(2.11) when all layers in the actuator are assumed to be isotropic materials, like the case of a THUNDER-type actuator.

2.2.3 Total Potential Energy for THUNDER-Type Actuators with Tabs

The formulations of the total potential energy discussed in Sections 2.2.1 and 2.2.2 are for the laminated actuators neglecting the existence of tabs because all the layers are assumed to have the same inplane dimensions L_x by L_y. Generally, tabs are included in the construction of an actuator by making some or all of the passive layers longer than the piezoceramic layer, as can be noticed in Figures 1.9 and 1.14, and 1.11 for THUNDER and LIPCA actuators, respectively. The extra length extends outward beyond two opposite edges of the piezoceramic and the other passive layers, and holes or slots are then machined in the

extensions for accepting small screws or other mechanical fasteners for attaching the actuator to a base or structure. Shown in Figure 2.3 are schematic diagrams of a THUNDER actuator with tabs on the *x*-edges before being cooled to room temperature. Here it will be assumed that the steel layer is 20% longer in the *x*-direction than the piezoceramic and aluminum layers. The notation L_x denotes the length of the piezoceramic and aluminum layers, i.e., the active portion of the actuator, and L_x^t denotes the length of the tab on each edge of the actuator. Referring to Figure 2.3, there is thus a 10% additional length beyond $x = +L_x/2$ and 10% beyond $x = -L_x/2$.

To calculate manufactured shapes of THUNDER actuators with tabs, the total potential energy in Equation (2.8) is modified in order to take into account the tab regions.

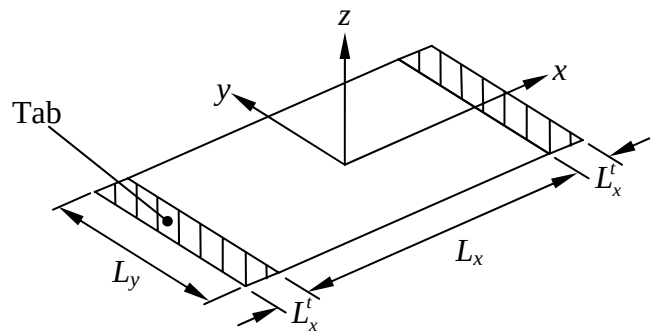

(a) Initial Shape of THUNDER Actuator with Tabs

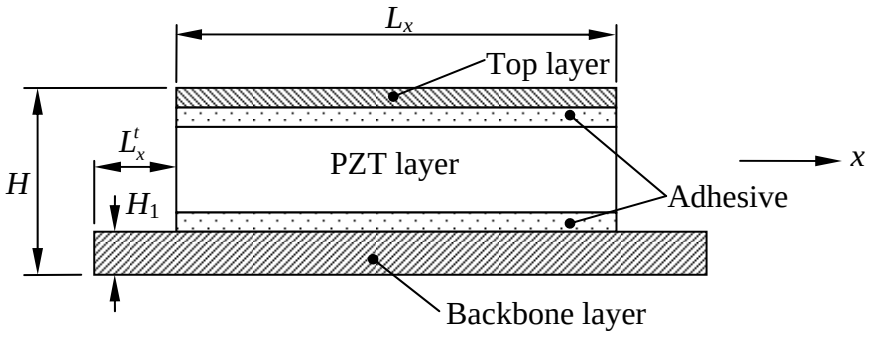

(b) Cross Section of THUNDER Actuator with Tabs

Figure 2.3: THUNDER Actuator with Tabs

The additional strain energy associated with the tabs on both ends of the actuator can be expressed as

$$U_t = \int_{+\frac{L_x}{2}}^{+\frac{L_x}{2}+L_x^t} \int_{-\frac{L_y}{2}}^{+\frac{L_y}{2}} \int_{-\frac{H}{2}}^{-\frac{H}{2}+H_1} \left(\left(\sigma_x - \sigma_x^T \right) \varepsilon_x + \left(\sigma_y - \sigma_y^T \right) \varepsilon_y + \tau_{xy} \gamma_{xy} \right) dxdydz \qquad (2.24)$$

All stresses defined in Equation (2.24) are stresses in the backbone layer, which is stainless steel in this case. Note that there is no factor of ½ in front of the integral sign due to its cancellation with the factor of two from doubling the strain energy from just one tab. Consequently, the modified total potential energy including the strain energy of the tabs is written as

$$\Pi = \frac{1}{2} \int_{-\frac{L_x}{2}}^{+\frac{L_x}{2}} \int_{-\frac{L_y}{2}}^{+\frac{L_y}{2}} \{ (N_x - \hat{N}^T \Delta T) \varepsilon_x^0 + (N_y - \hat{N}^T \Delta T) \varepsilon_y^0 + N_{xy} \gamma_{xy}^0 \qquad (2.25)$$
$$+ (M_x - \hat{M}^T \Delta T) \kappa_x^0 + (M_y - \hat{M}^T \Delta T) \kappa_y^0 + M_{xy} \kappa_{xy}^0 \} dxdy + U_t$$

Before closure of this section, it should be noted here that all total potential energy expressions developed in this dissertation except Equation (2.25) do not consider the existence of tabs. It is believed that contrary to some designs that include rather lengthy tabs, for small actuators, alternative fastening techniques, such as bonding, are applicable since the force levels are not large. Tabs add weight to the actuator and represent a region of the actuator that contributes nothing to the actuation capability.

2.2.4 The Rayleigh-Ritz Approach

After formulating the total potential energy of a cooled laminated actuator, approximate solutions of this problem can be obtained by employing the Rayleigh-Ritz approach. This is done by approximating the reference surface displacement fields in the forms of linear combinations of known functions multiplied by unkown coefficients, which are solved for by extremizing the total potential energy with respect to these coefficients. Based on the observed shapes of real actuators (see Figure 1.14) and extending the previous analysis conducted by Jilani and Hyer [35, 36], the displacement fields are approximated as

$$
\begin{aligned}
w^0(x,y) &= c_1x^2 + c_2y^2 + c_3x^4 + c_4y^4 + c_5x^2y^2 + c_6x^4y^2 + c_7x^2y^4 + c_8x^6 + c_9y^6 \\
u^0(x,y) &= c_{10}x + c_{12}x^3 + c_{14}xy^2 + c_{16}x^5 + c_{18}x^3y^2 + c_{20}xy^4 + c_{22}x^7 \\
v^0(x,y) &= c_{11}y + c_{13}y^3 + c_{15}x^2y + c_{17}y^5 + c_{19}x^2y^3 + c_{21}x^4y + c_{23}y^7
\end{aligned}
\tag{2.26}
$$

There are 23 unknown coefficients in the above equations. The first two terms for $w^0(x,y)$ and the first terms for $u^0(x,y)$ and $v^0(x,y)$ represent the linear solution to the problem, which can be determined in closed form, as shown in Appendix A. The higher powers of *x* and *y* represent deviations from the linear solution. Additionally, it should be noted that the polynomials used for $w^0(x,y)$ are a linear combination of monomial even functions of *x* and *y* complete to order six, whereas the polynomials used for $u^0(x,y)$ ($v^0(x,y)$) are linear combinations of monomial odd functions of *x* (*y*) and even functions of *y* (*x*) complete to order five. The assumed functions are intuitively selected by considering the symmetry and antisymmetry of the various components of the deformations with respect to *x*- and *y*- axes (see Figure 2.1). The orders of the polynomials for u^0, v^0, and w^0 are systematically chosen by examining the convergence of unknown coefficients after extremizing the total potential energy. The validation of these assumed deformation fields will be shown later when comparing with the finite-element analyses from ABAQUS.

To proceed, the expressions for the three components of displacement are substituted into the strain and curvature expressions of Equations (2.3) and (2.4), and these in turn, are substituted into the expressions for the force and moment resultants, Equation (2.9). All of these results are then substituted into the expression for the total potential energy, Equation (2.8). Integration with respect to *x* and *y* can be carried out explicitly, The final result is an algebraic expression for the total potential energy that is a function of the material properties, the geometric dimensions of the actuator and, of course, the 23 unknown coefficients.

At this point, the actuator, which was initially described as a continuous laminated plate, is discretized into a lumped system with 23 degrees of freedom governing the shape. The total potential energy of this lumped system needs to be extremized in order

to obtain the equilibrium shape of the actuator, or, in the other words, to solve for the 23 unknown coefficients. The extremization is accomplished by taking the first variation of the total potential energy with respect to each unknown coefficient, as indicated below:

$$\delta\Pi = \frac{\partial\Pi}{\partial c_1}\delta c_1 + \frac{\partial\Pi}{\partial c_2}\delta c_2 + \ldots + \frac{\partial\Pi}{\partial c_{22}}\delta c_{22} + \frac{\partial\Pi}{\partial c_{23}}\delta c_{23} \tag{2.27}$$
$$= f_{c_1}\delta c_1 + f_{c_2}\delta c_2 + \ldots + f_{c_{22}}\delta c_{22} + f_{c_{23}}\delta c_{23}$$

As the first variation must be zero for equilibrium, the result leads to 23 nonlinear algebraic equations for the 23 unknowns $c_1, c_2, \ldots, c_{22}, c_{23}$. These equations are of the form

$$f_{c_1} = 0 \qquad f_{c_2} = 0 \;\ldots\; f_{c_{22}} = 0 \qquad f_{c_{23}} = 0 \tag{2. 28}$$

They can be solved and numerical results obtained for specific values of material and geometric parameters with the aid of *Mathematica*™ [40].

The second variation of the total potential energy also must be examined in order to evaluate stability of the equilibrium shapes found above. The second variation can be written as

$$\delta^2\Pi = \{q\}^T [C]\{q\} \tag{2.29}$$

where

$$\{q\}^T = \{\delta c_1 \quad \delta c_2 \quad \ldots \quad \delta c_{22} \quad \delta c_{23}\} \tag{2.30}$$

and the matrix $[C]$ is called Hessian matrix given by

$$[C] = \begin{bmatrix} \frac{\partial f_{c_1}}{\partial c_1} & \frac{\partial f_{c_1}}{\partial c_2} & \ldots & \frac{\partial f_{c_1}}{\partial c_{22}} & \frac{\partial f_{c_1}}{\partial c_{23}} \\ \frac{\partial f_{c_2}}{\partial c_1} & \frac{\partial f_{c_2}}{\partial c_2} & \ldots & \frac{\partial f_{c_2}}{\partial c_{22}} & \frac{\partial f_{c_2}}{\partial c_{23}} \\ \vdots & \vdots & \ddots & \vdots & \vdots \\ \frac{\partial f_{c_{22}}}{\partial c_1} & \frac{\partial f_{c_{22}}}{\partial c_2} & \ldots & \frac{\partial f_{c_{22}}}{\partial c_{22}} & \frac{\partial f_{c_{22}}}{\partial c_{23}} \\ \frac{\partial f_{c_{23}}}{\partial c_1} & \frac{\partial f_{c_{23}}}{\partial c_2} & \ldots & \frac{\partial f_{c_{23}}}{\partial c_{22}} & \frac{\partial f_{c_{23}}}{\partial c_{23}} \end{bmatrix} \tag{2.31}$$

The equilibrium shape is stable if and only if $\delta^2\Pi$ is positive for every vector $\{q\}$, or equivalently, the Hessian matrix is positive definite. The shape is unstable if $\delta^2\Pi$ is negative for any vector $\{q\}$, or the Hessian matrix is not positive definite. (It is not necessary for it to be negative definite.) In this analysis, the positive definiteness of matrix $[C]$ is examined by calculating its eigenvalues. If all eigenvalues are positive, $[C]$ is positive definite and the equilibrium solution is stable, otherwise if any eigenvalue is zero, $[C]$ is semi-positive definite and the equilibrium solution is critical, or if any eigenvalue is negative, the equilibrium solution is unstable.

2.3 Modeling Extension to Include Application of Electric Field

The strain response of a piezoelectric material when an electric field is applied can be quite complicated. In the case of a high applied quasi-static electric field relative to the coercive field, the motion of Weiss domain boundaries (domain walls) and electrostrictive effects, i.e., electrostrictive strain is proportional to the square of electric field, can be significant. Thus, the relationship between piezoelectrically-induced strains and an applied electric field may not be linear. Also, there is the potential for interaction between the state of stress in the piezoelectric material and electric field effects. Furthermore, the presence of the electric field can change the elastic properties of the piezoelectric material, the so-called ferroelastic effect. If the electric field is periodic in time, the response can be frequency dependent, and include hysteresis. However, to gain physical insight into the change in curvature caused by activating the piezoceramic layer with an electric field through its thickness, the linear converse piezoelectric effect in Equation (1.3) is assumed and employed in the following model regardless of the magnitude and rate of change with time of the applied electric field.

2.3.1 Total Potential Energy

The extension of the energy-based Rayleigh-Ritz model to include the piezoelectric effect is analogous to the model for the dilatational strains produced by a temperature change in isotropic materials, an effect modeled in Section 2.2. Therefore, piezoelectric effects can be added to the effects of a temperature change. The plane-stress stress-strain relations for a THUNDER-type actuator, which were given in Equation 2.5, are modified as follows:

$$\begin{aligned}\sigma_x &= Q\left(\varepsilon_x - \alpha\Delta T - d_{31}E_3\right) + \nu Q\left(\varepsilon_y - \alpha\Delta T - d_{31}E_3\right)\\ \sigma_y &= \nu Q\left(\varepsilon_x - \alpha\Delta T - d_{31}E_3\right) + Q\left(\varepsilon_y - \alpha\Delta T - d_{31}E_3\right)\\ \tau_{xy} &= \frac{1}{2}(1-\nu)Q\gamma_{xy}\end{aligned} \tag{2.32}$$

or

$$\begin{aligned}\sigma_x &= Q\varepsilon_x + \nu Q\varepsilon_y - \sigma^T - \sigma^E\\ \sigma_y &= \nu Q\varepsilon_x + Q\varepsilon_y - \sigma^T - \sigma^E\\ \tau_{xy} &= \frac{1}{2}(1-\nu)Q\gamma_{xy}\end{aligned} \tag{2.33}$$

where

$$\sigma^E = (1+\nu)Qd_{31}E_3 \tag{2.34}$$

In the above, d_{31} is the transverse piezoelectric coefficient of the piezoceramic material and $d_{31}E_3$ is the dilatational strain in the *x*- and *y*-directions produced by the electric field E_3 in the *z*-direction. It is assumed the piezoelectric effect is the same in the *x*- and *y*-directions. The similarities between dilatational strains due to a temperature change and converse piezoelectric effect in Equations (2.32) and (2.33) are obvious.

Substitution of the stress-strain relations in Equation (2.33) into the total potential energy expression of Equation (2.32) and again integrating through the thickness results in the following terms being appended to the integrand of the total potential energy expression of Equation (2.8):

$$\hat{N}^E E_3 = \left\{ \int_{-\frac{H}{2}}^{+\frac{H}{2}} \left(Q\left(1+\nu\right) d_{31} \right) dz \right\} E_3$$

$$= \left\{ \sum_{k=1}^{N} \frac{E_k d_{31k}}{1-\nu_k} \left(z_k - z_{k-1} \right) \right\} E_3 \tag{2.35}$$

$$\hat{M}^E E_3 = \left\{ \int_{-\frac{H}{2}}^{+\frac{H}{2}} \left(Q\left(1+\nu\right) d_{31} \right) z dz \right\} E_3$$

$$= \left\{ \frac{1}{2} \sum_{k=1}^{N} \frac{E_k d_{31k}}{1-\nu_k} \left(z_k^2 - z_{k-1}^2 \right) \right\} E_3 \tag{2.36}$$

By the form of these terms, it is obvious that they should be inserted, with a minus sign, next to $\hat{N}^T \Delta T$ and $\hat{M}^T \Delta T$ in Equation (2.8). Certainly the only layer contributing to the summations in the above expressions is the piezoceramic layer.

For LIPCA-type actuators, the extension of the total potential energy to include the converse piezoelectric effect is analogous to that of THUNDER-type actuators. The effects of the dilatational piezoelectrically-induced strains produced by an electric field need to be included in the constitutive equation of Equation (2.15). Thus, the modified stress-strain relations for a given layer in a LIPCA actuator is written as

$$\begin{Bmatrix} \sigma_x \\ \sigma_y \\ \tau_{xy} \end{Bmatrix} = \begin{bmatrix} \bar{Q}_{11} & \bar{Q}_{12} & \bar{Q}_{16} \\ \bar{Q}_{12} & \bar{Q}_{22} & \bar{Q}_{26} \\ \bar{Q}_{16} & \bar{Q}_{26} & \bar{Q}_{66} \end{bmatrix} \begin{Bmatrix} \varepsilon_x \\ \varepsilon_y \\ \gamma_{xy} \end{Bmatrix} - \begin{Bmatrix} \sigma_x^T \\ \sigma_y^T \\ \tau_{xy}^T \end{Bmatrix} - \begin{Bmatrix} \sigma_x^E \\ \sigma_y^E \\ \tau_{xy}^E \end{Bmatrix} \tag{2.37}$$

where $\sigma_x^E, \sigma_y^E,$ and τ_{xy}^E are piezoelectrically-induced stresses, which are related to the piezoelectrically-induced strains as follows:

$$\begin{Bmatrix} \sigma_x^E \\ \sigma_y^E \\ \tau_{xy}^E \end{Bmatrix} = \begin{bmatrix} \bar{Q}_{11} & \bar{Q}_{12} \\ \bar{Q}_{12} & \bar{Q}_{22} \\ \bar{Q}_{22} & \bar{Q}_{26} \end{bmatrix} \begin{Bmatrix} d_{31} E_3 \\ d_{31} E_3 \end{Bmatrix} \tag{2.38}$$

Again, it is assumed the piezoelectric effect is the same in the *x*- and *y*-directions.

Including Equation (2.38) in Equation (2.12) in the same manner as the thermally-induced strains were included results in effective piezoelectrical inplane force and moment resultants, which are expressed as

$$\begin{aligned}
\hat{N}_x^E E_3 &= \left\{\sum_{k=1}^{N}\left(\bar{Q}_{11k}d_{31k} + \bar{Q}_{12k}d_{31k}\right)\left(z_k - z_{k-1}\right)\right\}E_3 \\
\hat{N}_y^E E_3 &= \left\{\sum_{k=1}^{N}\left(\bar{Q}_{12k}d_{31k} + \bar{Q}_{22k}d_{31k}\right)\left(z_k - z_{k-1}\right)\right\}E_3 \\
\hat{N}_{xy}^E E_3 &= \left\{\sum_{k=1}^{N}\left(\bar{Q}_{16k}d_{31k} + \bar{Q}_{26k}d_{31k}\right)\left(z_k - z_{k-1}\right)\right\}E_3 \\
\hat{M}_x^E E_3 &= \left\{\frac{1}{2}\sum_{k=1}^{N}\left(\bar{Q}_{11k}d_{31k} + \bar{Q}_{12k}d_{31k}\right)\left(z_k^2 - z_{k-1}^2\right)\right\}E_3 \\
\hat{M}_y^E E_3 &= \left\{\frac{1}{2}\sum_{k=1}^{N}\left(\bar{Q}_{12k}d_{31k} + \bar{Q}_{22k}d_{31k}\right)\left(z_k^2 - z_{k-1}^2\right)\right\}E_3 \\
\hat{M}_{xy}^E E_3 &= \left\{\frac{1}{2}\sum_{k=1}^{N}\left(\bar{Q}_{16k}d_{31k} + \bar{Q}_{26k}d_{31k}\right)\left(z_k^2 - z_{k-1}^2\right)\right\}E_3
\end{aligned} \tag{2.39}$$

These effective force and moment resultants, with a minus sign, are appended the integrand of the total potential energy expression of Equation (2.20) adjacent to the effective force and moment resultants caused by thermal effect from cooling process. As stated above, the only layer contributing to the summations in Equation (2.39) is the piezoceramic layer.

2.3.2 The Rayleigh-Ritz Approach

To determine the predicted deformations caused by the electric field, the same 23-term approximation to the displacement fields given in Equation (2.26) is used in the appended total potential energy expression and 23 simultaneous nonlinear algebraic equations result. The forcing terms now include the additive effects of temperature change and electric field, and the solution for the coefficients $c_1, c_2, \ldots, c_{22}, c_{23}$ reflect the totality of the effects.

2.4 Modeling Extension to Include Mechanical Moments and Forces

When in use, besides being subjected to an application of electric field, an actuator can be subjected to an applied mechanical load, i.e., a bending moment and/or force. The associated deformations and stresses developed due to the simultaneously applied electric field and mechanical load could be catastrophic and stop the actuator from functioning. Therefore, it is necessary to be able to predict the deformations and stresses under the action of loads in order to be able to analyze the operational range and eventually design a suitable actuator for a specific working condition. Again, the Rayleigh-Ritz model can be implemented to investigate these issues by including an additional term representing the work done by the applied moment and force.

2.4.1 Total Potential Energy

The work term caused by the moments, W_M, as illustrated in Figure 2.4, can be written as

$$W_M = \int_{-\frac{L_y}{2}}^{+\frac{L_y}{2}} \left\{ M_x^s \left(-\frac{\partial w^0}{\partial x} \right)\Bigg|_{x=+\frac{L_x}{2}} + M_x^s \left(\frac{\partial w^0}{\partial x} \right)\Bigg|_{x=-\frac{L_x}{2}} \right\} dy + \int_{-\frac{L_x}{2}}^{+\frac{L_x}{2}} \left\{ M_y^s \left(-\frac{\partial w^0}{\partial y} \right)\Bigg|_{y=+\frac{L_y}{2}} + M_y^s \left(\frac{\partial w^0}{\partial y} \right)\Bigg|_{y=-\frac{L_y}{2}} \right\} dx \tag{2.40}$$

where M_x^s is the uniform moment applied along the edges $x = +L_x/2$ and $x = -L_x/2$, and M_y^s the uniform moment applied along the edges $y = +L_y/2$ and $y = -L_y/2$. The minus signs in front of the out-of-plane deflection gradients evaluated at the positive x- and y-edges indicate that the positive applied moments illustrated in Figure 2.4 cause the negative rotations on the corresponding edges. On the contrary, the minus signs are not required for the out-of-plane deflection gradients evaluated at the negative x- and y-edges because the positive applied moments cause the positive rotations on these edges. For equilibrium, the

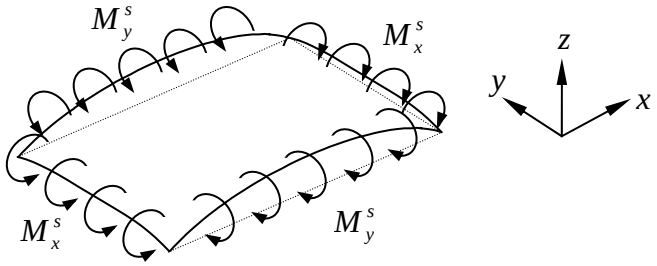

Figure 2.4: Actuator Subjected to Positive Edge Moments

moments applied on the positive edges are equal in magnitude to the ones applied on the negative edges.

The work done by forces applied to the actuator can be formulated similarly to Equation (2.40). As an example and as a way to further determine the force-carrying capability of the actuator based on the already-developed Rayleigh-Ritz model in Sections 2.2.1 and 2.2.2, the force application schematic is illustrated in Figure 2.5. It is assumed that the actuator is supported in the center, as shown. Hence, the corresponding work done can be expressed as

$$W_F = P\,w^0\Big|_{(x,y)=\left(+\frac{L_x}{2},0\right)} + P\,w^0\Big|_{(x,y)=\left(-\frac{L_x}{2},0\right)} + R\,u\Big|_{(x,y,z)=\left(+\frac{L_x}{2},0,-\frac{H}{2}\right)} - R\,u\Big|_{(x,y,z)=\left(-\frac{L_x}{2},0,-\frac{H}{2}\right)} \quad (2.41)$$

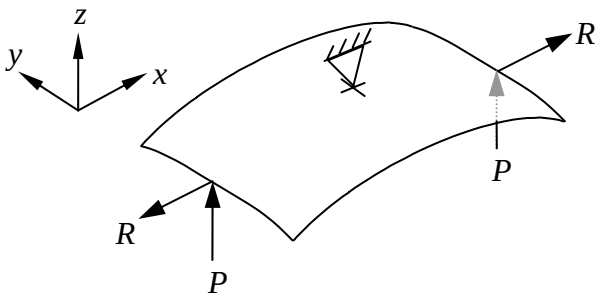

Figure 2.5: Actuator Subjected to Concentrated Forces

where u is the x-direction deformation at a point in the actuator where the load is applied and is defined as

$$u = u^0 - z\frac{\partial w^0}{\partial x} \tag{2.42}$$

It should be noted that the u displacement is evaluated at $z = -H/2$, i.e., the lower surface of the actuator, as that is most likely where contact with the edge of the actuator would be made, especially for force P.

Thus, the modified total potential energy for THUNDER actuators subjected to applications of an electric field and the mechanical loads is

$$\Pi = \frac{1}{2}\int_{-\frac{L_x}{2}}^{+\frac{L_x}{2}}\int_{-\frac{L_y}{2}}^{+\frac{L_y}{2}}\{(N_x - \hat{N}^T\Delta T - \hat{N}^E E_3)\varepsilon_x^0 + (N_y - \hat{N}^T\Delta T - \hat{N}^E E_3)\varepsilon_y^0 + N_{xy}\gamma_{xy}^0$$
$$+ (M_x - \hat{M}^T\Delta T - \hat{M}^E E_3)\kappa_x^0 + (M_y - \hat{M}^T\Delta T - \hat{M}^E E_3)\kappa_y^0 + M_{xy}\kappa_{xy}^0\}dxdy - W_M - W_F \tag{2.43}$$

Likewise, the modified total potential energy for LIPCA actuators is written as

$$\Pi = \frac{1}{2}\int_{-\frac{L_x}{2}}^{+\frac{L_x}{2}}\int_{-\frac{L_y}{2}}^{+\frac{L_y}{2}}\{(N_x - \hat{N}_x^T\Delta T - \hat{N}_x^E E_3)\varepsilon_x^0 + (N_y - \hat{N}_y^T\Delta T - \hat{N}_y^E E_3)\varepsilon_y^0$$
$$+ \left(N_{xy} - \hat{N}_{xy}^T\Delta T - \hat{N}_{xy}^E E_3\right)\gamma_{xy}^0 + (M_x - \hat{M}_x^T\Delta T - \hat{M}_x^E E_3)\kappa_x^0$$
$$+ (M_y - \hat{M}_y^T\Delta T - \hat{M}_y^E E_3)\kappa_y^0 + (M_{xy} - \hat{M}_{xy}^T\Delta T - \hat{M}_{xy}^E E_3)\kappa_{xy}^0\}dxdy - W_M - W_F \tag{2.44}$$

2.4.2 The Rayleigh-Ritz Approach

Overall deformation shapes and the associated inplane stresses can be evaluated by employing the Rayleigh-Ritz approach with the same 23-term approximate displacement field as presented in Section 2.2.4, namely Equation (2.26) The forcing terms in this case include the temperature change effect, piezoelectric effect, and mechanical load effect.

This modeling extension can be used to further characterize the physical behavior and performance of the actuator. For instance, if there exist multiple manufactured shapes of the actuator due to geometrically nonlinear effects, the magnitude and direction of the edge moments that can be applied to snap the actuator from one shape to another shape

can be investigated. Additionally, blocking forces of the actuator can be determined by using the total potential energy of Equation (2.44) and by implementing the Rayleigh-Ritz approach with a supplementary algorithm. This algorithm will be discussed in the next section.

2.4.3 Blocking Force Calculation

As discussed in Section 1.3.1, a blocking force is another measure of performance of laminated actuators. In practice, a blocking force is measured by using a force load cell or force sensor. The load cell is held unmovable and its probe is bonded to a point of an actuator so the point is fixed in the direction of the probe alignment, regardless of the electric field strength applied to the actuator. Normally, the desired point is selected at the region where the deflection of the actuators is maximal in order to obtain strong output signal from the probe. Thus, based on the extended model developed in Section 2.4.1 and illustrated in Figure 2.5, forces P, or P and R, can be used to represent blocking forces of the actuator, since the maximum deflection occurs on the x-edge. If the subscript 'bl' denotes blocking force, then P_{bl} is the force P evaluated in such a way that when the actuator is subjected to an electric field there is no motion in the z-direction (no w^0) at the point of the applied force relative to no-field configuration. Similarly, forces P_{bl} and R_{bl} are the forces P and R evaluated in such a way that there is no motion in both the z- and x-directions (no w^0 and u, respectively). Viewing differently, P_{bl} or P_{bl} and R_{bl} are equivalent to the forces generated at the supports of the actuator as pinned-roller or pinned-pinned support conditions, respectively, when the actuator is clamped at the central point and subjected to an electric field, as illustrated in Figure 2.6.

Obviously, the approximate displacement field of Equation (2.26) cannot be used directly to represent the kinematics of the pinned-roller and pinned-pinned cases. Furthermore, with the variational approach, the determination of the forces at the location of the kinematic constraints is not straightforward. However, considerable expenditure of time

and effort were devoted to developing computational schemes based on the approximate displacement field of Equation (2.26). Thus, this displacement field was used as the basis to compute the blocking forces associated with the pinned-roller and pinned-pinned cases of Figure 2.6 as follows:

To calculate the blocking force for a pinned-roller support case by using the displacement field of Equation (2.26), P_{bl} is the vertical force applied at the support position $\left((x, y, z) = (\pm L_x/2, 0, -H/2)\right)$ such that the relative deformation w^0 at that position due to the force and electric field strength E cancels the relative deformation w^0 resulting from only the applied electric field strength E. (It is now clear why in previous equations contact was assumed to occur at $z = -H/2$, the bottom surface of the actuator.) Consequently, an additional iterative algorithm can be created to directly solve for P_{bl}, as shown in the flowchart in Figure 2.7, by employing the following algebraic equation;

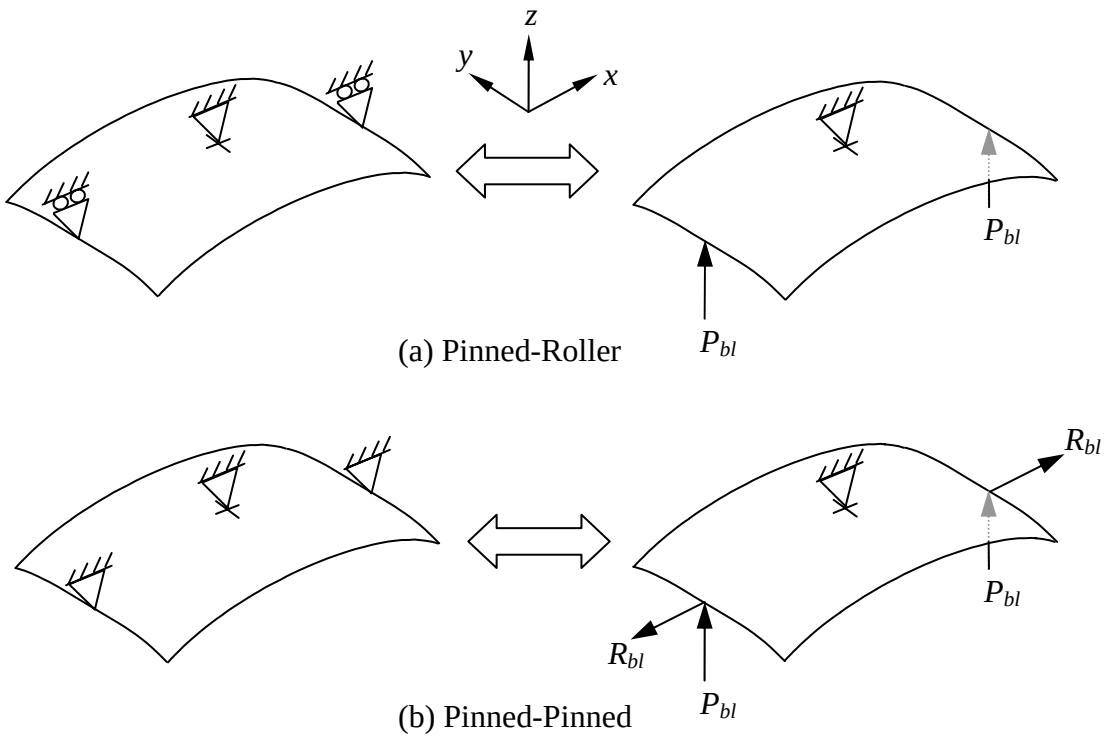

Figure 2.6: Equivalence between Mathematical and Physical Models

$$\Delta w^0\Big|_{(x,y)=(+L_x/2,0)} = a_1 P + a_2 \tag{2.45}$$

where $\Delta w^0\Big|_{(x,y)=(+L_x/2,0)}$ is relative deformation w^0 at $(x,y)=(+L_x/2,0)$ due to the force P and electric field strength E. In terms of a mathematical expression,

$$\Delta w^0\Big|_{(x,y)=(+L_x/2,0)} = w^0\left(E_3 = E, P \neq 0\right)\Big|_{(x,y)=(+L_x/2,0)} - w^0\left(E_3 = 0, P = 0\right)\Big|_{(x,y)=(+L_x/2,0)} \tag{2.46}$$

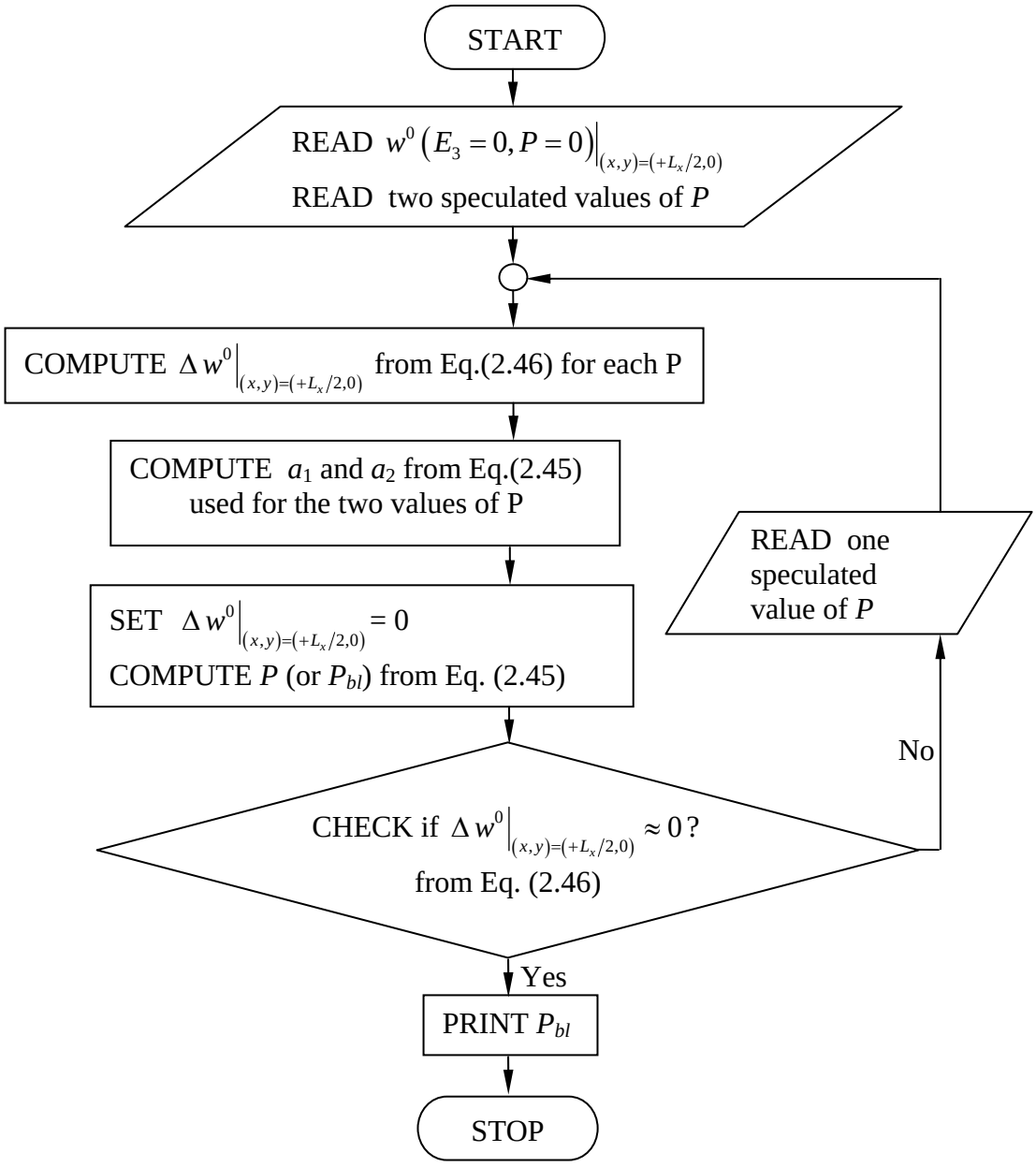

Figure 2.7: Flowchart of P_{bl} Calculation

Constants a_1 and a_2 are blocking force-deflection parameters for the pinned-roller case, and they are determined and updated in each iteration used to determine the value of P_{bl}. As shown in Figure 2.7, the computation starts with speculating two possible blocking force values and substituting them each into Equation (2.46). This results in two values of $\Delta w^0\big|_{(x,y)=(+L_x/2,0)}$ and the associated two values of P, which in turn are each substituted in Equation (2.45) to give two algebraic equations in a_1 and a_2. With two algebraic equations, parameters a_1 and a_2 can be evaluated. Then, setting $\Delta w^0\big|_{(x,y)=(+L_x/2,0)}$ equal to zero, the value of P, which is now P_{bl}, can be calculated from (2.45). However, the calculated P_{bl} might not be accurate, since the parameters a_1 and a_2 are obtained from the two initially speculated forces P. Therefore, iterations need to be conducted to obtain a more accurate estimate of P_{bl}. To do so, another speculated value of P, in addition to the just-calculated value, P_{bl}, can be used. The new speculated P can be more systematically chosen based on the first P_{bl} value obtained. For example, a value of P just 10% difference from the P_{bl} value first calculated could be used as the new speculated P. Then, the same calculations could be repeated and as a result, a more accurate value of P_{bl} is acquired. Iteration will continue until the value of P_{bl} converges and approximately satisfies

$$\left[w^0\left(E_3 = E, P = P_{bl}\right) - w^0\left(E_3 = 0, P = 0\right)\right]\Big|_{(x,y)=(+L_x/2,0)} = 0 \qquad (2.47)$$

Likewise, blocking forces P_{bl} and R_{bl} for the pinned-pinned case can be computed by implementing another iterative algorithm, of which flowchart is illustrated in Figure 2.8. Note that rather than checking only relative out-of-plane deformation, as done in the pinned-roller case, both relative inplane and out-of-plane deformations need to be taken into consideration simultaneously in this case. Therefore, analogous to Equation (2.45), the assumed linear relations between the two relative deformations and forces P and R are

$$\Delta w^0\big|_{(x,y)=(+L_x/2,0)} = b_1 P + b_2 R + b_3 \qquad (2.48)$$

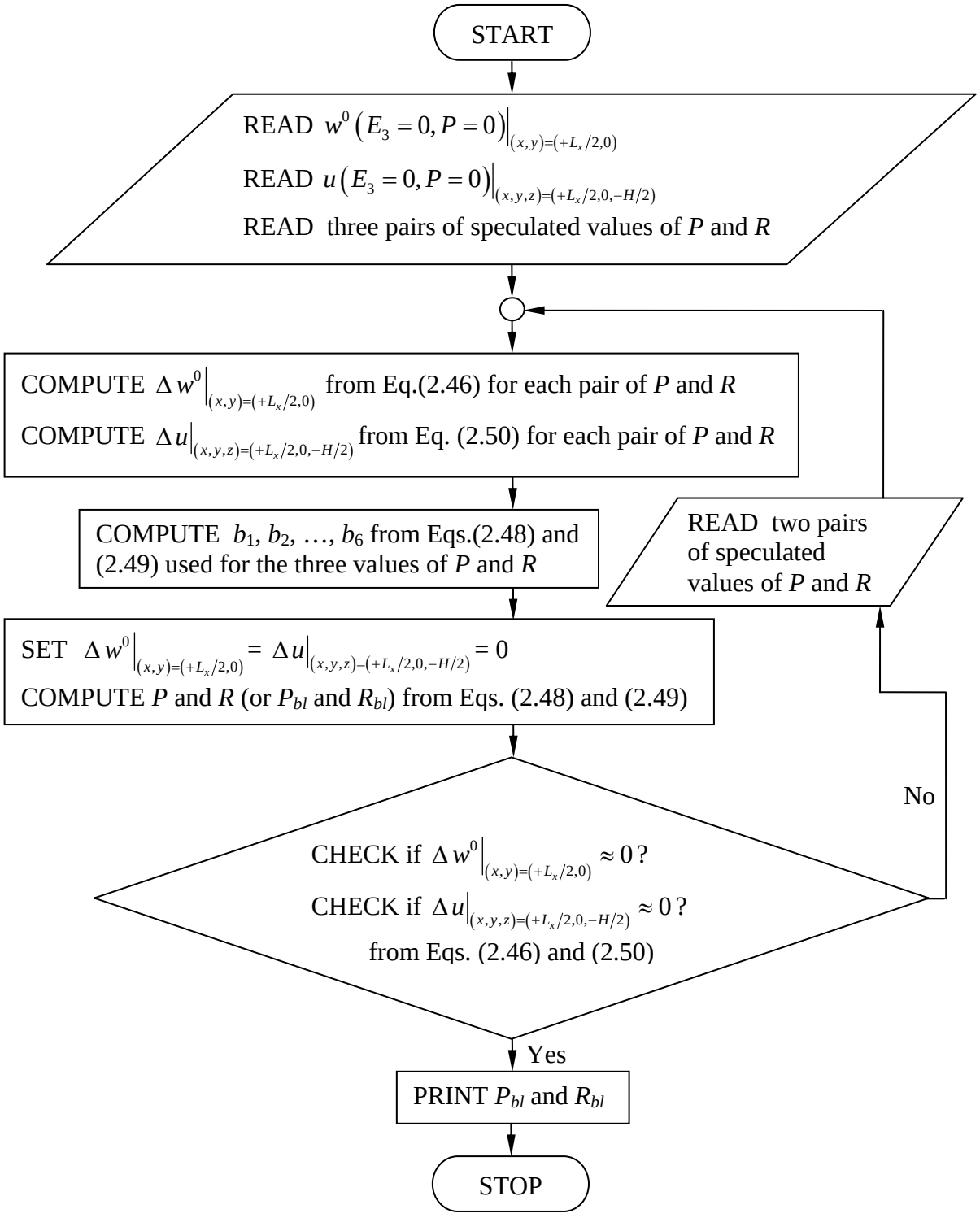

Figure 2.8: Flowchart of P_{bl} and R_{bl} Calculation

as well as

$$\Delta u\big|_{(x,y,z)=(+L_x/2,0,-H/2)} = b_4 P + b_5 R + b_6 \tag{2.49}$$

where $\Delta w^0\big|_{(x,y)=(+L_x/2,0)}$ has been defined already in Equation (2.46) and $\Delta u\big|_{(x,y,z)=(+L_x/2,0,-H/2)}$ is relative deformation u at $(x,y,z)=(+L_x/2,0,-H/2)$ due to the forces P and R and electric field strength E. In terms of a mathematical expression,

$$\begin{aligned}\Delta u\big|_{(x,y,z)=(+L_x/2,0,-H/2)} &= u\left(E_3 = E, P \neq 0, R \neq 0\right)\Big|_{(x,y,z)=(+L_x/2,0,-H/2)} \\ &\quad - u\left(E_3 = 0, P = 0, R = 0\right)\Big|_{(x,y,z)=(+L_x/2,0,-H/2)}\end{aligned} \tag{2.50}$$

constants b_1, b_2, …, b_6 are blocking force-deflection parameters for pinned-pinned case, and they are determined and updated in each iteration. According to Figure 2.8, three pairs of forces P and R are guessed initially. Then, the relative deformations in Equations (2.46) and (2.50) can be computed. Utilizing Equations (2.48) and (2.49), this results in six algebraic equations with six unknown blocking force-deflection parameters; thus b_1, b_2, …, b_6 can be solved for. Because of the definition of blocking forces previously stated, the relative deformations are set to be zero, and thus P_{bl} and R_{bl} can be calculated from Equations (2.48) and (2.49). However, since the blocking force-deflection parameters are obtained from the speculated forces P and R, the accuracy of the acquired P_{bl} and R_{bl} may not be desirable. Therefore, the computational iteration indicated in Figure 2.8 is necessary. Two more pairs of speculated forces P and R besides the pair of P_{bl} and R_{bl} just calculated are required to repeat the computation. Again, values of the new forces P and R could be assumed to be within 10% difference from the value of P_{bl} and R_{bl} just obtained. Until the blocking forces converge to desired accuracy level and approximately satisfy Equations (2.47) and a similar equation for u, namely

$$\left[u\left(E_3 = E, P = P_{bl}, R = R_{bl}\right) - u\left(E_3 = 0, P = 0, R = 0\right)\right]\Big|_{(x,y,z)=(+L_x/2,0,-H/2)} = 0 \tag{2.51}$$

more iterations are necessary.

It should be noted here that the blocking forces P_{bl}, or P_{bl} and R_{bl}, represent concentrated forces generated at the pinned-roller or pinned-pinned supports, respectively. As stated earlier, the supports are in contact with the actuator on the bottom surface at a midpoint of its two opposite edges. Therefore, $z = -H/2$ is used. Although these supports appear simple, they can be difficult to incorporate into a real experiment. However, there are two important reasons for considering these cases: (1) the physical interaction of the supports with the actuator is easy to understand and incorporate to the Rayleigh-Ritz model, and the cases provide valuable information regarding the actuator characteristics; (2) the supports considered here do not interfere with or distort the manufactured shapes of the actuator, since they act at points. This is not the case for clamped supports with a flat clamping fixture. A flat clamping fixture will suppress the anticlastic curvature of the actuators which develops during the cooling process. This will adversely affect the overall characteristics of the actuators when subjected to applications of electric field and mechanical loads.

2.5 Finite-element Modeling

2.5.1 Modeling of Manufactured Shapes

As a comparison to the Rayleigh-Ritz approach, the commercial code ABAQUS, version 6.3, is employed to conduct finite-element modeling of the actuator cooling process. For each finite-element analysis, nine-node shell elements (S9R5), which impose the Kirchhoff assumptions numerically in the element, are used. A S9R5 element provides for arbitrarily large rotation but only small strains. The composite shell section option in the code is utilized so as to be able to define the laminated materials and their physical properties. All nodes are situated on the element reference surface, which by default in ABAQUS is the midplane of the laminate. The actuator is assumed to be free on the four edges. However, due to the lines of symmetry about x- and y-axes, only one-quarter

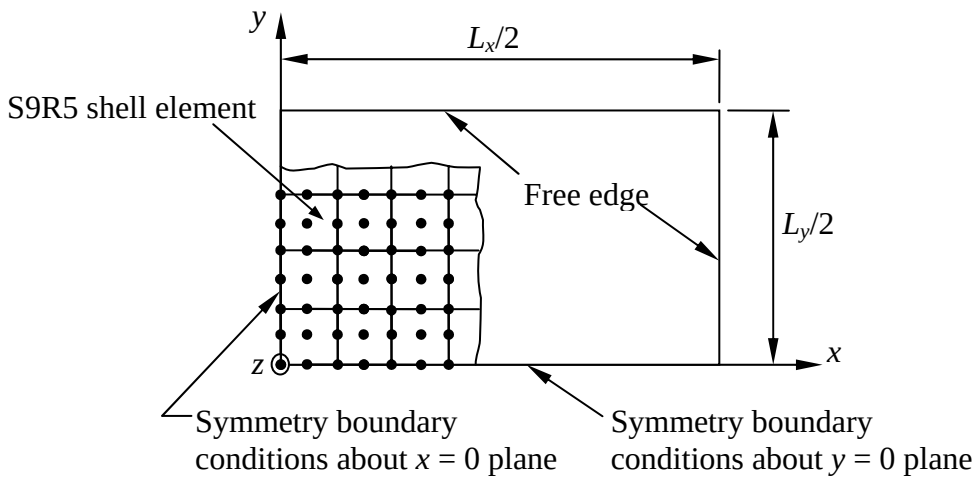

Figure 2.9: Finite-Element Model of a Quarter of Actuator

of the actuator is modeled, as shown in Figure 2.3. The geometric center of the actuator, which is located at the origin of the coordinate axes, is additionally fixed in the *z*-direction to revent a rigid body translation along the *z*-axis. The boundary conditions specified at the nodes along the symmetric planes $x = 0$ and $y = 0$ are $u^0 = 0$ and $\partial w^0/\partial x = 0,$ and $v^0 = 0$ and $\partial w^0/\partial y = 0,$ respectively. A constant temperature change is applied at every node. The geometrically nonlinear algorithm NLGEOM is used to capture the geometrically nonlinear behavior of the actuator due to large out-of-plane deformations. Displacements and curvatures of the actuator are computed by ABAQUS at every node. Stresses are obtained at integration points through-the-thickness of each layer. Force and moment resultants defined in the integral definitions of Equation (2.9) are also obtained at the integration points within the elements on the reference surface.

It must be stated that the finite-element analysis of the actuator will always converge to only one equilibrium solution at any particular geometry and cooling temperature. Multiple equilibrium shapes have never been revealed with the normal analysis procedure. Jilani [35] has proposed a method to acquire other stable equilibrium solutions, if they exist, by introducing a slight imperfection in the initial shape of the actuator. Thus,

according to [35], to obtain multiple stable equilibrium shapes, two series of finite-element calculations have to be conducted. However, Jilani could not find a way to obtain the unstable equilibrium solution from ABAQUS. Thus, Jilani could not verify some of the results obtained with the four-term Rayleigh-Ritz solution regarding the existence of bifurcation points and unstable solutions. In the present study, a method to obtain multiple equilibrium solutions from ABAQUS, including both stable and unstable configurations, is developed as follows: To coax ABAQUS to the other equilibrium shapes, the ABAQUS computation process needs to be divided into two steps. Initially, the out-of-plane deformations due to cooling are evaluated by the 23-term Rayleigh-Ritz approach. Then, in the first step in ABAQUS, each node is forced to deform out-of-plane the same amount as the deformations obtained from Rayleigh-Ritz approach, and the inplane deformations throughout the actuator are solved for. Therefore, at the end of this step, the deformation state of the actuator will approximate the cooled equilibrium state that will eventually be obtained from ABAQUS. In the second step, which occurs in ABAQUS right after the first step is complete, the out-of-plane deformation restraint is released from the already-deformed actuator, and the change in temperature representing the cooling process is applied to the actuator. Consequently, the analysis will readily converge to the desired equilibrium shape because of the similarity of the initial and final configurations within the second step. In the case of convergence to unstable equilibrium shapes occurring, ABAQUS will give a warning message that at least one negative eigenvalue of the tangent stiffness matrix of the problem is encountered.

2.5.2 Modeling of Manufactured Shapes with Tabs Inclusion

The ABAQUS models previously discussed are also modified to include the tabs in the analysis. The additional mesh for the tab region is generated in a one-quarter actuator model in ABAQUS. However, care must be taken regarding the midplane and reference surface of the tab, since ABAQUS will automatically use the midplane of the tab portion as

the reference plane, so in the finite-element model the tab would erroneously not be a part of the backbone layer of the actuator, but instead would be attached to the PZT layer and share the nodes along the $x = L_x/2$ edge with the actuator active portion. To correct this, the offset option in ABAQUS is used to translate the tab portion in the z-direction so the midplane of the tab coincides with the midplane of the backbone layer, yet the reference surface of the tab remains the same as the reference surface of the active portion of the actuator.

2.5.3 Modeling of Actuated Shapes

Besides the ABAQUS models developed in the previous section in order to compare manufactured shapes of an actuator with the 23-term Rayleigh-Ritz model, a comparison of actuated shapes is sometimes required to ensure the validity of the extended Rayleigh-Ritz model presented in Section 2.3. However, ABAQUS version 6.3 does not provide a shell element with the inclusion of piezoelectric effects in its constitutive laws; it only has a three-dimensional element (a so-called brick element) that possesses piezoelectricity properties. Even though the brick element is more powerful and accurate in modeling the behavior of a piezoelectric material, it consumes considerable computational memory and time, especially for geometrically nonlinear large-scale problems. Thus, to avoid these undesirable issues and still keep the finite-element model simple and meaningful, the thermally-induced expansion (or contraction) analogy to the converse piezoelectric effects, as seen in Section 2.3, is employed to predict actuated shapes of the actuator. More specifically, the induced dilatational strains caused by a temperature change (ΔT), which is denoted by ε^T, and an electric field applied in the z-direction (E_3), which is denoted by ε^E, in the piezoceramic layer are expressed as

$$\varepsilon^T = \alpha \Delta T \tag{2.52}$$

and

$$\varepsilon^E = d_{31} E_3 \tag{2.53}$$

Thus, the thermally-induced strain analogy to the combination of these two strains can be written as

$$\alpha_a \left(\Delta T_a \right) = \alpha \Delta T + d_{31} E_3 \tag{2.54}$$

where α_a is the analogous coefficient of thermal expansion, and ΔT_a the analogous temperature change. If it is assumed in the finite-element model that the analogous temperature change of the actuator is the same as the actual temperature change, i.e., $\Delta T_a = \Delta T$, the analogous coefficient of thermal expansion is expressed as

$$\alpha_a = \alpha + \frac{d_{31} E_3}{\Delta T} \tag{2.55}$$

As a result, actuated shapes of the actuator can be predicted using the same ABAQUS model presented in Section 2.5.1 by altering the actual thermal coefficient of expansion of the piezoceramic layer to be the analogous coefficient of thermal expansion in Equation (2.55). No other modeling changes are necessary.

2.6 Chapter Summary

In this chapter, a Rayleigh-Ritz model for predicting the room-temperature shapes of rectangular THUNDER-type and LIPCA-type actuators without tabs has been developed. The assumptions adopted to develop the model, the expression for the total potential energy, including thermally-induced strain effects, the constitutive equations, the strain-displacement relations with the inclusion of geometrical nonlinearities, the approximate displacement fields, equilibrium, and stability were discussed. An extension of the Rayleigh-Ritz model to predict the manufactured shapes of THUNDER-type actuators with tabs has also been established by adding the strain energy contributed from the tabs to the total potential energy of the no-tab case. Additionally, the Rayleigh-Ritz model is modified to include (1) the piezoelectric actuation and (2) mechanical loads. Subsequently,

the modified models can be used to investigate performances and characteristics of the actuators such as free actuation response and load-carrying capability. Blocking forces of the actuators with pinned-roller or pinned-pinned supports can also be determined by utilizing the latter modified model with the supplementary algorithm that relates actuator deformations at the support position to forces applied at the same positions but with the supports removed. Besides the Rayleigh-Ritz model and its derivatives, a finite-element modeling using thin shell elements in ABAQUS version 6.3 is also developed to predict manufactured shapes as a comparison. A thermal analogy to the converse piezoelectric effect is utilized in the ABAQUS models to further predict the actuated shapes of the actuators by only altering the thermal expansion coefficient of the piezoelectric layer.

In the next chapter, numerical results for deformation and force characteristics of THUNDER-type actuators are presented. Cooled shapes of THUNDER actuators will be predicted as functions of actuator geometry and cooling temperature relative to the curing temperature. All equilibrium configurations within the parametric range of interest are found by employing the Rayleigh-Ritz model developed in this chapter. Stability of the configurations found is determined. Validity of the Rayleigh-Ritz model used to predict the cooled shapes will be compared with the ABAQUS model. Additionally, effects of tabs on manufactured shapes of THUNDER actuators will be considered. Performances of THUNDER actuators will be investigated, i.e., free actuation responses and blocking forces. Dependency of the performances evaluated on the actuator geometries and applied electric fields will be examined.

Chapter 3

NUMERICAL RESULTS OF THUNDER CHARACTERISTICS

3.1 Introduction

This chapter presents shape predictions of rectangular THUNDER actuators by employing the energy-based Rayleigh-Ritz approach discussed in Chapter 2. The cooled shapes of the actuators are calculated as functions of temperature decrement relative to the curing temperature of the polyimide adhesive and their sidelength-to-thickness ratio. Finite-element modeling using the commercial package ABAQUS, version 6.3, in order to provide a comparison with the Rayleigh-Ritz approach, is also developed. Actuated shapes of the rectangular THUNDER actuators are computed by utilizing the modified Rayleigh-Ritz model with the inclusion of peizoelectrically-induced strains. Finally, blocking forces of the THUNDER actuators subjected to an application of electric field with pinned-roller and pinned-pinned supports are calculated and discussed.

3.2 Numerical Results for Cooled Shapes

3.2.1 Deformation Characteristics of THUNDER without Tabs

To illustrate the results predicted by the energy-based Rayleigh-Ritz approach, consider a rectangular THUNDER actuator without tabs consisting of 5 layers, as depicted in Figure 1.10. In the following analyses, the material properties and thicknesses of the layers are taken from [38], and they are given here in Table 3.1. Steel is used as the backbone of the actuator, PZT 4 as the actuating layer, and aluminum foil as the top layer. It is assumed that the three materials are bonded together with a film adhesive that cures at

Table 3.1: THUNDER Material Properties

Properties	Steel	Aluminum foil	PZT 4	Adhesive
Thickness (μm)	127.0	25.4	173.0	50.8
E (GPa)	207.0	70.0	69.0	3.45
ν	0.3	0.3	0.31	0.4
$\alpha\left(10^{-6}/°\text{C}\right)$	10.8	23.4	2.0	45.0
$d_{31}\left(10^{-12}\text{m/V}\right)$	-	-	-122	-

T_{cure} = 325 °C, and the whole laminate is cooled to the service temperature, or room temperature, $T = 25$ °C.

In practice, THUNDER actuators are vacuum bagged in specially-made molds during the time they are cured at the elevated temperature T_{cure} and then cooled to room temperature. Though stresses develop during the curing process, the mold essentially forces the actuator to remain flat until the pressure is released after it cools. The model presented above is formulated such that if the actuator was not forced to remain flat, but rather could deform freely as it was cooled, by virtue of the through-thickness asymmetry of the material properties, the shape of the actuator at any temperature below cure can be predicted. Alternatively, if the cured actuator was heated from the room-temperature condition, the shape as a function of temperature above room temperature could also be predicted. This approach of modeling the actuator deformations during cooling is fictitious because, as stated, the mold restrains the deformations of the actuator, but since the process is modeled as being reversible, e.g., when there is no slippage or friction in the mold, the approach is valid.

Figure 3.1 illustrates the deformation behavior of a square THUNDER actuator (L_y/L_x=1) with a length-to-thickness ratio L_x/H of 100. Considering the numerical values of thicknesses in Table 3.1, this represents an actuator 42.7 by 42.7 mm, a relatively small actuator. In the figure, the relations between the average curvatures along the centerlines of

the actuator in the $x-$ and $y-$directions (K_x and K_y, respectively) and the temperature change relative to the cure temperature T_{cure} are shown. The average curvatures and the temperature change are defined by

$$\mathrm{K}_x = \frac{1}{L_x}\int_{-\frac{L_x}{2}}^{+\frac{L_x}{2}} \kappa_x^0(x,0)dx$$
$$\mathrm{K}_y = \frac{1}{L_y}\int_{-\frac{L_y}{2}}^{+\frac{L_y}{2}} \kappa_y^0(0,y)dy \qquad (3.1)$$

$$\Delta T = T - T_{cure} \qquad (3.2)$$

Thus, ΔT = 0 °C at the beginning of the cooling process when T is equal to the curing temperature of 325 °C, and ΔT = -300 °C at the end of the cooling process when T is equal to the room temperature of 25 °C. It must be noted that from this point on, all of the figures associated with the average curvatures have the negative average curvature ($-\mathrm{K}_x$ or $-\mathrm{K}_y$) as an ordinate axis. This arrangement is used because of the minus signs in the definition of the curvatures in Equation (2.4). Also, it is important to note that curvature is used as the measure of shape rather than, for example, the displacement of the edges of the actuator relative to the center (i.e., so called dome height), because a relative displacement measure involves curvature and the dimensions of the actuator. Two actuators could have significantly different curvatures in the *x*-direction and therefore have different shapes, but because the dimensions of an actuator that is almost flat could be larger, the relative displacement could be the same as that of an actuator with a significant curvature but smaller dimensions. A displacement measure would indicate the two actuators have the same shape when, in fact, they do not.

Point A in Figure 3.1 represents the actuator flat at its elevated curing temperature, i.e., $-\mathrm{K}_x$ = 0 and $-\mathrm{K}_y$ = 0. When the temperature is reduced, the actuator develops positive average curvature in the *x*- and *y*-directions, i.e., deforms as in Figure 2.1 (b). The two average curvatures are equal and increase in magnitude in a slightly nonlinear

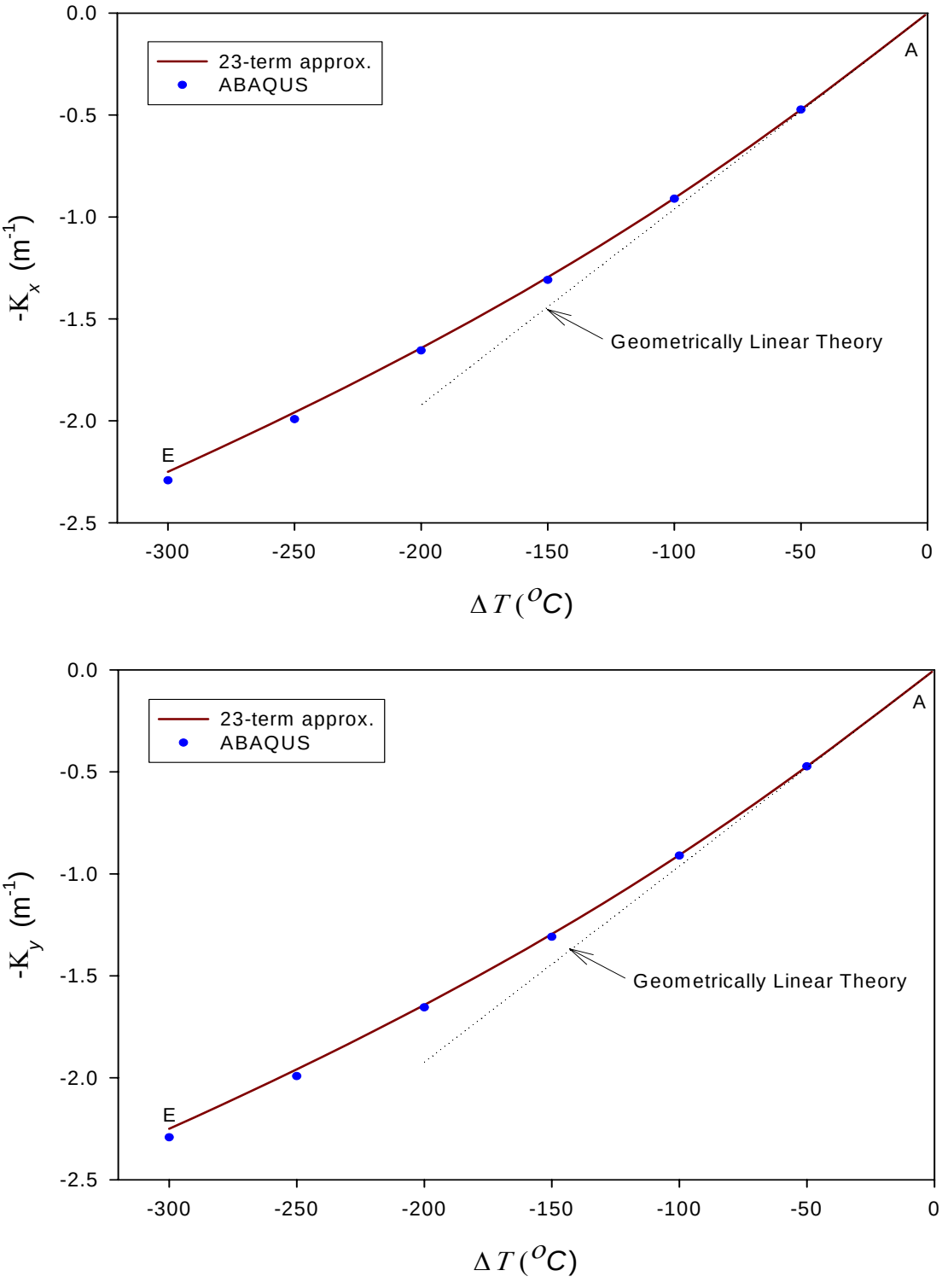

Figure 3.1: Temperature vs. Curvature Relations of Square THUNDER (L_x /H = 100)

fashion as temperature is decreased. The 30 by 20 mesh finite-element modeling of a quarter of this actuator is also conducted as a comparison. The 23-term Rayleigh-Ritz and ABAQUS models are in very good agreement. Also shown in Figure 3.1 is the prediction of the geometrically linear model, for which curvatures are a linear function of temperature change. The slope of the geometrically linear model is tangent to the temperature-curvature relation at point A. It is seen that the linear model overpredicts the magnitude of the average curvatures relative to the nonlinear models. All models predict stable curvatures throughout the temperature range. Figure 3.2 illustrates the room-temperature shapes (ΔT = -300 °C) as predicted by 23-term Rayleigh-Ritz and finite-element models, point E in Figure 3.1. In the figure the out-of-plane displacement has been normalized by the actuator thickness H and the x- and y-axes have been normalized by L_x and L_y, respectively. In an average sense, the predicted room-temperature shape is near-spherical, or dome-like, in nature, with almost equal curvatures in all directions. There is some twist curvature, especially in the corners

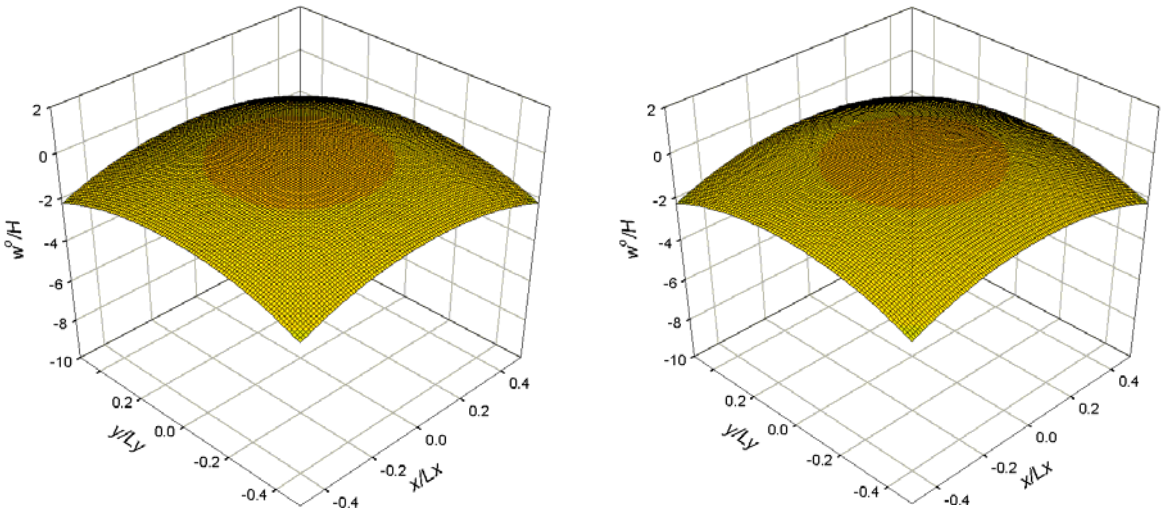

(a) 23-term Rayleigh-Ritz (b) ABAQUS

Figure 3.2: Equilibrium Shapes of Square THUNDER at Point E (refer to Figure 3.1)

due to the contribution form the non-zero coefficients c_5 through c_7 in the first equation of Equation (2.26), but it is small compared to curvatures in the *x*- and *y*-directions.

The influence of simply doubling the sidelengths L_x and L_y of the actuator is illustrated in Figures 3.3 and 3.4. As can be seen, the behavior of this actuator as a function of temperature is more complicated than that of the smaller actuator. Again, at the curing temperature, point A, the actuator is flat. As the actuator is cooled, the *x*- and *y*-direction average curvatures are equal and increase in magnitude. At point B, following the solid line, the solution bifurcates into branches BC, BD, and BE. The various branches correspond to different shapes of the actuator. Following branch BC, at room temperature, point C, the actuator has a small average curvature in the *x*-direction and a large average curvature in the *y*-direction. Conversely, following branch BD, at room temperature, point D, the actuator has a small average curvature in the *y*-direction and a large average curvature in the *x*-direction. The room-temperature shapes represented by these two branches can be described as near-cylindrical, since the average curvature in one direction is only about 16% as large as the average curvature in the other direction. Following branch BE, the actuator has equal average curvatures in the two directions, similar to the smaller actuator previously discussed. However, in this case, the solutions on branch BE correspond to unstable equilibrium solutions, while the solutions on the other two branches represent stable equilibrium solutions. The 23-term Rayleigh-Ritz solutions agree very well with the ABAQUS solutions, which are based on 57 by 57 mesh, except near room temperature for unstable branch BE. The lack of stability means that the configuration described by that solution, which corresponds to a dome-like shape, will never be observed. The existence of two near-cylindrical shapes at room temperature means the actuator can be transformed, or snapped, from one cylindrical shape to the other by applying external moments to the edges of the actuator. The magnitude and direction of the moment required for snapping can be predicted by the Rayleigh-Ritz approach. The influence of applying external moments will

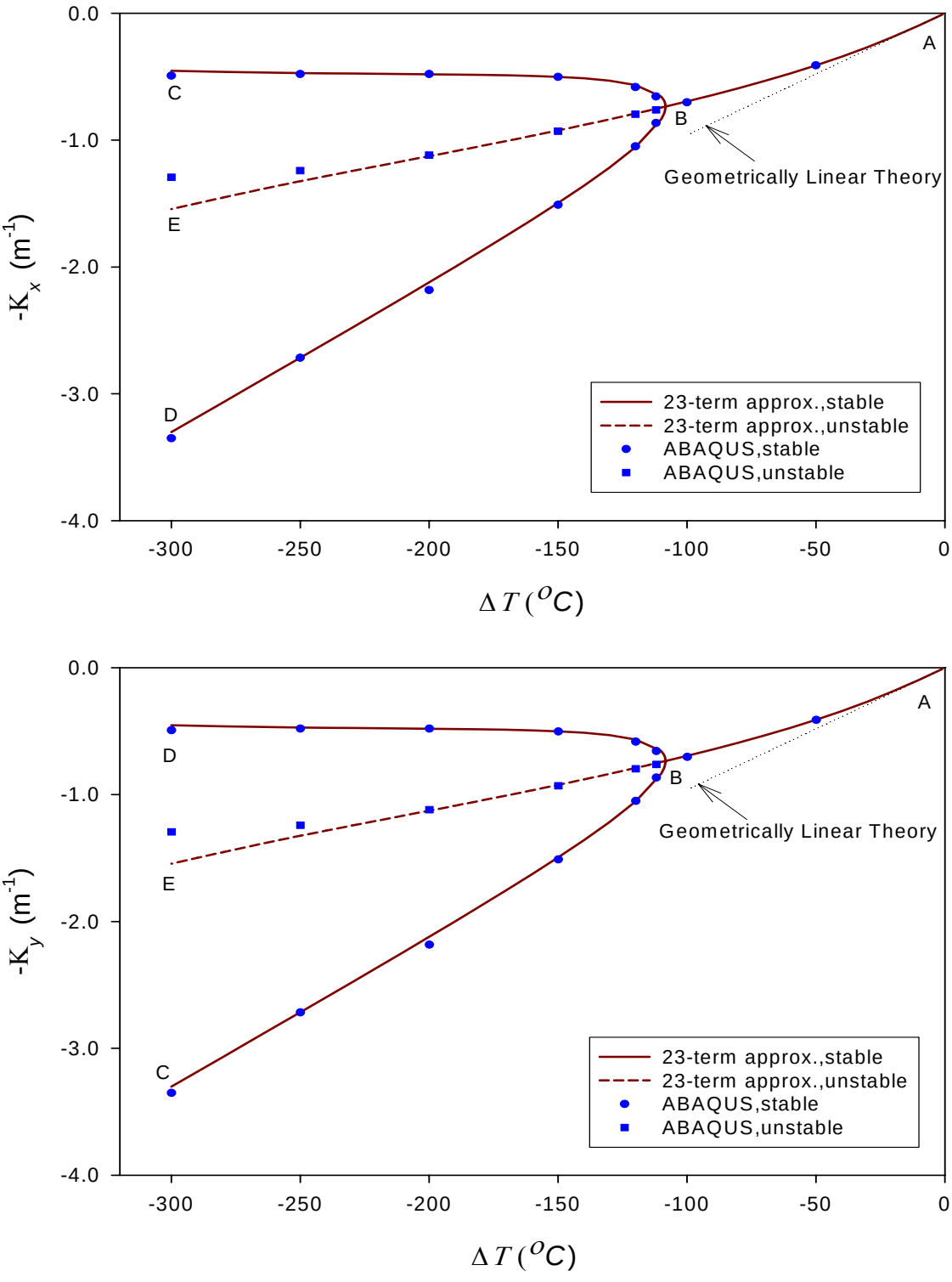

Figure 3.3: Temperature vs. Curvature Relations of Square THUNDER (L_x /H = 200)

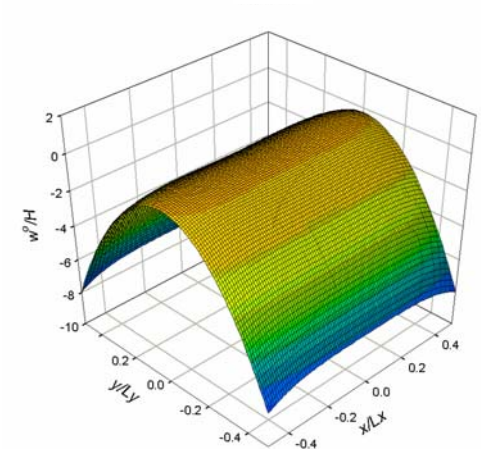

(a) 23-term Rayleigh-Ritz at point C

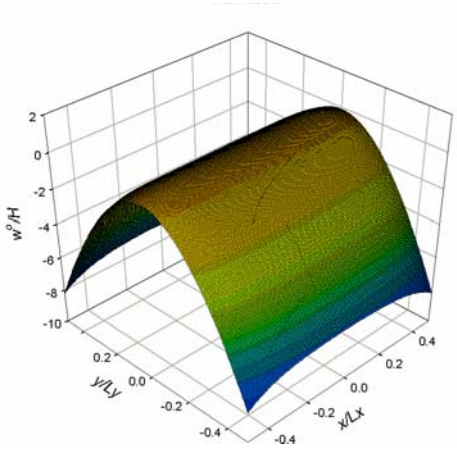

(b) ABAQUS at point C

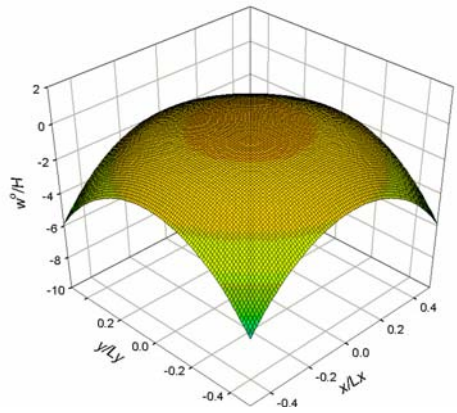

(c) 23-term Rayleigh-Ritz at point E

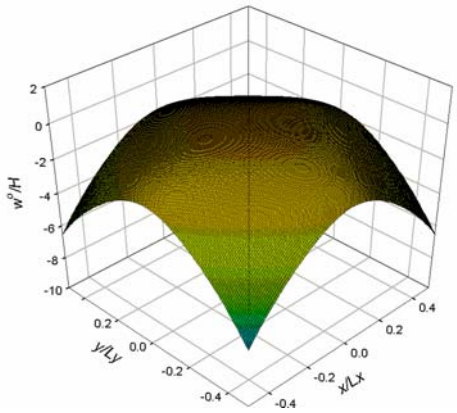

(d) ABAQUS at point E

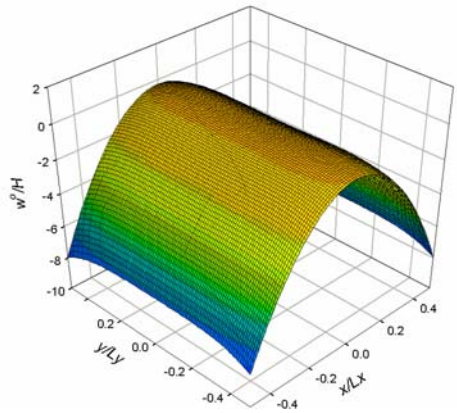

(e) 23-term Rayleigh-Ritz at point D

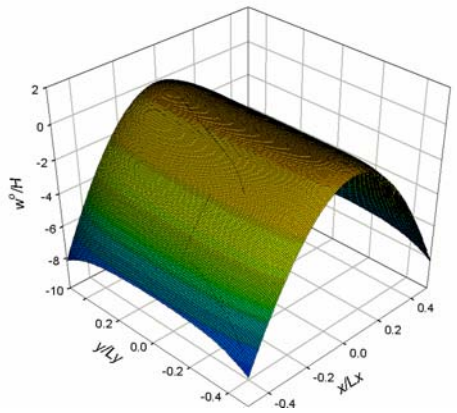

(f) ABAQUS at point D

Figure 3.4: Equilibrium Shapes of Square THUNDER (refer to Figure 3.3)

be discussed in Section 3.2.3. The geometrically linear prediction is again given by the line tangent to branch AB at the cure temperature, and, of course, there is only a single stable branch with this prediction. Such a prediction is clearly off the mark. Geometrically nonlinear behavior could be expected, since the actuator is a plate-like structure and the out-of-plane deflections are many times the actuator thickness, as can be observed in Figure 3.4, which illustrates the predicted room-temperature shapes for the three branches. Out-of-plane deflections on the order of eight actuator thicknesses are predicted. In Figure 3.4, the vertical scale is the same as the vertical scale in Figure 3.2, for comparison, but results in a somewhat exaggerated rendering of the deformed actuator. It is interesting to note that the single dome-like stable configuration, which characterizes the smaller 42.7 by 42.7 mm square actuator (L_x/H = 100), is unstable when the size of the actuator is increased (L_x/H = 200).

The influence of actuator sidelength for square actuators is illustrated in Figure 3.5. In this figure, the average room-temperature curvatures in the *x*- and *y*-directions as a function of the sidelength-to thickness ratio are shown. It can be seen that for sidelength-to-thickness ratio less than 120, the actuator has only one predicted room-temperature shape, namely the dome-like-shape, and the average curvatures are given by branch $A'B'$. For sidelength-to-thickness ratios greater than 120, the actuator has two possible stable shapes, given by branches $B'C'$ and $B'D'$. For sidelength-to-thickness ratios greater than 150, both shapes are near-cylindrical, as the ratio of the magnitudes of the average curvatures is at least three to one. For sidelength-to thickness ratios between 120 and 150, the shapes have noticeable average curvatures in both directions. Because of the bifurcation characteristic, manufacturing an actuator with a sidelength-to-thickness ratio near 120 could result in unexpected behavior, particularly during dynamic operation. Interestingly, for sidelength-to-thickness ratios between 120 and 200, the 23-term Rayleigh-Ritz solution predicts three solutions, one of which is unstable. However, beyond sidelength-to-thickness of 200, five

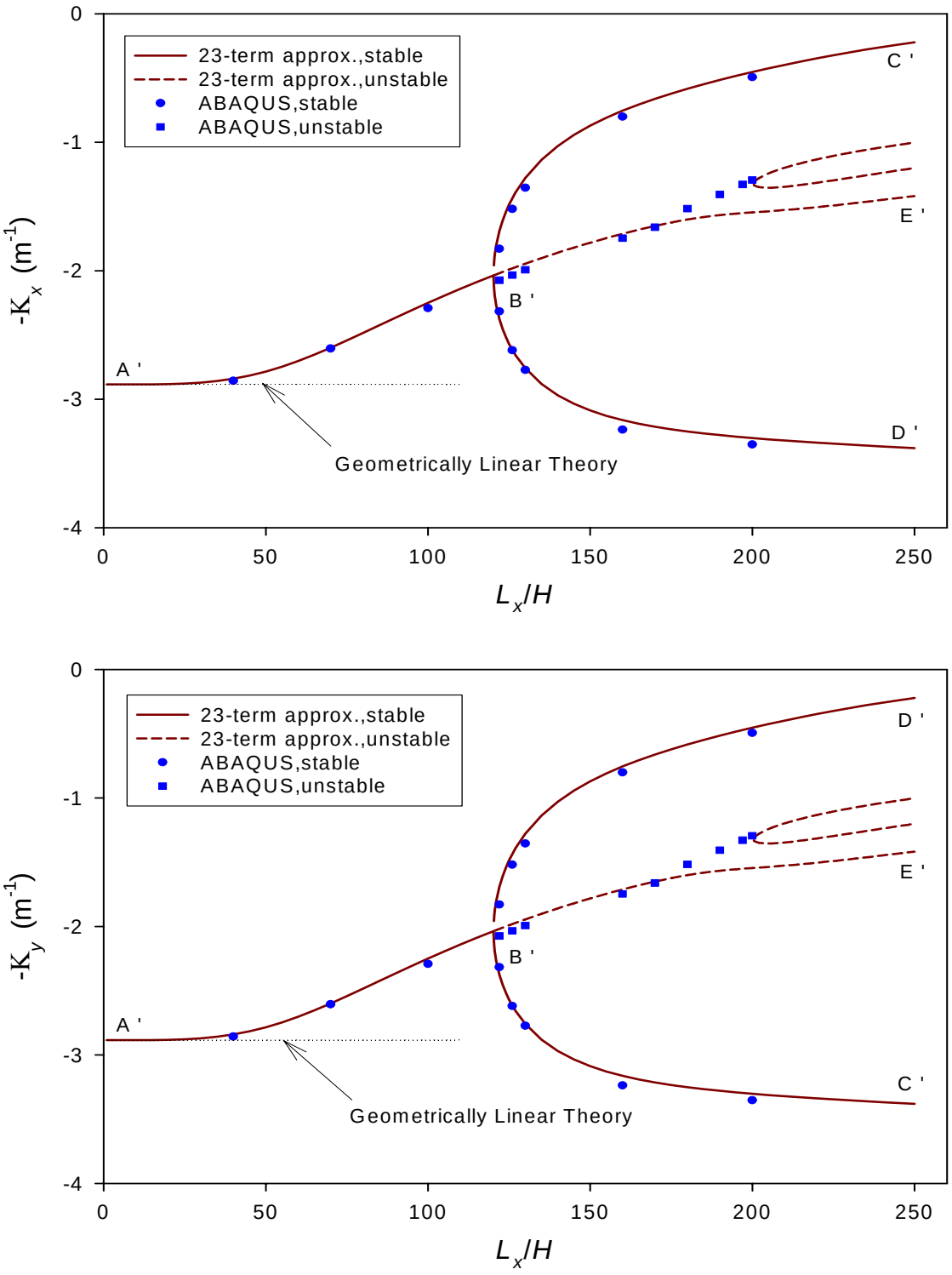

Figure 3.5: Sidelength-to-Thickness Ratio vs. Curvature Relations of Square THUNDER (ΔT = -300 °C)

solutions are predicted, three of which are unstable. The ABAQUS solutions for the stable shapes are in good agreement with the 23-term Rayleigh-Ritz model. For the unstable shapes, near the region where the number of solutions from the 23-term Rayleigh-Ritz models increases from three to five, the Rayleigh-Ritz model is not in agreement with the ABAQUS calculations. The unstable solutions from the ABAQUS model beyond L_x/H = 200 seem to follow one of the two just-emerging unstable branches resulting from Rayleigh-Ritz approach. The prediction of a linear theory would be given by a horizontal line coincident with point A′ and corresponds to an actuator with a sidelength-to-thickness ratio approaching to zero. The shape corresponding to the linear theory would always be dome-like, independent of actuator length-to-thickness ratio.

The aspect ratio of the actuator, L_y/L_x, has an interesting influence on the predicted shapes. The average curvature vs. temperature relation for a rectangular actuator with an aspect ratio of 0.7 and a sidelength-to-thickness ratio of 200 is shown in Figure 3.6. Except for a slightly smaller dimension in the *y*-direction, this actuator is identical to the one described in Figures 3.3 and 3.4. Considering the 23-term Rayleigh-Ritz predictions, as the temperature is initially reduced from the curing temperature, the actuator develops equal average curvatures in the *x*- and *y*-directions. Upon cooling 150 °C, the *x*-direction average curvature begins to increase more rapidly with temperature decrease, while the *y*-direction average curvature begins to decrease. Continued cooling along this path results in an actuator at room temperature that has a large positive average curvature in the *x*-direction and average curvature in the *y*-direction about 25% as large, as indicated by point D on the figure. The shape of the actuator is near-cylindrical, but less so than the case shown in Figure 3.3. At a temperature decrease of about 200 °C, at point B, limit point behavior is exhibited, resulting in two more branches, branches BC and BE. Branch BC represents stable shapes, whereas branch BE represents unstable shapes. The room-temperature shape at point C represents an actuator with a large positive average curvature in the *y*-direction

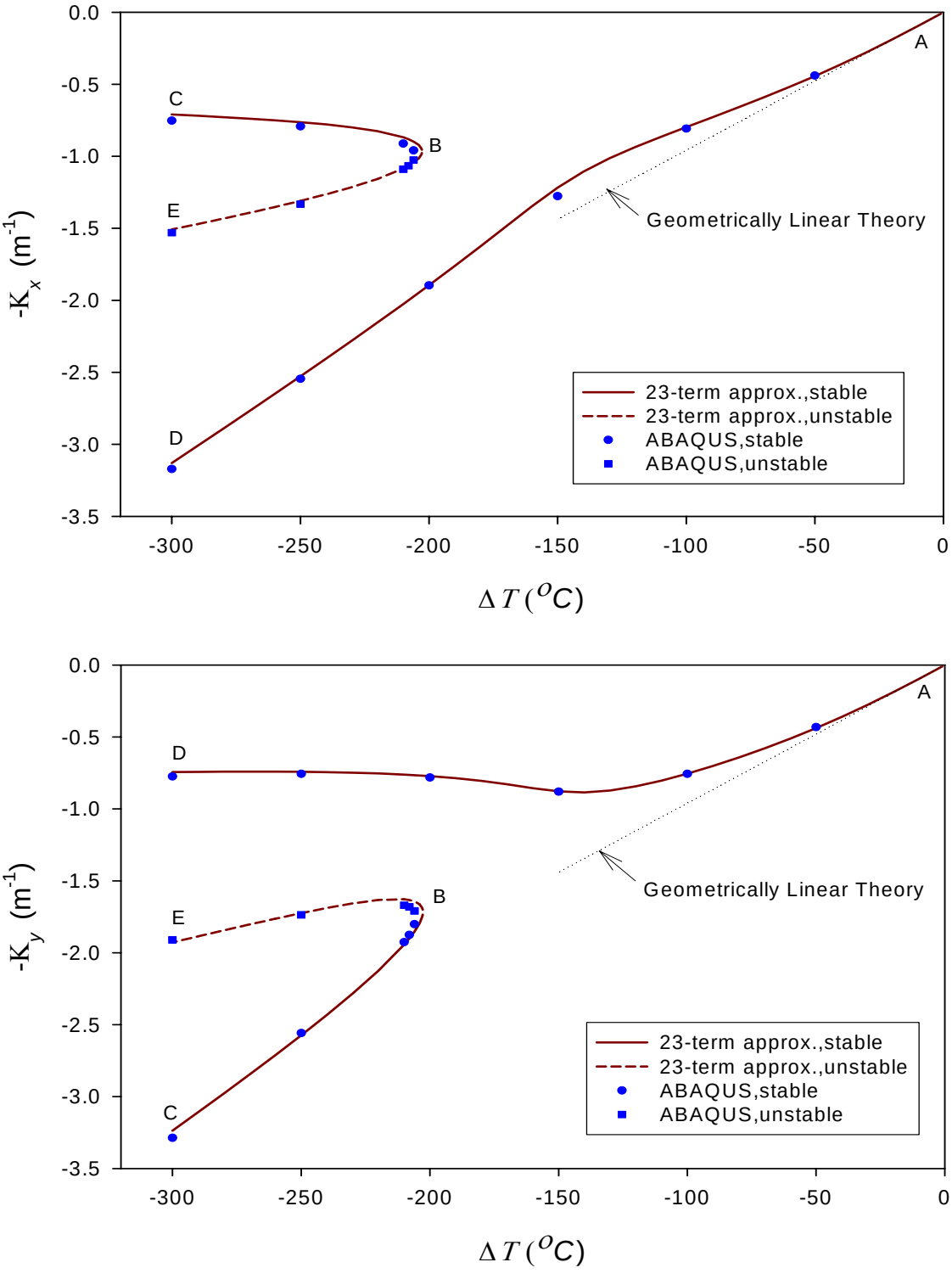

Figure 3.6: Temperature vs. Curvature Relations of Rectangular THUNDER ($L_y / L_x = 0.7$, $L_x / H = 200$)

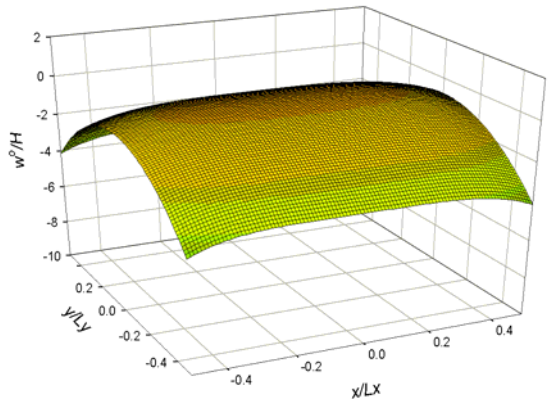

(a) 23-term Rayleigh-Ritz at point C

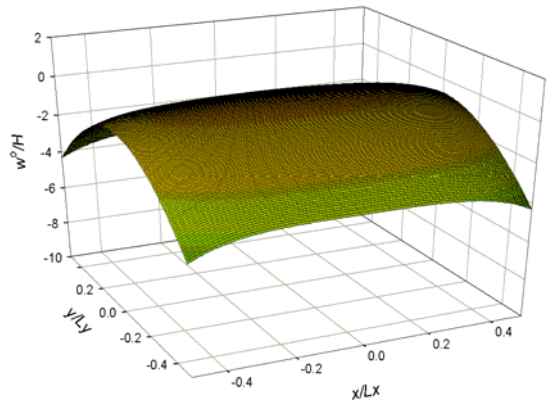

(b) ABAQUS at point C

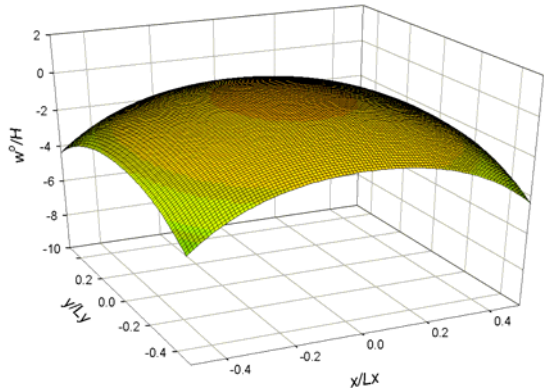

(c) 23-term Rayleigh-Ritz at point E

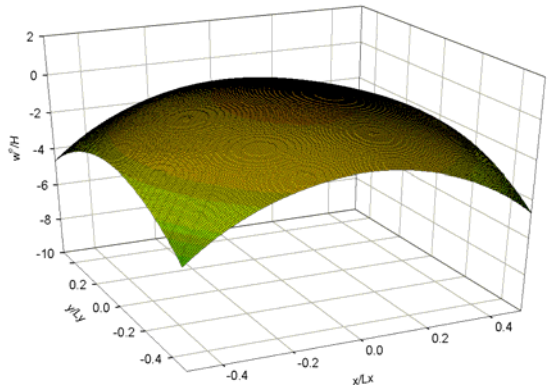

(d) ABAQUS at point E

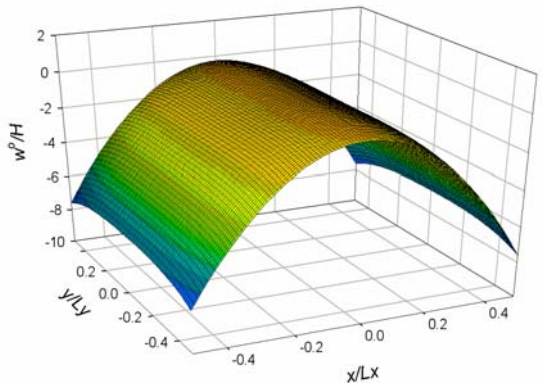

(e) 23-term Rayleigh-Ritz at point D

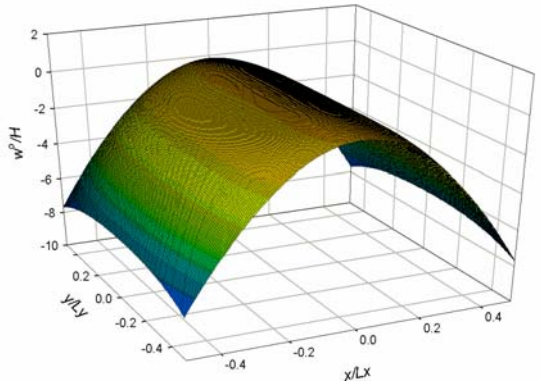

(f) ABAQUS at point D

Figure 3.7: Equilibrium Shapes of Rectangular THUNDER (refer to Figure 2.9)

and a smaller positive average curvature in the *x*-direction, the smaller average curvature again being about only 25% of the larger average curvature. The unstable solutions at point E have almost equal average curvatures in the *x*-and *y*-directions, and could be described as dome-like. The 23-term Rayleigh-Ritz calculations are in good agreement with the ABAQUS results, including the limit point behavior. The geometrically linear analysis again gives the curvature prediction as the tangential straight lines at point A. It should be noted that the slope of the lines are equal to the counterpart ones in Figures 3.1 and 3.3. In accordance with the geometrically linear model, this indicates that the curvature vs. temperature relations are all the same regardless of inplane dimensions, i.e., at the same cooling temperature, the curvatures are predicted to be the same no matter how large or what the aspect ratio of the actuator is. In reality, as shown in Appendix A, the *x*- and *y*-direction curvatures predicted from the linear theory depend only on the material properties and thickness of each layer in the laminate. The shapes at room-temperature points C, D, and E in Figure 3.6 are illustrated in Figure 3.7, where the rectangular aspect ratio of the actuator is represented. It should be mentioned that more than likely a THUNDER actuator with an aspect ratio of 0.7 would be manufactured with the intent to have the larger curvature in the *x*-direction, as in Figure 3.7(e) and (f). The excellent agreement between the shape prediction of the Rayleigh-Ritz and the finite-element models should also be noted.

The dependence of room-temperature shape on the sidelength-to-thickness ratio, L_x/H, for actuators with an aspect ratio $L_y/L_x = 0.7$ is illustrated in Figure 3.8. It is seen that for thickness ratios less than 166, a single shape exists at room temperature. Recall from Figure 3.5 that for square actuators it was necessary to have L_x/H less than 120. Above a sidelength-to-thickness ratio of 166, multiple room-temperature shapes are predicted to exist, although some shapes are unstable. Another difference attributable to aspect ratio is that for square actuators, bifurcation behavior occurs (point B′ in Figure 3.5), while for the rectangular actuators limit point behavior, point B′ in Figure 3.8, prevails. The linear

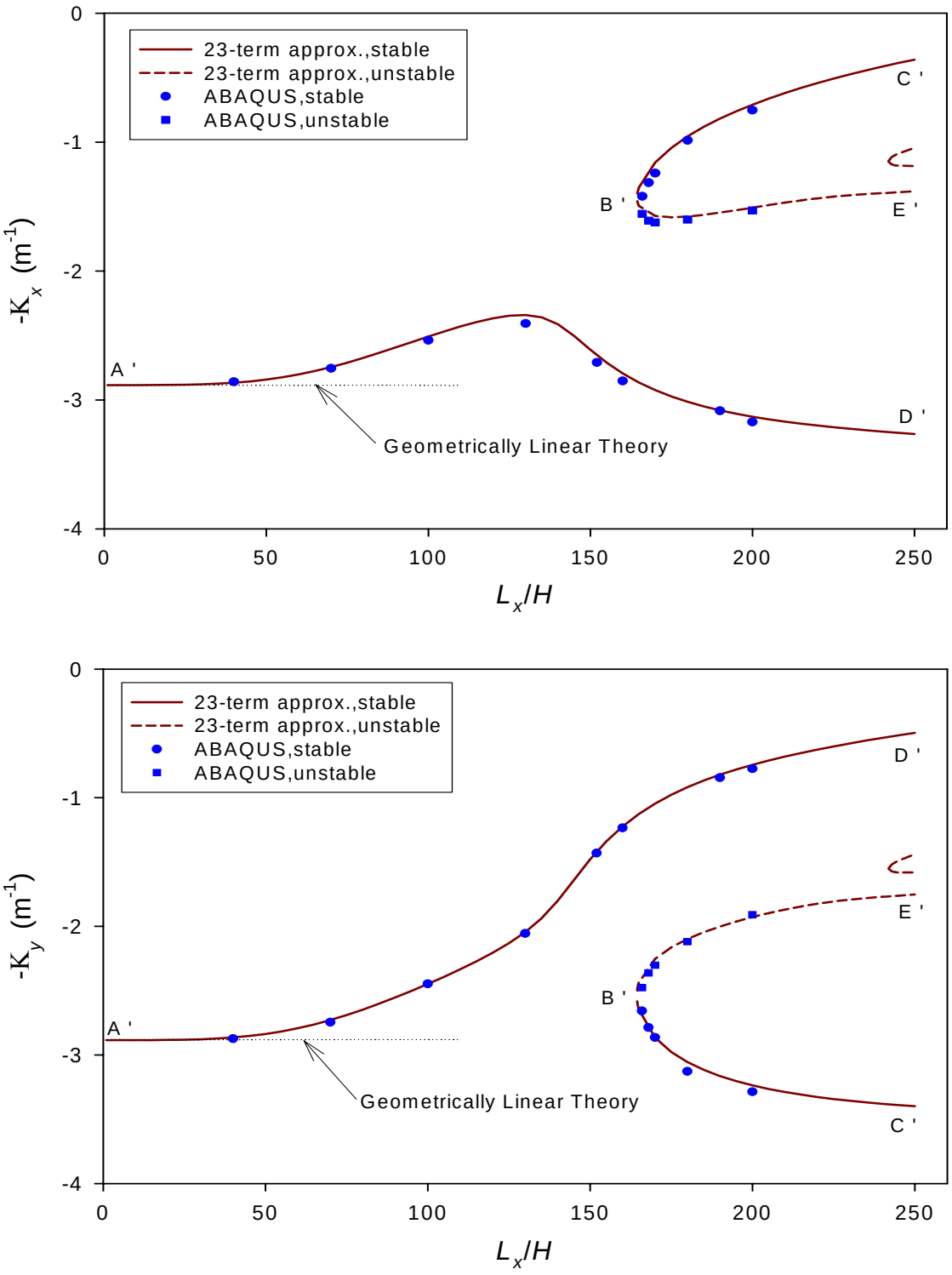

Figure 3.8: Sidelength-to-Thickness Ratio vs. Curvature Relations of Rectangular THUNDER ($L_y/L_x = 0.7,\ \Delta T = -300\,°C$)

solution to the problem corresponds to horizontal lines coincident with point A′ on the two curvature relations. To be noted both in Figures 3.5 and 3.8 is that with sidelength-to-thickness ratios above 160, the curvature in the *x*-direction along the branch A′D′ is enhanced relative to the linear prediction, while the curvature in the *y*-direction is suppressed considerably, leading to the near-cylindrical shape. Along branch B′C′, the reverse occurs, the curvature in the *x*-direction being suppressed and the curvature in the *y*-direction being enhanced. Since the actuator is smaller in dimension in the *y*-direction, the deflection enhancement is not as noticeable for this branch. This enhancement and suppression of the curvatures is clearly a nonlinear effect and is felt to be a beneficial effect. For the rectangular actuator, Figure 3.8, it can be seen that beyond the sidelength-to-thickness ratio of around 240, there are five solutions predicted from the 23-term Rayleigh-Ritz method rather than three, the additional two being unstable.

Finally, Figure 3.9 illustrates the influence of sidelength-to-thickness ratio on the average curvatures for actuators with an aspect ratio $L_y / L_x = 0.3$. This represents a more beam-like actuator than the previous aspect ratios considered. Only the 23-term Rayleigh-Ritz solution is shown, and to be noted is the lack of multiple solutions. The linear solution would correspond to a straight horizontal line coincident with point A′. For sidelength-to-thickness ratio up to 100, the linear solution is accurate. This value of L_x/H corresponds to an actuator 42.7 mm long and 14.23 mm wide. The agreement for values of L_x/H up to 100 should be compared to deviations from the linear solution for sidelength-to-thickness ratios of 50 or less for the other aspect ratios considered above. For the shorter actuators with an aspect ratio of 0.3, the average curvatures in the two directions are equal, though because of the longer dimension in the *x*-direction, the curvature in that direction would be more noticeable. As the length of the actuator increases, geometrically nonlinear effects begin to suppress the average curvatures in both directions. The curvature in the *y*-direction is suppressed more, making the actuator flatter in the *y*-direction than in the *x*-direction. Again,

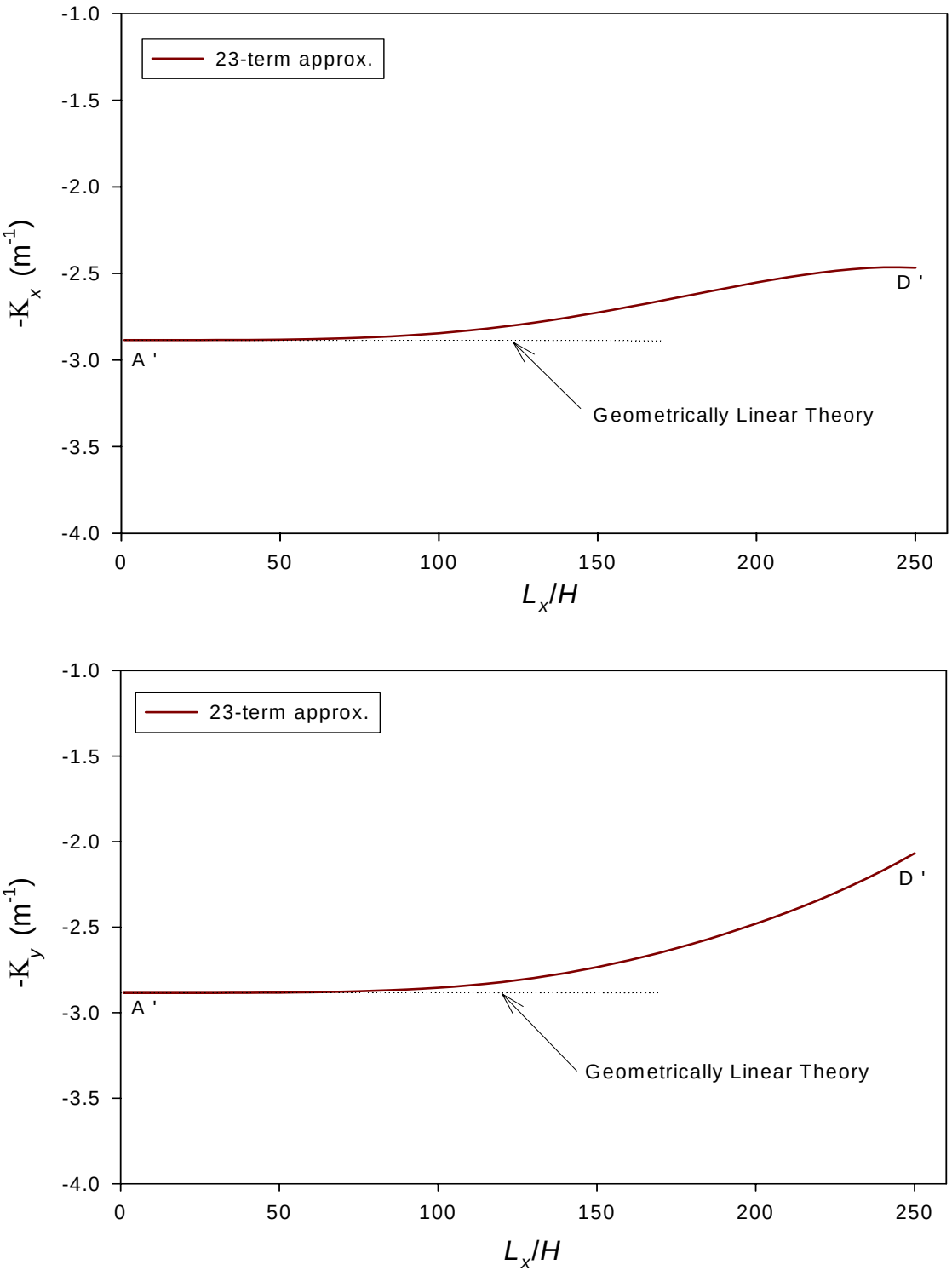

Figure 3.9: Sidelength-to-Thickness Ratio vs. Curvature Relations of Beam-Like THUNDER ($L_y / L_x = 0.3,\ \Delta T = -300\,°C$)

since the actuator is longer in the *x*-direction, the curvature in the *x*-direction would be even more pronounced. Also, note that since the THUNDER actuators with an aspect ratio of 0.3 is beam-like, it is interesting to compare the *x*-direction curvature in Figure 3.9 with that predicted by either geometrically nonlinear or linear laminated beam models, as derived in Appendix B. By using Equation (B.36) or (B65), $K_x = 2.97\ m^{-1}$, a constant over the range of sidelength-to-thickness ratios considered. This value is only a few percent different than the geometrically linear calculation of $K_x = 2.88\ m^{-1}$ from the 23-term Rayleigh-Ritz solution.

3.2.2 Force and Moment Resultant and Stress Characteristics of THUNDER without Tabs

As stated earlier, the curvatures due to cooling are accompanied by residual stresses, and hence residual force and moment resultants, as defined in Equation (2.9). From the ABAQUS calculations, the force and moment resultants at room temperature for a rectangular actuator with aspect ratio of 0.7 and sidelength-to-thickness ratio of 200 are illustrated in Figure 3.10. The actuator is in the configuration given by point D in Figures 3.6 and 3.7, and hence has significant average curvature in the *x*-direction and is relatively flat in the *y*-direction. As mentioned, this is most likely the configuration the manufacturing process is intended to produce. Since the boundaries of the actuator are traction free, specific force and moment resultants are zero on the boundaries, as seen in Figure 3.10. Also illustrated in the figure, extreme values of the force and moment resultants occur in narrow regions along the edges of the actuator. These force and moment resultants build in magnitude quite rapidly as the edges are approached from the central portion. Away from the edges, the magnitudes of the force and moment resultants are more uniform, and in some cases quite small. It is important to note that for a geometrically linear analysis, all force and moment resultants are exactly zero, so all the force and moment resultants illustrated in Figure 3.10 are due to geometric nonlinearities. The nonzero values associated with the geometrically nonlinear analysis can be explained briefly as follows: For a geometrically linear analysis, the room-temperature shape of the actuator is dome-like, with equal

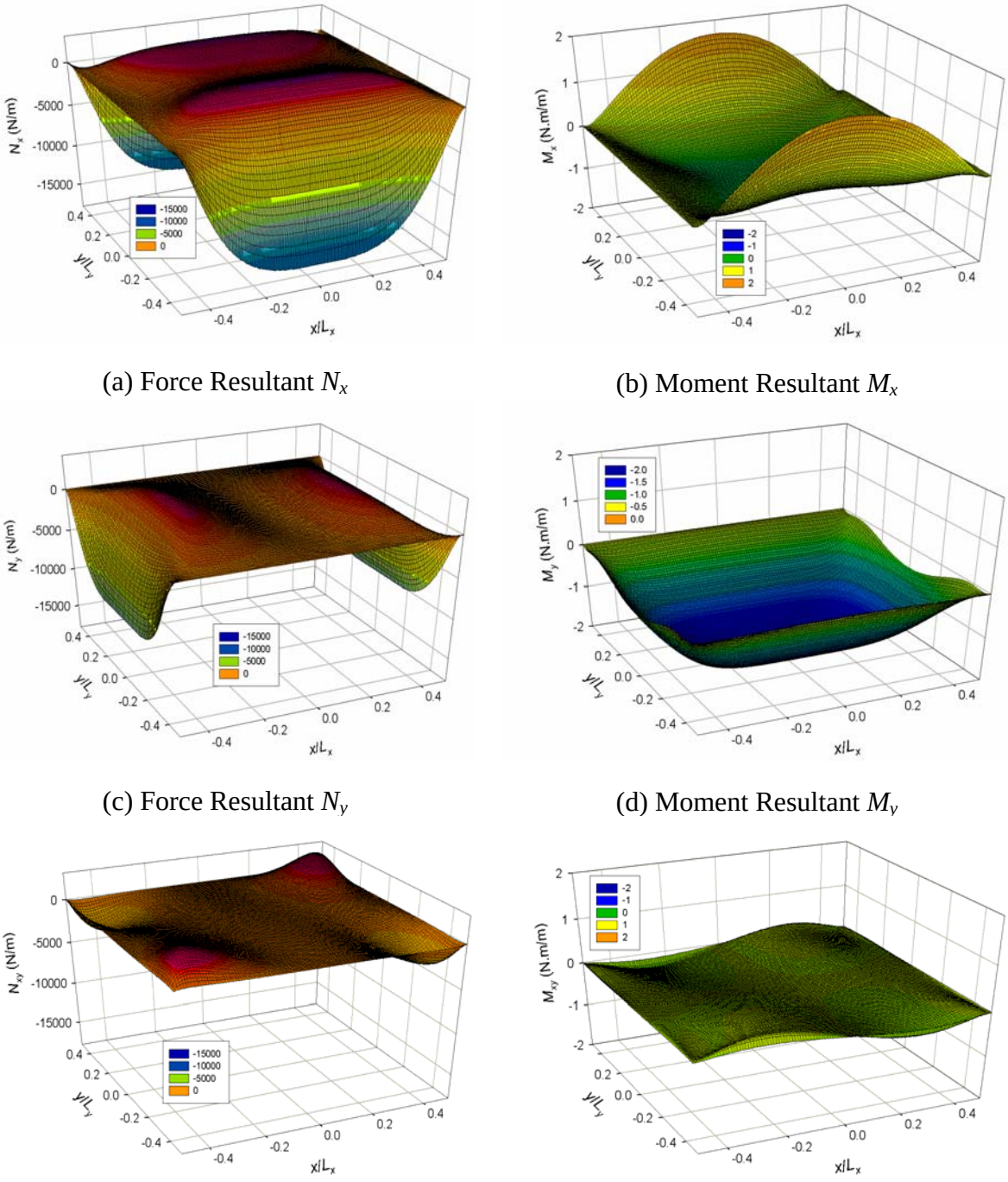

(a) Force Resultant N_x

(b) Moment Resultant M_x

(c) Force Resultant N_y

(d) Moment Resultant M_y

(e) Force Resultant N_{xy}

(f) Moment Resultant M_{xy}

Figure 3.10: Force and Moment Resultants in Rectangular THUNDER (L_y /L_x = 0.7, L_x/H = 200, ΔT = -300 °C)

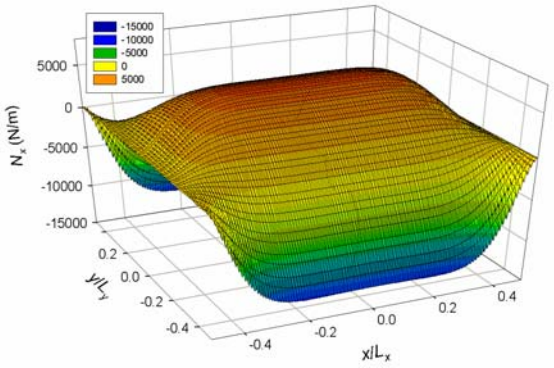

(a) Force Resultant N_x

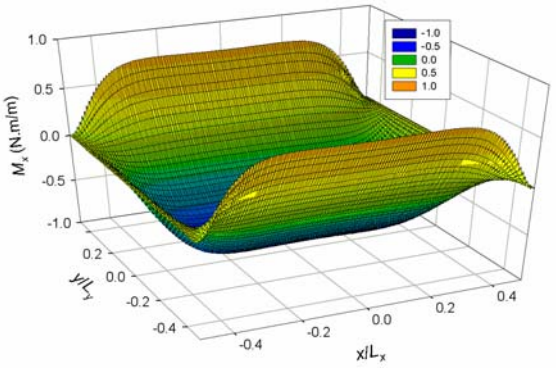

(b) Moment Resultant M_x

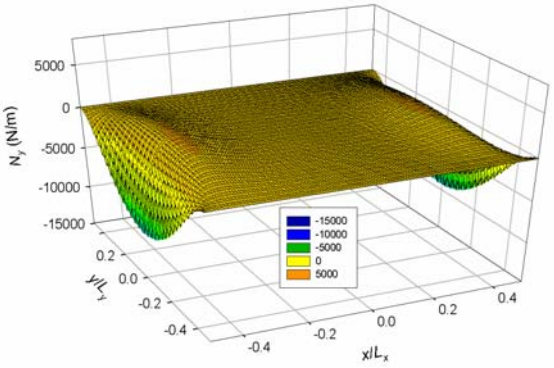

(c) Force Resultant N_y

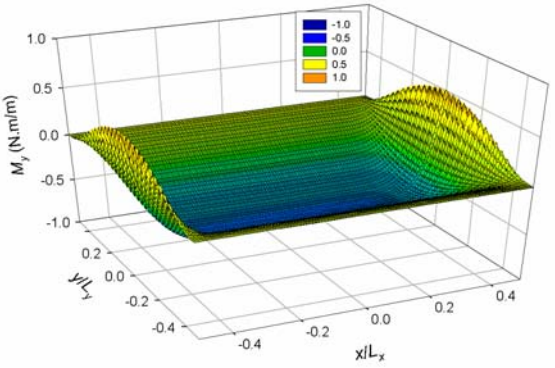

(d) Moment Resultant M_y

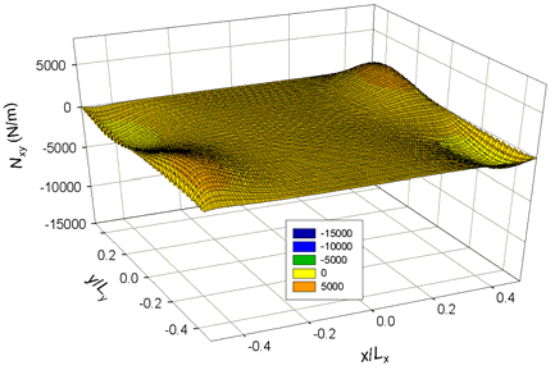

(e) Force Resultant N_{xy}

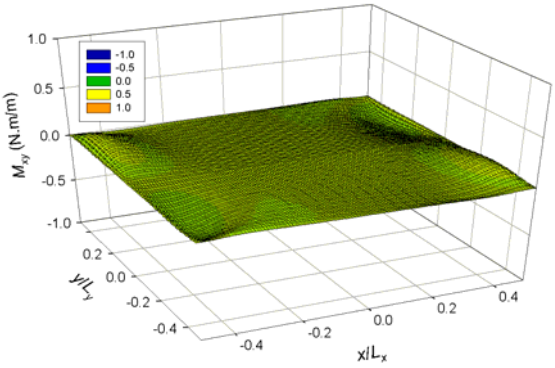

(f) Moment Resultant M_{xy}

Figure 3.11: Force and Moment Resultants in Rectangular THUNDER (L_y/L_x = 0.3, L_x/H = 200, ΔT = -300 °C)

curvatures in the x- and y-directions (see Figures 3.6 and 3.8). For the geometrically nonlinear analysis, for the situation shown in Figure 3.10, as noted, the actuator is relatively flat in the y-direction, but still has curvature in the x-direction. Such a shape could be generated by starting with the dome-like configuration, and then applying the appropriate force and moment resultants along the edges by some mechanical means, or by starting with the flat actuator and applying different force and moment resultants along the edges. Because of the large out-of-plane deflections of the actuator as it cools, the thermal stresses within the various layers generate the forces and moments to make the room-temperature shape near-cylindrical rather than dome-like. When geometrical nonlinearities are considered, the near-cylindrical shape represents a lower total potential energy state for the actuator than the dome-like shape. In a sense, the actuator "self-generates" the forces and moments along the edges to achieve the lower total potential energy state near-cylindrical shape. Note that the extreme values of N_{xy} and M_{xy} are small compared to extreme values of N_x and N_y, and M_x and M_y, respectively. This is an indication that shear effects are minimal, though they are not zero.

A similar picture emerges for the more beam-like actuator. Figure 3.11 shows the force and moment resultants for the actuator with an aspect ratio of 0.3 and a sidelength-to-thickness ratio of 200. The magnitude of the force and moment resultants does depend on the aspect ratio, to some degree, but the general character of the spatial distribution changes only slightly with aspect ratio.

A sample of the stresses that lead to the force and moment resultants N_x, N_y, M_x, and M_y for the rectangular actuator with an aspect ratio of 0.7 and a thickness ratio of 200 are illustrated in Figures 3.12 and 3.13 for four locations within the actuator. The through-thickness distributions of the inplane normal stresses near the center of the actuator $x \cong 0$, $y \cong 0$ (see Figures 1.10 and 2.1) are illustrated in Figure 3.12 (a), while the distributions near the midpoints along the longer edge ($x \cong 0$, $y \cong L_y/2$) and near the shorter edge ($x \cong L_x/2$, $y \cong 0$)

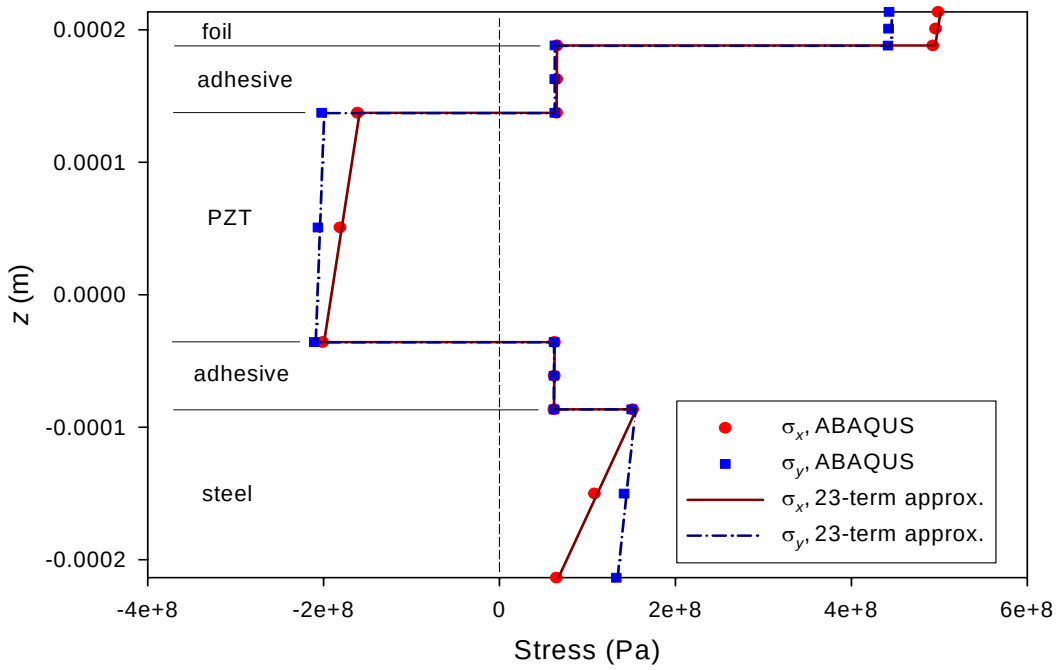

(a) Distribution of Normal Stresses at $x \cong 0$, $y \cong 0$

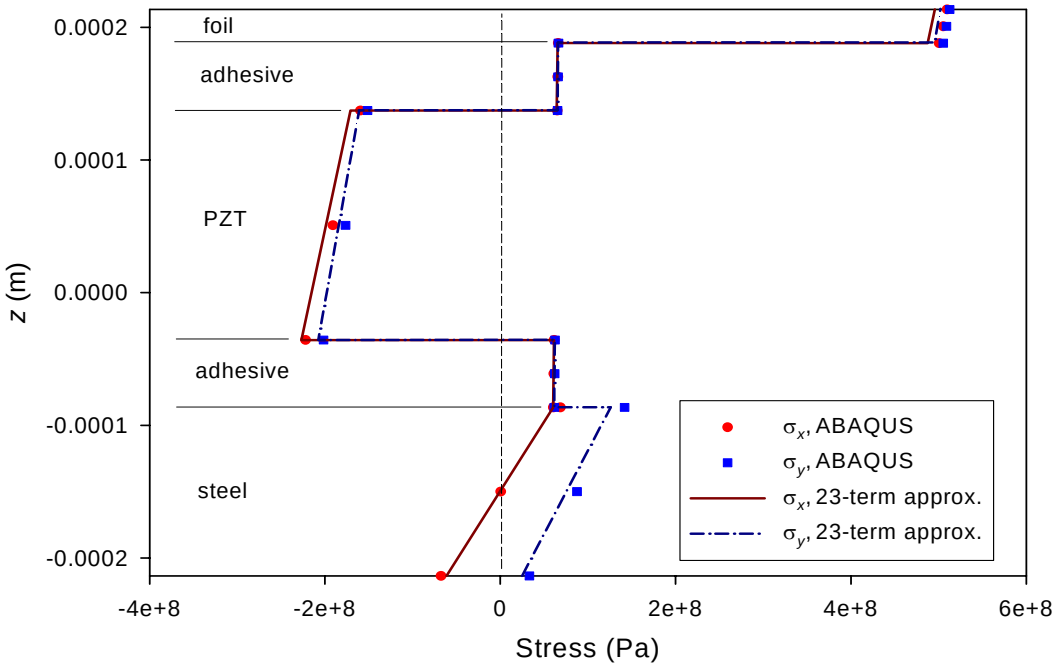

(b) Distribution of Normal Stresses at $x \cong 0$, $y \cong L_y/2$

Figure 3.12: Stress Distributions in THUNDER ($L_y/L_x = 0.7$, $L_x/H = 200$, $\Delta T = -300\,^{\circ}\mathrm{C}$) for Two Locations near Centerline $x = 0$

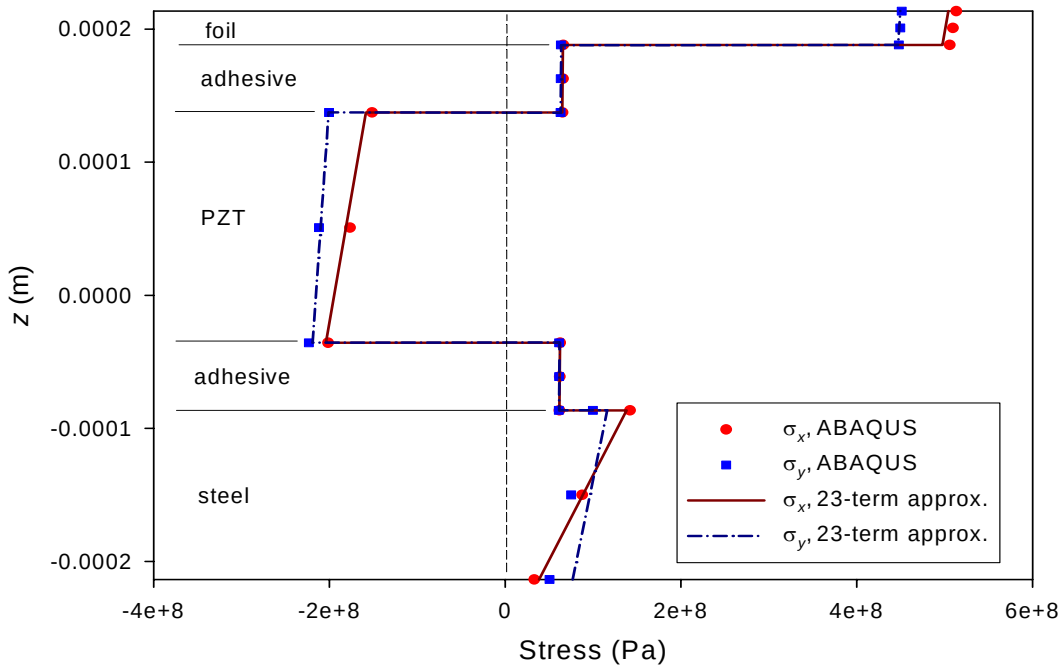

(a) Distribution of Normal Stresses at $x \cong L_x/2$, $y \cong 0$

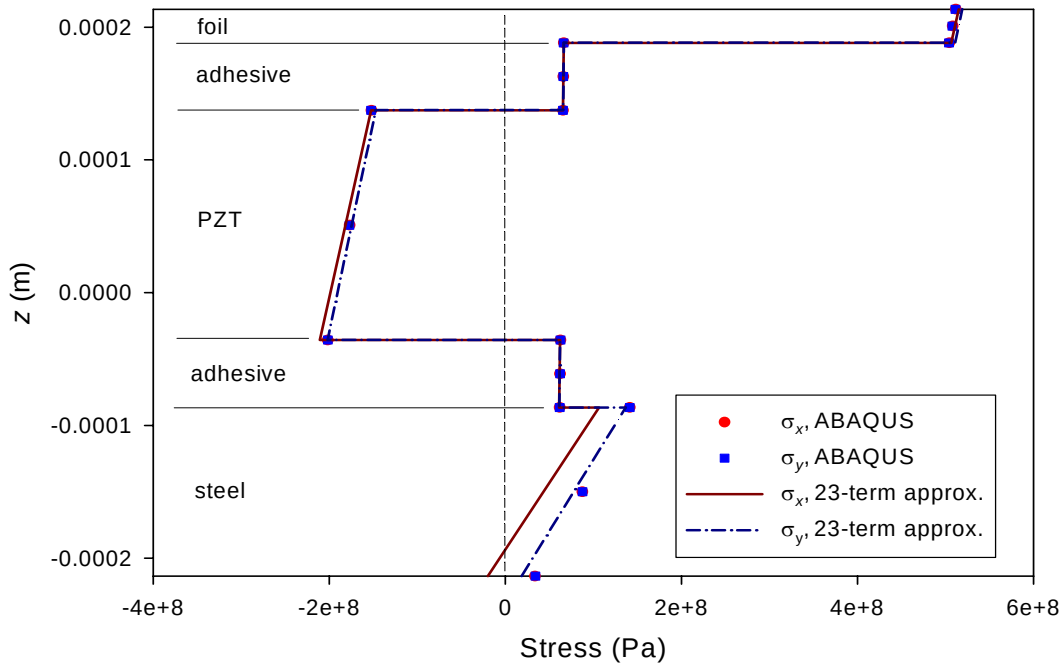

(b) Distribution of Normal Stresses at $x \cong L_x/2$, $y \cong L_y/2$

Figure 3.13: Stress Distributions in THUNDER ($L_y/L_x = 0.7$, $L_x/H = 200$, $\Delta T = -300\,^{\circ}\mathrm{C}$) for Two Locations near Boundary $x = L_x/2$

are illustrated in Figures 3.12 (b), and 3.13 (a), respectively. The distributions near a corner ($x \cong L_x/2$, $y \cong L_y/2$) are displayed in Figure 3.13 (b). Since the stress calculations resulting from the ABAQUS model are expected to be more accurate than from the 23-term Rayleigh-Ritz approach, the following discussions about the stress distributions are based on the finite-element results, although the stresses computed by the Rayleigh-Ritz approach are in good agreement with finite-element results.

At first glance all distributions look very similar, but upon a closer inspection, the distributions change from figure to figure, reflecting the dependence of the force and moment resultants on spatial location, as presented in Figure 3.10. For instance, when comparing the inplane normal stress σ_x distribution in Figure 3.12 (a) with the one in 3.12 (b), it is seen that the distributions of σ_x in every layer are roughly identical except for the steel backbone layer (the bottom layer). Near the center of the actuator, there is a net positive contribution to N_x from the steel layer in Figure 3.12 (a). However, near the midpoint along the longer edge, Figure 3.12 (b), the net contribution is close to zero, since the stress is linearly distributed and changes sign midway through the steel layer. Therefore, the difference in the distributions in the stainless steel layer leads to a more negative value of N_x, and a more positive value of M_x, near the edge than near the center. A comparison between the distribution of σ_x in Figure 3.12 (a) and the one in Figure 3.13 (a) can also be considered. Following the same explanation given above, the main difference is again in the steel layer. Due to the more positive values of σ_x in steel near the center, Figure 3.12 (a), than near the midpoint along the shorter edge, Figure 3.13 (a), the slightly positive value of N_x and slightly negative value of M_x near the center will decrease and increase, respectively, such that they are zero near the shorter edge, a consequence of the traction-free boundary conditions. In addition, it can be noticed that the distribution of σ_x in Figure 3.13 (a) that contributes to zero force and moment resultants at $x \cong L_x/2$, $y \cong 0$ is the same as the distributions of σ_x and σ_y near the corner $x \cong L_x/2$, $y \cong L_y/2$ in Figure 3.13 (b). This is again

a reflection of the traction-free boundary conditions imposed on all free edges. Note that both σ_x and σ_y in the PZT layer are compressive everywhere. Also, it should be mentioned that the geometrically linear theory would predict the inplane normal stresses at every point in the actuator to be almost identical to those near the corner, Figure 3.13 (b), because all force and moment resultants are zero according to the linear theory, as they are at the corner for the nonlinear theory.

3.2.3 Snap-Through Behavior of THUNDER without Tabs Induced by Moments

As stated in Sections 2.4.2 and 3.2.1, an actuator with geometric parameters such that it has multiple stable equilibrium shapes can be transformed, or snapped, from one stable shape to the other. The snap-through action can be accomplished by applying a pair of moments along two opposite edges of the actuator. It is instructive to study magnitudes and directions of the applied moments that can be employed to snap the actuator and study how the actuator behaves. The Rayleigh-Ritz model presented in Section 2.4 can be implemented to investigate these issues. By specifying values of the moments in Equation (2.40) and then substituting W_M into Equation (2.43) and omitting W_F, approximate equilibrium shapes of a THUNDER actuator subjected to the applied moments can be computed. Here the THUNDER actuator at room temperature with $L_y/L_x = 0.7$ and a sidelength-to-thickness ratio close to the limit point (L_x/H = 166 in Figure 3.8), i.e., within 15% of the limit point, or L_x/H = 190, is chosen as a calculation example of the snap-through phenomenon.

Consider the THUNDER actuator subjected to applied edge moments, as illustrated in Figure 2.4. In the case of $M_y^s = 0$, a relation between the average curvatures of the actuator and the applied moment M_x^s is presented in Figure 3.14. Initially, before M_x^s is applied on the edges $x = +L_x/2$ and $x = -L_x/2$, the manufactured room-temperature configuration is assumed to be on the stable branch $A'D'$ in Figure 3.8 and corresponds to point A^* on branch B^*C^* in Figure 3.14, where the average curvature in the x-direction is larger than that in the y-direction. Referring to Figure 3.14, when a positive value of M_x^s is

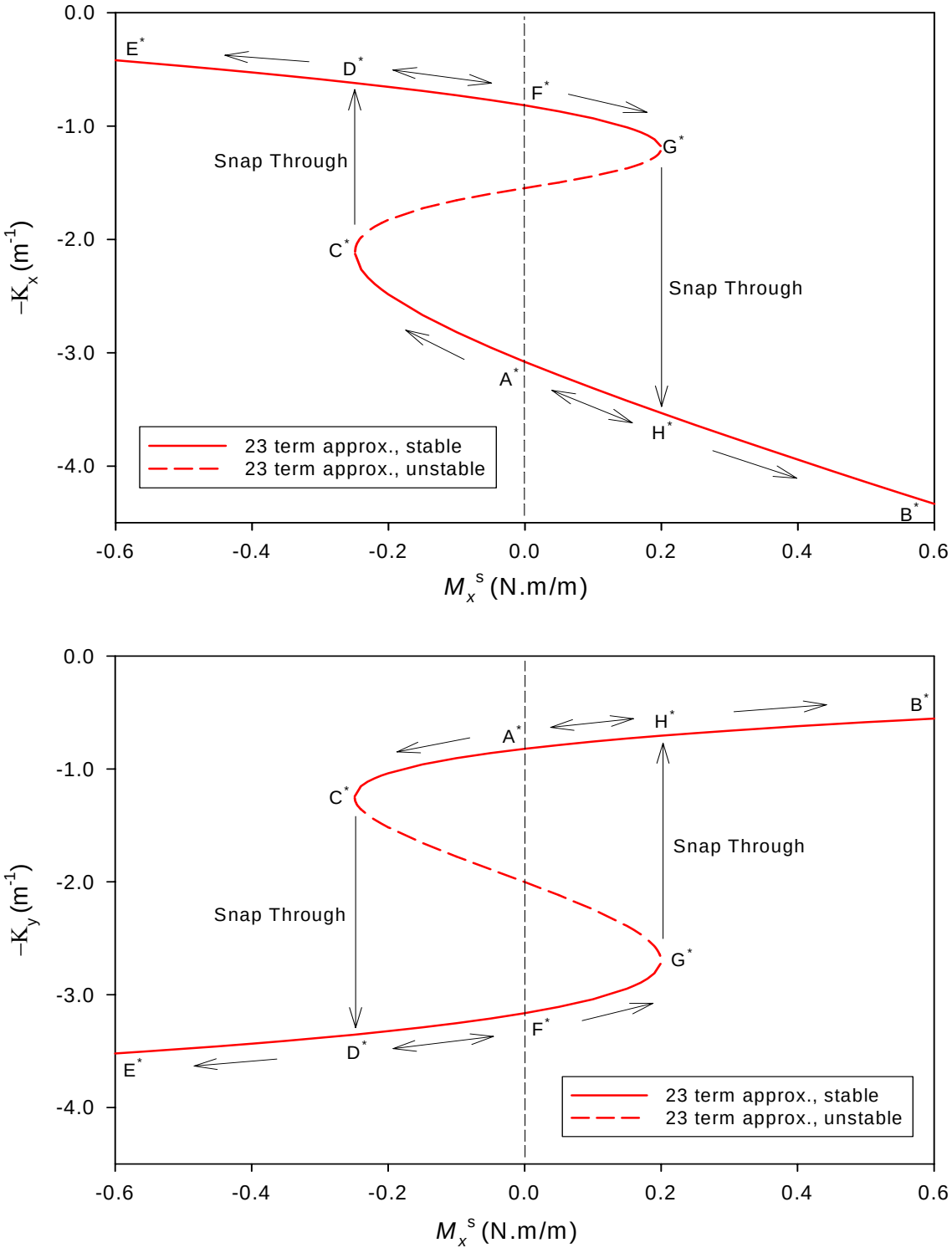

Figure 3.14: Moment along the *x* edges vs. Curvature Relations of Rectangular THUNDER (L_y/L_x = 0.7, L_x/H = 190, ΔT = -300 °C)

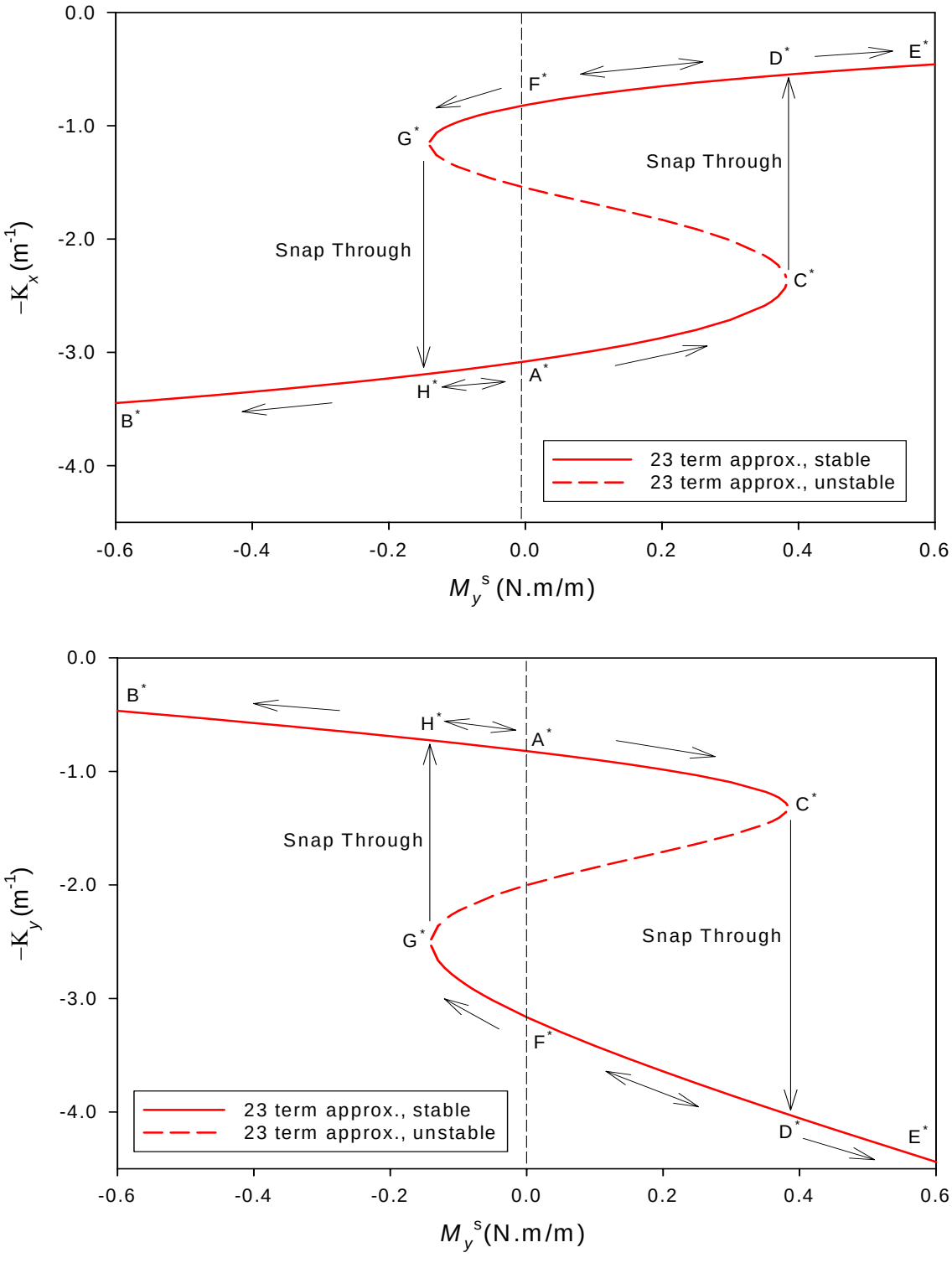

Figure 3.15: Moment along the *y* edges vs. Curvature Relations of Rectangular THUNDER (L_y /L_x = 0.7, L_x/H = 190, ΔT = -300 °C)

applied to the actuator, the actuator configuration moves from point A^* toward point B^* along branch B^*C^*. Its average curvature in the *x*-direction increases rapidly, whereas the average curvature in the *y*-direction decreases slowly due to the anticlastic curvature effect. Along the path from A^* to B^*, there exists no critical point where the actuator transforms from one stable shape to the other. Rather, the average curvatures change gradually relative to the stable shape at point A^*. On the other hand, starting at point A^*, when a negative value of M_x^s is applied to the actuator, the configuration moves toward point C^* on branch B^*C^* such that the *x*- and *y*-direction average curvatures decrease and increase, respectively. When the applied moment equals -0.25 N·m/m, the actuator suddenly changes configuration, or snaps through, from point C^* on stable branch B^*C^* to point D^* on stable branch E^*G^*. In the snapped configuration, the average curvature in the *x*-direction is smaller than that in the *y*-direction. If the a more negative moment is applied, the actuator's shape moves from point D^* toward point E^*. If the magnitude of the negative moment is decreased to zero, the configuration moves to point F^*, which corresponds to a point on branch $B'C'$ in Figure 3.8. Analogously, the manufactured shape of a THUNDER actuator given by point F^* can be transformed to the shape at point A^* by first applying a positive value of M_x^s of about 0.2 N·m/m. The configuration of the actuator will change from point F^* to G^* along branch E^*G^*, and then from G^* to H^* with a snap-through phenomenon. Finally, when the applied positive moment is decreased to zero from point H^*, the actuator assumes the manufactured shape given by point A^*.

Snap-through behavior can also be observed with the sole application of moment M_y^s, as illustrated in Figure 3.15. Again, the initial room-temperature shape of the actuator is assumed to be located at point A^*, the same configuration as point A^* in Figure 3.14. When the actuator is subjected to a negative value of M_y^s, its *x*- and *y*-direction average curvatures increase and decrease along branch B^*C^*, respectively. However, when the actuator is subjected to a positive value of M_y^s, its configuration moves toward point C^*.

When $M_y^s = 0.38$ N·m/m, the actuator snaps through to another configuration, point D^*, After the snap-through phenomenon, the actuator is in the new stable equilibrium state that lies on branch E^*G^*. The actuator's shape will follow this branch to point E^* if a higher positive M_y^s is applied, or point F^* if the moment is released. Note that point F^* in this figure is the same configuration as point F^* in Figure 3.14. At point F^*, if the actuator is subjected to a negative value of M_y^s which reaches a value of -0.12 N·m/m, the actuator's configuration will move to point G^* in such a way that its *x*- and *y*-direction average curvatures increase and decrease, respectively, and then the actuator snaps again to the stable branch B^*C^* at point H^*. Finally, the original stable shape at point A^* is obtained when the negative value of M_y^s is released.

In addition, according to Figures 3.14 and 3.15, two more important comments can be stated. Firstly, the actuator's configuration at point A^* seems to be more stable than that at point F^* because the required magnitude of the snapping moment (either M_x^s or M_y^s) that causes the configuration transformation from point A^* to F^* is always larger than the one that causes the transformation from point F^* to point A^*. Secondly, for the stable equilibrium shapes, structural compliance in the direction of the larger room-temperature average curvature is more than structural compliance in the direction of the smaller room-temperature average curvature. For example, the rate of change of the *x*-direction average curvature at point A^* with respect to moment M_x^s in Figure 3.14 is larger than the rate of change of the *y*-direction average curvature at point A^* with respect to moment M_y^s in Figure 3.15. An analogous comment can also be made regarding point F^*.

3.2.4 Effects of Tabs on Deformation Characteristics of THUNDER

As stated, the results of THUNDER actuators discussed above did not include attachment tabs. To consider effects of tabs on the deformation characteristics, the 23-term Rayleigh-Ritz model developed in Section 2.2.3 is employed to find room-temperature shapes of a THUNDER actuator with tabs. After taking the first and second variations of the

total potential energy in Equation (2.25), equilibrium and stability conditions of the cooled THUNDER actuator can be computed.

The relationships between the thickness ratio and the average curvatures for a THUNDER actuator with tabs for L_y/L_x = 0.7 and 1 are shown in Figures 3.16 and 3.17, respectively. Figures 3.16 and 3.17 can be compared with their counterpart Figures 3.8 and 3.5, respectively, which illustrate the same relationship for the case of no tabs. It can be seen that for rectangular actuators with and without tabs (L_y/L_x = 0.7), the overall characteristics of the average curvatures vs. sidelength-to-thickness ratio are similar. The analyses show that the existence of the tabs shifts the limit point to the right, from L_x/H = 166 to L_x/H = 170 according to the ABAQUS model, or to L_x/H = 178 according to the Rayleigh-Ritz model. A good agreement of the average curvatures between the ABAQUS and Rayleigh-Ritz models can be seen for branch $A'D'$, but not for branch $C'B'E'$. This difference occurs because the 23-term Rayleigh-Ritz model is capable of predicting the configurations of the actuator in an average sense only. It cannot accurately capture the local deformations of the small tab regions when there is a larger average curvature in the *y*-direction than in the *x*- direction, branch $C'B'E'$. An extremely high degree of assumed polynomial functions is needed to capture the local effects represented by branch $C'B'E'$. Thus, in this sense the Rayleigh-Ritz approach has a disadvantage compared with the finite-element model. However, overall, the Rayleigh-Ritz model is fairly good in terms of limit point prediction with less than 5% difference when compared with thousands of degrees of freedom of the finite-element model. An important point is that the ABAQUS model predicts the tabs have less influence on branch $C'B'E'$ than the Rayleigh-Ritz model predicts.

Comparison of Figures 3.17 and 3.5 shows the addition of tabs drastically changes the characteristics of the sidelength-to-thickness ratio vs. average curvature relations of actuators with a square active portion (L_y/L_x = 1). Immediately obvious is the fact that bifurcation behavior does not occur when tabs are included, rather limit point

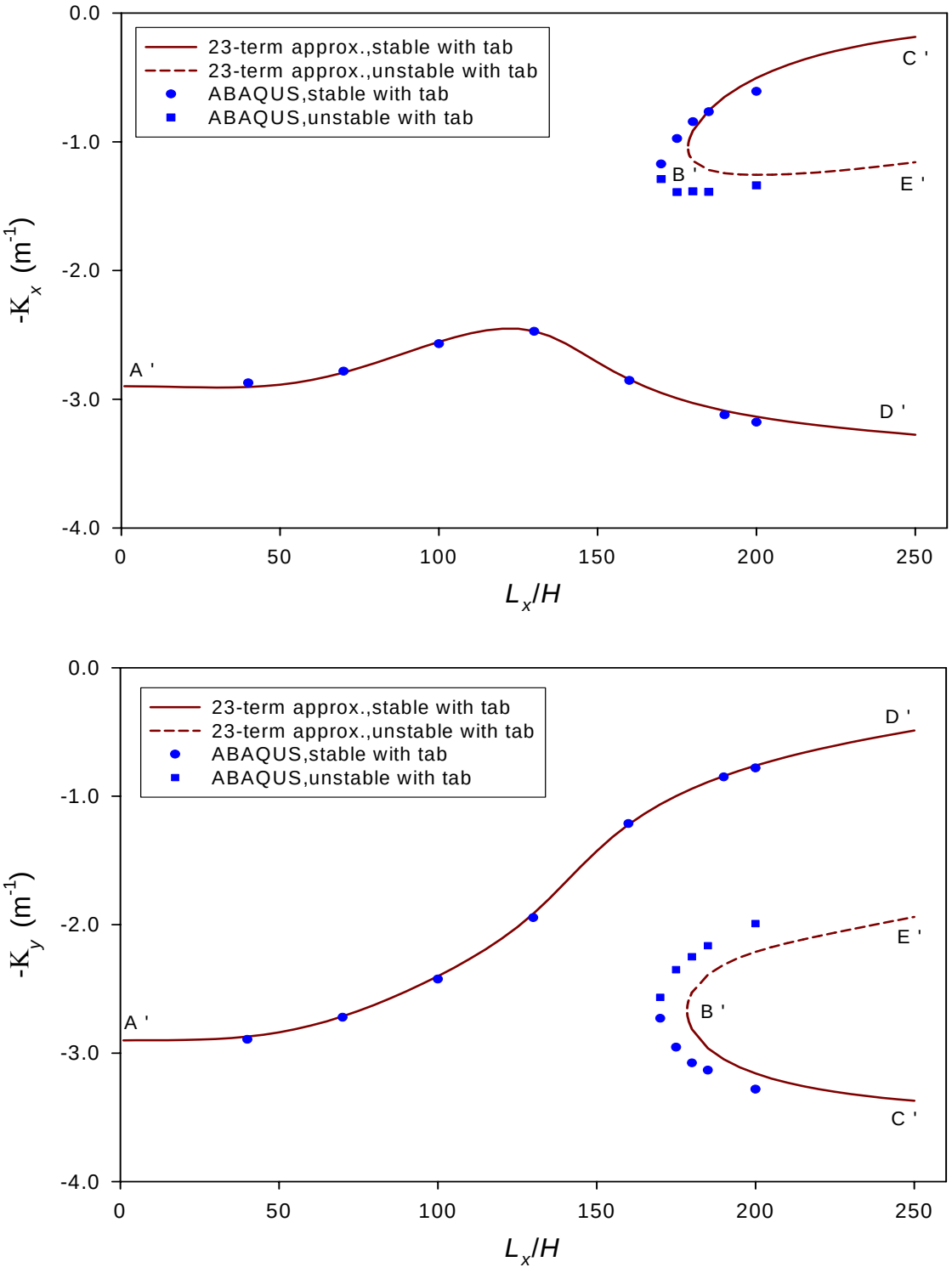

Figure 3.16: Sidelength-to-Thickness Ratio vs. Curvature Relations of Rectangular THUNDER with Tabs (L_y/L_x = 0.7, ΔT = -300 °C, $L_x^t = 0.1L_x$)

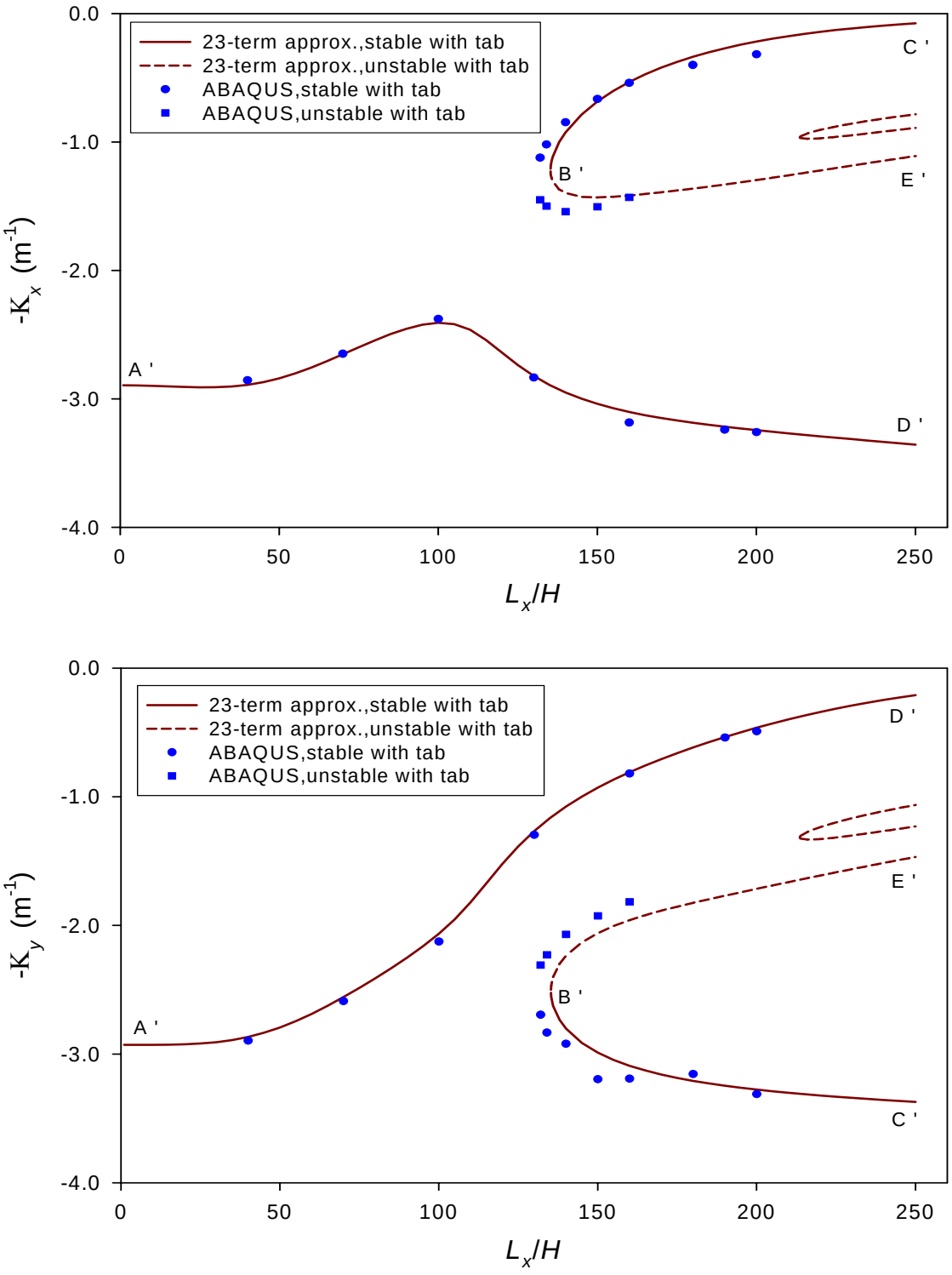

Figure 3.17: Sidelength-to-Thickness Ratio vs. Curvature Relations of Square THUNDER with Tabs ($L_y/L_x = 1,\ \Delta T = -300\,°\text{C},\ L_x^t = 0.1L_x$)

behavior characterizes the relationship. With no tabs, the relationship exhibits bifurcation behavior due to the symmetry of the actuator, i.e., $L_x = L_y$. With tabs along two opposite edges, that symmetry no longer exists and the relationship resembles that of an actuator with an aspect ratio of 0.7, Figure 3.8, and exhibits limit point behavior. The limit point behavior in Figure 3.17 occurs at $L_x/H = 132$, according to the finite-element analysis, whereas the bifurcation behavior in Figure 3.5 occurs at $L_x/H = 120$. The deviations between the 23-term Rayleigh-Ritz predictions and the ABAQUS results for branch C′B′E′ can be observed, but they are not as great as for rectangular actuators with tabs, i.e., Figures 3.16 vs. Figure 3.8. This is due to having less degree of structural orthotropy in the case of square actuators than in the case of rectangular ones. In Figure 3.17, difference in the limit point prediction is only 2 % between the Rayleigh-Ritz and ABAQUS models.

3.3 Numerical Results for Actuated Shapes

3.3.1 Deformation Characteristics of THUNDER subjected to Applied Electric Field

The effects of the electric field on the shape of a THUNDER actuator will be described two ways. An actuator with an aspect ratio of 0.7 will be considered. The effects of applying the electric field on the predicted average curvatures at ΔT = -300 °C as a function of the sidelength-to-thickness ratio are illustrated in Figure 3.18. The response to both positive and negative fields, relative to the direction of polarization, is shown. The field strength is assumed to be 2 MV/m, a very high field for the pizoceramic materials considered. The curvatures with no field, from Figure 3.8, are repeated on the figure. Tabs are not included. The vertical distance between the no-field relation and the relations with ± 2 MV/m represents the change in average curvature. What is to be noted is that the average curvature change is a function of the sidelength-to-thickness ratio of the actuator, and the average curvature in the *x*-direction does not necessarily change the same amount as the average curvature in the *y*-direction. For example, for an actuator with $L_x/H = 200$, for

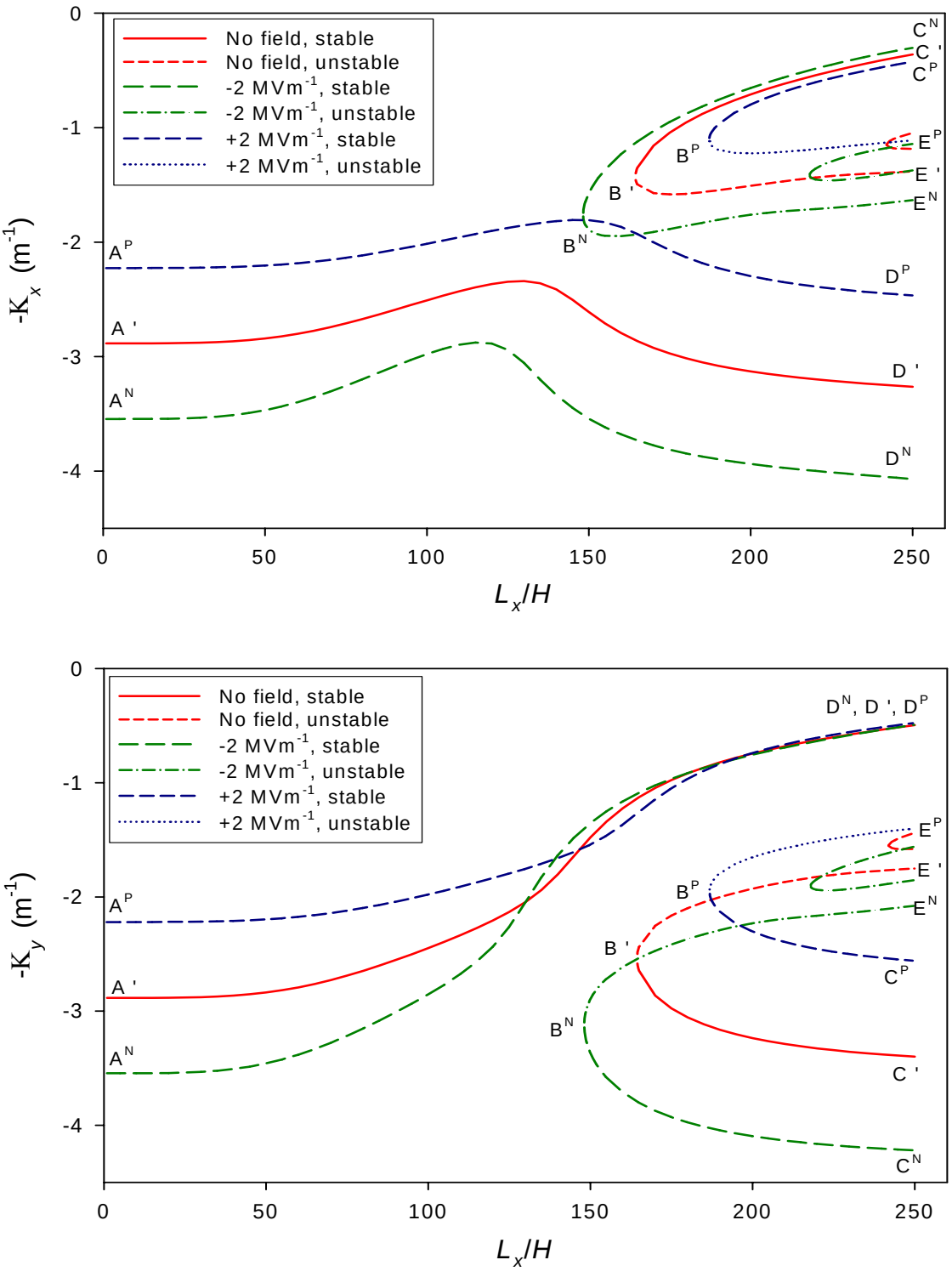

Figure 3.18: Influence of Actuation on the Change of Curvatures of Rectangular THUNDER ($L_y / L_x = 0.7,\ \Delta T = -300\,°C$)

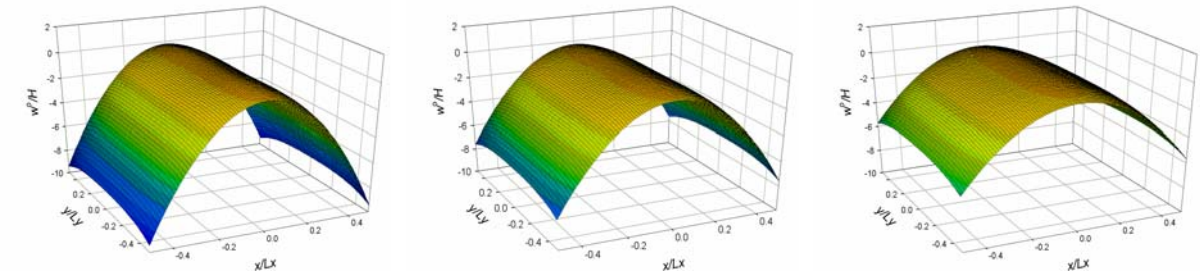

(a) With -2 MV/m field (on branch $A^N D^N$)

b) Without electrical field (on branch $A'D'$)

(c) With +2 MV/m field (on branch $A^P D^P$)

Figure 3.19: Out-of-Plane Shapes of THUNDER under Electrical Voltage Actuation (L_x/H = 200, L_y/L_x = 0.7, ΔT = -300 °C)

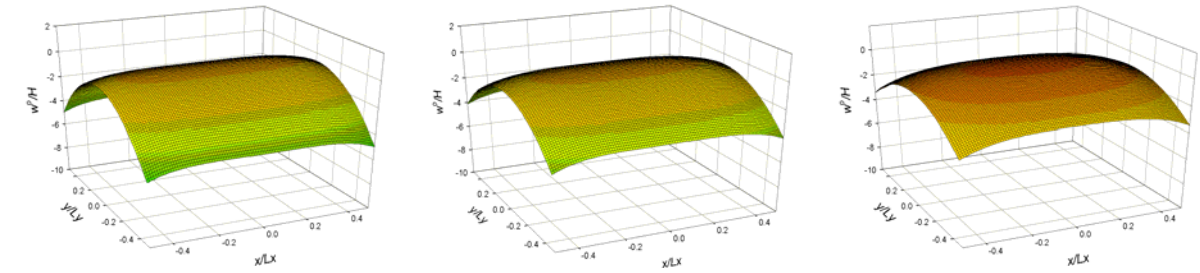

(a) With -2 MV/m field (on branch $B^N C^N$)

b) Without electrical field (on branch $B'C'$)

(c) With +2 MV/m field (on branch $B^P C^P$)

Figure 3.20: Out-of-Plane Shapes of THUNDER under Electrical Voltage Actuation (L_x/H = 200, L_y/L_x = 0.7, ΔT = -300 °C)

the shape on the branch referred to in Figures 3.8 and 3.18 as branch $A'D'$, the average curvature in the *y*-direction hardly changes, while the average curvature in the *x*-direction changes considerably. Figure 3.19 illustrates the shapes of the actuator with positive, negative, and no electric fields applied, assuming the actuator is characterized by branch $A'D'$. The zero field shape is repeated from Figure 3.7 (e). The change of one curvature more than the other due to the application of the electric field is a geometrically nonlinear effect. On the stable portion for the branch referred to in Figures 3.8 and 3.18 as branch

$C'B'E'$, the curvature in the *y*-direction changes much more than the curvature in the *x*-direction, as also shown in Figure 3.20. This again reflects a geometrically nonlinear effect. For an actuator with $L_x/H = 100$, the curvature in the *x*-direction changes slightly more than the curvature in the *y*-direction, and as L_x/H approaches the limit point value, the curvature changes even more in relation to the curvature change in the *y*-direction. Additionally, it can be noted that an applied electric field also alters the value of critical sidelength-to-thickness ratio. A positive field increases the critical limit point value, and a negative field decreases the limit point value. This makes sense, since the positive field tends to flatten the actuator (reduces the average curvatures), as illustrated in Figures 3.19 and 3.20, and, therefore, suppress the geometric nonlinearity due to the large out-of-plane deformation generated during the cooling process. As a result, the variations of the average curvatures in the *x*- and *y*-directions over the considered sidelength-to-thickness ratios for branch A^PD^P are less than those without an electric field applied, branch $A'D'$, and the emergence of the limit point or multiple solutions is shifted to a larger sidelength-to-thickness ratio (point B^P compared to point B'). These behaviors are trends toward the geometrically linear plate model. On the other hand, a negative field tends to bend the actuator more and, thus, enhance the geometric nonlinearity. This in turn causes more average curvature variation along branch A^ND^N in relation to sidelength-to-thickness ratio and reduces the critical sidelength-to-thickness ratio value (point B^N compared to point B'). The curvature changes predicted by the geometrically linear Rayleigh-Ritz model are given by the vertical distances at point A', specifically from A' to A^P for positive field and from A' to A^N for negative field, in Figure 3.18. The curvature changes for the linear model are independent of the sidelength-to-thickness ratio.

Figure 3.21 illustrates the average curvature of square THUNDER actuators at $\Delta T = -300\,°C$ due to an application of ± 2 MV/m electric fields vs. sidelength-to-thickness ratio. The stable and unstable branches from Figure 3.5 are also included for reference. The

same conclusions can be drawn from Figure 3.21 as were drawn from Figure 3.18, except that in this case the critical points are bifurcation points instead of limit points. For example, for L_x/H = 200, application of the electric field has very little effect on the *y*-direction curvature for branch $B'D'$, and very little effect on the *x*-direction curvature for branch $B'C'$.

It should be noted that in Figures 3.18 and 3.21, suppression or enhancement of the curvature change, relative to the geometrically linear prediction, occurs and is a function of sidelength-to-thickness ratio. For example, looking at Figure 3.18, the vertical distance between branches A^PD^P and A^ND^N for L_x/H = 100 is less than the vertical distance of $L_x/H \approx 0$, the linear prediction. This is evidence that geometrically nonlinear effects are detrimental. On the other hand, at L_x/H = 250 the vertical distance between those two branches is considerably greater than the linear prediction. This is evidence that for this value of L_x/H, geometrically nonlinear effects are beneficial.

Actuation responses of beam-like THUNDER actuators at ΔT = -300 °C with an aspect ratio of 0.3 to an applied electric field of ± 2 MV/m illustrated in Figure 3.22. Again, the average curvatures with zero electric field shown in Figure 3.9 are included here for reference. Unlike the two previous cases of L_y/L_x = 0.7 and 1, which posses multiple branches in sidelength-to-thickness ratio vs. average curvature relations, the Rayleigh-Ritz model predicts only one stable branch for each actuation field applied to actuators with L_y/L_x = 0.3. As seen, the average curvature changes in the *x*- and *y*-directions gradually decrease as sidelength-to-thickness ratio increases, until the ratio reaches the value of around 200. When the sidelength-to-thickness ratio is more than this value, the change in the *x*-direction average curvature slightly increases, whereas that in the *y*-direction decreases monotonically. Interestingly, and especially for the *y*-direction average curvature, the average curvature change caused by a positive voltage is not equal in magnitude to the curvature change caused by a negative voltage. This, again, is a direct effect of geometric

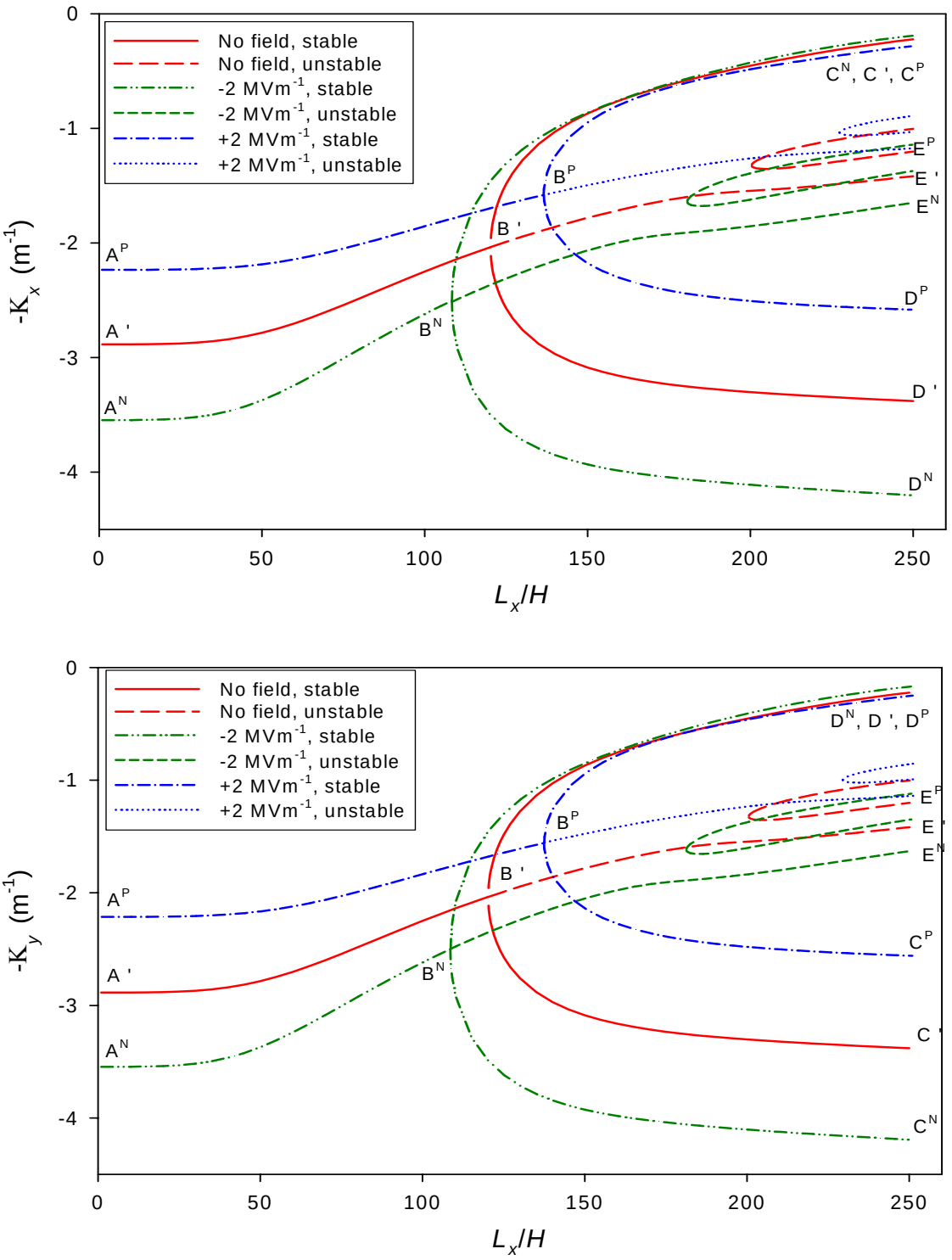

Figure 3.21: Influence of Actuation on the Change of Curvatures of Square THUNDER (L_y/L_x = 1, ΔT = -300 °C)

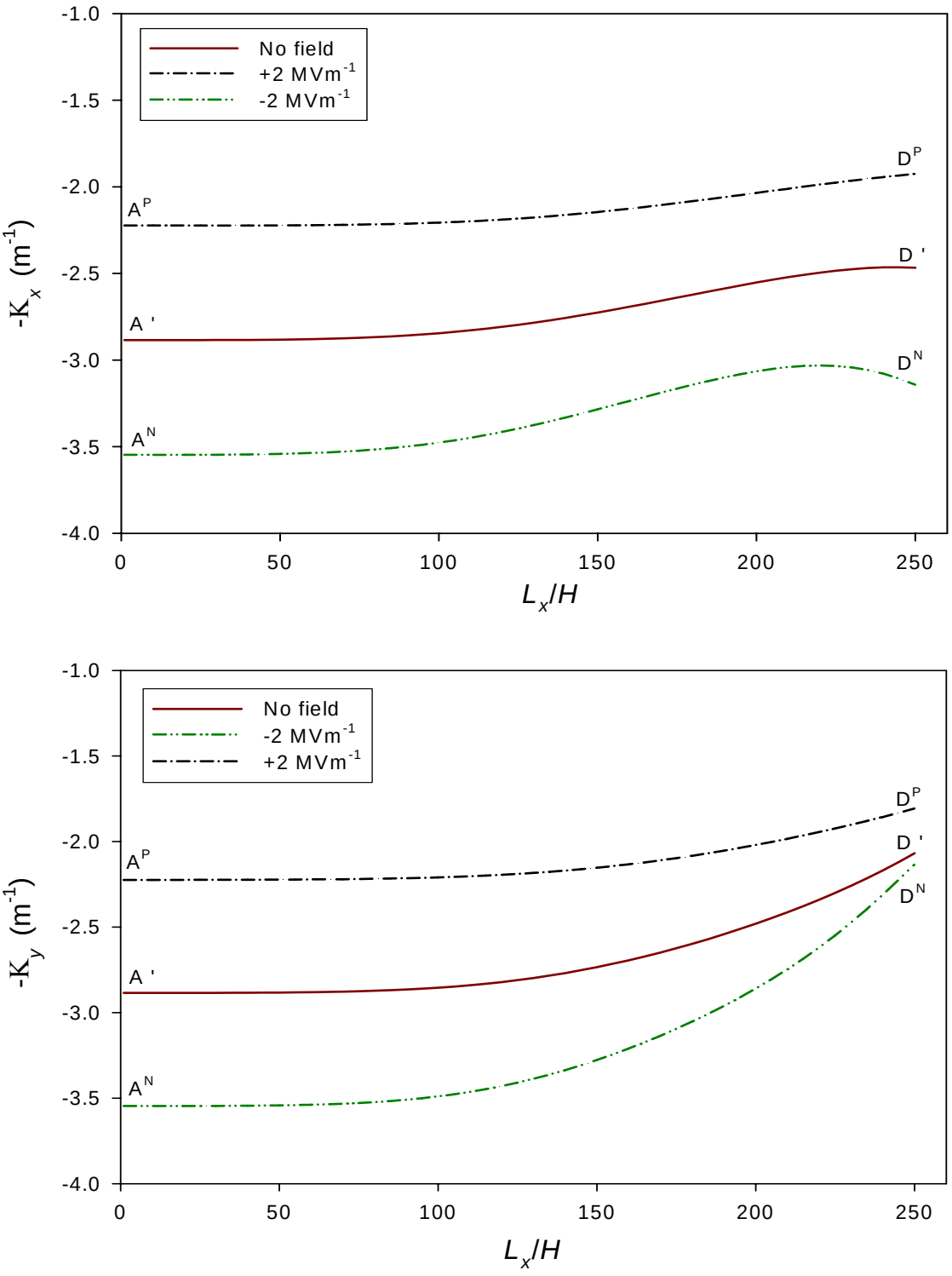

Figure 3.22: Influence of Actuation on the Change of Curvatures of Beam-Like THUNDER (L_y/L_x = 0.3, ΔT = -300 °C)

nonlinearities and has ramifications for dynamic behavior due to, for example, a harmonic variation of electric field strength. Also, note that since the actuator is beam-like, the comparison of the *x*-direction curvatures due to the applied electric field strengths between the presented Rayleigh-Ritz model and the beam theories developed in Appendix B is of interest. By employing Equation (B.42) or (B.68), $K_x = 2.31\ m^{-1}$ and $3.63\ m^{-1}$ for ±2 MV/m, respectively. The curvatures are uniform over the range of sidelength-to-thickness ratios considered and their values are close to the values of the *x*-direction actuated curvatures predicted by the geometrically linear Rayleigh-Ritz model of $K_x = 2.22\ m^{-1}$ and $3.55\ m^{-1}$ for ±2 MV/m. Though they are not shown in Figure 3.22, the actuated curvatures predicted by the geometrically linear Rayleigh-Ritz model can be represented by straight horizontal lines tangent to point A^P and A^N for +2 MV/m and -2 MV/m field strengths, respectively. It is obvious that for shorter actuators, the geometrically linear theory is sufficient.

Viewed differently, the average curvature changes as a function of electric field strength can be considered. For example, THUNDER actuators with two different actuator sidelength-to-thickness ratios are investigated in Figure 3.23, $L_x/H = 200$ in Figure 3.23 (a) and $L_x/H = 100$ in Figure 3.23 (b). The aspect ratio for both actuators is 0.7. These figures also include the curvature changes predicted by the geometrically linear Rayleigh-Ritz model and the average curvature changes predicted for a flat actuator. The geometrically linear prediction is indicated by the dotted lines in the figures. The analysis for the flat actuator is conducted with the same 23-term Rayleigh-Ritz analysis, but using a temperature change of zero. Referring to Figure 3.23 (a) and the average curvature change from branch $A'D'$ to branches A^PD^P and A^ND^N of Figure 3.18, it is again observed that the average curvature change in the *y*-direction due to actuation is very small, while that in the *x*-direction is quite large. The geometrically linear analysis predicts less curvature change in the *x*-direction, and the curvature changes in the *x*- and *y*-directions are equal rather than the change in the *y*-direction being close to zero. For a flat actuator the *x*- and *y*-direction

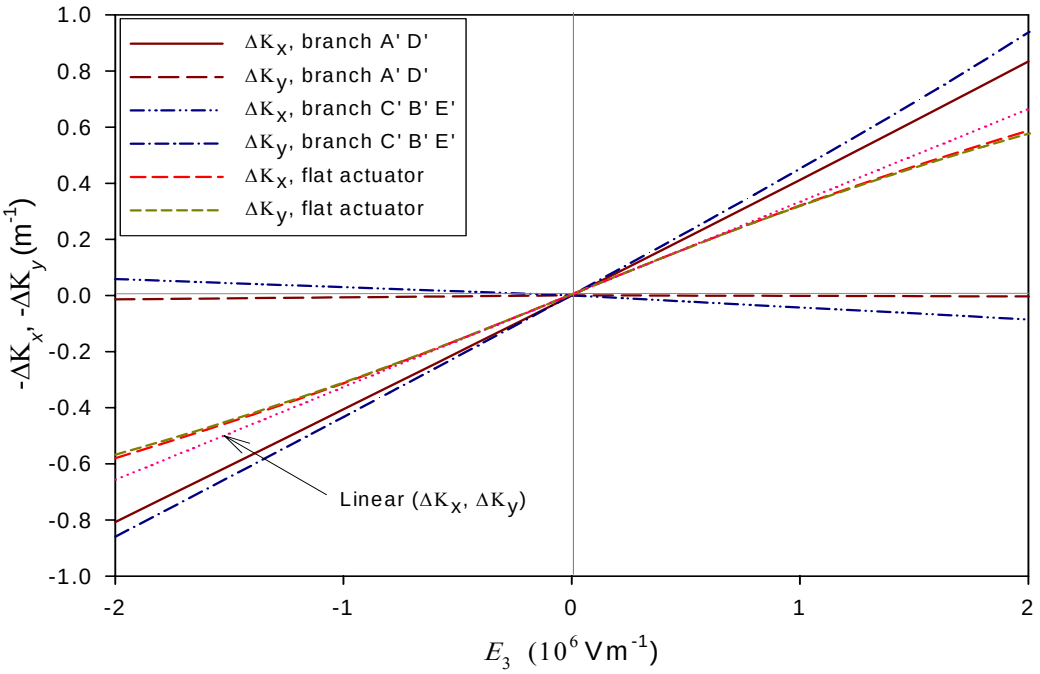

(a) L_x/H = 200

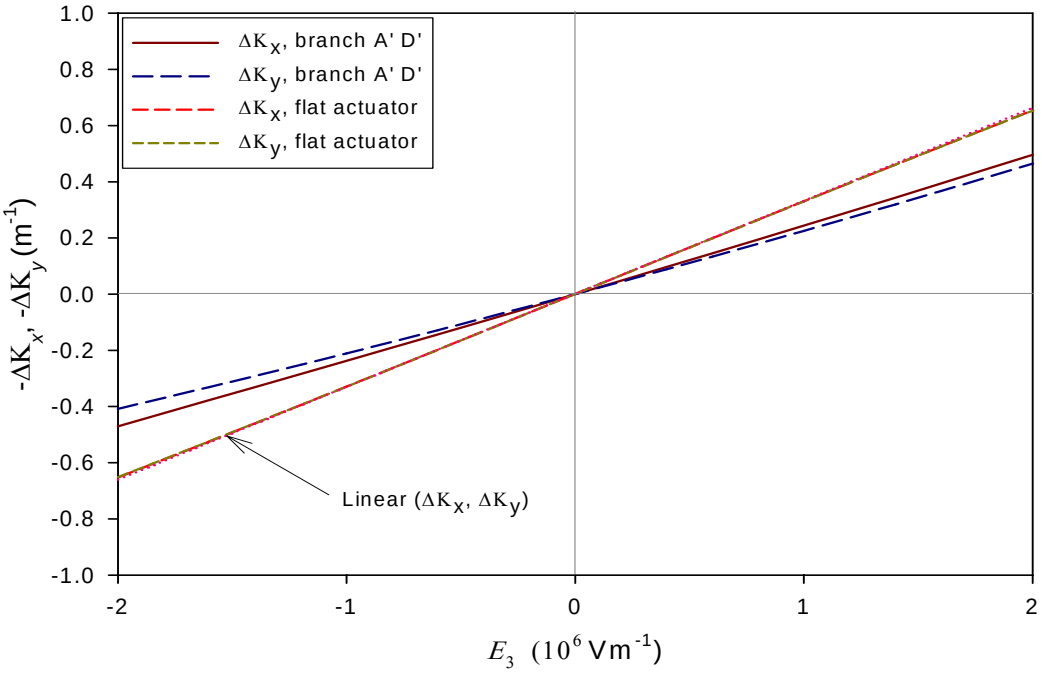

(b) L_x/H = 100

Figure 3.23: Change of Average Curvatures as a Function of Electric Field Strength for THUNDER and Counterpart Flat Actuators, L_y/L_x = 0.7

curvature change vs. field strength relations are practically identical and similar to the linear relations, but are slightly nonlinear and the curvature change is less than for the linear analysis. Near E_3 = 0 V/m, the slope of curvature change for the geometrically linear analysis is equal to the slopes in both the *x*- and *y*-directions for a flat actuator, but is not close to those for a curved THUNDER actuator, the latter having greater slopes for ΔK_x for branch A′D′ and for ΔK_y for branch C′B′E′. Since superposition of deformation is applicable to the geometrically linear analysis, the deformations due to the cooling process do not have an effect on the change in the average curvatures induced by an electric field. Thus, the curvature change gradients based on the linear analysis are equal to those of a flat actuator (no the cooling process) subjected to a weak electric field, i.e., E_3 near zero. Compared to a flat actuator, the average curvature change in the *x*-direction for branch A′D′ is greater by a factor of about 1.4. This enhancement is clearly a geometrically nonlinear effect in the curved actuator.

Considering the stable portion of branch C′B′E′ in Figure 3.18 and referring to Figure 3.23 (a), the characteristics of the curvature changes in the *x*- and *y*-directions are reversed relative to branch A′D′ just discussed. For branch C′B′E′ the curvature change in the *y*-direction is considerably larger than that in the *x*-direction, and about 1.5 times larger than the *y*-direction curvature change predicted for a flat actuator.

For the case of thickness ratio L_x/H = 100, illustrated in Figure 3.23 (b), geometrically nonlinear effects in a curved actuator result in less curvature change due to activation than would occur in a flat actuator. Furthermore, the geometrically linear model reveals the corresponding change in curvatures to be very close to those of a flat actuator and practically indistinguishable. Specifically, the curvature change in the *x*-direction for a curved actuator is about 0.8 of the curvature change for a flat actuator. This characteristic is in contrast to the case of L_x/H = 200, where it was seen that the existence of initial curvature can be an advantage. Furthermore, for the case of L_x/H = 100, activation for either a curved

actuator or a flat actuator results in almost equal curvature changes in the *x*- and *y*-directions.

3.3.2 Stress Characteristics of THUNDER subjected to Applied Electric Field

Before closing Section 3.3 it is of value to examine the change in stresses caused by actuation of the piezoceramic material. The through-thickness distribution of the thermally-induced inplane normal residual stresses at room temperature in a rectangular actuator with L_y/L_x = 0.7 and L_x/H = 200 were described in Figures 3.12 and 3.13. These stress distributions are shown again in Figures 3.24 and 3.25 for two locations near the center $\left(x \cong 0, y \cong 0\right)$ and near the midpoint of the shorter edge$\left(x \cong 0, y \cong L_y / 2\right)$, along with the distributions resulting from ±2 MV/m electric fields through the thickness of the piezoceramic material. It can be seen from the figures that application of the electric field has little influence on the distribution or the magnitude of the stresses in any particular layer. The piezoceramic layer remains in compression, while the foil remains in tension, the location of zero stress changes somewhat in the steel, and the adhesive is unaffected, due to its relatively low extensional modulus. That the piezoceramic remains in compression bodes well for there being little potential for tension cracking in the piezoceramic, a characteristic of a brittle material.

In addition, the changes in the normal stresses in each layer due to the application of electric fields are consistent with the deformations of the actuator. For example, when -2 MV/m field is applied, both the *x*- and *y*-direction curvatures increase in magnitude as seen in Figures 3.18 and 3.19. Consequently, the normal stresses in each layer in Figures 3.24 and 3.25 are higher in magnitude and gradient. In contrast, when +2 MV/m field is applied, both the *x*- and *y*-direction curvatures decrease in magnitude and therefore, lessen the magnitude and gradient of normal stresses in each layer.

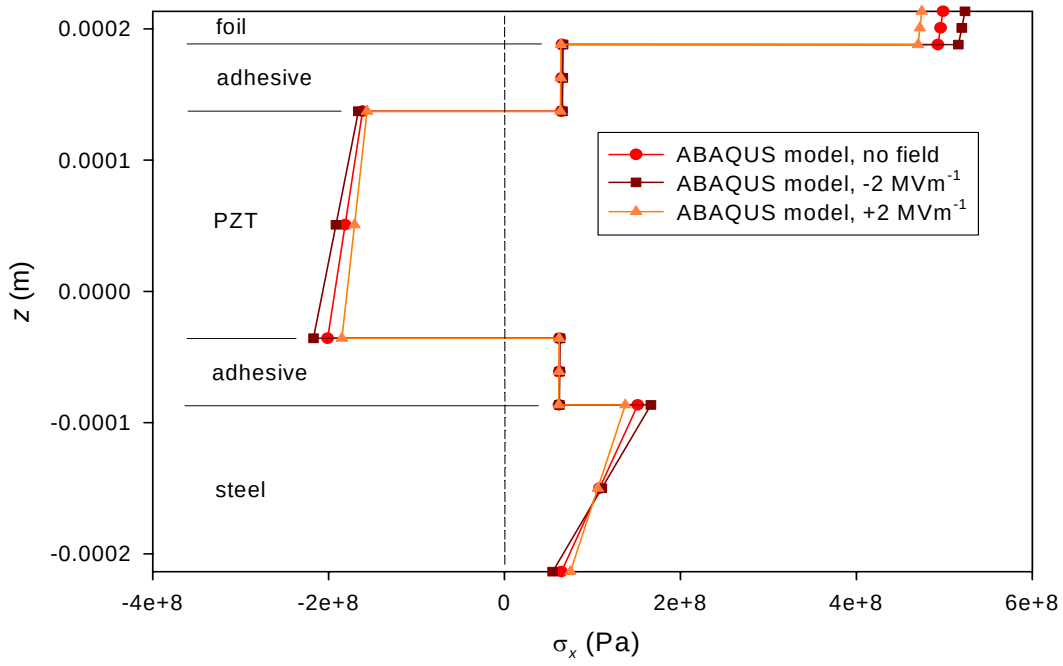

(a) Distribution of Normal Stress in the *x*-direction near Center, $x \cong 0$, $y \cong 0$

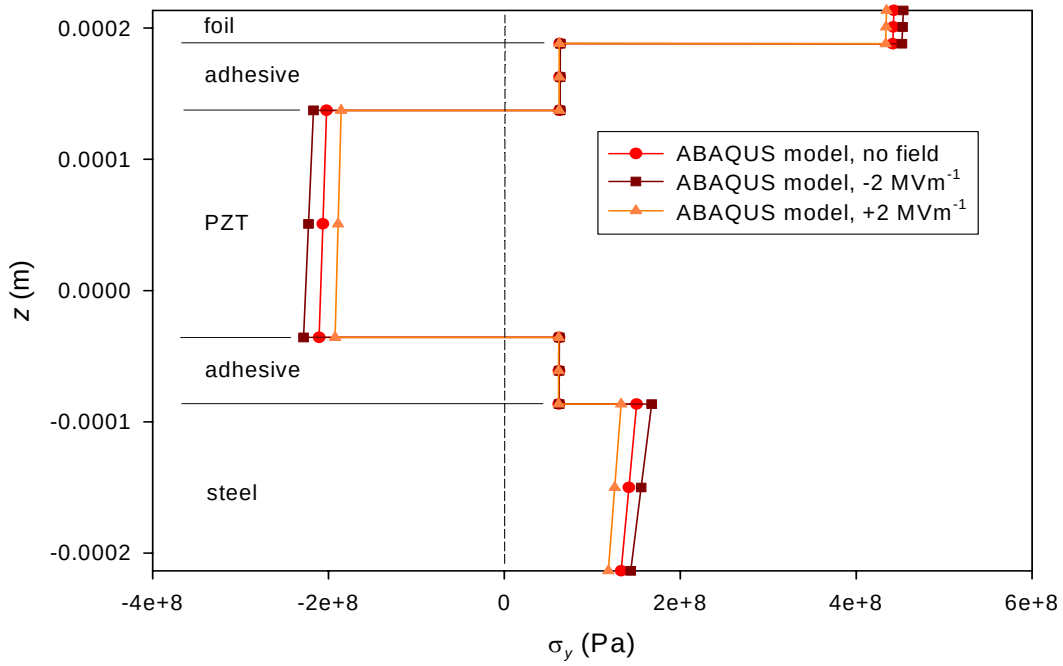

(b) Distribution of Normal Stress in the *y*-direction near Center, $x \cong 0$, $y \cong 0$

Figure 3.24: Stress distributions in rectangular THUNDER near center when subjected to applied electric fields, $L_y/L_x = 0.7$, $L_x/H = 200$

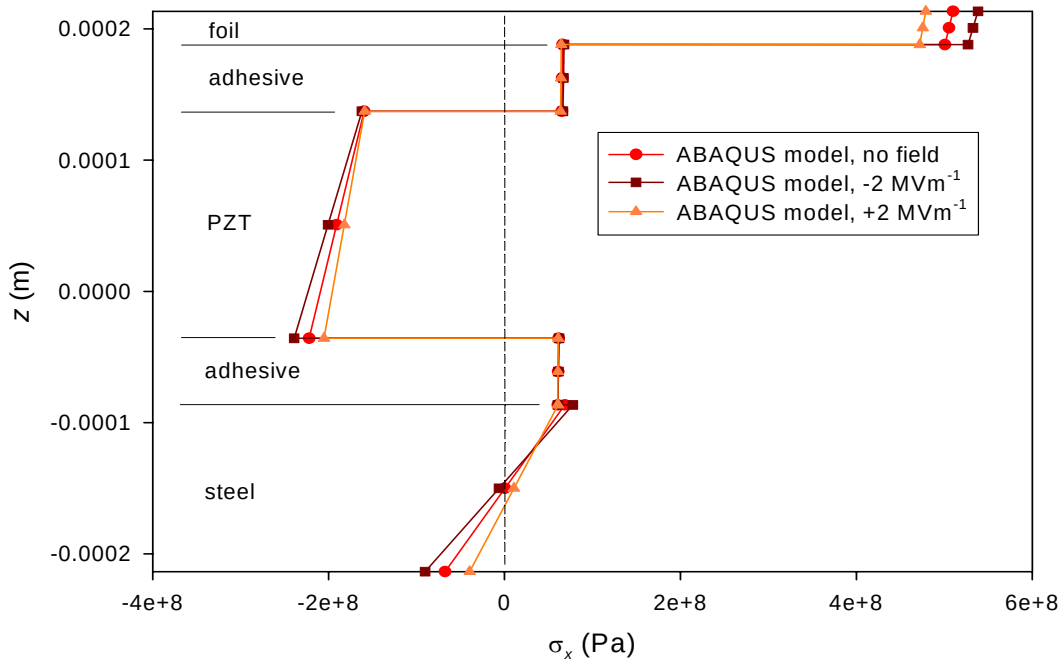

(a) Distribution of Normal Stress in the x-direction near Edge, $x \cong 0$, $y \cong L_y/2$

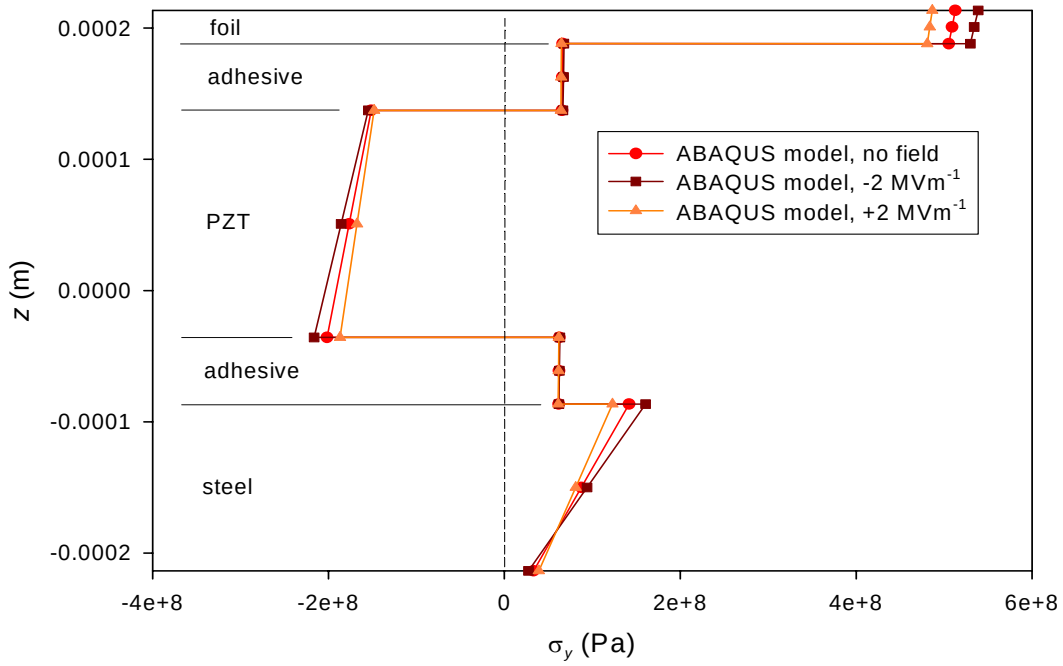

(b) Distribution of Normal Stress in the y-direction near Edge, $x \cong 0$, $y \cong L_y/2$

Figure 3.25: Stress distributions in rectangular THUNDER near midpoint of longer edge when subjected to applied electric fields, $L_y/L_x = 0.7$, $L_x/H = 200$

3.4 Numerical Results for Blocking Forces

3.4.1 Blocking Forces of THUNDER as a Function of Electric Field Strength

As discussed in Chapter 2, with an aid of the supplementary algorithms presented in Section 2.4.3, the blocking force of an actuator with pinned-roller and pinned-pinned supports can be determined. To facilitate discussion of the results from the blocking force calculations, it is of value to repeat the physical meaning of blocking forces. For the pinned-roller case, Figure 2.6 (a), if the actuator is subjected to an applied electric field and is completely fixed at its central point, the blocking force P_{bl} represents the force that must be applied on the two opposite edges at positions $(x, y, z) = (\pm L_x/2, 0, -H/2)$ to fully restrain the *z*-direction deformation at these points. Alternatively, if the actuator is pinned-roller supported, force P_{bl} is half of the dead-weight load that the activated actuator can carry at the central point and still have no vertical deflection of that point. Analogously, for pinned-pinned cases, Figure 2.6 (b), the blocking forces P_{bl} and R_{bl} represent the forces that must be applied on the two opposite edges at positions $(x, y, z) = (\pm L_x/2, 0, -H/2)$ to keep the positions fixed in both the *x* and *z*-directions when the actuator that is fixed at the central point is subjected to an electric field. Like the pinned-roller case, force P_{bl} can also be interpreted as half of a dead-weight load that can be placed on the activated actuator at the central point such that the point has no net deflections.

First, consider rectangular THUNDER actuators with an aspect ratio $L_y/L_x = 0.7$ and sidelength-to-thickness ratios of 100 and 200 with shapes given by branch A′D′ in Figure 3.8. Figure 3.26 shows relations between their blocking forces and applied electric field E_3. For comparison, predictions when geometric nonlinearities are ignored are included. The blocking forces of the THUNDER actuators with both types of supports are illustrated in the figure for comparison purposes. From the figure, it is seen that blocking forces predicted from the nonlinear theory vary almost linearly with electric field strength. Slight nonlinearities of the blocking force vs. electric field relationships can be observed

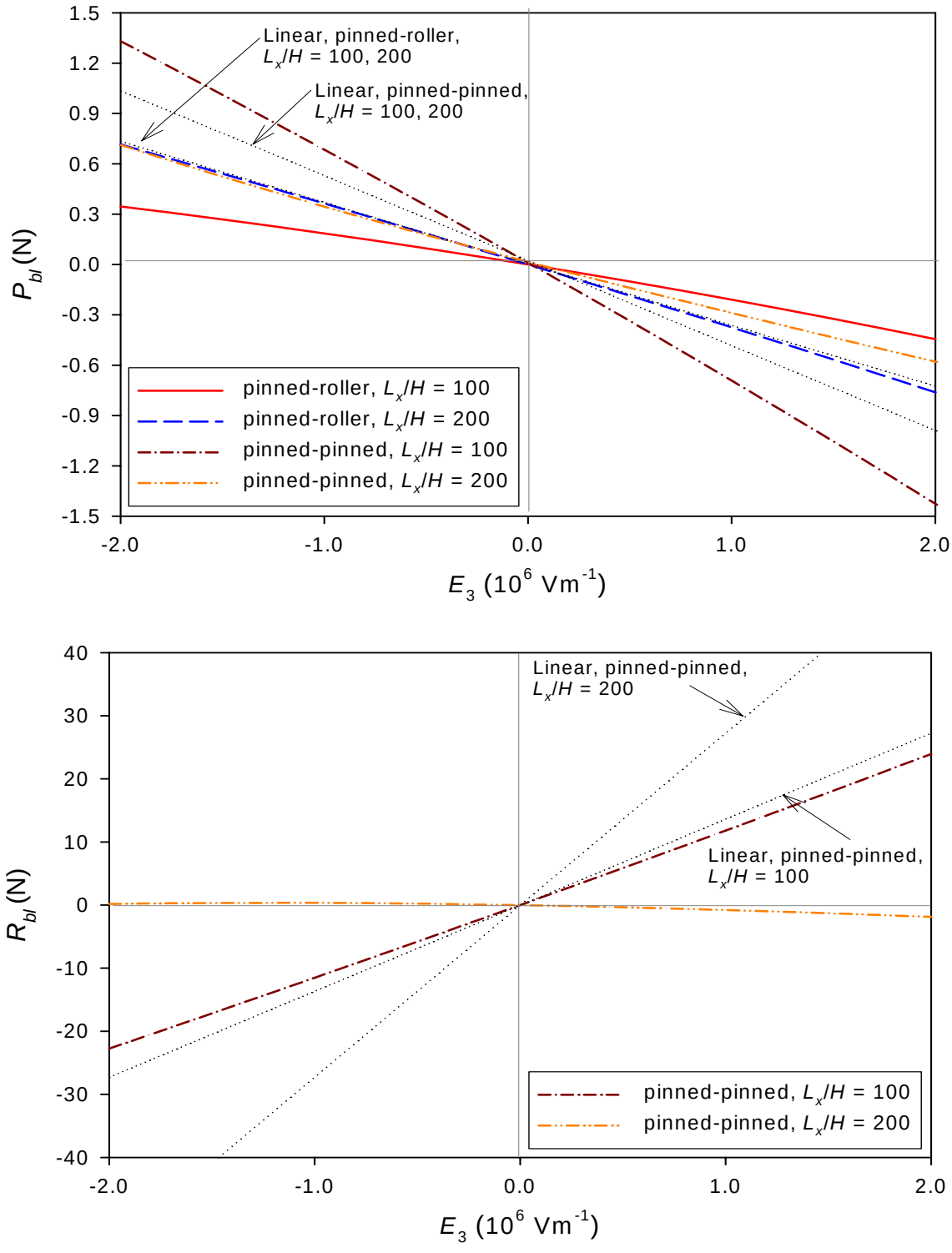

Figure 3.26: Blocking Force vs. Electric Field Relations of Rectangular THUNDER (L_y/L_x = 0.7)

when the field strength is stronger than ±1 MV/m. For the pinned-roller case, force P_{bl} for the actuator with L_x/H = 200 is approximately two times as large as that with L_x/H = 100 over the range of electric field strength considered. Indeed, force P_{bl} seems to be proportional to the change in curvature in the x-direction, ΔK_x, due to electrical actuation shown in Figure 3.23. There is no force R_{bl} because the supports can freely move in the x-direction. The geometrically linear theory predictions are independent on the sidelength-to-thickness ratios. For the pinned-pinned case, opposite behaviors can be noticed. The value of force P_{bl} for the actuator with L_x/H = 200 is approximately two times smaller than that for an actuator with L_x/H = 100. The magnitude of force R_{bl} for the actuator with L_x/H = 100 is very high (around 15 times as high) compared to the value of associated force P_{bl}. By contrast, the magnitude of force R_{bl} of the actuator with L_x/H = 200 is relatively small. As such, associated force P_{bl} is fairly close to P_{bl} from the pinned-roller case, for which force R_{bl} is exactly zero. The linear theory predictions of P_{bl} are again independent of sidelength-to-thickness ratio. However, the linear theory predictions of R_{bl} are not; the larger the sidelength-to-thickness ratio, the larger force R_{bl}. In fact, for force R_{bl}, the force and sidelength-to-thickness ratio are linearly proportional.

The relations between blocking forces and electric field strength for square actuators with L_x/H = 100 and 200 with shapes given by branch A′D′ in Figure 3.5 are illustrated in Figure 3.27. The effects of geometrical nonlinearities on the relations can be noticed more easily when the sidelength-to-thickness ratio is increased from 0.7 to 1. Only within the range of ±0.5 MV/m can the relations be approximated to be linear. Similarities to Figure 3.26 in blocking force behaviors can be observed. Overall, the influence of sidelength-to-thickness ratio on the blocking forces of the square actuators is amplified when compared to those of the actuators with L_y/L_x = 0.7 with the same type of support. An exception is for force P_{bl} for the square actuators with pinned-pinned supports, for which the

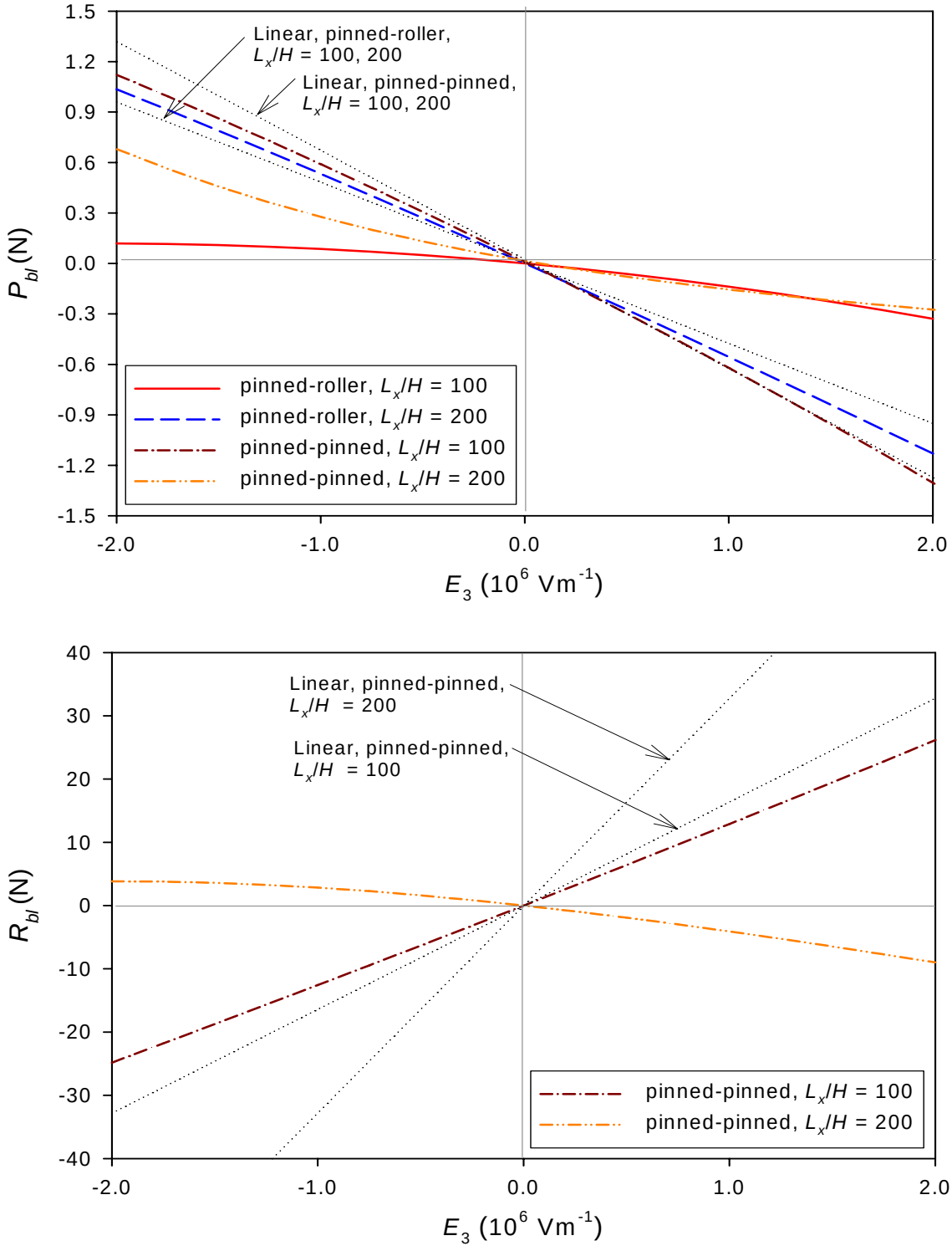

Figure 3.27: Blocking Force vs. Electric Field Relations of Square THUNDER

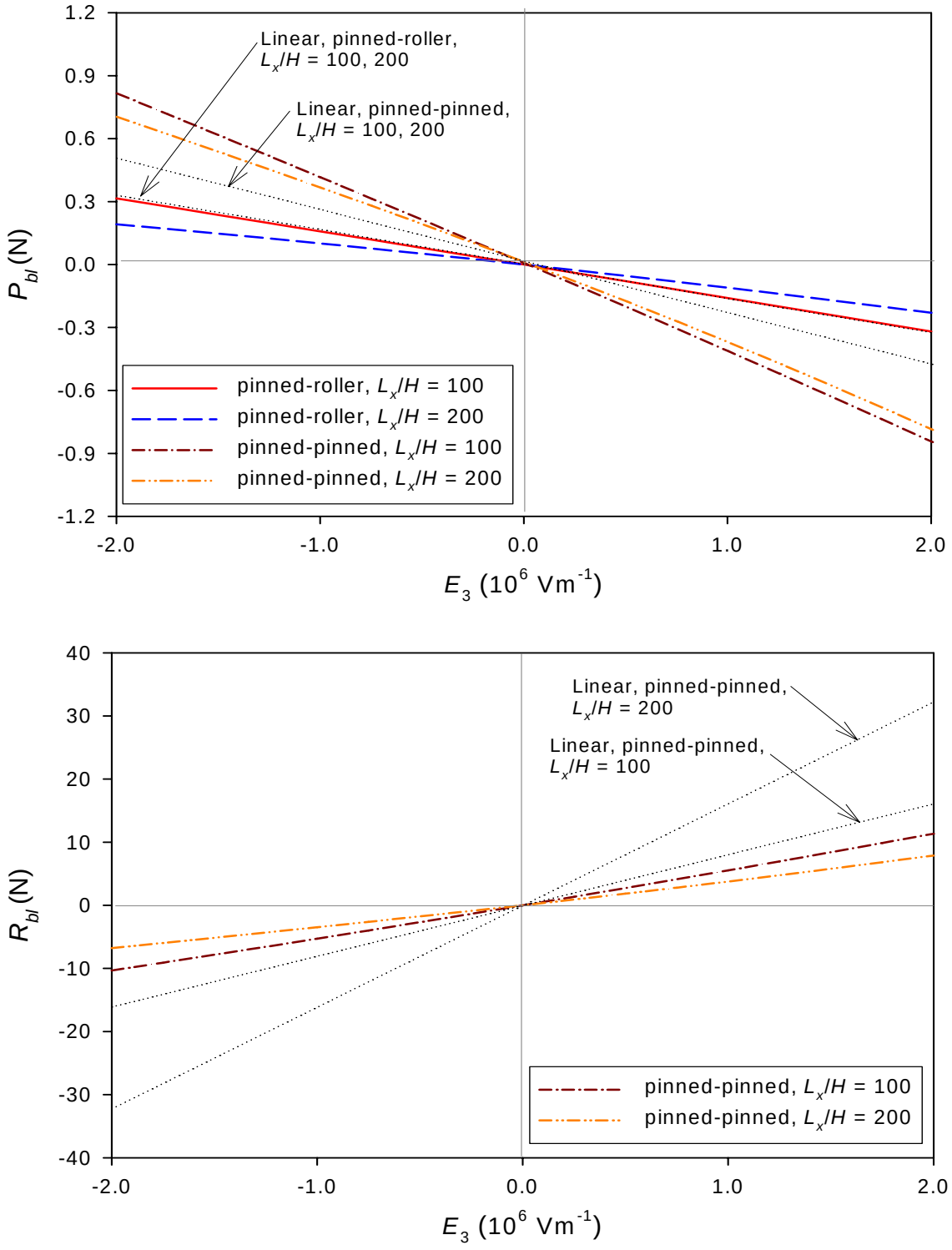

Figure 3.28: Blocking Force vs. Electric Field Relations of Beam-Like THUNDER (L_y/L_x = 0.3)

electric field vs. force P_{bl} relation for L_x/H = 200 and negative field strengths is noticeably nonlinear. This causes the reduction in the influence of sidelength-to-thickness ratio.

Finally, consider beam-like actuators with an aspect ratio of 0.3 and sidelength-to-thickness ratios of 100 and 200 with shapes given by branch $A'D'$ in Figure 3.9. As illustrated in Figure 3.28, the relations of blocking forces vs. electric field strength are quite linear over the whole range of ±2 MV/m. The overall behaviors of the relations are similar to the results in Figures 3.26 and 3.27. Yet the influence of sidelength-to-thickness ratio on the blocking forces of the actuators with the same type of support is reduced for this smaller aspect ratio. It must be pointed out that even though the relations seem to be linear, geometrically nonlinear effects are still appreciable because all the relations deviate from the linear theory predictions. The smallest deviation between linear and nonlinear predictions is for force P_{bl} of the actuator with pinned-roller supports and L_x/H = 100. Actually, this makes sense, since when considering Figures 3.9 and 3.22, the manufactured and actuated curvatures of the actuator with L_x/H = 100 are very close to the ones predicted by the linear theory (represented by the horizontal lines tangent to points A', A^P, and A^N). For the pinned-pinned case there are differences between the predictions of the linear theory and those of the nonlinear theory. These occur as a result of the large magnitude of R_{bl} (approximately ten times as high as that of associated force P_{bl}) that is required to restrain the *x*-direction deformation at the support, this restraint, coupled with geometric nonlinearities, thereby altering the structural stiffness of the curved actuator.

3.4.2 Blocking Forces of THUNDER as a Function of Sidelength-to-Thickness Ratio: Pinned-Roller Case

Relations of the blocking forces vs. sidelength-to-thickness ratio are quite informative. These relations not only show variations of load-carrying capability as a function of actuator geometry, but also provide information as to how to select an actuator to meet both the actuation displacement and load-carrying capability requirements.

Figure 3.29 illustrates the relations between blocking force P_{bl} and sidelength-to-thickness ratio for pinned-roller supported THUNDER actuators with an aspect ratio of 0.7 with shapes given by branch A′D′ in Figure 3.8 and subjected to ±2 MV/m. For both the +2 MV/m and -2 MV/m field strengths, the ordinate axis is normalized by a blocking force of a THUNDER actuator with L_x/H approaching zero, the result for the geometrically linear theory. Therefore, at very small values of sidelength-to-thickness ratio $\left(0 < L_x/H < 30\right)$, the normalized values of P_{bl} for ±2 MV/m are approximately equal to one. When the value of L_x/H increases, the normalized relation for P_{bl} for +2 MV/m separates from the normalized relation for -2 MV/m, but the relations have similar trends. Indeed, this somewhat indicates the degree of nonlinearities induced by electric field strength. If the relations resulting from ±2 MV/m coincided, then the relation between the blocking force and electric field strength would be linear. On the other hand, if the relations are separated from each other, the more

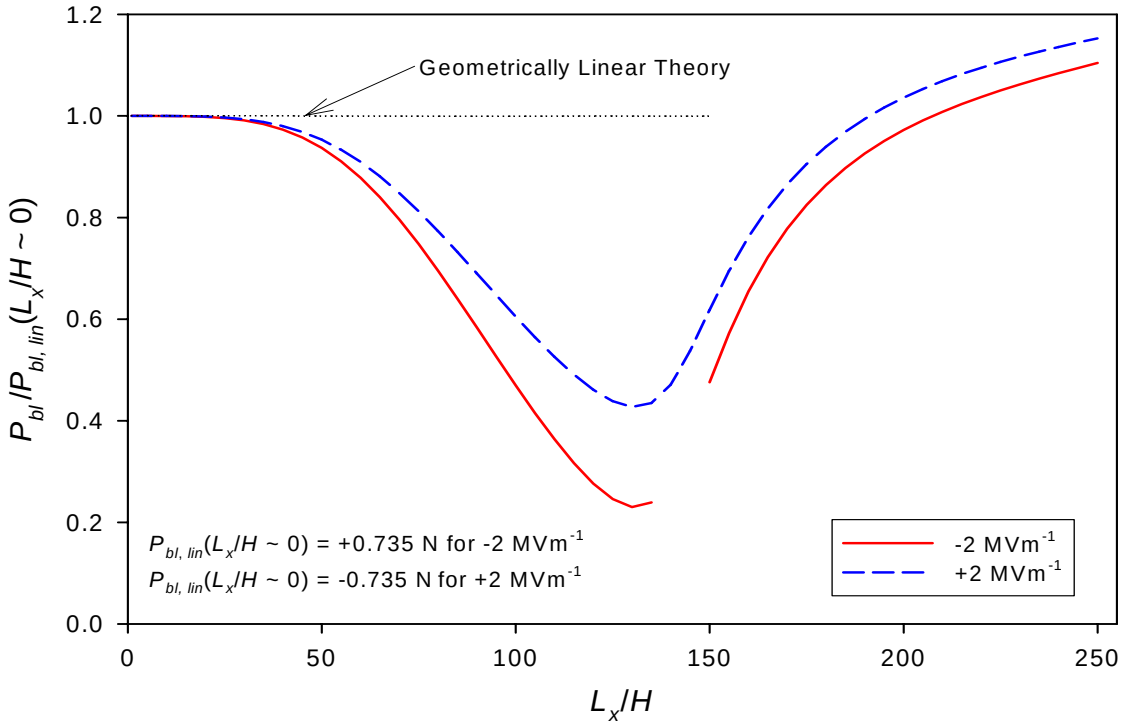

Figure 3.29: Blocking Force vs. Sidelength-to-Thickness Ratio Relations of Pinned-Roller Supported Rectangular THUNDER (L_y/L_x = 0.7)

they separate the more nonlinear should be the relations observed. In the range of $30 < L_x/H < 130$, both normalized relations for P_{bl} decrease and are less than one. In actuality, the same phenomenon can be seen in Figure 3.18, where the change in curvature due to +2 MV/m is different than change in curvature due to -2 MV/m (the vertical distance from branch $A'D'$ to A^PD^P, and A^ND^N). These differences are a function of sidelength-to-thickness ratio. Also, the changes in curvature in the *x*-direction in the region $30 < L_x/H < 130$ decrease and are less than those in the region $0 < L_x/H < 30$. The minimum values of P_{bl} for ±2 MV/m field strengths occur around L_x/H = 130, where the changes in actuated curvatures shown in Figure 3.18 are also lowest. These behaviors evidently show the proportionality between a change in curvature due to an application of electric field and blocking force for the pinned-roller support case. Also at the sidelength-to-thickness ratio of 130, the separation of the normalized values of P_{bl} for ±2 MV/m is largest (difference of 0.2). When L_x/H > 130, the normalized blocking force increases and the separation gap between ±2 MV/m cases reduces. It should be noted here that in the region where $135 < L_x/H < 150$, the normalized blocking force for -2 MV/m cannot be obtained by the algorithm presented in Section 2.4.3 because the algorithm fails to converge. This occurs because it is believed that actuators with L_x/H in this range will snap to another equilibrium configuration. However, this phenomenon does not arise when the actuators are subjected to +2 MV/m, since geometrically nonlinear effects are reduced slightly, as discussed in Section 3.3.1, such that this rules out the possibility of the actuators snapping to another configuration. When the sidelength-to-thickness ratio is large enough (L_x/H > 200), the normalized values of P_{bl} are larger than one. The blocking force relations predicted by the geometrically linear theory, $P_{bl,lin}$, are also illustrated in the figure. The prediction exhibits constant blocking forces for ±2 MV/m (∓ 0.735 N, respectively) regardless of sidelength-to-thickness ratio and therefore are drawn as coincident horizontal lines with values equal to one. The signs of all the blocking forces resulting from both linear and nonlinear theories are

consistent with the predicted curvature changes of Figure 3.18. Specifically, without blocking forces the free edges of the actuator will move up (down) due to a curvature decrease (increase) when the positive (negative) electric field is applied, and thus negative (positive) blocking forces are required to hold the support positions fixed. Finally, it is very important to note that according to Figure 3.29, designing a pinned-roller supported THUNDER actuator in the region of $30 < L_x/H < 200$ results in an actuator with less blocking force than a counterpart flat actuator with the same stacking material sequence and dimensions. Such a flat actuator, which can be approximately modeled by the linear theory, is predicted to perform the task better, since its normalized blocking force is one, whereas the dashed and solid lines in Figure 3.29 are considerably less than one.

Analogous to Figure 3.29, Figure 3.30 illustrates the relations between the blocking force and sidelength-to-thickness ratio for pinned-roller supported THUNDER actuators with an aspect ratio of one subjected to ±2 MV/m. Equilibrium manufacturing configurations of the THUNDER actuators considered in this case have shapes given by stable branch $A'B'D'$ shown in Figure 3.5. Again, the vertical axis of the plot is normalized by the blocking forces of the same actuators for ±2 MV/m predicted by the geometrically linear theory. In general, the relations in Figure 3.30 have very similar behaviors to those in Figure 3.29. Behavior predicted by the linear theory occurs when L_x/H is small, as the values of normalized blocking forces for ±2 MV/m are approximately equal to one. However, the range of L_x/H for which the linear theory is valid is shorter than that of the actuators with an aspect ratio of 0.7 because it covers the range of $0 < L_x/H < 25$. When $L_x/H > 25$, the normalized blocking force decreases rapidly. For -2 MV/m, the normalized value of P_{bl} reaches the minimum value close to zero at L_x/H = 110, while for +2 MV/m, the normalized value of P_{bl} has the lowest value of 0.15 at L_x/H = 120. Note that unlike the smoothly changing slope in Figure 3.29, where the blocking force is a minimum for +2 MV/m, there is a slope discontinuity at the minimum blocking force on the plot of normalized P_{bl} vs. L_x/H

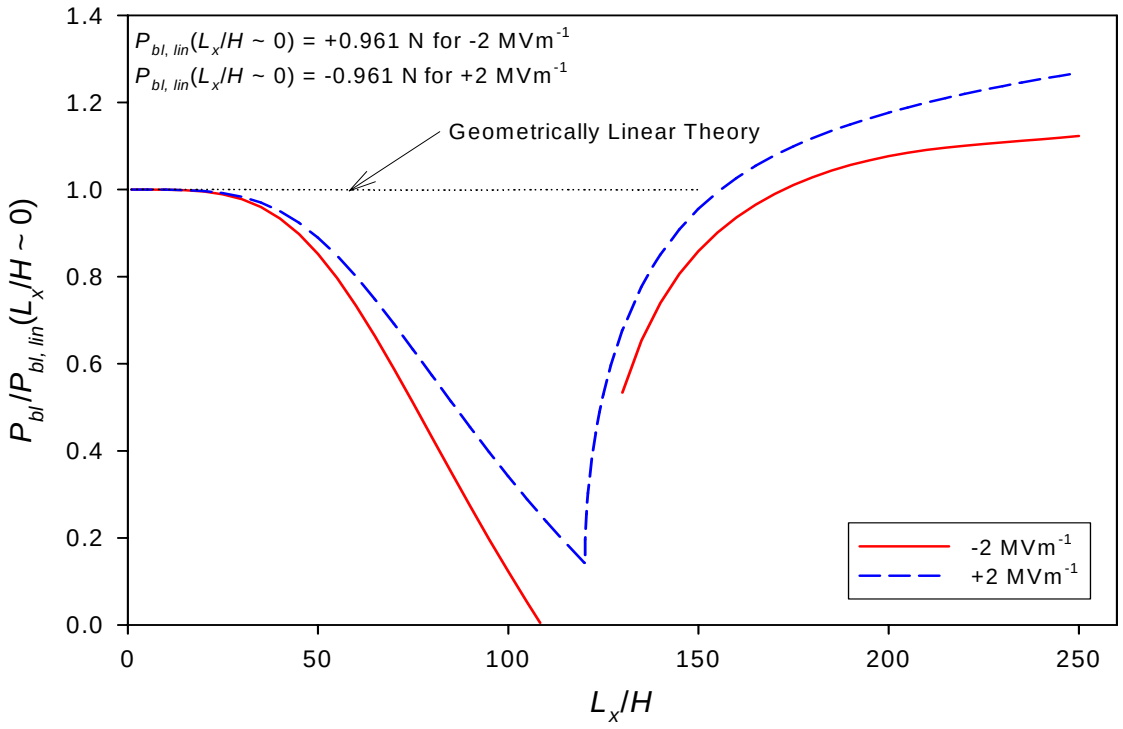

Figure 3.30: Blocking Force vs. Sidelength-to-Thickness Ratio Relations of Pinned-Roller Supported Square THUNDER (L_y/L_x = 1)

for +2 MV/m illustrated in Figure 3.30. This discontinuity in slope occurs due to the immediate change in curvature at bifurcation point B′ in Figure 3.5. After the minimum points, the normalized blocking force increases monotonically in relation to the increase of sidelength-to-thickness ratio and exceeds the value of one around L_x/H = 160 (compared to L_x/H = 200 for THUNDER with $L_y/L_x = 0.7$). Again, the algorithm failed to converge for the -2 MV/m case in the range of $110 < L_x/H < 130$. Additionally, like the case of the aspect ratio of 0.7, the blocking forces predicted by the linear theory, $P_{bl,lin}$, are independent of the actuator sidelength-to-thickness ratio, so they are represented by straight horizontal lines with the unit value. The force $P_{bl,lin}$ of the square actuator is equal to ∓ 0.961 N for ±2 MV/m, respectively. Compared with the pinned-roller supported THUNDER actuators with L_y/L_x = 0.7, the pinned-roller supported square ones have 30.7% higher blocking force based

on the linear theory, and they are 42.9% larger in terms of size. Like actuators with aspect ratio 0.7, as discussed in Figure 3.29, it can be stated that designing a square pinned-roller supported THUNDER actuator in the region of $25 < L_x/H < 160$ results in an actuator with less blocking force than a counterpart flat actuator with the same stacking material sequence and dimensions.

Now, consider pinned-roller supported THUNDER actuators subjected to ±2 MV/m field strength with an aspect ratio of 0.3. The manufactured shapes of the actuators are given in Figure 3.9. Shown in Figure 3.31 are relations between the normalized blocking force and sidelength-to-thickness ratio. When $L_x/H < 70$, the relations can be approximated by the geometrically linear theory very well. This linear region is the largest of all for three aspect ratios considered because of the weak geometrical nonlinearity associated with the beam-like configuration. When $L_x/H > 70$, the normalized blocking force decreases gradually and reaches the lowest value at $L_x/H = 250$. Similar to that of aspect ratio 0.7, the blocking force separation for the positive and negative fields is maximal at the lowest value of blocking force. The lowest normalized values of P_{bl} for ±2 MV/m are 0.6 and 0.45, respectively. Unlike the actuators with aspect ratios of 0.7 and 1, the actuators with an aspect ratio of 0.3 have no evidence of blocking force enhancement for the pinned-roller support case within the considered range of sidelength-to-thickness ratio. The value of P_{bl} predicted from the geometrically nonlinear theory is usually lower than ones predicted from the linear theory, a theory associated with a flat actuator. Since a transformation between multiple equilibrium states is not an issue for the beam-like actuators, there does not appear to be any range of L_x/H for which snap-through would occur. The linear theory predicts $P_{bl,lin}$ to be ∓ 0.331 N for ±2 MV/m field strength, respectively. The value of $P_{bl,lin}$ in this case is lower than the linearly predicted value for an aspect ratio of 0.7 by 55.0%, while the active area of the beam-like actuator is less than that of the rectangular one by 57.1%. Additionally, it can be noted that because of the comparatively small aspect ratio, it

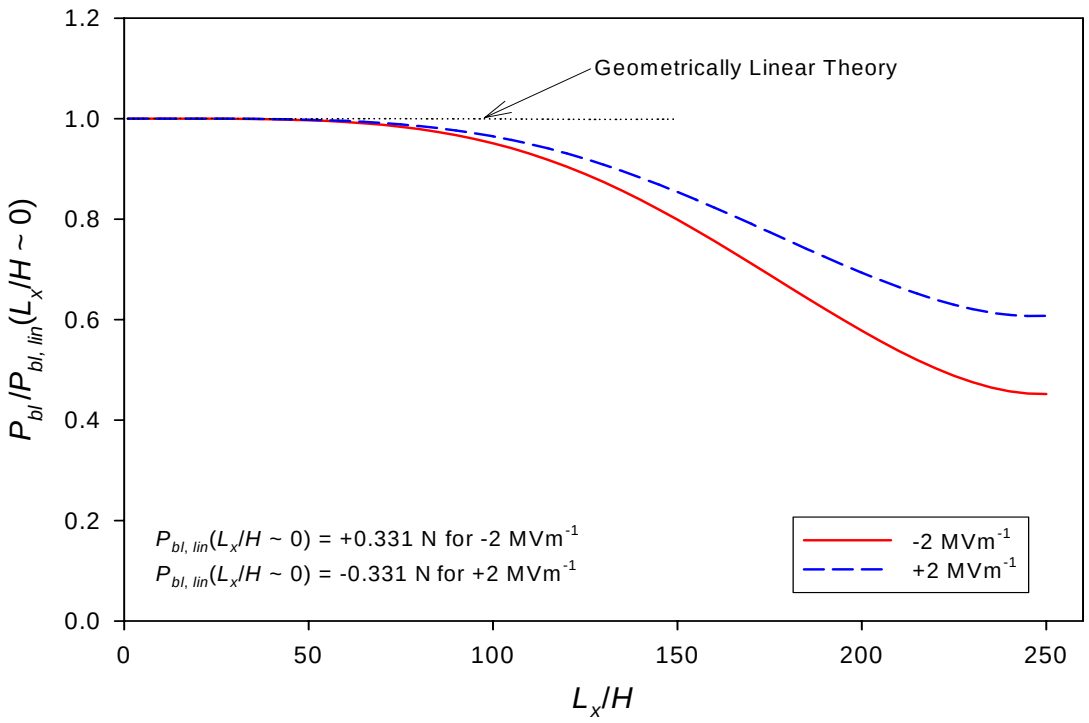

Figure 3.31: Blocking Force vs. Sidelength-to-Thickness Ratio Relations of Pinned-Roller Supported Beam-Like THUNDER (L_y/L_x = 0.3)

is interesting to compare the blocking forces in Figure 3.31 with the ones computed from the nonlinear and linear beam theories developed in Appendix B. By utilizing Equation (B.41) or (B.67), and setting the relative transverse deflection, w^0, due to ±2 MV/m field strength to be zero at $x = \pm L_x/2$, the blocking force predictions based on beam theory can be solved for and found to be ∓ 0.326 N for ± 2 MV/m, respectively. These blocking forces are independent of the sidelength-to-thickness ratio, like those predicted from the geometrically linear theory illustrated as the dotted line in Figure 3.31.

3.4.3 Blocking Forces of THUNDER as a Function of Sidelength-to-Thickness Ratio: Pinned-Pinned Case

In this section, blocking forces of an actuator with pinned-pinned supports as a function of sidelength-to-thickness ratio are taken into consideration. Illustrated in Figure

3.32 are relations of blocking forces P_{bl} and R_{bl} for ±2 MV/m for a THUNDER actuator with an aspect ratio of 0.7. The influence of restraining the motion in the *x*-direction is evidently strong because the normalized P_{bl} relations shown in Figure 3.32 are totally different from those shown in Figure 3.29. The ordinate axis of the plot illustrating the behavior of force R_{bl} for +2 MV/m and -2 MV/m is normalized by the value of R_{bl} predicted by the geometrically linear theory ($R_{bl,lin}$) for +2 or for -2 MV/m, respectively. When the sidelength-to-thickness ratio is less than 10, both normalized values of P_{bl} and R_{bl} coincide with the linear predictions. As the sidelength-to-thickness ratio increases, the normalized values of P_{bl} deviate from the linear predictions and increase moderately in magnitude, while values of R_{bl} are still in agreement with the linear predictions and increase considerably in magnitude. The deviation of P_{bl} from the linear theory occurs at a lower value of L_x/H compared to Figure 3.29 because the magnitude of the associated force R_{bl} is relatively large and changes the structural stiffness of the actuator in a manner not represented by the linear theory. The normalized values of P_{bl} and R_{bl} reach their peak within the region $90 < L_x/H < 120$, and then decrease monotonically as L_x/H increases further. Note that for sidelength-to-thickness ratios between 120 and 165, the blocking forces of the actuators subjected to the application of -2 MV/m electric field strength are not shown. A lack of solution algorithm convergence, as discussed in connection with in Figures 3.29 and 3.30, again occurs, When $L_x/H \cong 200$, the values of R_{bl} are equal to zero, and thus the values of P_{bl} in Figure 3.32 are identical to those in Figure 3.29. As L_x/H increases beyond 200, the normalized values of R_{bl} change sign. In the other words, force R_{bl} changes direction. According to Figures 3.32 and 3.29, except when $L_x/H > 200$, the value of P_{bl} for the pinned-pinned supported actuators is higher than that for the pinned-roller supported actuators. This occurs because when $L_x/H < 200$, the direction of R_{bl} favors the magnitudes of P_{bl}, namely the load-carrying capability in the vertical direction. However, when normalized values of R_{bl} are negative, the load carrying capability in the vertical direction is

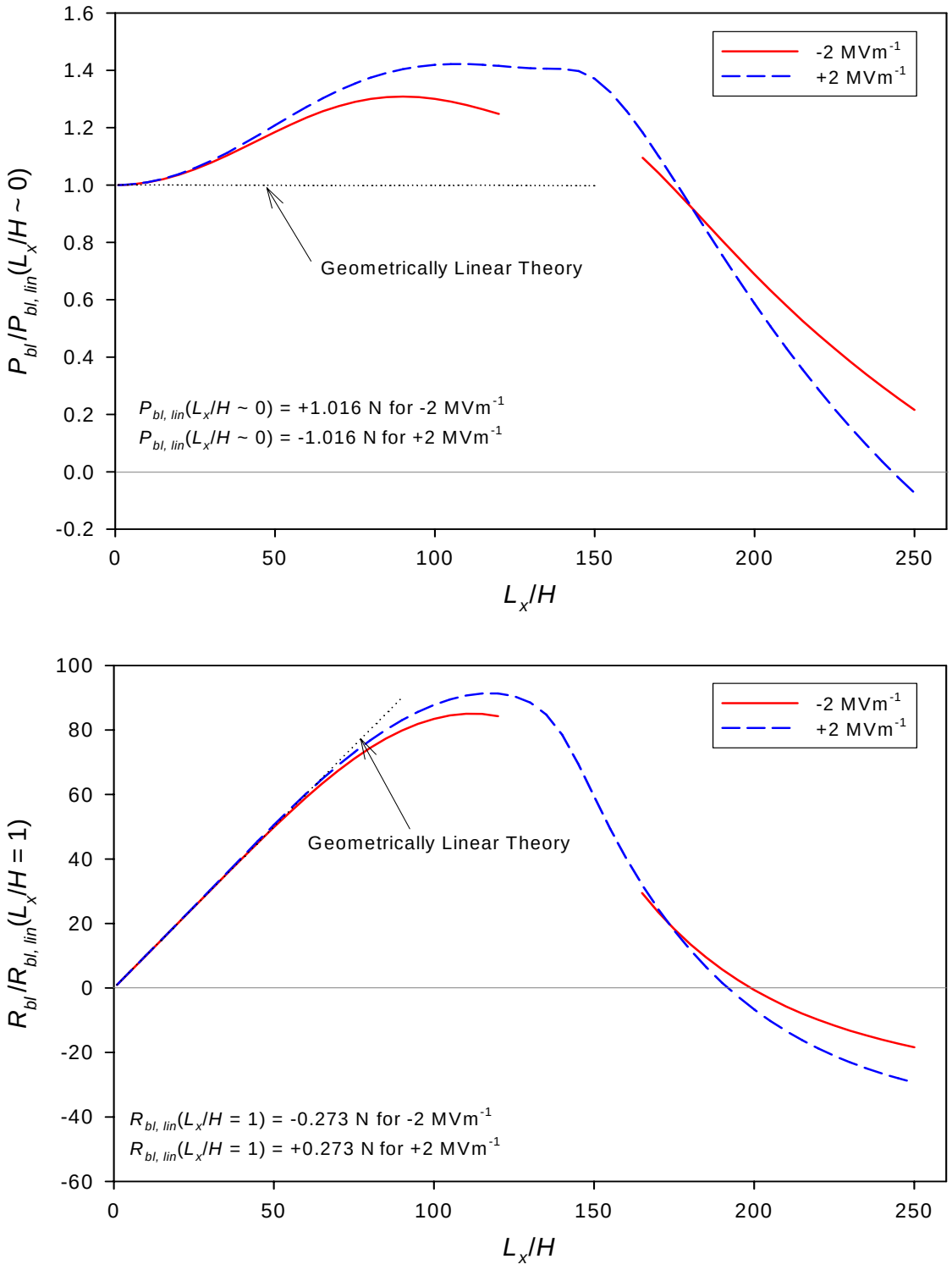

Figure 3.32: Blocking Force vs. Sidelength-to-Thickness Ratio Relations of Pinned-Pinned Supported Rectangular THUNDER (L_y/L_x = 0.7)

deteriorated. Indeed, the differences of the blocking force results between the two types of support conditions are attributed to effects of the manufactured curvatures of the actuators that are not attainable by a flat actuator. The predictions of $P_{bl,lin}$ from the linear theory again reveal values independent of sidelength-to-thickness ratio, i.e., ∓ 1.016 N for ±2 MV/m. The values of $P_{bl,lin}$ are greater than the linear values of the forces for the pinned-roller case by 38.2%. However, the values of $R_{bl,lin}$ are dependent on sidelength-to-thickness ratio. As can be inferred from the lower portion of Figure 3.32, without the normalization factor $R_{bl,lin}$ force R_{bl} for ±2 MV/m is a linear function of L_x/H with a slope of ±0.273 N, respectively.

As a comparison with Figure 3.32 and for an examination of the influences of aspect ratio, L_y/L_x, on blocking forces of pinned-pinned supported actuators, the values of P_{bl} and R_{bl} for square and beam-like (L_y/L_x = 0.3) actuators as a function of sidelength-to-thickness ratio are illustrated in Figure 3.33 and 3.34, respectively. Considering Figure 3.33, the overall relations are very similar to the ones in the Figure 3.32 except for the unusual behavior, i.e., the slope discontinuity in the relations, that appears at L_x/H = 120. This behavior corresponds to bifurcation point B′ on branch A′B′D′ in Figure 3.5. It should be noted that at $L_x/H \cong 160$, the normalized values of R_{bl} are zero and they change direction (sign) when L_x/H is larger. It should be noted that this occurred at $L_x/H \cong 200$ for aspect ratio of 0.7. Therefore, for sidelength-to-thickness ratios less than 160, the values of P_{bl} for pinned-pinned case are always higher than the values of P_{bl} for pinned-roller case because the direction of R_{bl} is beneficial and enhances the load-carrying capability in the vertical direction. Beyond L_x/H = 160, the converse results are predicted, since the direction of R_{bl} generates an adverse effect on the load-carrying capability. Additionally, the geometrically linear theory predicts $P_{bl,lin}$ to be constant over the considered sidelength-to-thickness ratios, i.e., ∓ 1.3 N for ±2 MV/m, respectively. The values of $P_{bl,lin}$ for this case are higher than the values $P_{bl,lin}$ of the pinned-pinned supported actuator with an aspect ratio of 0.7 by 28.0%, while the actuators in this case are larger than those of the previous case by 42.9%.

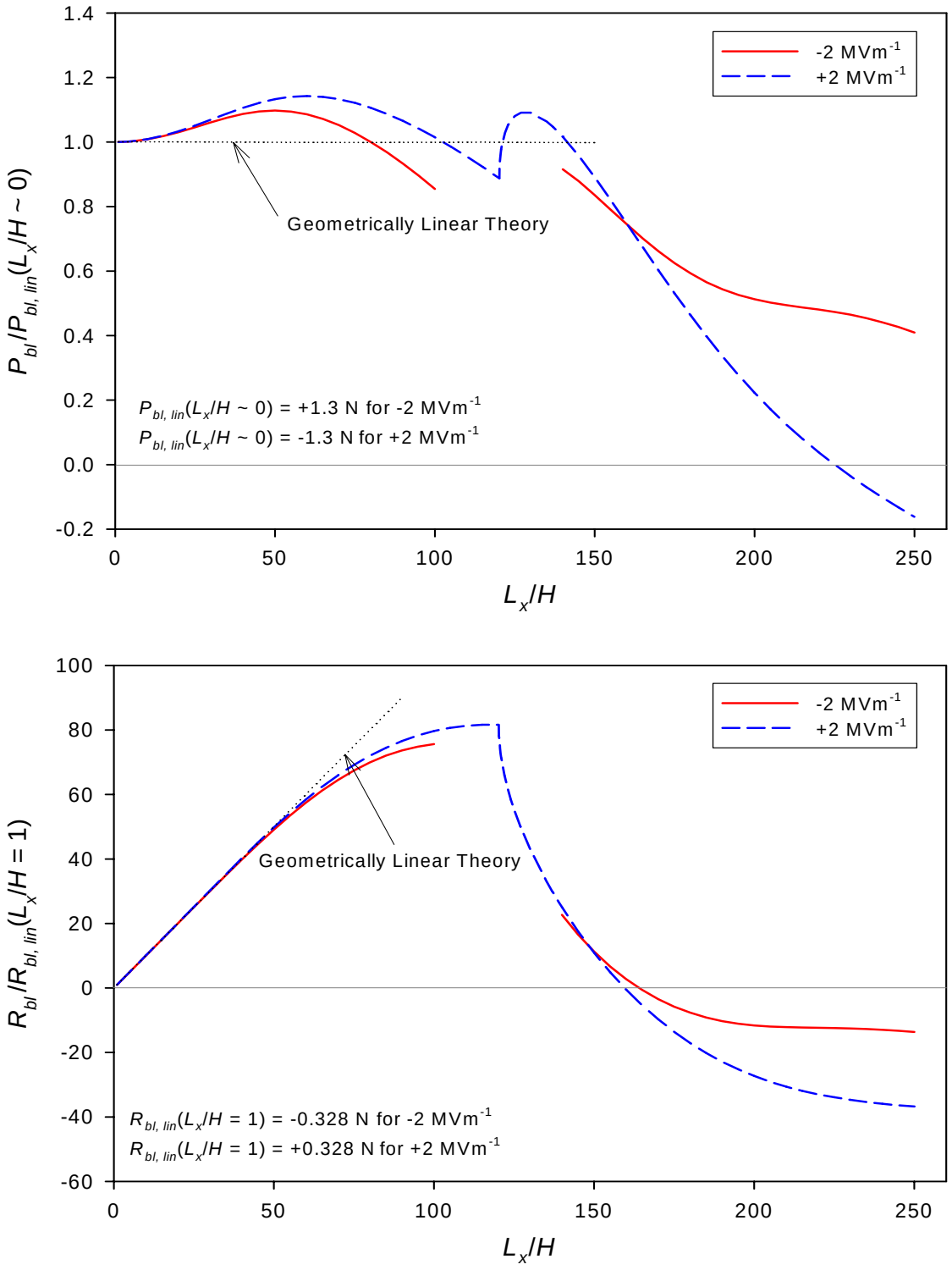

Figure 3.33: Blocking Force vs. Sidelength-to-Thickness Ratio Relations of Pinned-Pinned Supported Square THUNDER

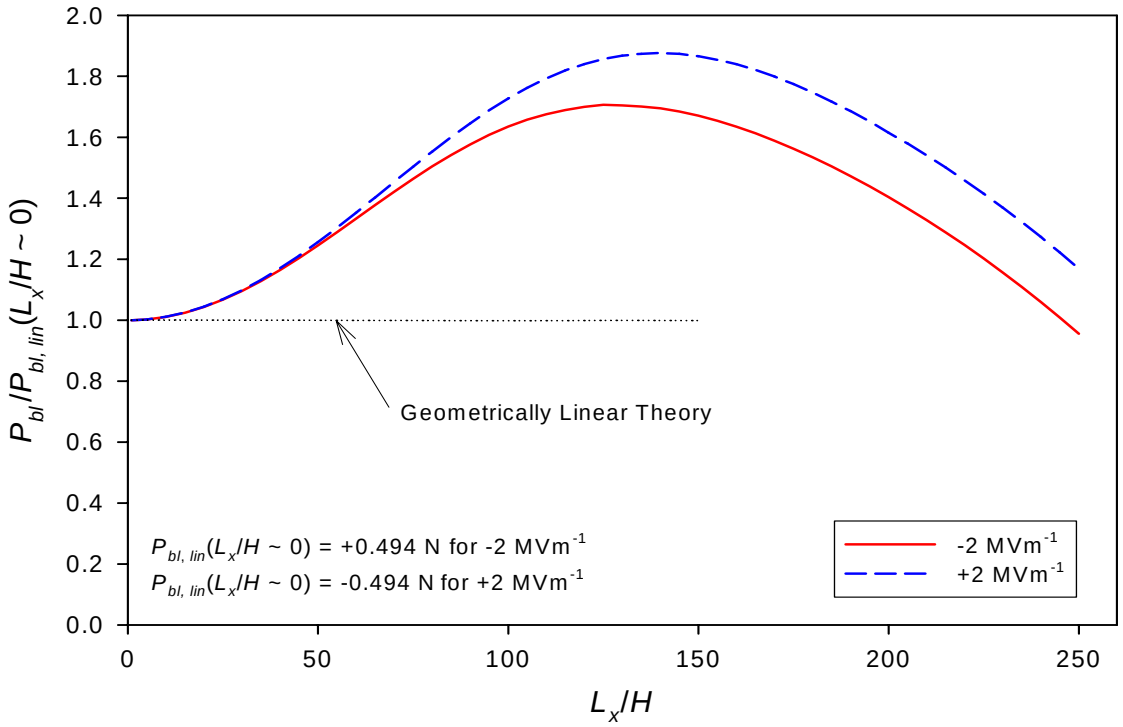

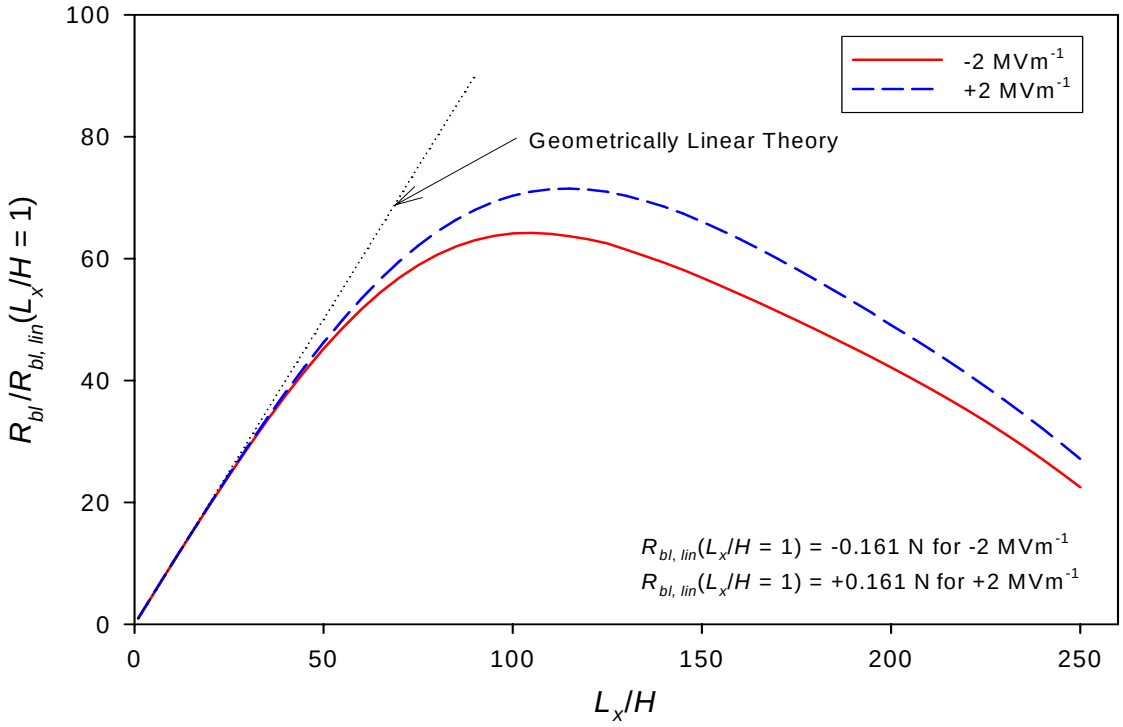

Figure 3.34: Blocking Force vs. Sidelength-to-Thickness Ratio Relations of Pinned-Pinned Supported Beam-Like THUNDER (L_y/L_x = 0.3)

Furthermore, by adding restraint in the *x*-direction at the support points, the values of $P_{bl,lin}$ are increased by 35.3% compared to the pinned-roller square actuator case of Figure 3.30. For the linear theory, the slope of the relation between values of $R_{bl,lin}$ and sidelength-to-thickness ratio is 0.328 N, which is 20.1% increase from the case of aspect ratio 0.7.

Lastly, the relations of blocking forces vs. sidelength-to-thickness ratio for pinned-pinned supported THUNDER actuators with an aspect ratio of 0.3 are considered in Figure 3.34. Similar to the relations in Figures 3.32 and 3.33, the normalized values of P_{bl} are in good agreement with the linear predictions for small sidelength-to-thickness ratios (less than 10). Beyond $L_x/H = 10$, the normalized values of P_{bl} deviate from the horizontal line representing the linear blocking force prediction, $P_{bl,lin}$. Nonetheless, for $L_x/H < 30$, the normalized values of R_{bl} agree well with the normalized values of $R_{bl,lin}$ as predicted by the linear theory. Note that for this aspect ratio the values of R_{bl} do not change sign as they did for the other two aspect ratios discussed. Consequently, the direction of R_{bl} will always enhance P_{bl}, which in turn results in it always being larger than P_{bl} for the pinned-roller case in Figure 3.31. The geometrically linear theory predicts the values of $P_{bl,lin}$ to be ∓ 0.494 N for ±2 MV/m, respectively. These values are 51.4% less than the values of $P_{bl,lin}$ for the pinned-pinned supported actuator with an aspect ratio of 0.7, while the active area of the actuators in this case is less than the case with an aspect ratio of 0.7 by 57.1%. Moreover, by adding restraint in the *x*-direction at the support points, the values of $P_{bl,lin}$ are increased by 49.2%, compared to the values for the pinned-roller case cited in Figure 3.31. For the linear theory, the slope of the relation between $R_{bl,lin}$ and sidelength-to-thickness ratio is 0.161 N, which is a 41.0% decrease from the case of the actuators with pinned-pinned supports and aspect ratio 0.7.

3.4.4 Blocking Forces of THUNDER as a Function of Electric Fields: Non-convergence

Before closing Chapter 3, more details of the missing sections of the solid lines in the relations between the blocking force at -2 MV/m and sidelength-to-thickness ratio in

Figures 3.29, 3.30, 3.32 and 3.33 should be discussed. As an example, the relations for the THUNDER actuators with an aspect ratio of 0.7 in Figures 3.29 and 3.32 are selected for the examination. Seen in Figures 3.35 and 3.36 are the blocking forces P_{bl}, and P_{bl} and R_{bl}, for pinned-roller and pinned-pinned cases, respectively, as a function of electric field strength. The abscissa axis is for negative electric field strength so more focus can be put on the lack of convergence of the solution algorithm for the pinned-roller supported and pinned-pinned supported actuators in the region of $135 < L_x/H < 150$ and $120 < L_x/H < 165$, respectively. Therefore, sidelength-to-thickness ratios presented in the figures are chosen to be 135, 137.5, 140, 142.5, 145, 147.5, and 150 for the pinned-roller case, and 120, 127.5, 135, 142.5, 150, 157.5, and 165 for the pinned-pinned case.

Seen in Figure 3.35 are the values of P_{bl} for the pinned-roller case over the range $135 < L_x/H < 150$ as a function of electric field strength. The symbol '×' marks the point where lack of convergence begins as the magnitude of electric field strength increases. Obviously, the sidelength-to-thickness ratios which result in a lack of convergence are strongly coupled with the minimum applicable electric field strengths. At L_x/H = 135, force P_{bl} can be solved for with a negative electric fields of magnitude 2 MV/m. With L_x/H > 135, if a negative electric field stronger than 2 MV/m in magnitude is applied to the actuators, then the relations between P_{bl} and the applied electric field cannot be solved by using the algorithm presented in Chapter 2. Thus, with L_x/H > 135, under the solvability condition, if the negative electric field strength increases in magnitude to more than 2 MV/m, then an envelop of solvability starts to develop. However, when the sidelength-to-thickness ratio reaches a value within $142.5 < L_x/H < 145$, the maximum magnitude applicable electric field strengths stop decreasing, and the envelope turns back to higher magnitude electric field strengths. Not until L_x/H = 150 does the maximum magnitude negative electric field strength does return to be 2 MV/m and the solvability of force P_{bl} is possible over the remaining range of the sidelength-to-thickness ratios considered. The envelop also implies

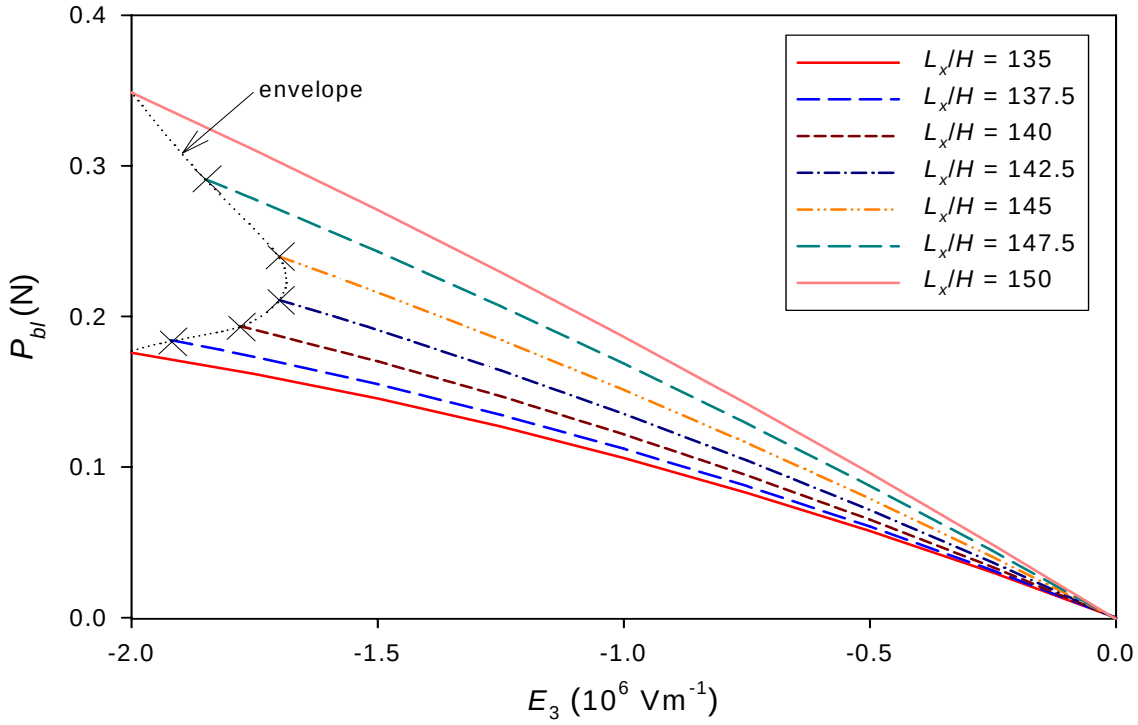

Figure 3.35: Blocking Force vs. Electric Field Strength Relations of Pinned-Roller Supported Rectangular THUNDER (L_y/L_x = 0.7) in Non-converging Region

that there are families of plots similar to Figure 3.29 for any other electric field strengths with varying unsolvable regions of blocking force. For instance, for an applied electric field of -1.7 MV/m, the unsolvable region will be within $142.5 < L_x/H < 145$, as clearly indicated in Figure 3.35.

A similar conclusion can be made from Figure 3.36, in which relations between blocking forces P_{bl} and R_{bl} and electric field strength for the pinned-pinned case in the region $120 < L_x/H < 165$ are illustrated. Compared to the relations for the pinned-roller case in Figure 3.35, the values of P_{bl} and R_{bl} for the pinned-pinned case are related to electric field strength in a more linear fashion. Additionally, the envelope of non-converging values P_{bl} is narrower; thus it is more difficult to be detected. This is because the actuators with pinned-pinned supports are much stiffer structurally than the actuators with pinned-roller

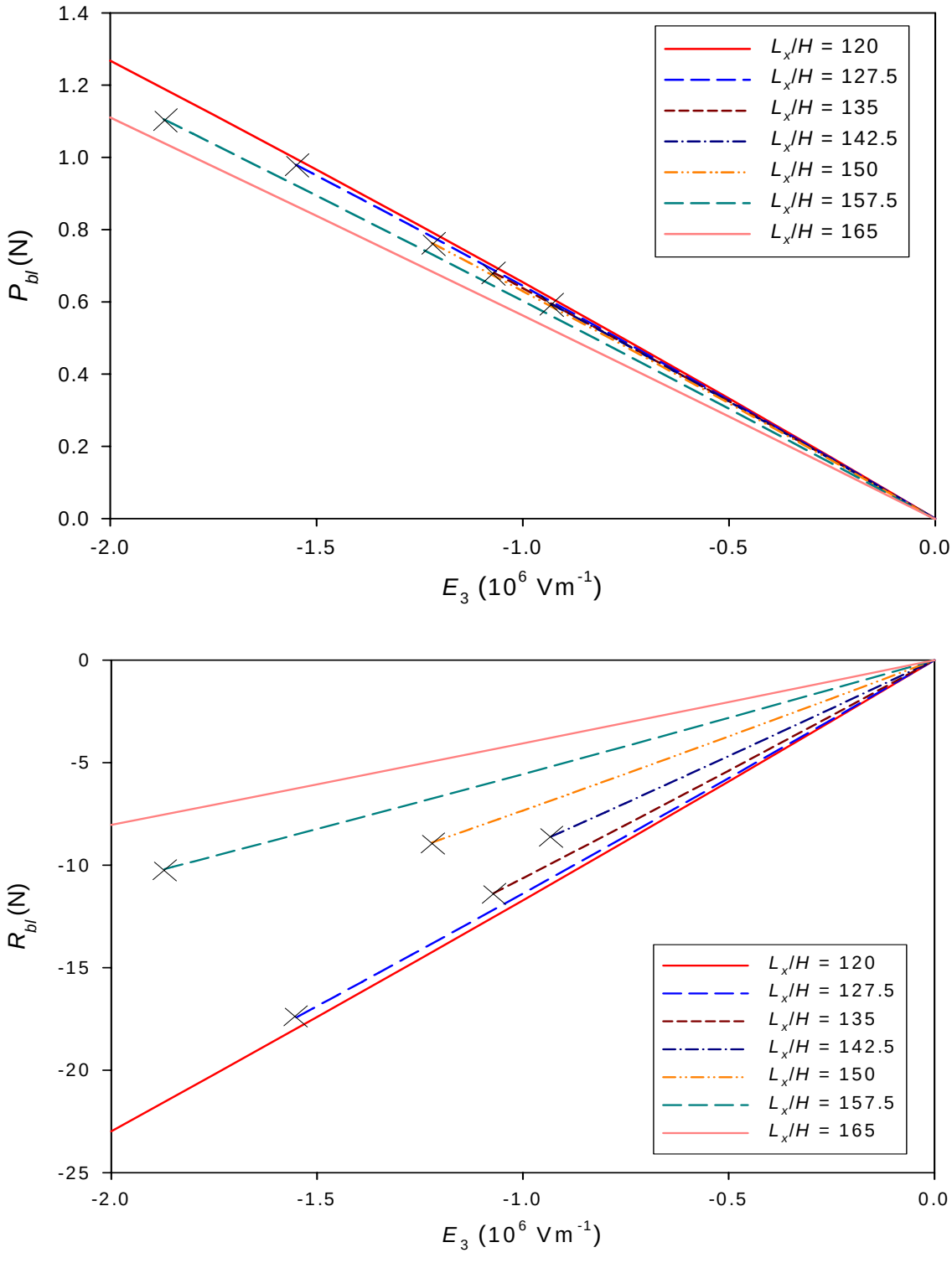

Figure 3.36: Blocking Force vs. Electric Field Strength Relations of Pinned-Pinned Supported Rectangular THUNDER (L_y/L_x = 0.7) in Non-converging Region

supports, so the blocking force P_{bl} in Figure 3.36 is less sensitive to a sidelength-to-thickness ratio. In contrast, the envelope of unsolvable R_{bl} is more observable than that of P_{bl}. Finally, it should be pointed out that at the same value of sidelength-to-thickness ratios, the applied electric fields corresponding to the minimum applicable blocking forces for the pinned-pinned case are lower than those for the pinned-roller case. This is again due to the increased structural stiffness and larger blocking forces that actuators with pinned-pinned supports possess, and as a result, more tendency to snap to other configurations.

3.5 Chapter Summary

In this chapter, the numerical results for cooled and manufactured shapes of THUNDER-type actuators are first presented. Without tabs, the model presented in Chapter 2 was shown to have a good agreement with the finite-element results obtained using ABAQUS. The Rayleigh-Ritz model was shown to have several formulative and computational advantages over finite-element analysis. These advantages include simplicity of formulation, much less computational time, and potentially relative ease of extending the model to include piezoelectric-induced deformations and computing blocking forces. This is in contrast to ABAQUS, which, as the code is presently configured, requires a three-dimensional analysis to model the piezoelectric-induced deformations, several calculation steps, and difficulties in obtaining multiple solutions directly. The results indicate that the predicted shapes for square and rectangular THUNDER actuators strongly depend on cooling temperature and sidelength-to-thickness ratio because of geometrically nonlinear effects. This is interpreted to mean that for values of cooling temperature and sidelength-to-thickness ratio greater than the critical value (bifurcation or limit point), a THUNDER actuator exhibits multiple shapes. Two of the shapes are stable and, in general, near cylindrical. The remaining shape is dome-like and unstable. The Rayleigh-Ritz model is able to predict the multiple equilibrium shapes quite easily. On the other hand, ABAQUS always

converges to one equilibrium shape and has to be coaxed to obtain the remaining solutions. The existence of a critical value of sidelength-to-thickness ratio suggests that care should be taken when designing rectangular THUNDER actuators. Indeed, two similar but slightly different rectangular THUNDER actuators that are each manufactured with a geometry that is very close to the critical value may behave quite differently, depending on whether L_x/H is slightly less than or slightly greater than the critical value. The snap-through behavior between two stable equilibrium states of THUNDER actors due to applied edge moments was also discussed. The behavior indicates the magnitude and direction of the snapping moments. Also the effects of tabs for actuator fastening proposes were investigated. The effects of tabs on the general characteristics of square THUNDER actuators are more obvious than those of rectangular ones. Rather than the appearance of a bifurcation point as with square actuators without tabs, a limit point emerges instead for square actuators with tabs. Generally, the presence of tabs in THUNDER actuators increases the critical sidelength-to-thickness ratios.

In addition, the results of extension of the Rayleigh-Ritz model to predict the actuation response at service temperature of rectangular THUNDER actuators were presented. The average curvature change caused by piezoelectric actuation is a function of the sidelength-to-thickness ratio of actuators. The average curvature in the *x*-direction does not necessary change the same amount as the average curvature in the *y*-direction. This is due to geometrically nonlinear effects. As observed in Figures 3.18 and 3.21, For THUNDER actuators with aspect ratios of 0.7 and 1, the *x*-direction actuation responses on branch A′D′ are enhanced when their sidelength-to-thickness ratios are relative large (L_x/H approximately more than 150). In contrast, as observed in Figure 3.22, there is no enhancement in the actuation response in the *x*-direction on branch A′D′ of THUNDER actuators with an aspect ratio of 0.3 due to their beam-like configuration. However, suppression of the *y*-direction actuation responses on branch A′D′ is clearly noticeable for

the THUNDER actuators with the three aspect ratios considered. Figure 3.23 is quite revealing. It shows that the relationship between the change in average curvatures and the applied electric field for THUNDER actuators with an aspect ratio of 0.7 and L_x/H = 200 and 100 is rather linear. Due to enhancement of geometrically nonlinear effects, the change in the *x*-direction average curvature for L_x/H = 200 is more than that for L_x/H = 100.

Finally, the blocking force predictions from the extension of the Rayleigh-Ritz model used to predict cooled shapes and actuated shapes of THUNDER-type actuators were presented. All numerical results of the blocking forces are computed based on manufactured shapes given by branch $A'D'$ and their associated actuated shapes given by branches A^PD^P and A^ND^N, as illustrated in Figures 3.18, 3.21, and 3.22, for THUNDER actuators subjected to +2 MV/m and -2 MV/m, respectively. For equivalently pinned-roller supported THUNDER actuators with aspect ratios of 0.3, 0.7, and 1, blocking force P_{bl} is normally less than those of the counterpart flat actuators except for THUNDER actuators with aspect ratios of 0.7 and 1, and sidelength-to-thickness ratios larger than 200 and 160, respectively. In actuality, for the pinned-roller case this indicates some degree of proportionality between a change in the *x*-direction curvature due to an application of electric field and a blocking force P_{bl}. Over the sidelength-to-thickness ratio for which the actuation response is suppressed (or enhanced) relative to the linear prediction, the blocking force P_{bl} will decrease (or increase) relative to the linear prediction. For equivalently pinned-pinned supported THUNDER actuators, the existence of force R_{bl} strongly influences the magnitude of blocking force P_{bl}, since the comparatively large magnitude of force R_{bl} alters the structural stiffness of THUNDER actuators. The direction of R_{bl} increases the magnitude of P_{bl} for the pinned-pinned case in the region of the sidelength-to-thickness ratio that force P_{bl} for the pinned-roller case is less than the linear predictions. Oppositely, the direction of R_{bl} reduces the magnitude of P_{bl} for the pinned-pinned case in the region of the sidelength-to-thickness ratio that force P_{bl} for the pinned-roller case is more than the linear predictions.

Consequently, in order to design an actuator to carry a transverse load or an inplane normal load, a careful analysis on actuator performance should be conducted, since its service-temperature shape and support type have very strong effects on the actuator capability. Each specific actuator configuration has its own advantages over others in a specific task and operating condition.

In the next chapter, the numerical results of characteristics of LIPCA-C1 actuators will be presented, analogous to those of THUNDER actuators discussed in this chapter. Shape and associated stress predictions of LIPCA-C1 actuators at service temperature due to the manufacturing process and an application of a quasi-static electric field will be given. Equilibrium and stability of the calculated shapes will be determined. In some selected problems, validity of the Rayleigh-Ritz model with an incorporation of composite material layers will be examined by the ABAQUS model. Blocking forces of LIPCA-C1 actuators with two different support types, i.e., pinned-roller and pinned-pinned supports will be presented in relation to electric field strength and sidelength-to-thickness ratios.

Chapter 4

NUMERICAL RESULTS OF LIPCA-C1 CHARACTERISTICS

4.1 Introduction

This chapter presents shape predictions of rectangular LIPCA-C1 actuators by employing the energy-based Rayleigh-Ritz approach with the incorporation of the constitutive equations for composite layers, as discussed in Chapter 2. The manufactured shapes of the actuators are computed as a function of sidelength-to-thickness ratio. Predictions of ABAQUS models are correlated with those of the Rayleigh-Ritz approach for selected problems. Actuated shapes of the rectangular LIPCA-C1 actuators are also calculated by utilizing the modified Rayleigh-Ritz model with the inclusion of piezoelectrically-induced strains. Finally, blocking forces of the LIPCA-C1 actuators subjected to the application of an electric field with pinned-roller and pinned-pinned supports are calculated and discussed.

4.2 Numerical Results for Manufactured Shapes

4.2.1 Deformation Characteristics of LIPCA-C1 Actuators without Tabs

To illustrate the results of LIPCA-C1 actuators predicted by the energy-based Rayleigh-Ritz model presented in Section 2.2.2, consider a rectangular LIPCA-C1 actuator without tabs consisting of 4 layers, as illustrated in Figure 1.12. The LIPCA-C1 design utilized two layers of glass-epoxy on the bottom and a unidirectional carbon-epoxy layer with its fibers in the *x*-direction as the top layer. The glass-epoxy layers have the same elastic properties in the *x*- and *y*-directions, so in a limited sense are isotropic in orientation

Table 4.1: LIPCA Material Properties

Properties	Carbon-epoxy	PZT-5H	Glass-epoxy
Thickness (μm)	100.0	250.0	90.0
E_1 (GPa)	231.2	67.0	21.7
E_2 (GPa)	7.2	67.0	21.7
G_{12} (GPa)	4.3	25.57	3.99
ν_{12}	0.29	0.31	0.13
$\alpha_1\left(10^{-6}/°\text{C}\right)$	-1.58	3.0	14.2
$\alpha_2\left(10^{-6}/°\text{C}\right)$	32.2	3.0	14.2
$d_{31}\left(10^{-12}\,\text{m/V}\right)$	-	-190	-

used. The piezoceramic material is sandwiched between the two composite layers. The curing temperature of the epoxy matrix is taken to be $167\,°\text{C}$. The end of the cooling process is when temperature is equal to the room temperature of $25\,°\text{C}$. Thus ΔT, which was defined in Equation (3.2), is equal to $-142\,°\text{C}$. In the following analyses, the material properties and thicknesses of the layers are taken from Yoon et al [33], and they are given here in Table 4.1. It should be kept in mind that for a given value of sidelength-to-thickness ratio, a LIPCA-C1 actuator is longer in the *x*-direction than a THUNDER actuator with the same sidelength-to-thickness ratio due to the larger value of *H* for the LIPCA-C1 cross section. (For THUNDER $H = 0.427$ mm, for LIPCA-C1 $H = 0.530$ mm.)

Figure 4.1 illustrates the relations between average curvature and sidelength-to-thickness ratio of LIPCA-C1 actuators with an aspect ratio of 0.7. As seen in the figure, the room-temperature curvature in the *x*-direction depends little on the sidelength-to-thickness ratio, and the curvature prediction is close to the geometrically linear value, which is shown as the dotted horizontal straight line tangent to point A'. Geometrically nonlinear effects neither suppress nor enhance the room-temperature curvature to any significant degree. By way of contrast, the *y*-direction room-temperature curvature is influenced by geometrically nonlinear effects and is a strong function of sidelength-to-thickness ratio. Unlike the

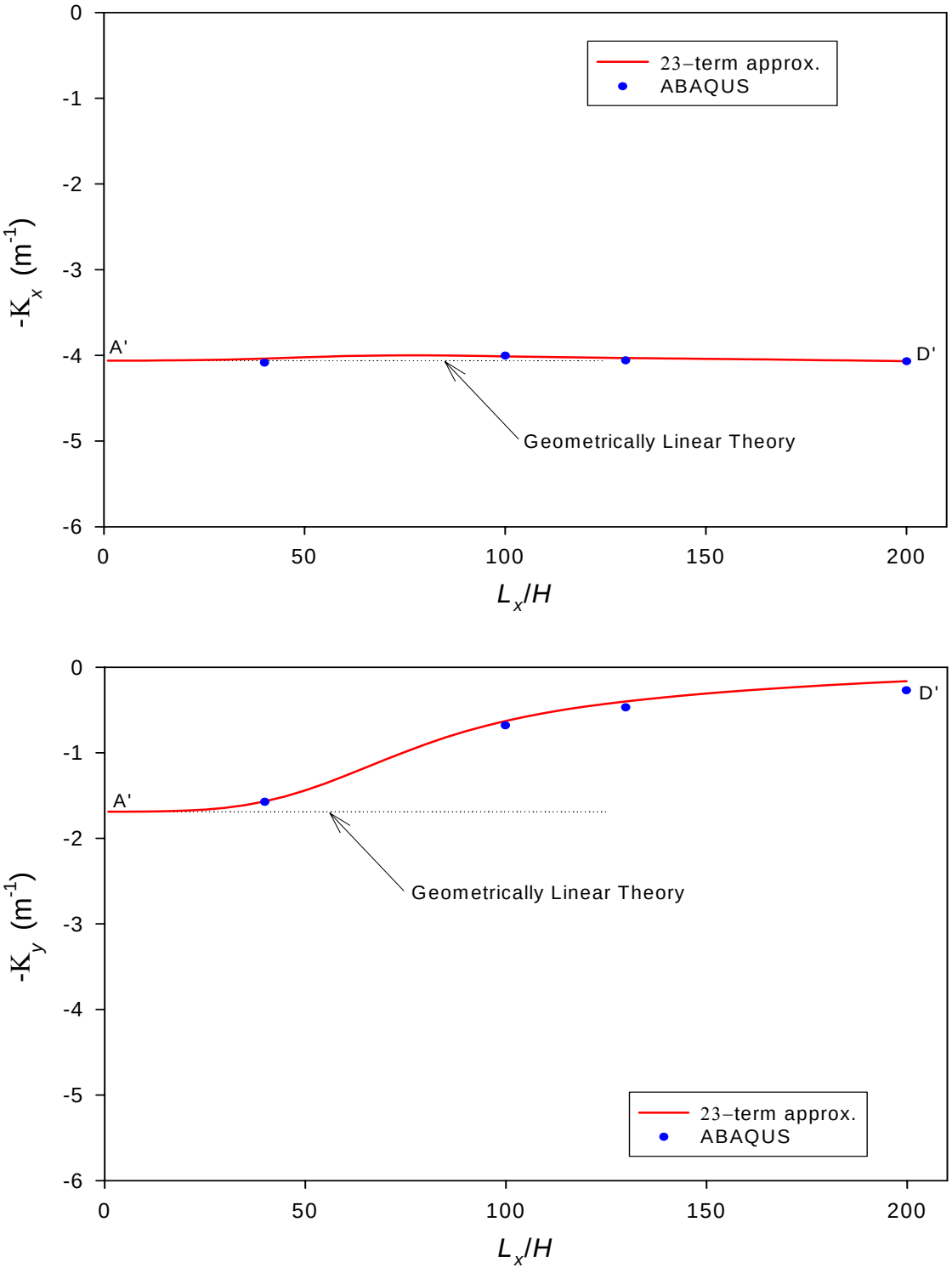

Figure 4.1: Sidelength-to-Thickness Ratio vs. Curvature Relations of Rectangular LIPCA-C1 ($L_y / L_x = 0.7,\ \Delta T = -142\,^{\circ}\mathrm{C}$)

THUNDER actuators with an aspect ratio of 0.7, as illustrated in Figure 3.8 and discussed in Section 3.2.1, there are no multiple equilibrium branches of LIPCA-C1 actuator shapes over the range of sidelength-to-thickness ratios considered. Also the room-temperature curvatures in the two directions are not equal over the considered range, the curvature in the *y*-direction being somewhat less than half the value of the curvature in the *x*-direction for sidelength-to-thickness ratios less than 50. This is believed to occur because of the inplane elastic property orthotropy of the carbon-epoxy layer. For larger sidelength-to-thickness ratios, nonlinear effects make the *y*-direction curvature even smaller than the *x*-direction curvature. The suppression of the *y*-direction room-temperature curvature with increasing sidelength-to-thickness ratio is similar to the behavior of THUNDER actuators on branch A′D′ in Figure

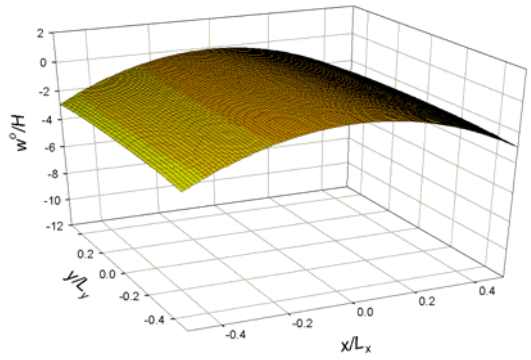

(a) 23-term Rayleigh-Ritz, L_x/H = 100

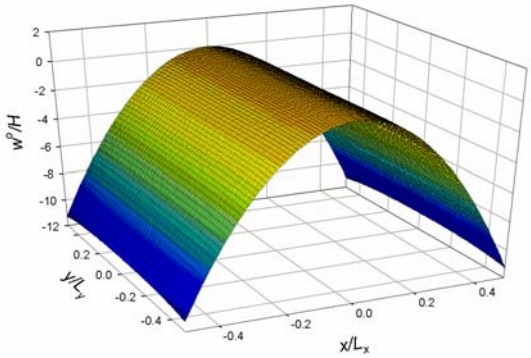

(b) 23-term Rayleigh-Ritz, L_x/H = 200

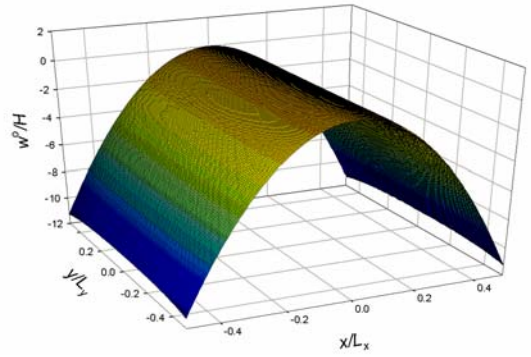

(c) ABAQUS, L_x/H = 200

Figure 4.2: Equilibrium Shapes of Rectangular LIPCA-C1 (L_y/L_x = 0.7, ΔT = -142 °C)

3.8. Also in Figure 4.1, the average room-temperature curvatures as predicted by the 23-term Rayleigh-Ritz model are compared with those predicted by the finite-element model from ABAQUS, and the comparison is good. The room-temperature shapes of rectangular actuators with L_y/L_x = 0.7 and L_x/H = 100 and 200 are illustrated in Figure 4.2. As seen, for actuators with the same thickness H, the x-direction curvature for L_x/H =100 is less pronounced than that for L_x/H = 200, despite the values of their x-direction curvatures being almost equal. This is because the actuator with L_x/H =100 is a factor of two shorter than one with L_x/H =200. In addition, the curvatures in the y-direction are difficult to detect due to their smaller magnitudes and the smaller y-dimension compared to the x-dimention. Figures 4.2 (b) and (c) also depict the comparison of the room-temperature shape of the actuator with a sidelength-to-thickness ratio of 200 between the 23-term Rayleigh-Ritz and ABAQUS models. Again the comparison shows a very good agreement in the manufactured shape prediction. The very good correlations between the numerical results predicted from the developed 23-term Rayleigh-Ritz model incorporating the composite material layers and the finite-element model provide the validity of the former model. Therefore, the 23-term Rayleigh-Ritz model will be used to study other LIPCA-C1 characteristics with a high degree of confidence.

Considering square LIPCA-C1 actuators, the relationships between the sidelength-to-thickness ratio and the average room-temperature curvatures are illustrated in Figure 4.3. Overall, the relationships are very similar to the ones in Figure 4.1. Specifically, as can be seen, the x-direction room temperature curvature is still almost independent of sidelength-to-thickness ratio, like that of the actuators with L_x/H = 0.7. However, stronger geometrically nonlinear effects due to longer dimension L_y for the square actuators can be readily observed from the y-direction curvature in Figure 4.3, where the curvature is suppressed when the sidelength-to-thickness ratio is larger than 30. The suppression of the curvature in the y-direction is substantial for values of L_x/H > 150. The key reason for the

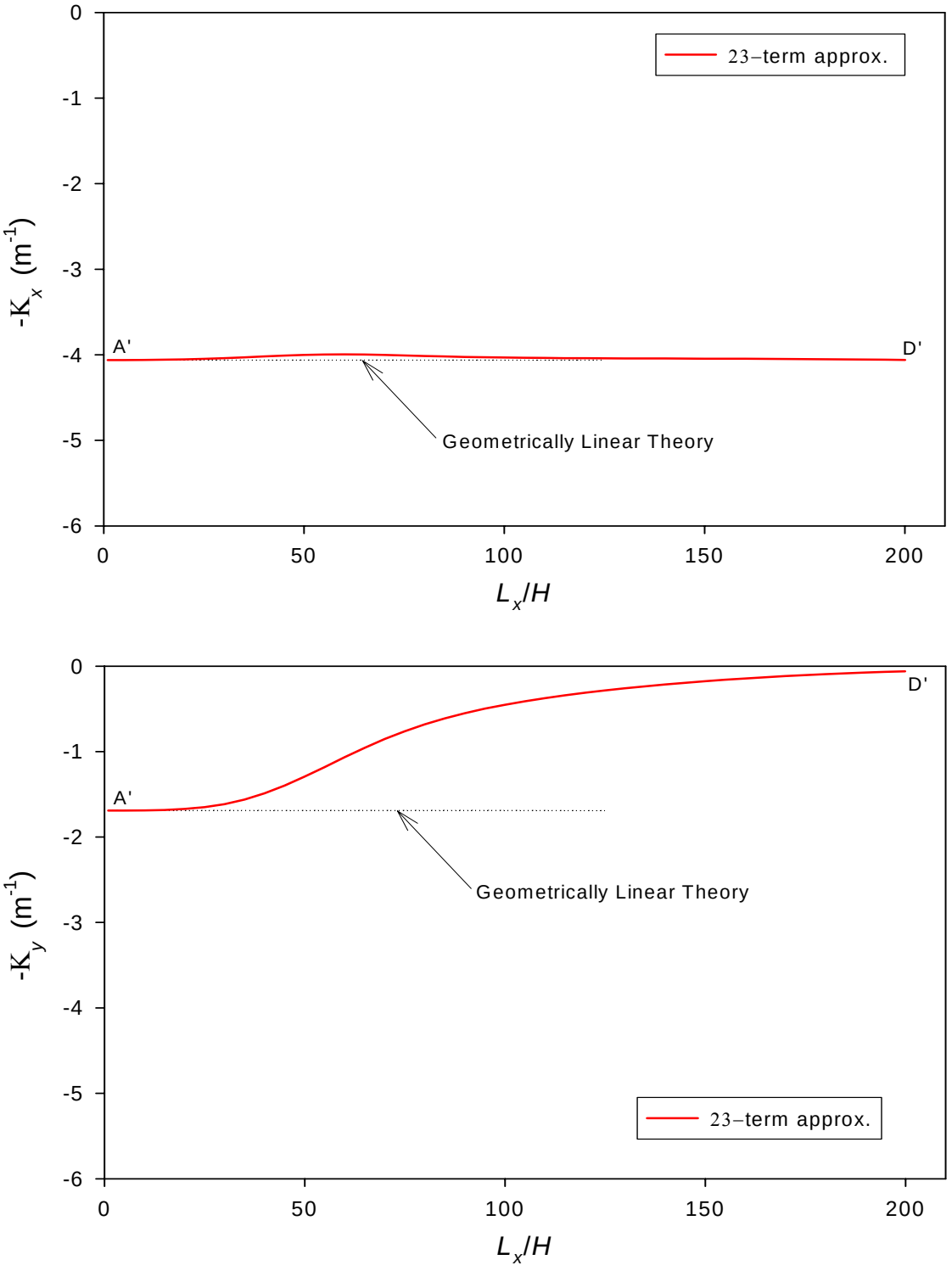

Figure 4.3: Sidelength-to-Thickness Ratio vs. Curvature Relations of Square LIPCA-C1 (ΔT = -142 °C)

value of the *x*-direction curvature barely changing and value of the *y*-direction curvature changing significantly is that geometrically nonlinear effects have stronger influence on the curvature with the smaller magnitude. Nonlinear effects will notably suppress the curvature with the smaller magnitude and only slightly suppress or even enhance the curvature with the larger magnitude. Also, the fiber direction of the carbon-epoxy layer is aligned longitudinally (along the *x*-direction), so the actuator is much stiffer in the *x*-direction than in the *y*-direction. The curvature in the *x*-direction is thus less susceptible to geometrically nonlinear effects than the *y*-direction curvature.

Finally, the influence of sidelength-to-thickness ratio on the room-temperature curvatures of a beam-like LIPCA-C1 actuator with an aspect ratio of 0.33 is illustrated in Figure 4.4. Note that the value of 0.33 is chosen because it is the value of the aspect ratio investigated by Yoon et al [33] in their work on LIPCA actuators. With L_y/L_x = 0.33, both the geometry and material 'favor' the *x*-direction. Like the results show in Figures 4.1 and 4.3 for aspect ratios L_y/L_x = 0.7 and 1, respectively, for the beam-like LIPCA-C1 actuator the room-temperature curvature in the *x*-direction is virtually insensitive to sidelength-to-thickness ratios. The *y*-direction room temperature is smaller by approximately a factor of two for short actuators, and gradually decreases as L_x/H increases, but not as much as for the other two aspect ratios studied. This indicates weaker effects of geometrical nonlinearities on the actuator shape characteristic, primarily because the dimension in the *y*-direction is small. Overall, except for magnitude and sign, the general characteristics of the curvature vs. sidelength-to-thickness ratio relations for the beam-like LIPCA-C1 actuators are similar to those of beam-like THUNDER actuators in Figure 3.9. Identical to the case of the aspect ratios of 0.7 and 1, the geometrically linear Rayleigh-Ritz model predicts spatially uniform *x*- and *y*-direction curvatures, K_x = 4.06 m^{-1} and K_y = 1.69 m^{-1}. Additionally, since the LIPCA-C1 actuators with L_y/L_x = 0.33 are beam-like, the *x*-direction curvature of the actuators can be computed from either geometrically nonlinear or linear laminated beam

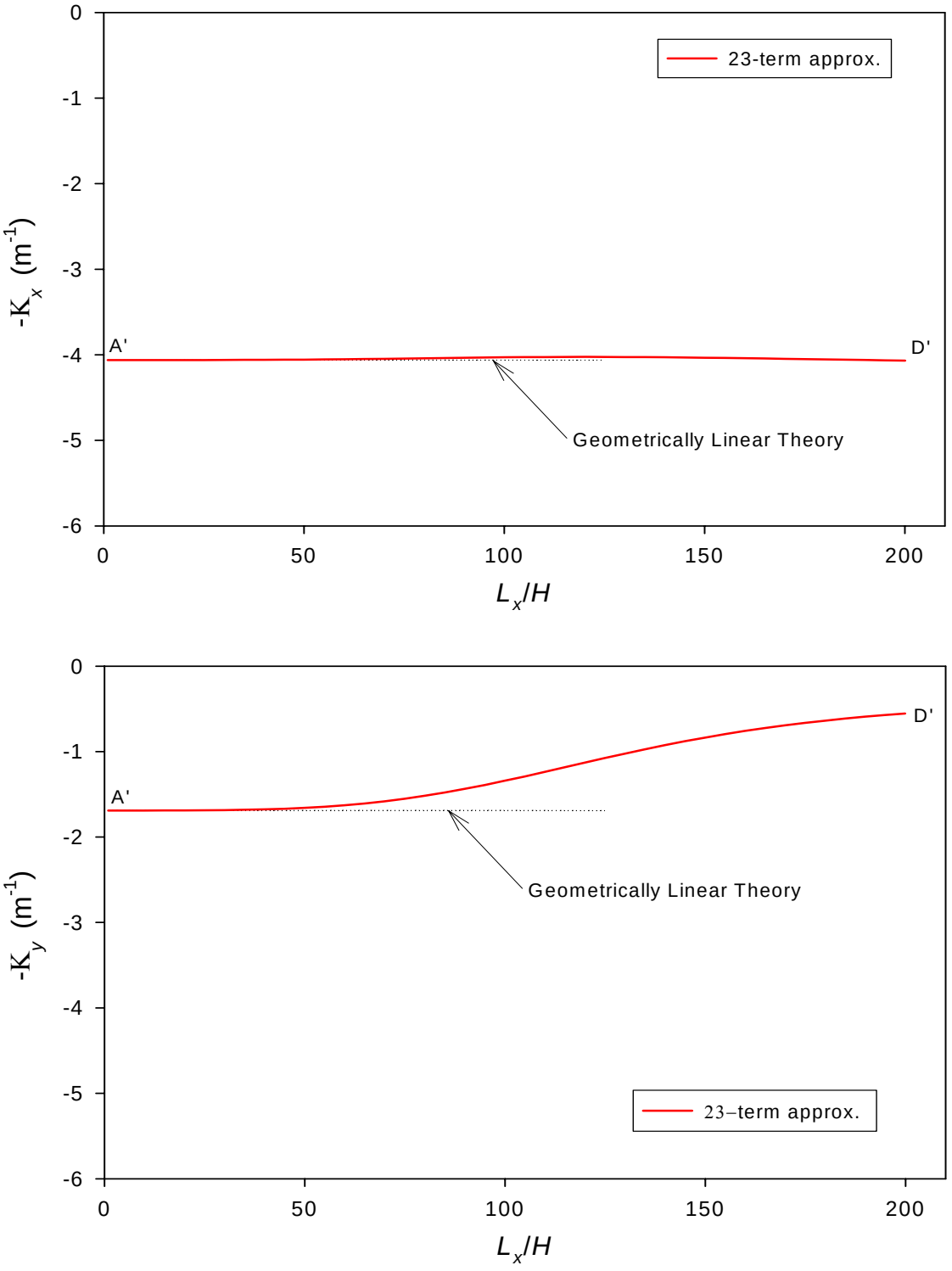

Figure 4.4: Sidelength-to-Thickness Ratio vs. Curvature Relations of Beam-like LIPCA-C1 (L_y/L_x = 0.33, ΔT = -142 °C)

models, as derived in Appendix B. Specifically, by using Equation (B.36) or (B.65), K_x = 4.31 m^{-1}, a constant over the range of sidelength-to-thickness ratios considered. This value is only around six percent different from the geometrically linear Rayleigh-Ritz model calculation. However, neither the geometrically linear Rayleigh-Ritz model nor either of the beam models is capable of accurately capturing the curvature in the y-direction over the whole range of sidelength-to-thickness ratios. Therefore, the geometrically nonlinear model represented by the Rayleigh-Ritz approach still plays an important role in predicting the manufactured configurations of the LIPCA-C1 actuators, particularly for relatively large values of L_x/H.

4.2.2 Force and Moment Resultant and Stress Characteristics of LIPCA-C1 without Tabs

As stated before, due to its elevated-temperature manufacturing process a LIPCA-C1 actuator, like a THUNDER actuator, inherently possesses residual stresses. From the ABAQUS calculations, the force and moment resultants, as defined in Equation (2.21), at room temperature for a rectangular LIPCA-C1 actuator with an aspect ratio of 0.7 and sidelength-to-thickness ratio of 200 are illustrated in Figure 4.5. The actuator is in the configuration given by point D′ in Figure 4.1 and its corresponding shape is depicted in Figure 4.2 (b), (c). Since the boundaries of the actuator are traction free, specific force and moment resultants are zero on the boundaries, as seen in Figure 4.5. Like Figure 3.10 for THUNDER actuators and illustrated in Figure 4.5 (a)-(c), extreme values of the force and moment resultants occur in narrow regions along the edges of the actuator. Also, the force and moment resultant characteristics in Figure 4.5 for the LIPCA-C1 actuator are similar to those for the THUNDER actuator in Figure 3.10 except for M_x, which has highly localized negative values along the edge $y = \pm L_y/2$ instead of the positive values in the THUNDER actuators of Figure 3.10 (b). However, omitting the negative values near the edges, the characteristic of M_x in the middle region of the LIPCA-C1 actuator are also similar to that of the THUNDER actuator, i.e., being slightly negative in the central region and increasing to

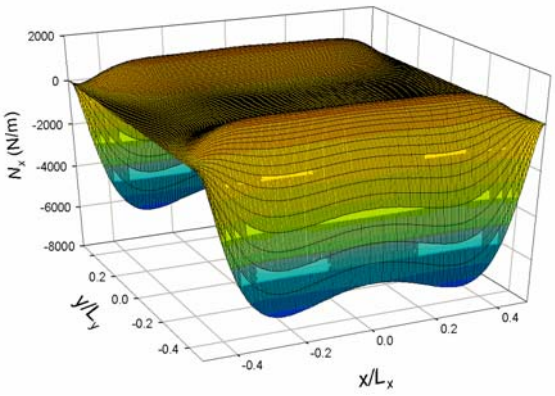

(a) Force Resultant N_x

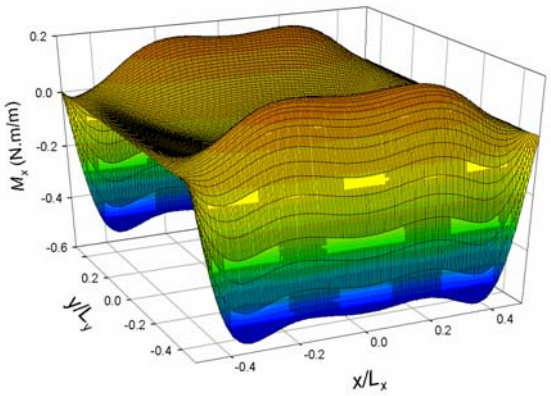

(b) Moment Resultant M_x

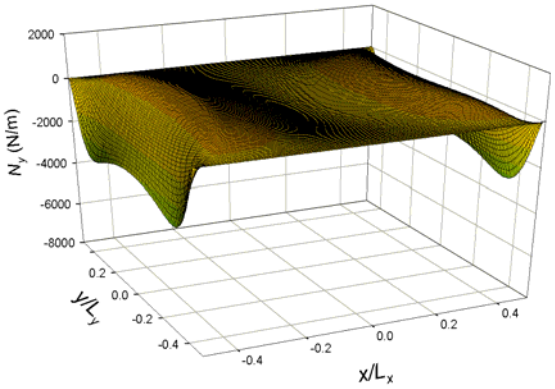

(c) Force Resultant N_y

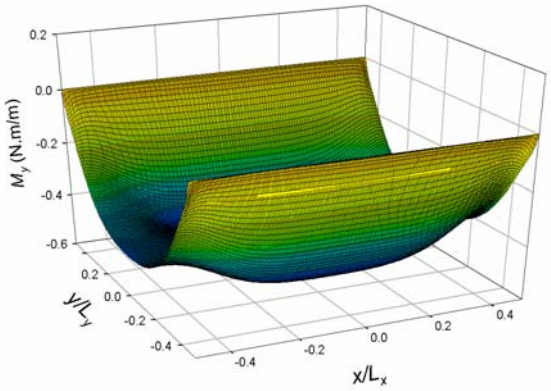

(d) Moment Resultant M_y

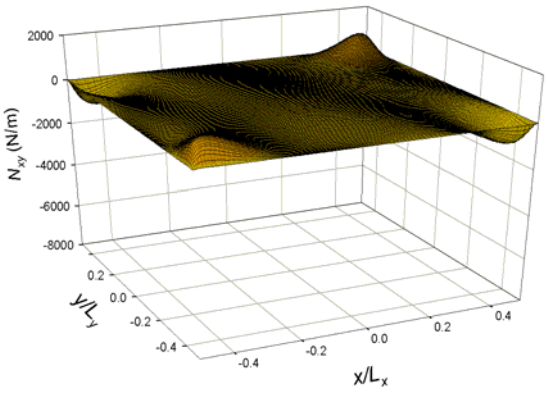

(e) Force Resultant N_{xy}

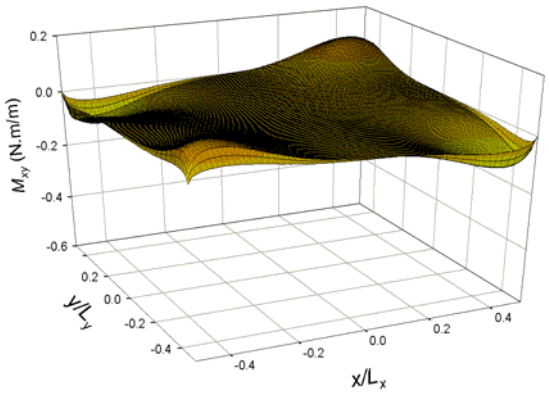

(f) Moment Resultant M_{xy}

Figure 4.5: Force and Moment Resultants in Rectangular LIPCA-C1 (L_y/L_x = 0.7, L_x/H = 200, ΔT = -142 °C)

positive values when approaching the actuator edges ($y = \pm L_y/2$). Note that the magnitudes of all force and moment resultants of the LIPCA-C1 actuator are smaller than those of the THUNDER actuator. The LIPCA-C1 actuator has the lower elevated processing temperature, so the values of the thermal-induced residual stresses at room-temperature are lower. As with the THUNDER actuators, the geometrically linear plate theory, as derived in Appendix A, will predict the values of the force and moment resultants to be exactly zero throughout. The lower values of stress resultants also confirm weaker geometrically nonlinear effects in the LIPCA-C1 actuator. As mentioned in Section 3.2.2 in relation to THUNDER actuators, it can be observed that though the extreme values of N_{xy} and M_{xy} in Figures 4.5 (e) and (f) are not zero, they are small compared to the extreme values of the other force and moment resultants, and they are confined to the corner regions of the actuator.

Figure 4.6 illustrates its force and moment stress resultants for the beam-like LIPCA-C1 actuator with an aspect ratio of 0.33. It is evident that the force and moment resultant are similar to those in Figure 4.5. This coincides with the similarity of the shape configurations predicted in Figure 4.1 and 4.4, as discussed above.

A sample of the stresses that lead to the force and moment resultants N_x, N_y, M_x, and M_y for the rectangular LIPCA-C1 actuator with an aspect ratio of 0.7 and a sidelength-to-thickness ratio of 200 are illustrated in Figures 4.7 and 4.8 for four locations within the actuator. The through-thickness distribution of the inplane normal stresses near the center of the actuator $x \cong 0,\ y \cong 0$ are shown in Figure 4.7 (a), while the distributions near the midpoints along the longer edge $(x \cong 0, y \cong L_y/2)$ and near the shorter edge $(x \cong L_x/2, y \cong 0)$ are illustrated in Figure 4.7 (b), and 4.8 (a), respectively. The distributions near a corner $(x \cong L_x/2, y \cong L_y/2)$ are displayed in Figure 4.8 (b). At room temperature, the piezoceramic layer experiences some tensile stress in the *x*-direction, but mostly compressive stresses, and is completely in compression in the *y*-direction. The tensile stress,

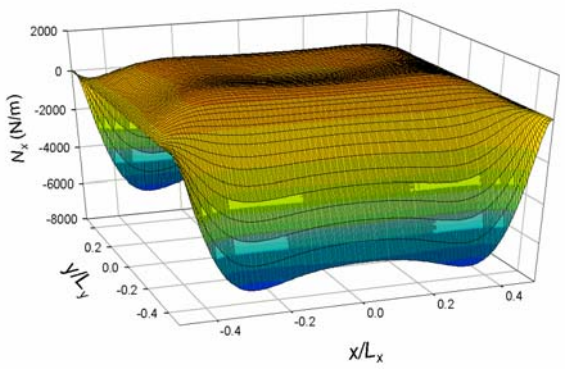

(a) Force Resultant N_x

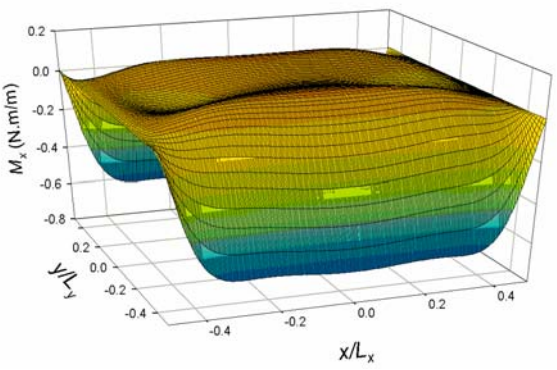

(b) Moment Resultant M_x

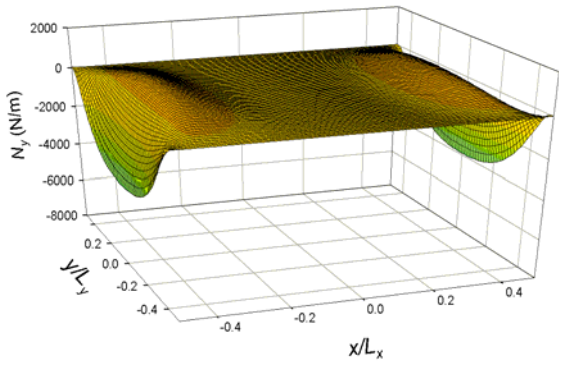

(c) Force Resultant N_y

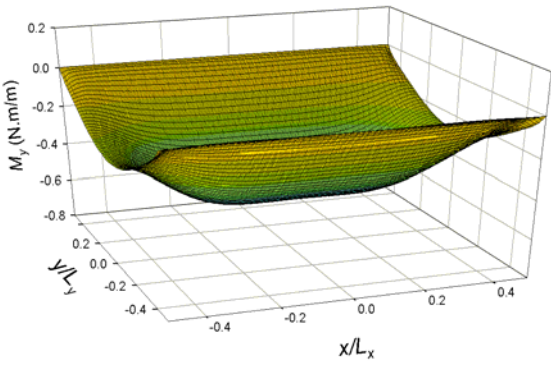

(d) Moment Resultant M_y

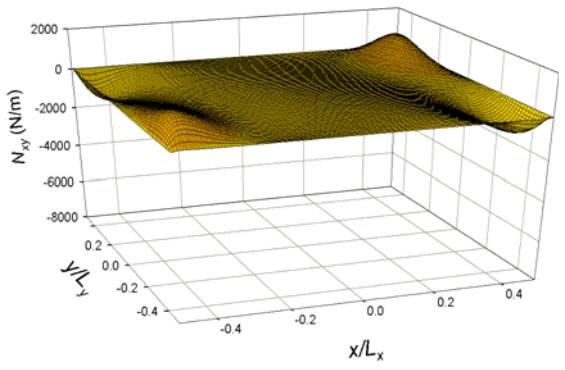

(e) Force Resultant N_{xy}

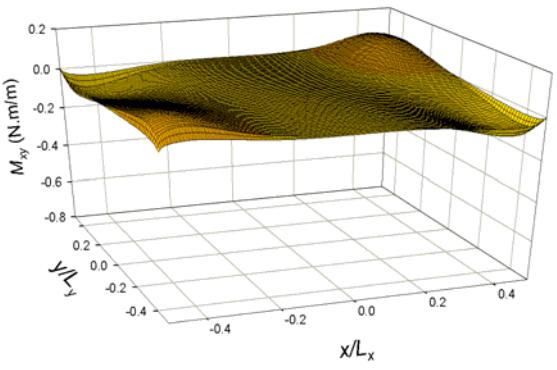

(f) Moment Resultant M_{xy}

Figure 4.6: Force and Moment Resultants in Beam-Like LIPCA-C1 (L_y/L_x = 0.33, L_x/H = 200, ΔT = -142 °C)

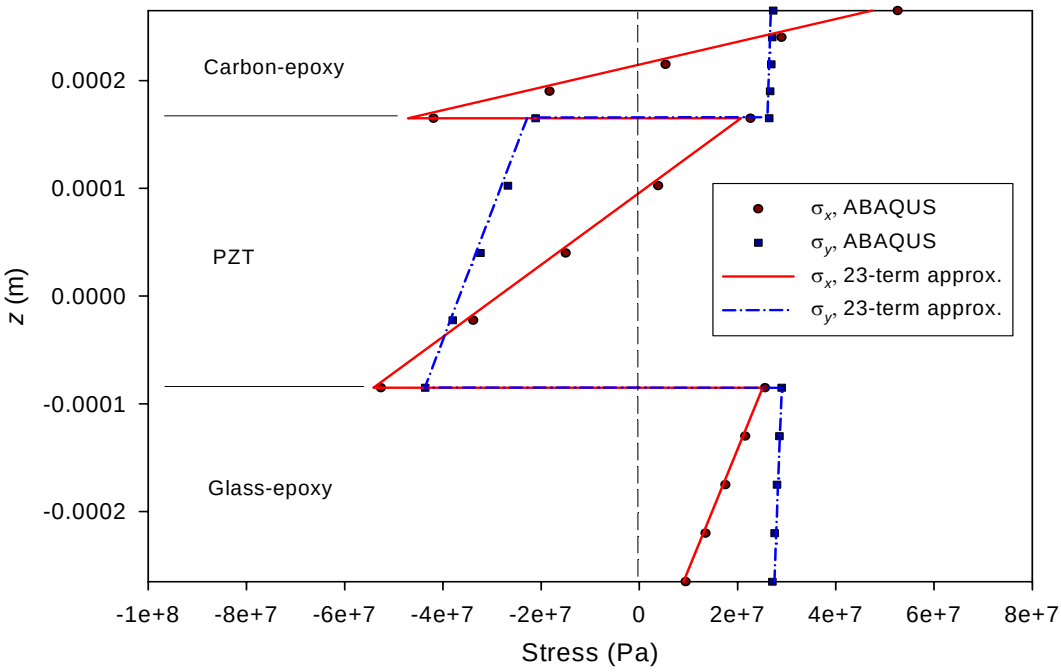

(a) Distribution of Normal Stresses at $x \cong 0,\ y \cong 0$

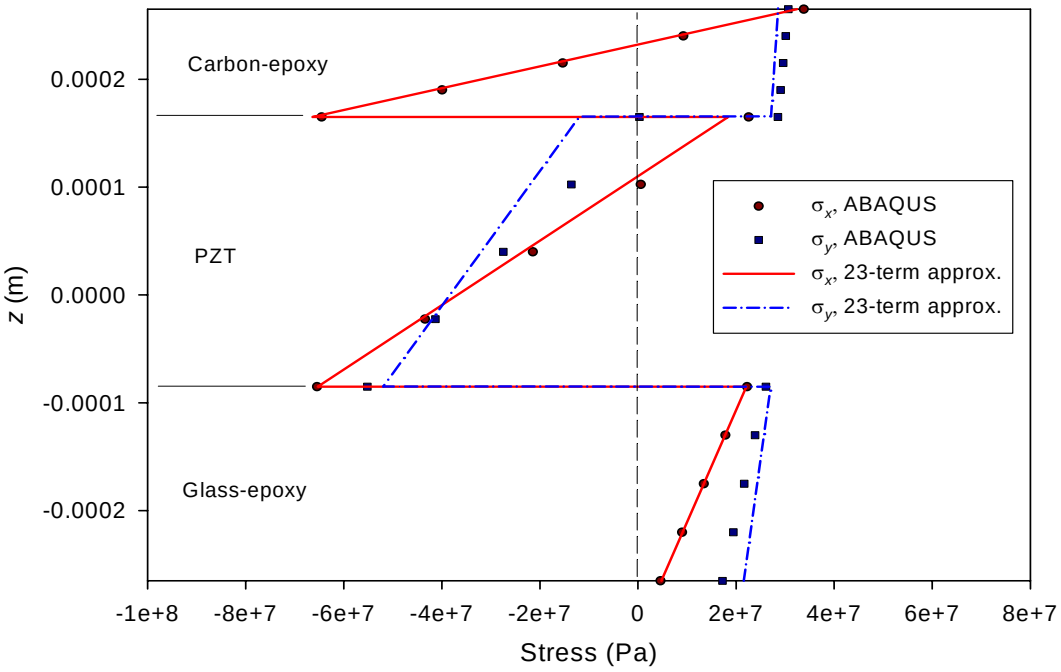

(b) Distribution of Normal Stresses at $x \cong 0,\ y \cong L_y/2$

Figure 4.7: Stress Distributions in LIPCA-C1 (L_y/L_x = 0.7, L_x/H = 200, ΔT = -142 °C) for Two Locations near Centerline x = 0

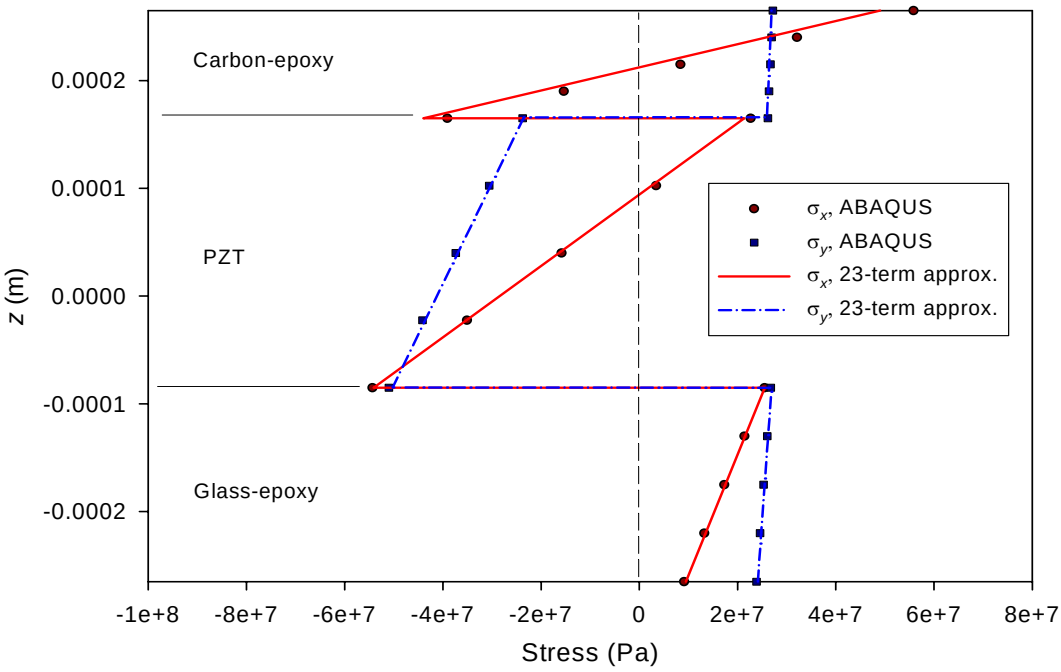

(a) Distribution of Normal Stresses at $x \cong L_x/2,\ y \cong 0$

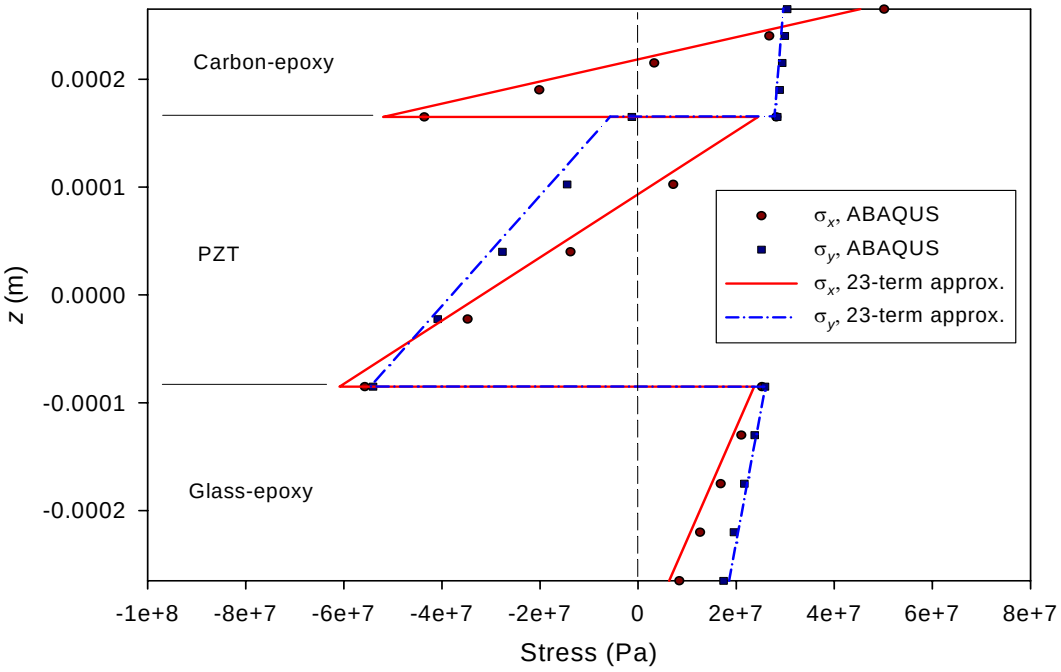

(b) Distribution of Normal Stresses at $x \cong L_x/2,\ y \cong L_y/2$

Figure 4.8: Stress Distributions in LIPCA-C1 (L_y/L_x = 0.7, L_x/H = 200, ΔT = -142 °C) for Two Locations near Boundary $x = L_x/2$

however, is not large. The carbon-epoxy layer also has both residual tensile and compressive stresses in the *x*-direction on top and bottom portions, respectively. Note that the stress gradient through the thickness of the actuator in the *x*-direction is larger than that in the *y*-direction due to the more room-temperature curvature in the former direction than in the latter direction. Also it is important to note that the magnitudes of the room-temperature stresses are lower than for the THUNDER actuator. This is again due mainly to the lower cure temperature for the epoxy in the carbon-epoxy and glass-epoxy layers in the LIPCA-C1 actuator than for the polyimide adhesive in the THUNDER actuators. That some force and moment resultants have increased magnitudes, on the specific edges, as illustrated in Figure 4.5, can also be explained from the stress distributions. However, unlike the case of the THUNDER actuator presented in Section 3.2.2, where the normal stress in the steel layer is chiefly attributable for the increased magnitudes, all layers play a key role in the case of the LIPCA-C1 actuator when considering N_x and M_x. The values of σ_x in all layers decrease when moving from the center to midpoint of the longer edges. This causes the values of N_x near $x = 0,\ y = L_y/2$ to be negative relative to the value at the center. Additionally, due to the carbon-epoxy layer having the highest stiffness in the *x*-direction and being the outermost layer, the decrement of the value of σ_x in the carbon-epoxy layer will dominate the contribution to moment resultant M_x and, as a result, produce the negative M_x near $x = 0,\ y = L_y/2$. Nonetheless, the extreme negative value of N_y at the midpoint near the shorter edge, $x = L_x/2,\ y = 0,$ is from the PZT and glass-epoxy layer, not the carbon-epoxy layer. This is because of the extensional modulus of the carbon-epoxy layer is relatively very small in the *y*-direction. Also illustrated in Figures 4.7 and 4.8, the comparison between the predictions of the stress distributions by 23-term Rayleigh-Ritz and ABAQUS models reveals a fairly good agreement. The most distinguishable disagreement is with the stress component σ_y in the PZT layer at $y \cong L_y/2.$ The rest of the good comparisons of the stress distributions demonstrates the generally good accuracy of the Rayleigh-Ritz model

developed with only 23 degrees of freedom, compared to thousands degrees of freedom for the finite element analysis.

4.3 Numerical Results for Actuated Shapes

4.3.1 Deformation Characteristics of LIPCA-C1 subjected to Applied Electric Field

For the rectangular geometry (L_y/L_x = 0.7), the actuated curvatures in the *x*- and *y*-directions of LIPCA-C1 actuators are illustrated in Figure 4.9. Also shown in the figure are the room-temperature curvatures in the *x*- and *y*-directions, which were illustrated in Figure 4.1 and are repeated here for comparison. When the LIPCA-C1 actuators are actuated with ±2 MV/m, the changes in curvature in the *x*-direction are only weakly dependent on sidelength-to-thickness ratio. There is a slightly noticeable enhancement for the negative field strength for sidelength-to-thickness ratio in the range 75-125. Also, like the room-temperature curvature in the *y*-direction, the changes in curvature in the *y*-direction due to actuation are suppressed for sidelength-to-thickness ratios greater than 50 owing to geometrically nonlinear effects. Interestingly, for shorter actuators, the actuated changes in curvature in the *y*-direction are larger in magnitude than the actuated changes in the *x*-direction. This difference in actuated curvature changes for the short actuators can be attributed to the relative bending stiffness of the actuators in the *x*- and *y*-directions. A LIPCA-C1 actuator with this aspect ratio would be intended to utilize the room-temperature curvature and the actuated change in curvature in the *x*-direction rather than in the *y*-direction, so the various characteristics of the *y*-direction curvature may be of little consequence. It should be noted that for an electric field of a given sign, the signs of the changes in curvature in the *x*- and *y*-directions are opposite each other. This was not the case for a THUNDER actuator and is believed to be due to the inplane material orthotropy of the LIPCA-C1 actuator compared to inplane material isotropy of a THUNDER actuator. For the LIPCA-C1 actuator, the carbon-epoxy layer is relatively stiff in the *x*-direction and

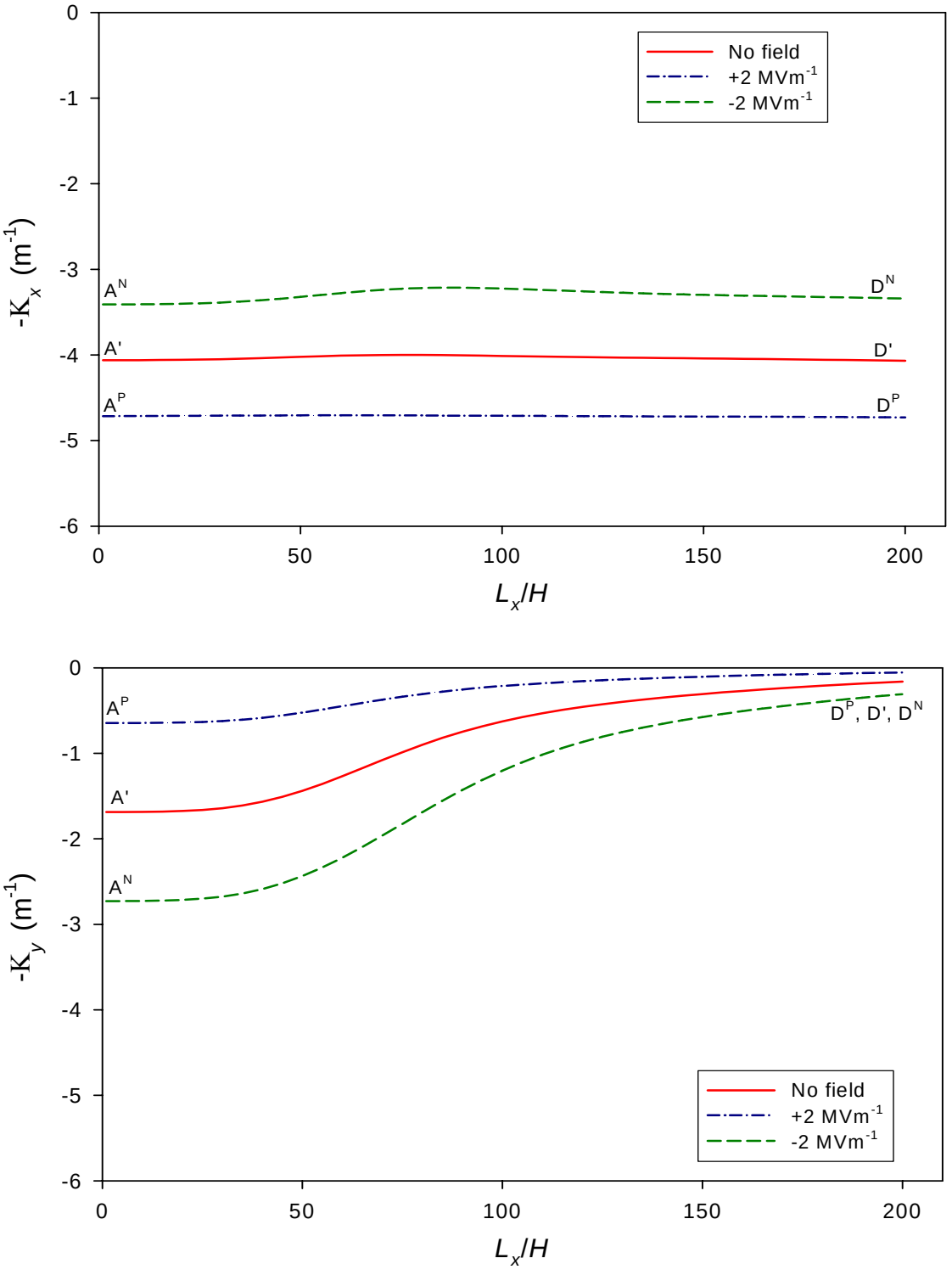

Figure 4.9: Influence of Actuation on the Change of Curvatures of Rectangular LIPCA-C1 (L_y/L_x = 0.7, ΔT = -142 °C)

compliant in the *y*-direction, whereas the glass-epoxy layer is softer in the *x*-direction and stiffer in the *y*-direction than the carbon-epoxy layer. Therefore, the carbon-epoxy layer acts as a virtual backbone layer in the *x*-direction in contrast to the glass-epoxy layer, which acts as a virtual backbone in the *y*-direction. This causes the LIPCA-C1 actuator to bend oppositely in the *x*-direction to the *y*-direction. Also, it should be noted that the curvature changes of the LIPCA-C1 actuator in the *x*-direction are close in value to the curvature changes in the x-direction for a THUNDER actuator when its room-temperature shape is given by branch A′D′ in Figure 3.18. In fact, considering branch A′D′ in Figure 3.18 for the THUNDER actuator, for aspect ratio 0.7 the general characteristics of the curvature vs. sidelength-to-thickness ratio relations are not all that different, despite the multiple-branch character of the relations for THUNDER actuators.

For the square geometry, the actuated curvatures in the *x*- and *y*-directions of LIPCA-C1 actuators are illustrated in Figure 4.10. Interestingly, the *x*-direction actuated curvatures are again almost independent of sidelength-to-thickness ratio. Furthermore, when compared to Figure 4.9 for the LIPCA-C1 actuator with an aspect ratio of 0.7, the changes in the *x*-direction curvature are also similar despite more than a 40% increase in aspect ratio. The change in the *x*-direction curvature is strongly influenced by the *x*-direction room-temperature curvature, which itself is hardly sensitive to sidelength to-thinkness and aspect ratios, as previously discussed. Analogous to the aspect ratio of 0.7, for the aspect ratio of 1 there is a slight enhancement for the negative field strength for sidelength-to-thickness ratio in the range 50-100. Compared to the rectangular actuator, for the square actuator the enhancement is shifted to smaller values of L_x/H. The changes in curvature in the *y*-direction due to the actuation, however, are suppressed noticeably more than for the actuator with the smaller aspect ratio (L_y/L_x = 0.7). Again, the changes in curvature in the *y*-direction are influenced by the *y*-direction room-temperature curvature. At a large sidelength-to-thickness ratio, the structural stiffness in the *y*-direction of the actuator developed during the cooling

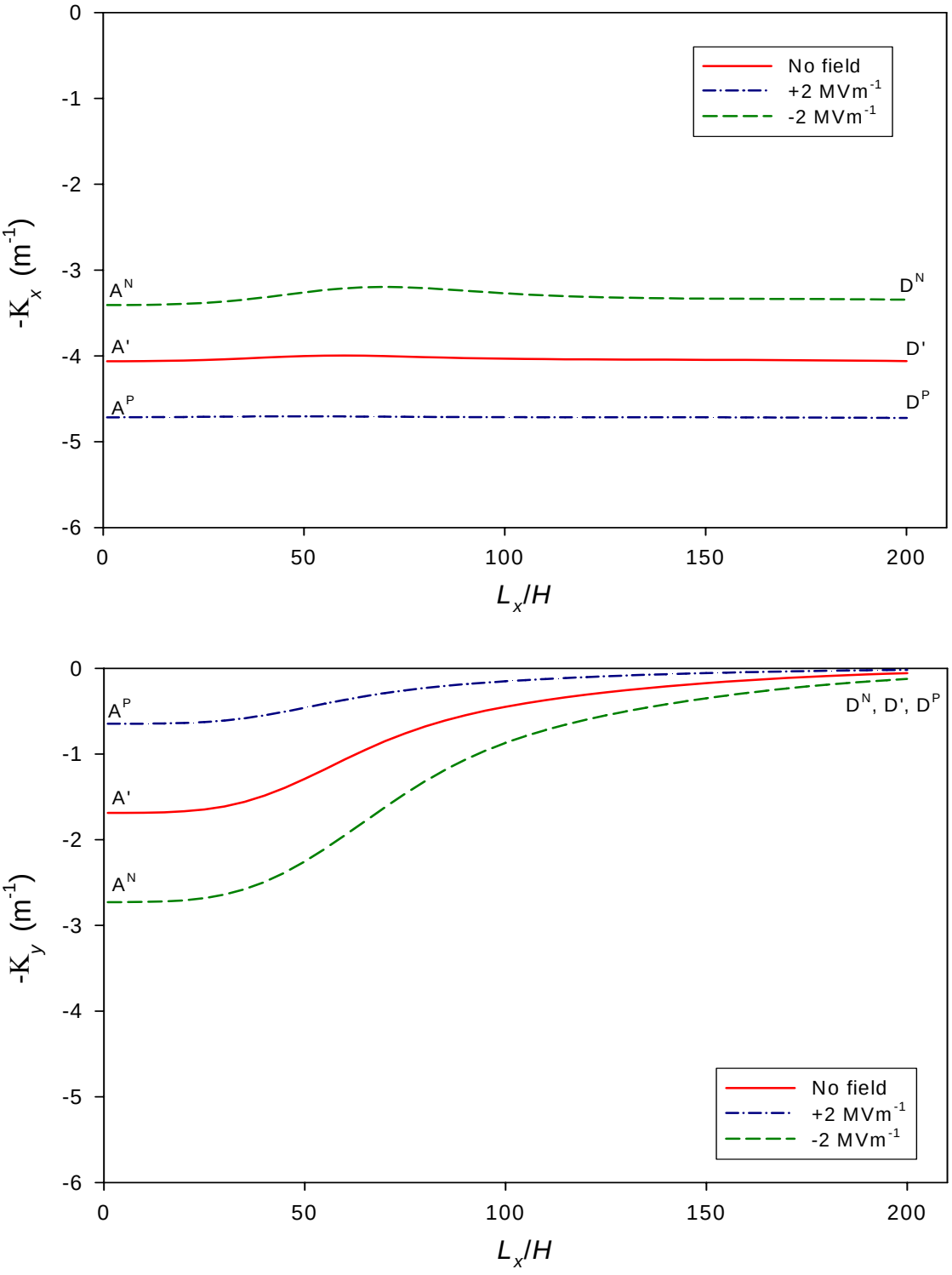

Figure 4.10: Influence of Actuation on the Change of Curvatures of Square LIPCA-C1 (L_y/L_x = 1, ΔT = -142 °C)

process is high due to geometrically nonlinear effects and the stiffness dominates actuated deformations in the *y*-direction at service temperature. Overall, the behaviors of the LIPCA-C1 actuators with an aspect ratio of 0.7 and 1 as a function of sidelength-to-thickness ratio when subjected to an applied electric field are quite similar.

The influence of sidelength-to-thickness ratio on actuated curvatures of LIPCA-C1 actuators with an aspect ratio of 0.33 is illustrated in Figure 4.11. Like the results shown in Figures 4.9 and 4.10 for aspect ratios L_y/L_x = 0.7 and 1, for the beam-like LIPCA-C1 actuators the actuation-induced curvature changes in the *x*-direction are quite independent of sidelength-to-thickness ratio. There is a slight enhancement of the *x*-direction curvature change with an actuation voltage of -2 MV/m for sidelength-to-thickness ratios greater than 125, though the enhancement is minimal. This enhancement is shifted to occur at larger sidelength-to-thickness ratios than for the larger aspect ratios considered previously. The actuated changes in curvature in the *y*-direction are also suppressed as actuator length increases, but not as much as for aspect ratios L_y/L_x = 0.7 and 1. Like the case of the larger aspect ratios considered, for shorter actuators the actuated changes in curvature in the *y*-direction are larger than the actuated changes in the *x*-direction since their characteristics can be governed by the geometrically linear theory, which are independent of actuator inplane dimensions. Also, like the case of aspect ratios L_y/L_x = 0.7 and 1, for an actuation voltage of a given sign, the signs of the curvature changes in the two directions are opposite each other. It should be noted that except for sign, the general characteristics of the curvature vs. sidelength-to-thickness ratio relations for the beam-like LIPCA-C1 actuators are quite similar to those of beam-like THUNDER actuators in Figure 3.22. In addition, due to the beam-like configuration, a comparison of the *x*-direction actuation-induced curvatures between the Rayleigh-Ritz predictions and the beam theories developed in Appendix B is of interest. The geometrically linear plate theory Rayleigh-Ritz approach predicts the *x*-direction actuated curvatures to be 4.72 m^{-1} and 3.41 m^{-1} for ±2 MV/m, respectively. For

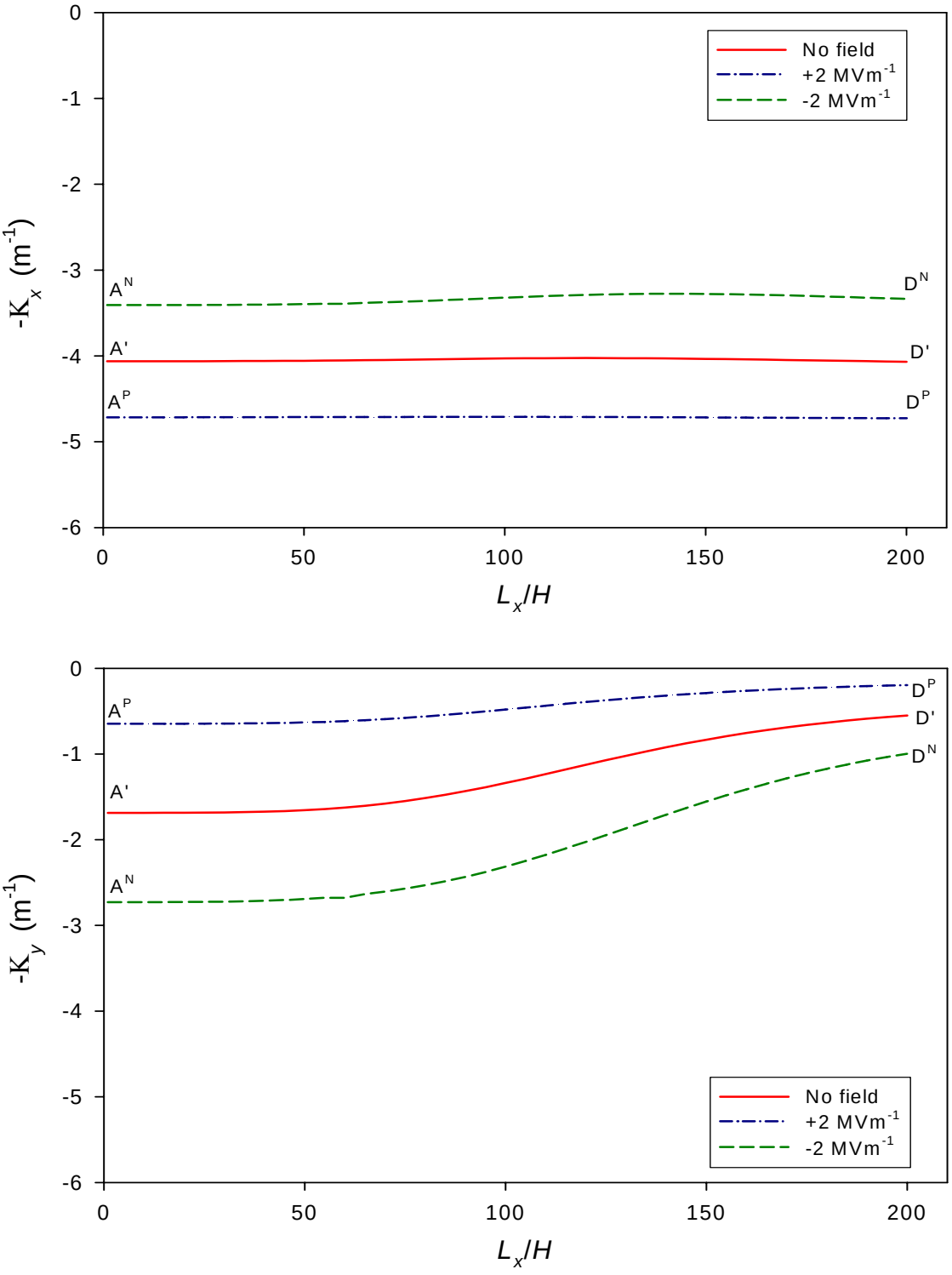

Figure 4.11: Influence of Actuation on the Change of Curvatures of Beam-Like LIPCA-C1 (L_y/L_x = 0.33, ΔT = -142 °C)

the beam theories, employing Equation (B.42) or (B.68) in Appendix B, $K_x = 4.91\ m^{-1}$ and $3.70\ m^{-1}$ for ±2 MV/m, respectively. The curvatures calculated from the geometrically linear Rayleigh-Ritz approach and geometrically nonlinear and linear beam theories are uniform over the range of sidelength-to-thickness ratio considered.

The actuation-induced average curvature changes as a function of electric field strength can be considered in another way. For example, LIPCA-C1 actuators with two different actuator sidelength-to-thickness ratios and the three aspect ratios are investigated in Figure 4.12, L_x/H = 200 in Figure 4.12 (a) and L_x/H = 100 in Figure 4.12 (b). Referring to Figure 4.12 (a) and the average curvature change from branch $A'D'$ to branches A^PD^P and A^ND^N of Figures 4.11, 4.9, and 4.10, it is again observed that for L_y/L_x = 0.7 and 1 the average curvature changes in the *y*-direction due to actuation are small due to suppression from nonlinear effects. For L_y/L_x = 0.33, due to the weaker suppression, the change in the *y*-direction actuated curvature is relatively large and its magnitude is around 60% as large as the magnitude of the associated change in the *x*-direction. The changes in the *x*-direction curvature for L_y/L_x = 0.33, 0.7, and 1 due to actuation are, to all intents and purposes, equal each other. Though the relationships between the changes in actuation-induced curvatures and electric field strength are slightly nonlinear; they can be accurately assumed to be linear in the region of -1 MV/m < E_3 < +1 MV/m. The opposite sign of changes in actuation-induced curvature in the *x*- and *y*- direction can be obviously noticed in the figure.

For the case of sidelength-to-thickness ratio L_x/H = 100, illustrated in Figure 4.12 (b), the changes in the *y*-direction curvatures due to actuation are close in value to or greater than the changes in the *x*-direction curvatures. Like the case of L_x/H = 200, the greater the aspect ratio, the less the change in the *y*-direction curvature. The changes in the *x*-direction actuation-induced curvature are again almost equal to each other over the range of the applied electric field considered; some trivial difference in the changes can be observed as the magnitude of the applied electric field strength is larger than 0.7 MV/m. In

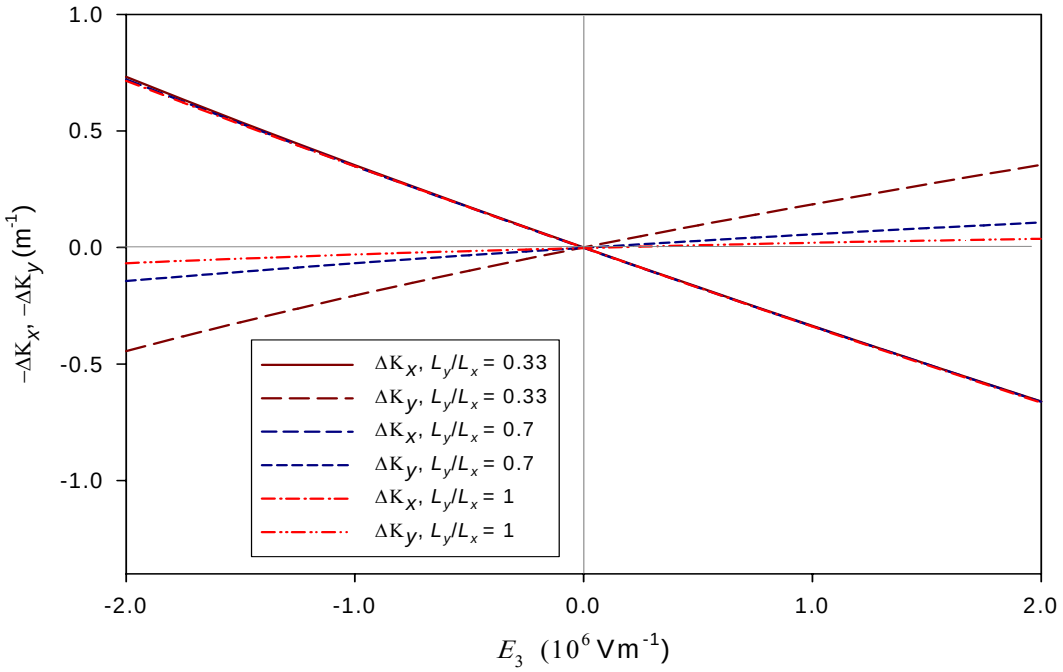

(a) L_x/H = 200

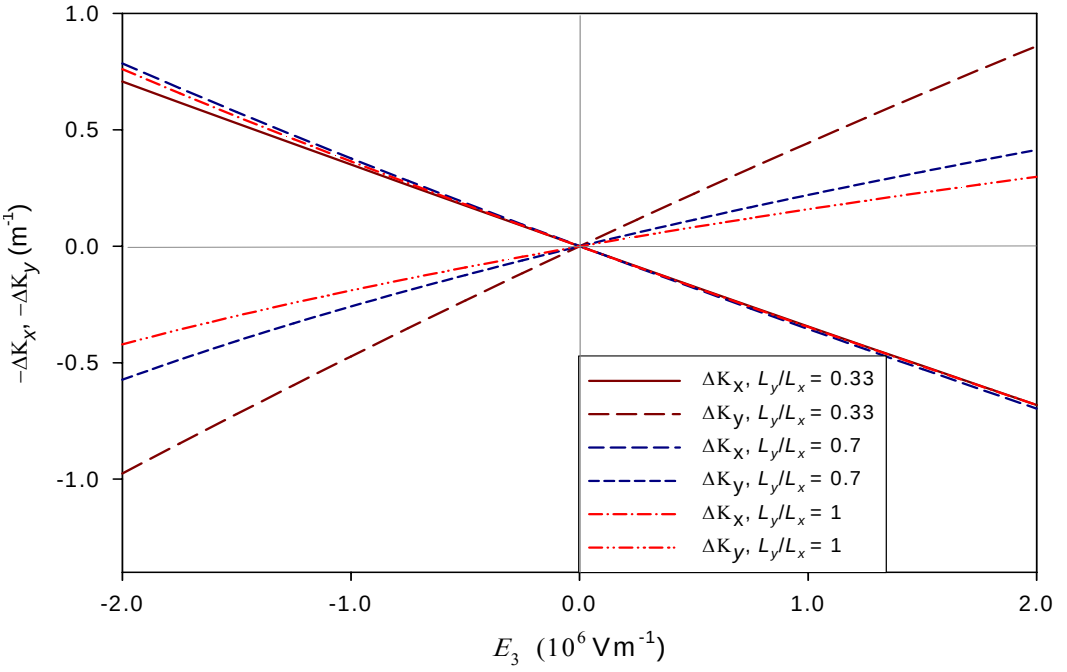

(b) L_x/H = 100

Figure 4.12: Influence of Actuation on the Change of Curvatures of LIPCA-C1 (ΔT = -142 °C)

actuality, the difference is caused by the slight enhancement in actuation responses, as discussed above. The changes in the *x*-direction curvature due to actuation for aspect ratio 0.33 is approximately in a linear relation over the entire range of applied electric field considered. Nevertheless, for aspect ratios of 0.7 and 1, the linear relation can be assumed only in the range of -0.7 MV/m < E_3 < +0.7 MV/m. Beyond this range, the geometrical nonlinearities occur and, as a result, the enhancement of the changes in the *x*-direction curvatures emerge.

4.3.2 Stress Characteristics of LIPCA-C1 subjected to Applied Electric Field

To complete the discussion of free actuation responses of a LIPCA-C1 actuator, stress distributions of a LIPCA-C1 actuator when subjected to an electric field will be presented in this section. Analogous to Figures 3.24 and 3.25 for THUNDER, the through-thickness distribution of the thermally-induced and piezoelectrically-induced inplane normal stresses at room temperature in a rectangular actuator with L_y/L_x = 0.7 and L_x/H = 200 are shown in Figures 4.13 and 4.14. The former and the latter figures illustrate the stress distributions near the center $\left(x \cong 0, y \cong 0\right)$ and near the midpoint of the shorter edge $\left(x \cong 0, y \cong L_y/2\right)$. The distributions of piezoelectrically-induced stresses are evaluated under the condition of ±2 MV/m electric fields through the thickness of the piezoceramic material. As can be seen, the stress components σ_x in the upper one-half of the piezoceramic layer and in the central portion of the carbon-epoxy layer changes sign when the electric field strength changes from +2 MV/m to -2 MV/m. However, the sign of the stress component σ_x in the bottom glass-epoxy layer does not change, nor do the signs of the stress components σ_y in any of the layers, except for a small portion of the piezoceramic layer. The sign changes in the stresses in the piezocermaic layer could be detrimental to the fatigue life of the actuator. Note that at a particular thickness location, the change in stress component σ_x in the carbon-epoxy layer is generally larger than the change in stress component σ_y in the same layer. This is because the layer is very stiff in the *x*-direction, so

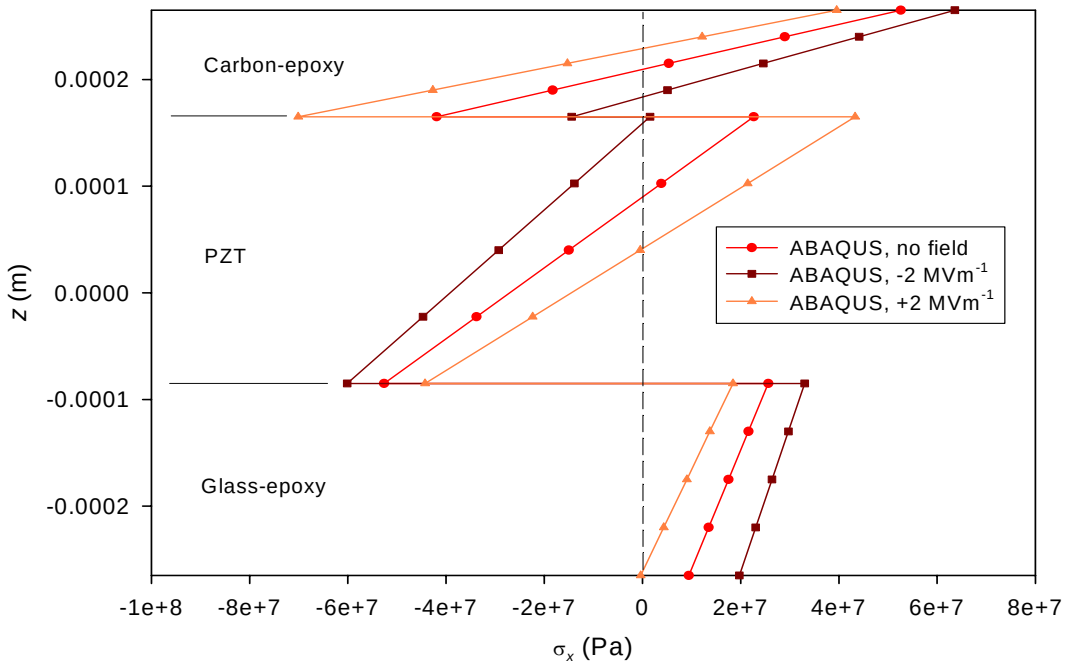

(a) Distribution of Normal Stress in the *x*-direction near Center, $x \cong 0$, $y \cong 0$

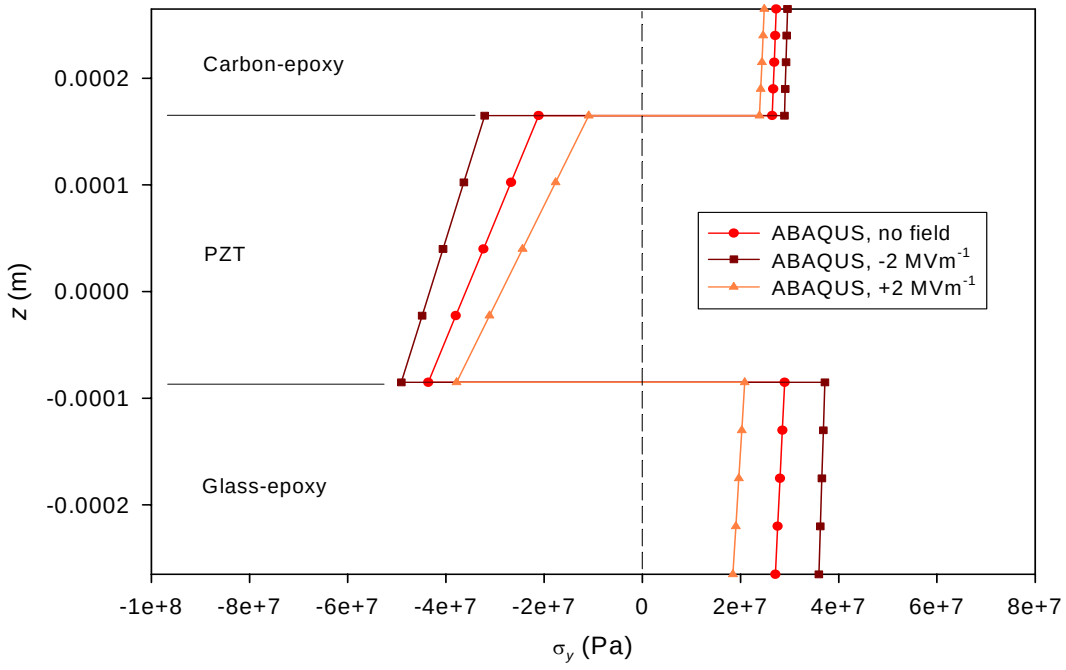

(b) Distribution of Normal Stress in the *y*-direction near Center, $x \cong 0$, $y \cong 0$

Figure 4.13: Stress distributions in rectangular LIPCA-C1 near center when subjected to applied electric fields, $L_y/L_x = 0.7$, $L_x/H = 200$

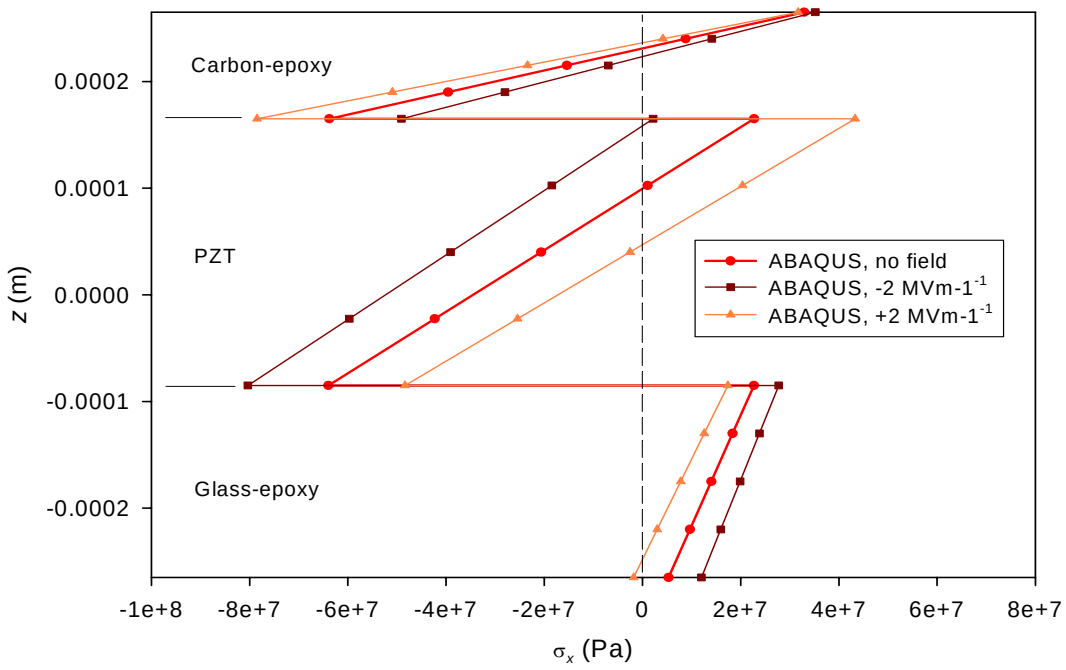

(a) Distribution of Normal Stress in the x-direction near Edge, $x \cong 0$, $y \cong L_y/2$

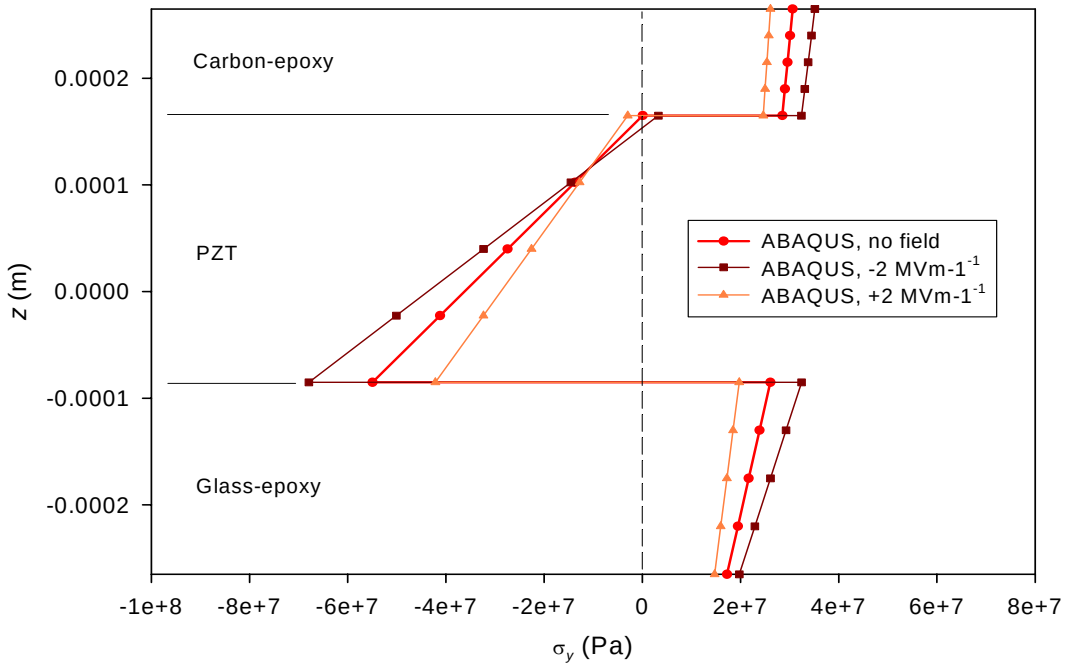

(b) Distribution of Normal Stress in the y-direction near Edge, $x \cong 0$, $y \cong L_y/2$

Figure 4.14: Stress distributions in rectangular LIPCA-C1 near midpoint of longer edge when subjected to applied electric fields, $L_y/L_x = 0.7$, $L_x/H = 200$

the changes in σ_x in the layer are significant due to actuation. On the other hand, the layer is very soft in the *y*-direction and thus the changes in σ_y in the layer are much less affected. This is due to highly orthotropy of material properties of the carbon-epoxy layer.

4.4 Numerical Results for Blocking Forces

4.4.1 Blocking Forces of LIPCA-C1 as a Function of Electric Field Strength

Consider LIPCA-C1 actuators with an aspect ratio $L_y/L_x = 0.7$ and sidelength-to-thickness ratios of 100 and 200 with shapes given by Figure 4.1 or 4.9. Figure 4.15 shows relations between the blocking forces and applied electric field E_3. The blocking forces of the LIPCA-C1 actuators with pinned-roller and pinned-pinned supports are illustrated in the figure. The relations are similar in character to those for THUNDER actuators in Figure 3.26. However, the sign of force P_{bl} for the pinned-roller case is opposite that of the THUNDER actuators. It is seen from Figure 4.15 that all blocking forces predicted from the nonlinear theory vary almost linearly with electric field strength over the entire range of electric field strength considered. For pinned-roller case, force P_{bl} for the actuator with $L_x/H = 100$ is approximately equal to that with $L_x/H = 200$. This corroborates the hypothesis of proportionality between the change in the *x*-direction curvature due to actuation and blocking force P_{bl} for the pinned-roller case because the changes in the *x*-direction curvature for $L_x/H = 100$ and 200 in Figures 4.9 and 4.12 are also almost equal to each other and relate linearly to the applied electric field strength. Again, the geometrically linear theory predictions are independent on the sidelength-to-thickness ratios. Also, they give a good correlation with blocking force P_{bl} predicted by the geometrically nonlinear theory. This is because the material properties, staking sequence, and cooling temperature collectively influence the actuator to more or less behave in the geometrically linear fashion in the *x*-direction. For the pinned-pinned case, as compared to the pinned-roller case, the opposite sign of blocking force P_{bl} is obtained at a given electric field strength. The magnitude of

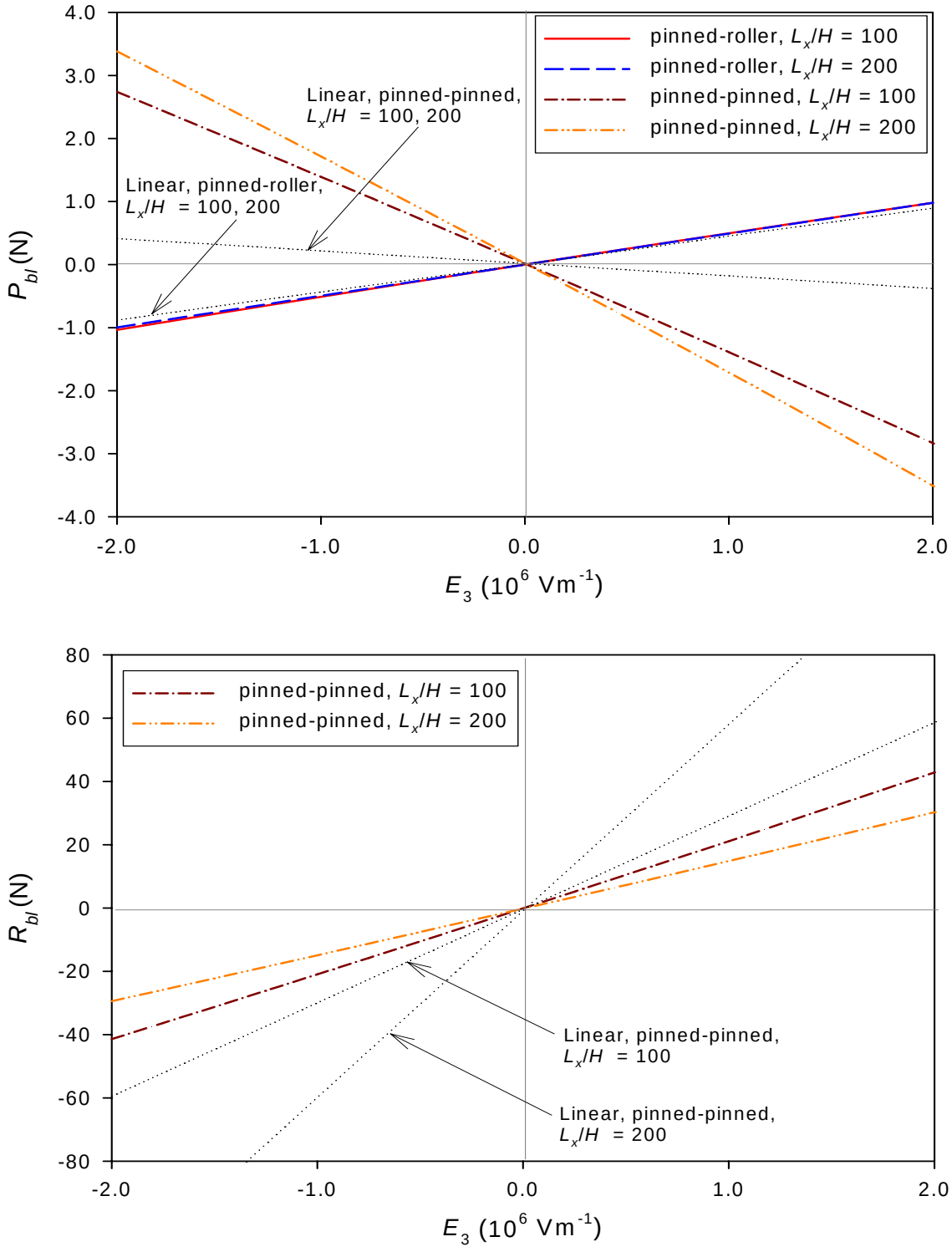

Figure 4.15: Blocking Force vs. Electric Field Relations of Rectangular LIPCA-C1 (L_y/L_x = 0.7)

force P_{bl} is larger than that for the pinned-roller case by a factor of more than two because of the presence of force R_{bl} in the horizontal direction. The magnitude of force P_{bl} for L_x/H = 100 is smaller than for L_x/H = 200, but the counterpart force R_{bl} at L_x/H = 100 is moderately larger than that for L_x/H = 200. Moreover, the magnitude of force P_{bl} is around 5-15 times smaller than the counterpart R_{bl}. The linear theory predictions of force P_{bl} are again independent of sidelength-to-thickness ratio. However, the linear theory predictions of force R_{bl} are dependent on sidelength-to-thickness ratio and the force R_{bl} and sidelength-to-thickness ratio are linearly proportional. Unlike the pinned-roller case, the geometrically linear predictions of both forces P_{bl} and R_{bl} for the pinned-pinned case give totally different values from the geometrically nonlinear theory predictions

The relations between blocking forces and electric field strength for square LIPCA-C1 actuators with L_x/H =100 and 200 are illustrated in Figure 4.16. For the pinned-roller case, it can be seen that force P_{bl} predicted by the geometrically nonlinear theory is increased slightly in magnitude due to the change in the aspect ratio from 0.7 to 1. Force P_{bl} at L_x/H = 100 and 200 is again nearly equal each other and relate to applied electric field in an approximately linear fashion. The predictions from the geometrically linear theory of force P_{bl}, which is independent of sidelength-to-thickness ratio, are similar to those from the nonlinear theory. For the pinned-pinned case, as mentioned, force P_{bl} has an opposite sign to force P_{bl} for the pinned-roller case, like the behavior of LIPCA-C1 actuators with an aspect ratio of 0.7 previously discussed. Nonetheless, magnitude of force P_{bl} is larger with this larger aspect ratio. Contrasting to the pinned-roller case, poor correlations of blocking forces P_{bl} and R_{bl} between the geometrically nonlinear and linear theories are clearly observed. This certainly indicates a stronger degree of nonlinearity in blocking forces of pinned-pinned supported LIPCA-C1 actuators compared to those of pinned-roller supported LIPCA-C1. In general, except for magnitudes of calculated blocking forces, Figures 4.15 and 4.16 share similar characteristics.

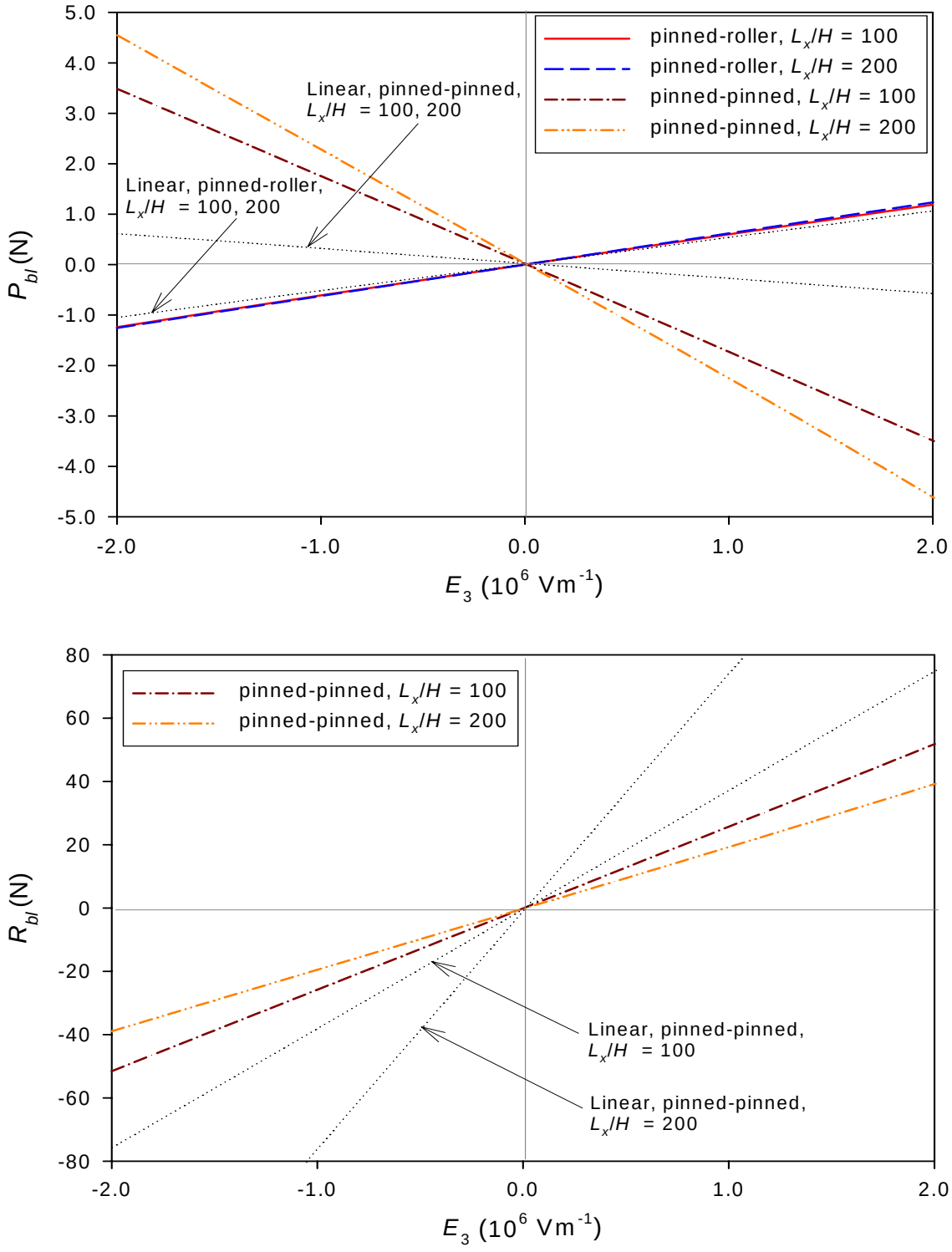

Figure 4.16: Blocking Force vs. Electric Field Relations of Square LIPCA-C1

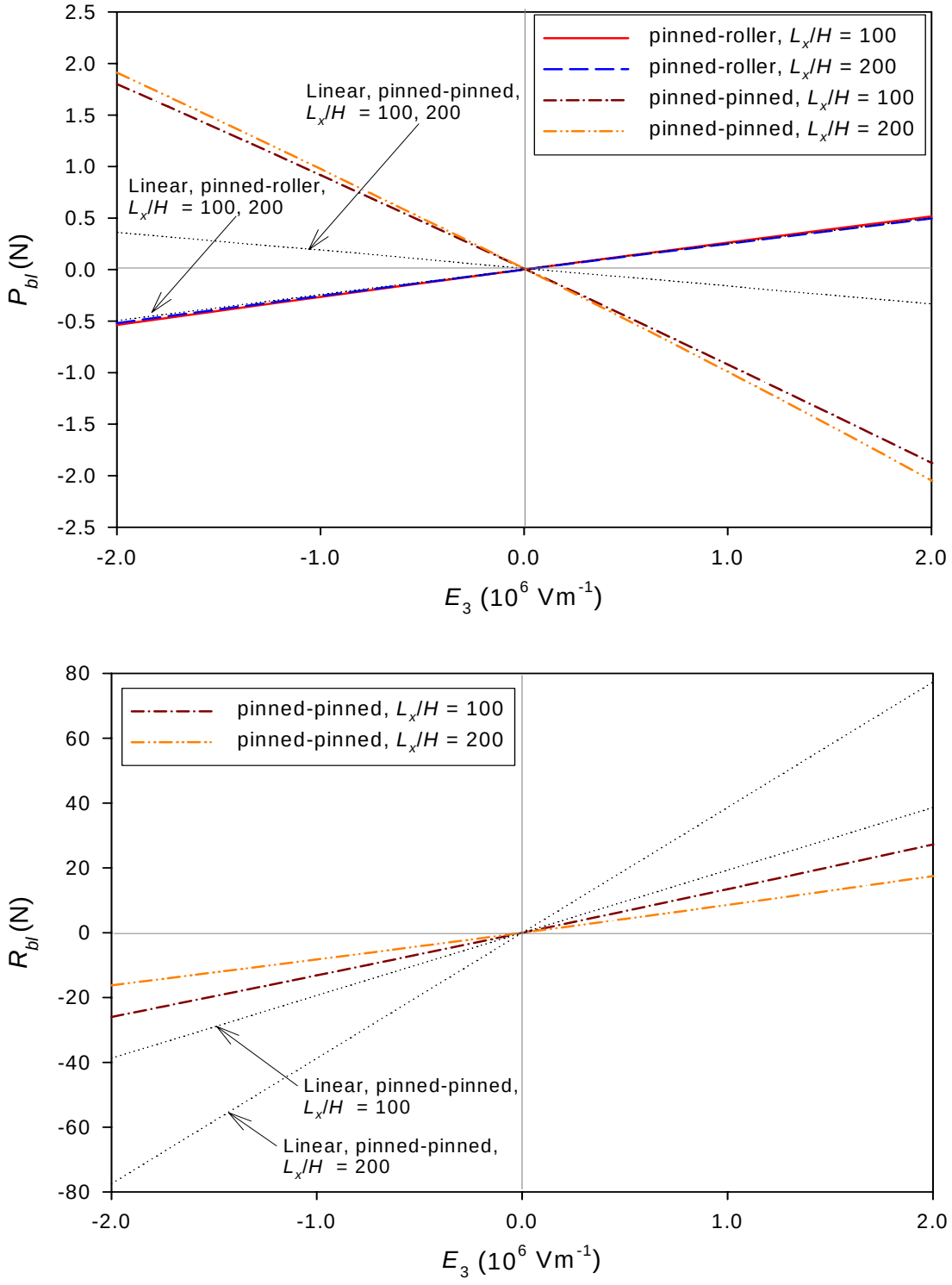

Figure 4.17: Blocking Force vs. Electric Field Relations of Beam-Like LIPCA-C1 (L_y/L_x = 0.33)

Lastly, beam-like LIPCA-C1 actuators with an aspect ratio of 0.33 and sidelength-to-thickness ratios of 100 and 200 are considered in Figure 4.17. As seen in the figure, the overall behaviors of the relations between blocking forces and electric field strength are very similar to those in Figures 4.15 and 4.16. However, it should be noted that the magnitudes of all blocking forces are smaller than the ones for the larger aspect ratio of 0.7 or 1. This happens because the amount of electrical energy that is applied to the actuator also depends on the planform area of the actuator or, in the other words, the aspect ratio of the actuator when the sidelength-to-thickness ratio is kept constant. Thus, if the aspect ratio is smaller, the amount of electrical energy is less and the output energy, which is in terms of actuation response or load-carrying capability of the actuator, is also less.

4.4.2 Blocking Forces of LIPCA-C1 as a Function of Sidelength-to-Thickness Ratio: Pinned-Roller Case

To complement the investigation of the performance characteristics of LIPCA-C1 actuators, in addition to the relations of free actuation responses vs. sidelength-to-thickness ratio presented in Section 4.3.1, relations of the blocking force vs. sidelength-to-thickness ratio will be presented next.

Figure 4.18 illustrates the relation between blocking force P_{bl} and sidelength-to-thickness ratio for pinned-roller supported LIPCA-C1 actuators with an aspect ratio of 0.7 and subjected to ±2 MV/m. Analogous to the figures illustrated in Section 3.4.2, for THUNDER actuators, from this point on until the end of this chapter, the axis of ordinate is normalized by a blocking force of a LIPCA-C1 actuator with L_x/H value approaching zero, the predictions of the geometrically linear theory. Therefore, at very small values of sidelength-to-thickness ratio, $0 < L_x/H < 25$ for this case, the normalized values of P_{bl} for ±2 MV/m are approximately equal to one. When the value of L_x/H increases, the normalized values of P_{bl} separate from each other, but they have similar trends. In the region of $25 < Lx/H < 200$, the normalized blocking force P_{bl} is always larger than one but less than

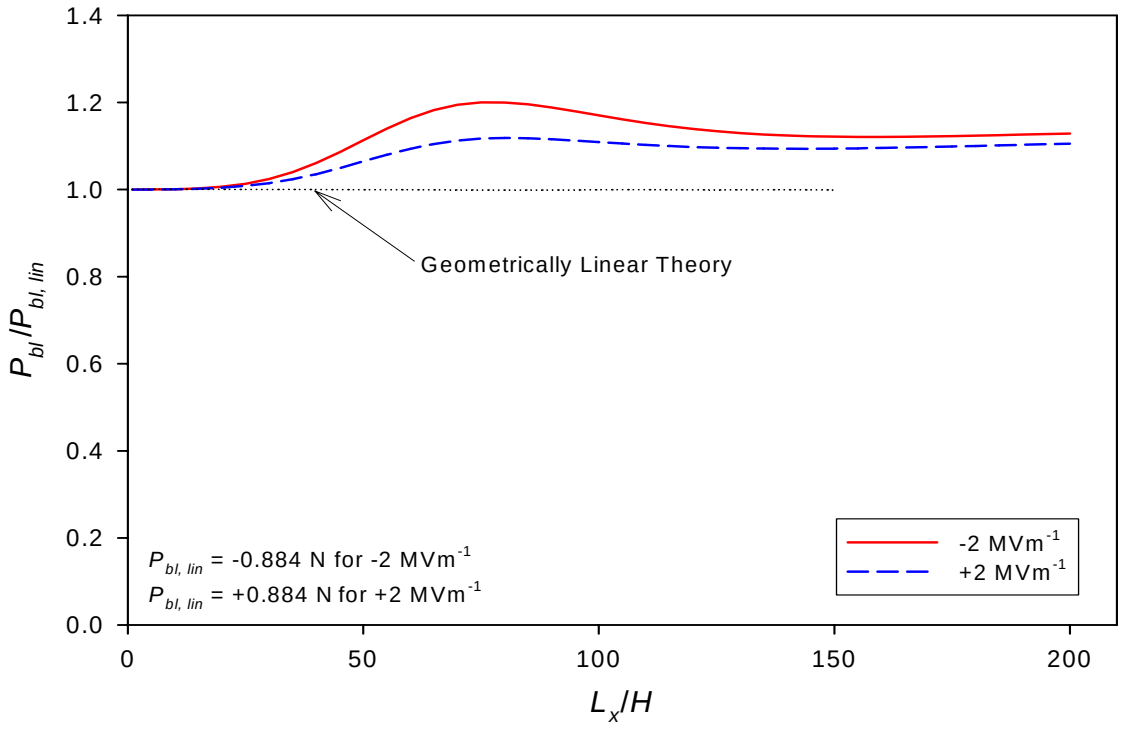

Figure 4.18: Blocking Force vs. Sidelength-to-Thickness Ratio Relations of Pinned-Roller Supported Rectangular LIPCA-C1 (L_y/L_x = 0.7)

1.2. This indicates that even though the enhancement of blocking force P_{bl} can be observed, the degree of enhancement is not much. The enhancement is more noticeable for -2 MV/m than for +2 MV/m and the largest enhancement occurs around L_x/H = 75. This actually is in agreement with the behavior of the free actuation response illustrated in Figure 4.9 and, therefore, confirms the proportionality between the change in curvature in the *x*-direction due to an application of electric field and the blocking force for the pinned-roller support case. Unlike the THUNDER actuators in Figure 3.29, at all values of L_x/H there is an enhancement for blocking force effects. On the other hand, THUNDER and LIPCA-C1 actuators exhibit similar characteristic, since wherever the separation between the +2 MV/m relation and -2 MV/m relation is greatest, nonlinear effects are strongest and, as a result, the effects extremize the enhancement or suppression of blocking force P_{bl} for the pinned-roller

case. The blocking forces predicted by the geometrically linear theory, $P_{bl,lin}$, are also illustrated in the figure. The prediction exhibits constant blocking forces for ±2 MV/m (±0.884 N, respectively) regardless of sidelength-to-thickness ratio values and therefore are drawn as coincident horizontal lines with values equal to one. Finally, it is essential to note that according to Figure 4.18, designing a pinned-roller supported LIPCA-C1 actuator in the region of $25 < L_x/H < 200$ to carry a transverse load has a slight advantage from geometrically nonlinear effects. However, when compared to that of a pinned-roller supported THUNDER actuator presented in Figure 3.29, the desirable load-carrying range of sidelength-to-thickness ratio of a pinned-roller supported LIPCA-C1 actuator is wider.

Analogous to Figure 4.18, Figure 4.19 illustrates the relation of the blocking force and sidelength-to-thickness ratio for pinned-roller supported LIPCA-C1 actuators with an aspect ratio of 1 subjected to ±2 MV/m. Generally, the relations in the figures are very similar to the case of aspect ratio 0.7 just discussed. A linear behavior of the relations takes place when L_x/H is small and the corresponding values of normalized blocking forces are equal to one. This linear zone is shorter than that of the LIPCA-C1 actuators with an aspect ratio of 0.7 because it covers the range $0 < Lx/H < 20$. When L_x/H > 20, the normalized blocking forces increase with increasing L_x/H and reach the largest value around L_x/H = 65. Again, the separation of the normalized values of P_{bl} for ±2 MV/m is highest (difference of 0.1) at the largest values of P_{bl}. Beyond L_x/H = 65, the values of the normalized P_{bl} decrease somewhat. Specifically, in the region of $20 < L_x/H < 200$, the normalized blocking force P_{bl} is always larger than one but less than 1.3. The blocking force predicted by the linear theory, $P_{bl,lin}$ is independent of the actuator sidelength-to-thickness ratio and is represented by straight horizontal lines with the unit value. The force $P_{bl,lin}$ of the square LIPCA-C1 actuator is equal to ±1.051 N for ±2 MV/m, respectively. Compared with the pinned-roller supported LIPCA-C1 actuators with L_y/L_x = 0.7, the pinned-roller supported square ones

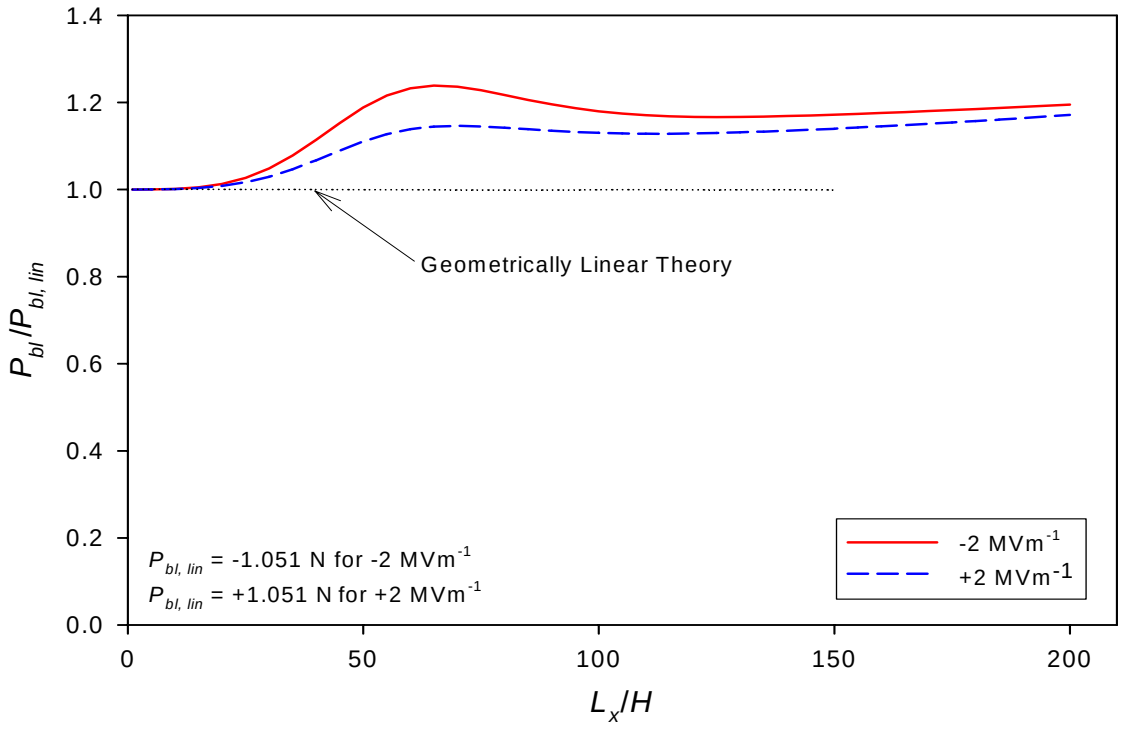

Figure 4.19: Blocking Force vs. Sidelength-to-Thickness Ratio Relations of Pinned-Roller Supported Square LIPCA-C1

have 18.9% higher blocking force based on the linear theory, and they are 42.9% larger in terms of size.

Considering pinned-roller supported LIPCA-C1 actuators subjected to ±2 MV/m field strength with an aspect ratio of 0.33, shown in Figure 4.20 are relations between the normalized blocking forces and sidelength-to-thickness ratio. When $L_x/H < 60$, the relations can be approximated by the geometrically linear theory very well. This linear region is the largest of the three aspect ratios considered because of the weak geometric nonlinearity associated with the beam-like configuration. As L_x/H increases beyond 60, the normalized blocking forces increase slightly and reach the highest values around $L_x/H = 140$. Similar to those of aspect ratios 0.7 and 1, the blocking force separation for the positive and negative fields are maximal at the highest values of blocking forces. The blocking force enhancement

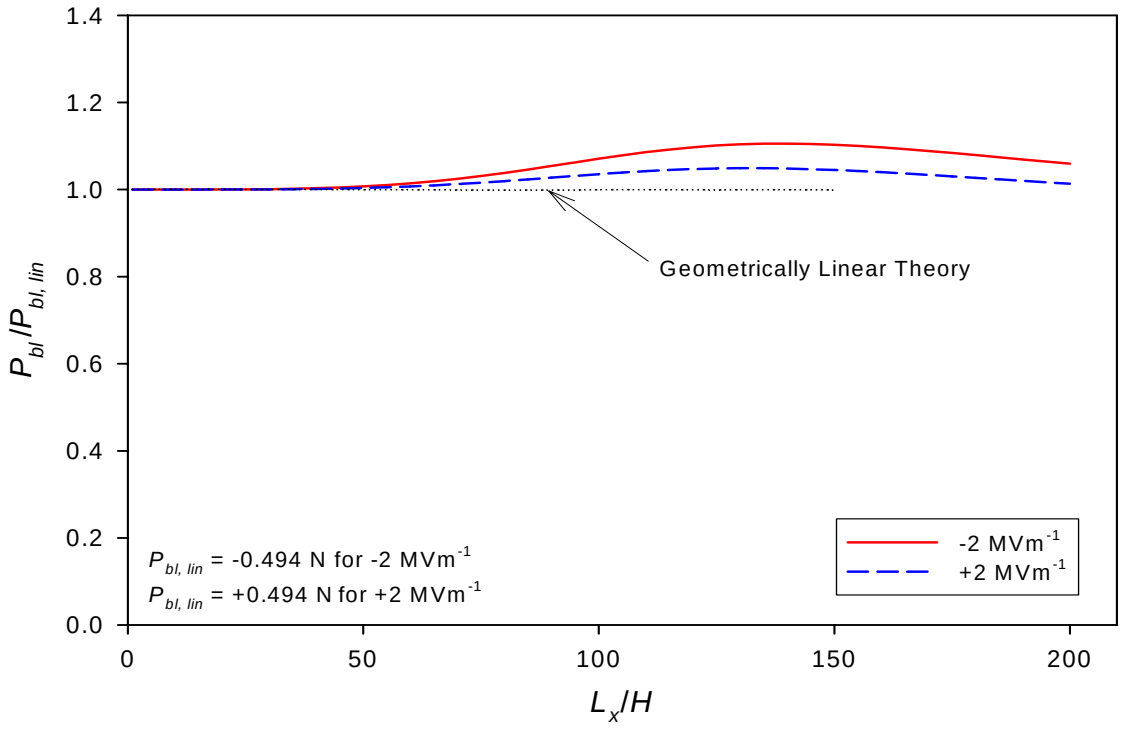

Figure 4.20: Blocking Force vs. Sidelength-to-Thickness Ratio Relations of Pinned-Roller Supported Beam-Like LIPCA-C1 (L_y/L_x = 0.33)

in the region of $60 < L_x/H < 200$ is small in this case, since the normalized values of P_{bl} are less than 1.1 over the sidelength-to-thickness ratio considered. Stated differently, the enhancement is less than 10% compared to the linear predictions. The linear theory predicts $P_{bl,lin}$ to be ±0.494 N for ±2 MV/m field strength, respectively. The values of $P_{bl,lin}$ in this case are lower than the linear value for an aspect ratio of 0.7 by 44.1%, while the active area of the beam-like actuator is less than that of the rectangular one by 52.9%. Additionally, it can be noted that because of the comparatively small aspect ratio, it is interesting to compare the blocking forces in Figure 4.20 with the ones computed from the nonlinear and linear beam theories developed in Appendix B. By utilizing Equation (B.41) or (B.67), and setting the relative transverse deflection, w^0, due to ±2 MV/m field strength to be zero at $x = \pm L_x/2$, the blocking force predictions based on the beam theories can be solved for and found to be

±0.462 N for ±2 MV/m, respectively. These blocking forces are independent of the sidelength-to-thickness ratio, like those predicted from the geometrically linear theory illustrated, as the dotted line in Figure 4.20.

4.4.3 Blocking Forces of LIPCA-C1 as a Function of Sidelength-to-Thickness Ratio: Pinned-Pinned Case

In this section, blocking forces of a LIPCA-C1 actuator with pinned-pinned supports as a function of sidelength-to-thickness ratio are taken into consideration. Illustrated in Figure 4.21 are relations for blocking forces P_{bl} and R_{bl} for ±2 MV/m for a LIPCA-C1 actuator with an aspect ratio of 0.7. The influence of restraining the motion in the x-direction at the support positions is obviously very strong because the normalized P_{bl} relations shown in Figure 4.21 are significantly different from those shown in Figure 4.18. Also, it should be noted that the sign of force P_{bl} (or the direction of force P_{bl}) at a particular sidelength-to-thickness ratio and applied electric field strength for the pinned-pinned case in Figure 4.21 is opposite that for the same sidelength-to-thickness ratio and applied electric field strength for the pinned-roller case in Figure 4.18. This, again, is due to the associated force R_{bl} generated by restraining the x-direction motion at the supports. It should also be noted that unlike the counterpart THUNDER actuator of Figure 3.32, the blocking force P_{bl} is enhanced for the range of sidelength-to-thickness ratios studied. For the LIPCA-C1 actuators, when sidelength-to-thickness ratio is less than 10, both the normalized values of P_{bl} and R_{bl} coincide with the linear predictions. As the sidelength-to-thickness ratio increases, the normalized values of P_{bl} deviate from the linear predictions and increase moderately in magnitude, while values of R_{bl} are still in agreement with the linear predictions and increase considerably in magnitude. Like the similar phenomenon that occurs with THUNDER actuators discussed in Section 3.4.3, the deviation of P_{bl} originates at a lower value of L_x/H compared to the pinned-roller case in Figure 4.18 because the magnitude of the associated R_{bl} is relatively large and this changes the structural stiffness of

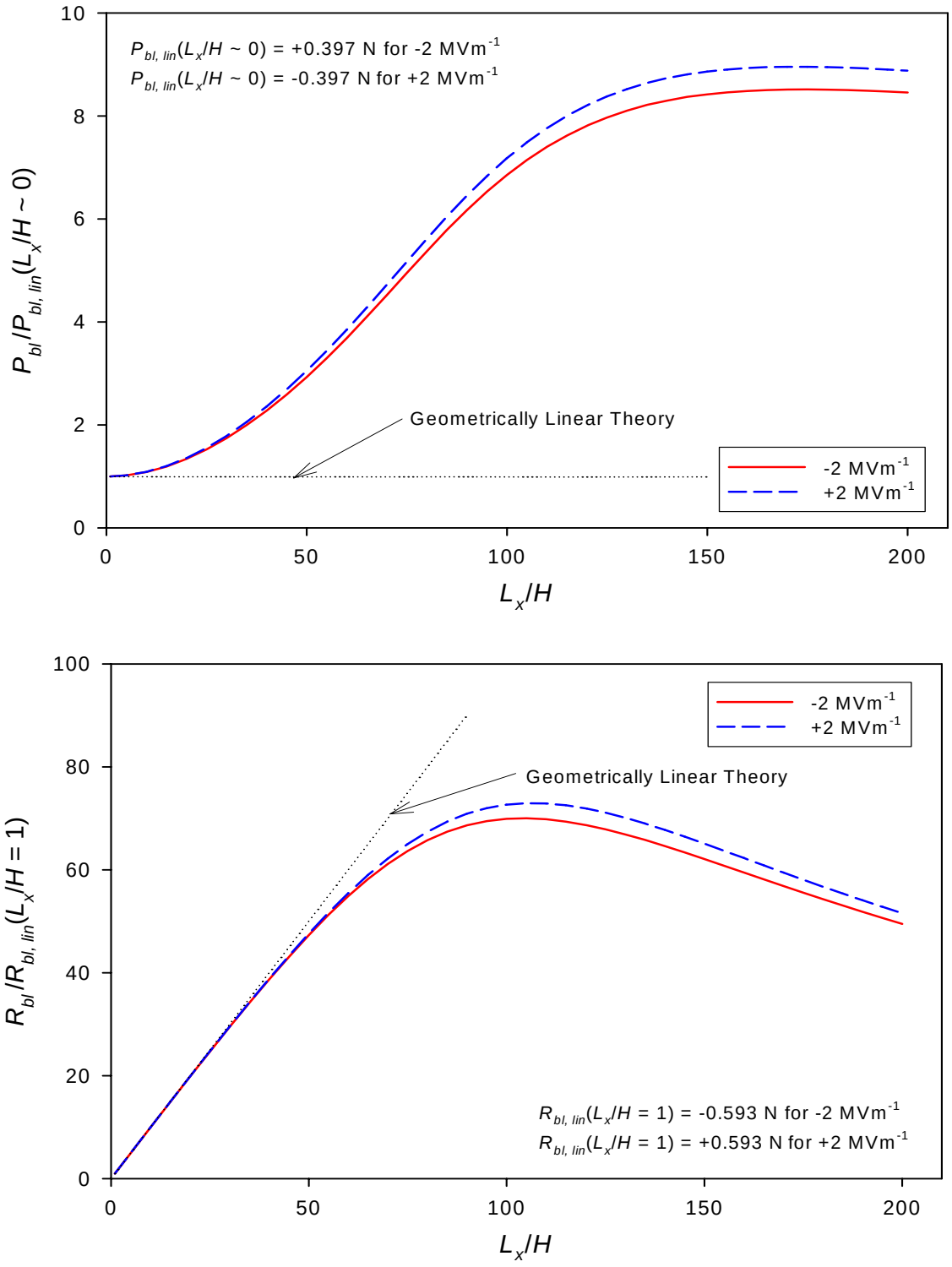

Figure 4.21: Blocking Force vs. Sidelength-to-Thickness Ratio Relations of Pinned-Pinned Supported Rectangular LIPCA-C1 (L_y/L_x = 0.7)

the actuator. The normalized values of P_{bl} reach their peak values around L_x/H = 170 and then decrease very little as L_x/H increases further, whereas normalized values of R_{bl} reach their maximum value around L_x/H = 105 and gradually decrease when the value of L_x/H is beyond 105. According to Figures 4.21 and 4.18, the magnitude of force P_{bl} of the pinned-pinned supported actuators is higher than that of the pinned-roller supported actuators with the same sidelength-to-thickness ratio when the sidelength-to-thickness ratio is approximately larger than 40. Therefore, it should be stated that in order to design a LIPCA-C1 actuator to carry a transverse load, the type of the actuator support must be properly selected such that the actuator can perform the task. In addition, the predictions of $P_{bl,lin}$ from the linear theory again reveal values independent of sidelength-to-thickness ratio, i.e., ∓ 0.397 N for ±2 MV/m, respectively. However, the values of $R_{bl,lin}$ for ±2 MV/m electric field strengths vary with sidelength-to-thickness ratio in a linear relation with slopes of ±0.593 N, respectively.

To examine the influences of the aspect ratio on blocking forces of a LIPCA-C1 actuator with pinned-pinned supports, the relations between blocking forces and sidelength-to-thickness ratio for LIPCA-C1 actuators with different aspect ratios than 0.7 are illustrated in Figures 4.22 and 4.23. The former figure is for a larger aspect ratio of one and the latter one is for a smaller aspect ratio of 0.33. Considering Figure 4.22, the overall relations are very similar to the ones in the previous figure for aspect ratio 0.7. For all sidelength-to-thickness ratios, the values of blocking forces P_{bl} and R_{bl} of the square actuators are higher than those of the actuators with an aspect ratio of 0.7 because of the square actuators having bigger active areas than the rectangular actuators with the same sidelength-to-thickness ratio. Additionally, according to Figures 4.22 and 4.19, the magnitude of force P_{bl} of the pinned-pinned supported actuators is higher than that of the pinned-roller supported actuators with the same sidelength-to-thickness ratio when the sidelength-to-thickness ratio is approximately larger than 40. This value of sidelength-to-thickness ratio is the same as

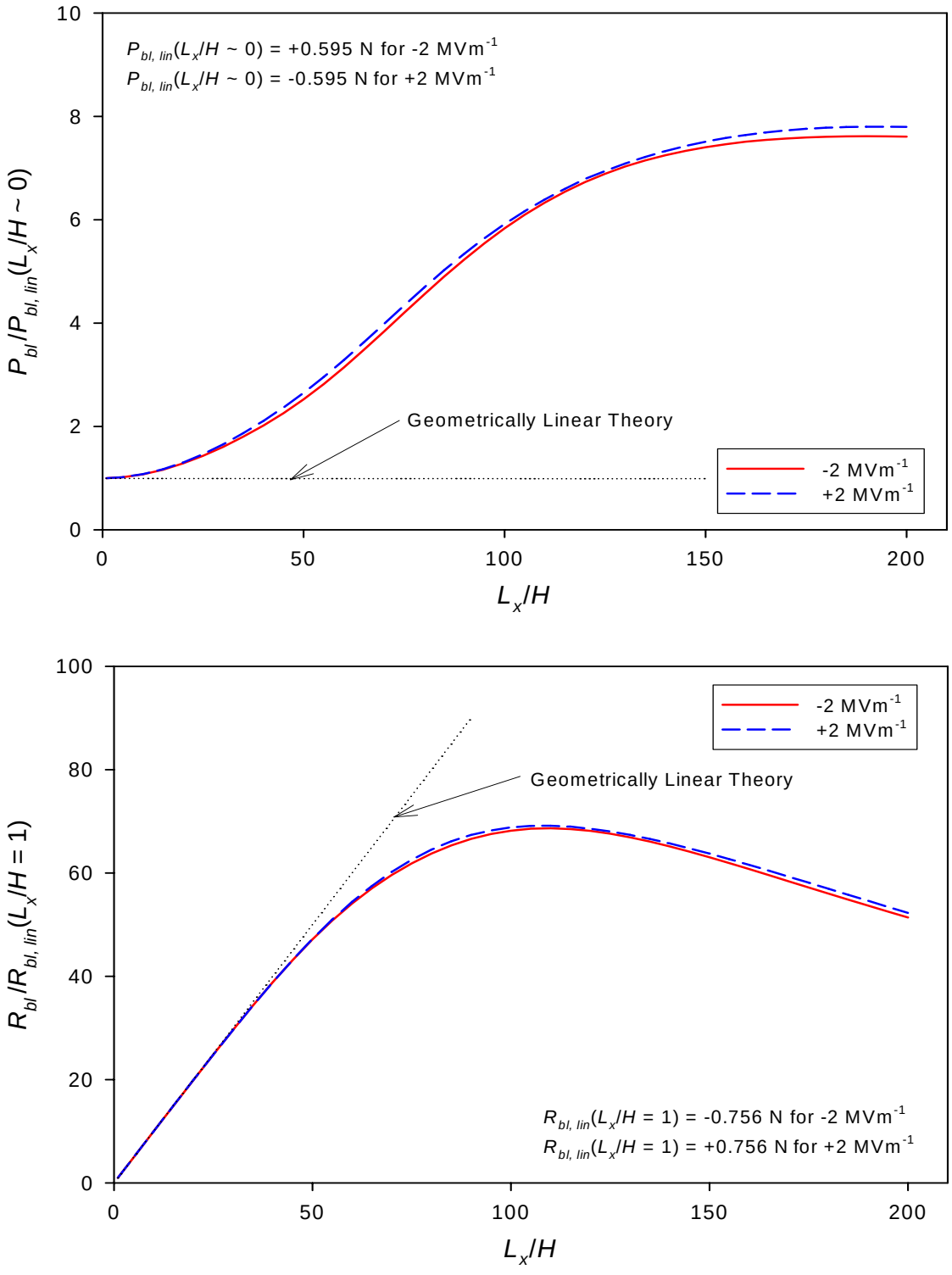

Figure 4.22: Blocking Force vs. Sidelength-to-Thickness Ratio Relations of Pinned-Pinned Supported Square LIPCA-C1 ($L_y/L_x = 1$)

that for the actuators with an aspect ratio of 0.7 previously discussed. As can also be seen in Figure 4.22, the normalized blocking force plots for ±2 MV/m are almost coincident. This means that the relations between blocking forces P_{bl} and R_{bl} and electric field strength are almost linear, as can be substantiated by Figure 4.16. Note that the higher degree of linearity in the blocking force vs. applied electric field relations in this case can be observed when compared with the case of an aspect ratio of 0.7 in Figure 4.15, from which slight nonlinearities in the relations can be noticed at high electric field strength. As stated before in Section 3.4.2, which discussing THUNDER actuators, the weaker nonlinearities in this case can also be inferred by the smaller separation between the plots for +2 MV/m and for -2 MV/m in Figure 4.22 than that in Figure 4.21. The geometrically linear theory, again, predicts $P_{bl,lin}$ to be constant over the considered sidelength-to-thickness ratio, i.e., ∓ 0.595 N for ±2 MV/m, respectively. The values of $P_{bl,lin}$ for this case are higher than the values $P_{bl,lin}$ of the pinned-pinned supported LIPCA-C1 actuator with an aspect ratio 0.7 by 49.9%, while the actuators in this case are larger than those of the previous case by 42.9%. A slope of the relation between normalized values of R_{bl} and sidelength-to-thickness ratio is 0.756, which is 27.5% increase from the case of aspect ratio 0.7.

Last of all three aspect ratios considered, the relations between blocking forces and sidelength-to-thickness ratio for pinned-pinned supported beam-like LIPCA-C1 actuators with an aspect ratio of 0.33 are illustrated in Figure 4.23. The figure is similar to the relations in Figures 4.21 and 4.22. For small sidelength-to-thickness ratios (less than 10) the normalized values of P_{bl} are in good agreement with the linear predictions. Beyond L_x/H = 10, the normalized values of P_{bl} deviate from the horizontal line representing the linear blocking force $P_{bl,lin}$. Nonetheless, for L_x/H up to 30 the normalized values of R_{bl} agree well with the normalized values of $R_{bl,lin}$ predicted by the linear theory. The values of blocking forces P_{bl} and R_{bl} of the beam-like actuators are always lower than those of the actuators with an aspect ratio of 0.7 due to the smaller piezoelectrically-active area of the beam-like

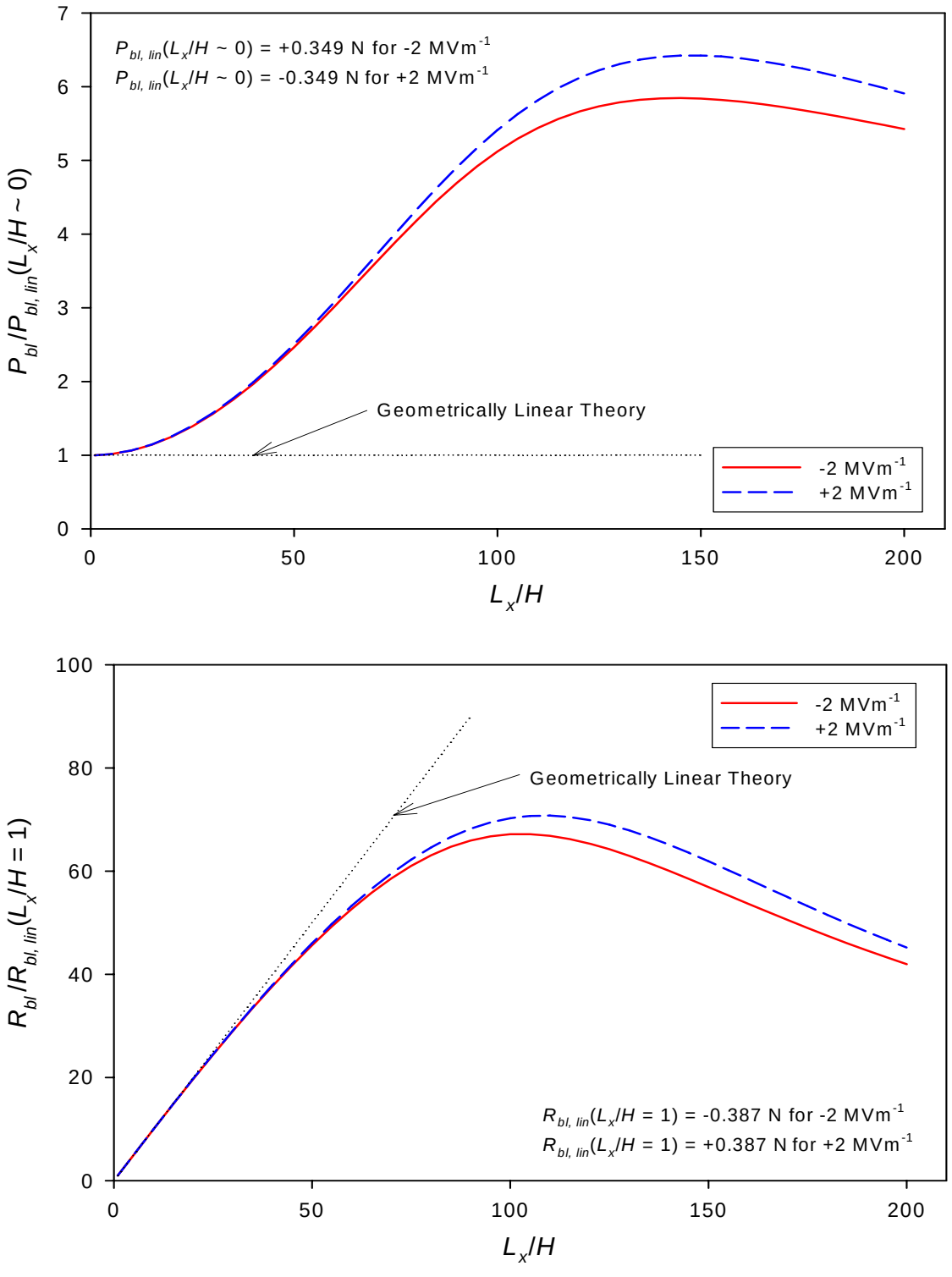

Figure 4.23: Blocking Force vs. Sidelength-to-Thickness Ratio Relations of Pinned-Pinned Supported Beam-Like LIPCA-C1 (L_y/L_x = 0.33)

actuators. Similar to the previous two aspect ratios, for the aspect ratio of 0.33 the magnitude of blocking force P_{bl} of the pinned-pinned supported LIPCA-C1 actuators shown in Figure 4.23 is larger than that of the pinned-roller supported LIPCA-C1 actuators with the same sidelength-to-thickness ratio shown in Figure 4.20 when $L_x/H > 30$. The apparent separation between the normalized blocking force plots for +2 MV/m and for -2 MV/m indicates some degree of nonlinearity in the relations between the blocking forces and applied electric field, as can be seen in Figure 4.17, especially in relations of force P_{bl} at high electric field strength. The geometrically linear theory predicts the values of $P_{bl,lin}$ to be ∓ 0.595 N for ± 2 MV/m, respectively. They are 12.1% less than the values of $P_{bl,lin}$ for the pinned-pinned supported actuator with an aspect ratio of 0.7, while the active area of the actuators in this case is less than the case with an aspect ratio of 0.7 by 52.9%. In addition, the slope of the relations between normalized R_{bl} and sidelength-to-thickness ratio is 0.387, which is a 34.7% decrease from the case of the actuators with pinned-pinned supports and aspect ratio 0.7.

4.5 Chapter Summary

In this chapter, the numerical results for manufactured shapes of LIPCA-C1 actuators were presented. The 23-term Rayleigh-Ritz model with an incorporation of composite material constitutive equations presented in Chapter 2 was shown to have a good agreement with the finite-element results obtained using ABAQUS for the selected cases compared. The results indicate that the predicted shapes for square and rectangular LIPCA-C1 actuators depend on sidelength-to-thickness ratio because of geometrically nonlinear effects. However, the manufactured room-temperature curvature in the *x*-direction is more or less insensitive to sidelength-to-thickness ratio, whereas the manufactured room-temperature curvature in the *y*-direction is suppressed as the sidelength-to-thickness ratio increases. The insensitivity of the *x*-direction curvature is mainly due to the high structural stiffness in the

x-direction contributed from the fibers in the carbon-epoxy layer running along the *x*-direction. Unlike THUNDER actuators that may exhibit multiple equilibrium shapes at room temperature, there exist no multiple equilibrium shapes for LIPCA-C1 in the range of parameters considered. All stable manufactured shapes are near-cylindrical; the larger curvature is always in the *x*-direction, and the smaller curvature in the *y*-direction.

In addition, the results of extension of the Rayleigh-Ritz model to predict the actuation response at room temperature of LIPCA-C1 actuators were presented. The average curvature changes in the *x*-direction caused by piezoelectric actuation, again, are almost independent of sidelength-to-thickness ratio. There is a slightly noticeable enhancement of the changes in the *x*-direction curvature for the negative field strength. The changes in the *y*-direction curvature due to piezoelectrical actuation, like the room-temperature curvature in the *y*-direction, are suppressed gradually as sidelength-to-thickness ratio increases. The actuation responses as a function of applied electric field were also discussed. Overall, the changes in the *x*-direction curvature due to actuation are practically linear in relation to electric field strength and roughly equal each other for the three aspect ratios considered over the range of the applied electric field. The changes in the *y*-direction curvature due to actuation can also approximately be assumed as linear functions of electric field strength to some extent, yet they are not equal each other owing to their dependency on aspect ratio. Additionally, it should be noted that for an actuation voltage of a given sign, the signs of the curvature changes of a LIPCA-C1 actuator in the two directions (the *x*- and *y*-directions) are opposite each other.

Finally, the blocking force predictions from the extension of the 23-term Rayleigh-Ritz model used to predict actuated shapes of LIPCA-C1 actuators were presented. All numerical results of the blocking forces are computed based on manufactured shapes given by branch $A'D'$ and their associated actuated shapes given by branches $A^{P}D^{P}$ and $A^{N}D^{N}$, as illustrated in Figures 4.9, 4.10, and 4.11, for LIPCA-C1 actuators subjected to +2

MV/m and -2 MV/m, respectively. For pinned-roller supported LIPCA-C1 actuators, blocking force P_{bl} is usually higher than force $P_{bl,lin}$, which are predicted by the geometrical linear theory, but not by much. In the other words, nonlinear effects enhance blocking force P_{bl} to a limited degree. For pinned-pinned supported LIPCA-C1 actuators, the existence of force R_{bl} strongly influences the characters of blocking force P_{bl} because the comparatively large magnitude of force R_{bl} alters the structural stiffness of the actuators. For the same aspect ratio, the magnitude of force P_{bl} decreases for short actuators and increases for long actuators, as well as the direction of force P_{bl} changes oppositely due to the presence of R_{bl}. The relations between blocking forces and applied electric field were also presented. Generally speaking, most of the relations are linear but do not correlate well with the predictions from the geometrically linear theory. In addition, the opposite directions (signs) of force P_{bl} influenced by the type of support can be clearly seen in the relations. Consequently, in order to design a LIPCA-C1 actuator to carry a transverse load or an inplane normal load, a careful analysis on actuator performance should be conducted, since its room-temperature shape and support type have very strong effects on the actuator capability.

In the next chapter, the numerical results of characteristics of LIPCA-C2 actuators will be presented, analogous to those of THUNDER and LIPCA-C1 actuators discussed in Chapter 3 and this chapter, respectively. Shapes and associated residual stress predictions of LIPCA-C2 actuators at service temperature due to manufacturing process and an application of a quasi-static electric field will be given. Equilibrium and stability of the calculated shapes will be determined. In some selected problems, validity of the Rayleigh-Ritz model with an incorporation of the composite material layers used in LIPCA-C2 will be examined by the ABAQUS model. Blocking forces of LIPCA-C2 actuators with two different support types, i.e., pinned-roller and pinned-pinned supports, will be presented in relation to electric field strength and sidelength-to-thickness ratios.

Chapter 5

NUMERICAL RESULTS OF LIPCA-C2 CHARACTERISTICS

5.1 Introduction

This chapter presents shape predictions of rectangular LIPCA-C2 actuators using the Rayleigh-Ritz model with the incorporation of composite layers into the constitutive equations. The manufactured shapes of the actuators are computed as a function of sidelength-to-thickness ratio. Actuated shapes of the rectangular LIPCA-C2 actuators are also calculated by utilizing the modified Rayleigh-Ritz model with the inclusion of piezoelectrically-induced strains. Results from ABAQUS models are compared with results from the Rayleigh-Ritz approach for selected problems. At the end of this chapter, blocking forces of the LIPCA-C2 actuators subjected to the application of an electric field with pinned-roller and pinned-pinned supports are calculated and discussed.

5.2 Numerical Results for Manufactured Shapes

5.2.1 Deformation Characteristics of LIPCA-C2 without Tabs

To illustrate the results of LIPCA-C2 actuators predicted by the Rayleigh-Ritz model with the incorporation of composite layers into the constitutive equations, as discussed in Section 2.2.2, consider a rectangular LIPCA-C2 actuator without tabs consisting of 5 layers, as illustrated in Figure 1.13. The LIPCA-C2 design is composed of three layers of glass-epoxy as the bottom, middle, and top layers, and a piezoceramic layer and a unidirectional carbon-epoxy layer with its fibers in the x-direction sandwiched between the bottom and the middle layers, and the middle and the top layers, respectively.

Thus, the carbon-epoxy layer and the piezoceramic layer are further apart than with the LIPCA-C1 design. This separation is intentional and is used to provide more authority to the actuator. In addition, like a LIPCA-C1 actuator, the glass-epoxy layers of the LIPCA-C2 actuator have the same elastic properties in the *x*- and *y*-directions, so in that sense are isotropic. The curing temperature of the epoxy matrix is taken to be the same as for a LIPCA-C1 actuator, namely, -142 °C. The material properties and thicknesses of the layers used in the analyses to follow are given in Table 4.1. It should be keep in mind that for a given value of sidelength-to-thickness ratio, the LIPCA-C2 actuator is longer in the *x*-direction than a THUNDER actuator or a LIPCA-C1 actuator due to the larger value of H for the LIPCA-C2 cross section. (for THUNDER H = 0.427 mm, for LIPCA-C1 H = 0.530 mm, for LIPCA-C2 H = 0.620 mm)

The relationships between the sidelength-to-thickness ratio and the average room-temperature curvatures for rectangular LIPCA-C2 actuators with an aspect ratio of 0.7 are illustrated in Figure 5.1. From the figure it can be seen that, like the LIPCA-C1 actuator, the relationships are single-valued. However, the behavior of the LIPCA-C2 design is different than the behavior of LIPCA-C1 design, and for that matter the THUNDER design, in that the room-temperature curvature in the *y*-direction is of opposite sign to the *x*-direction curvature. A review of Figures 3.8 and 4.1 shows that with THUNDER and LIPCA-C1 designs, the *x*- and *y*-direction room-temperature curvatures have the same sign. The difference in signs is due to the difference in the stacking sequence among the actuators. A second difference between the two composite actuator designs is the dependence of the *x*-direction curvature on sidelength-to-thickness ratio. With the rectangular LIPCA-C1 design, the *x*-direction curvature was hardly influenced by sidelength-to-thickness ratio, while the *y*-direction curvature was noticeably suppressed for the three aspect ratios considered. For the rectangular LIPCA-C2 design, the *x*-direction curvature can be approximated by the geometrical linear theory (independent of sidelength-to-thickness ratio) for $L_x/H < 40$ and is

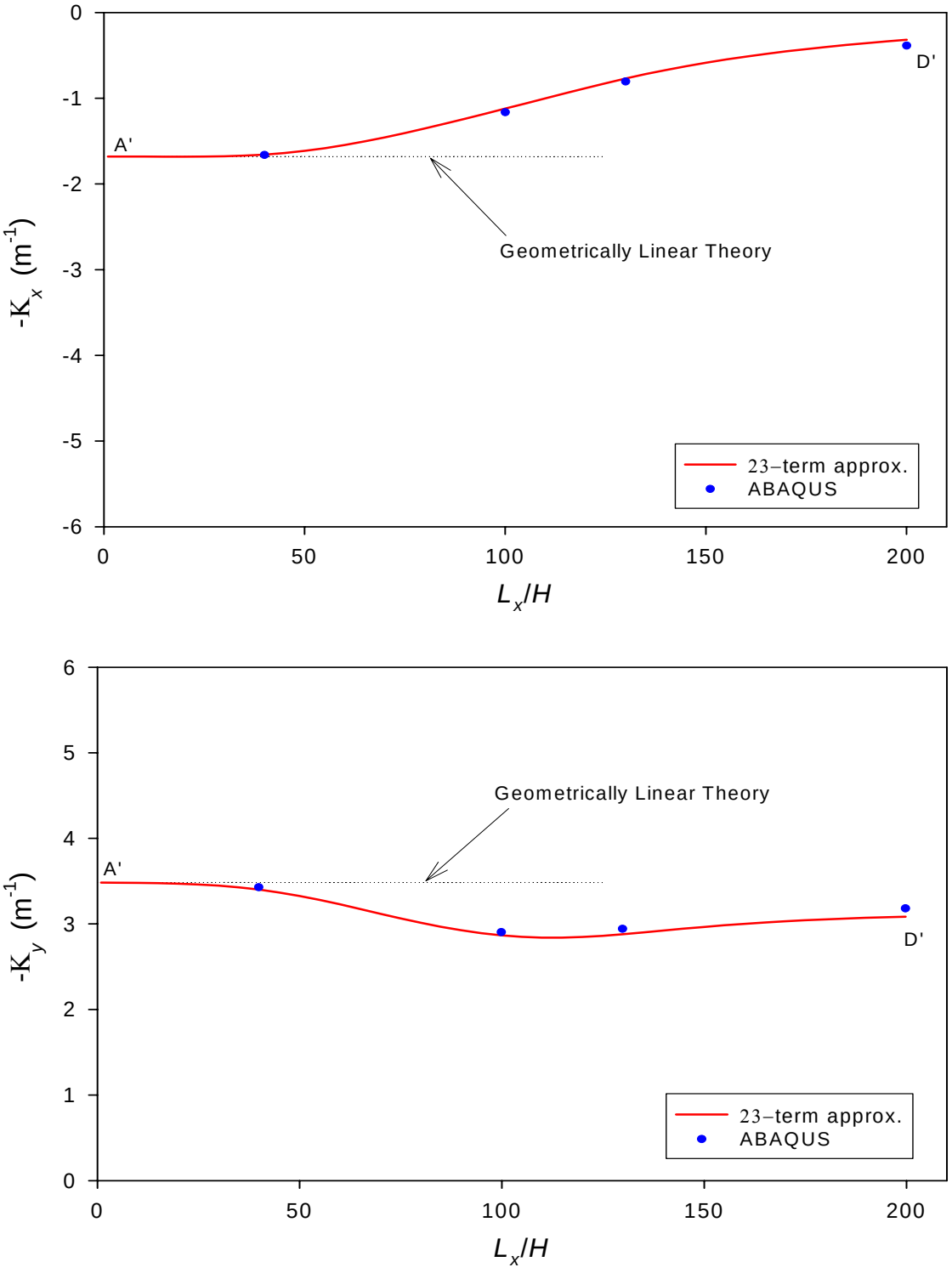

Figure 5.1: Sidelength-to-Thickness Ratio-Curvature Relations of Rectangular LIPCA-C2 ($L_y / L_x = 0.7,\ \Delta T = -142\,^{\circ}\mathrm{C}$)

suppressed with further increasing sidelength-to-thickness ratio, while the *y*-direction curvature remains somewhat constant, with little suppression in magnitude predicted compared to the geometrically linear predictions. The reason behind the second difference is believed to be caused by the magnitude of room-temperature curvatures in both *x*- and *y*-direction. As discussed in Chapter 4, nonlinear effects appear to markedly suppress the curvature that has the smaller magnitude and either slightly suppress or actually enhance the curvature that has the larger magnitude. Thus, when compared to LIPCA-C1, it should be noted that nonlinear effects have a much stronger influence on the shape characteristics of LIPCA-C2 actuators than modulus of elasticity of the materials does because the *x*-direction room-temperature curvature is suppressed considerably due to nonlinear effects, even though the LIPCA-C2 actuators are stiff in the *x*-direction due to the carbon fiber, like the LIPCA-C1 actuators are. Also illustrated in the figure are the finite element predictions by using ABAQUS. Again, it is apparent that the Rayleigh-Ritz formulation works well for the case of fiber-reinforced composite layers. The room-temperature shapes of rectangular actuators with L_y/L_x = 0.7 and L_x/H = 100 and 200 are illustrated in Figure 5.2. Opposite to the shape characteristics of LIPCA-C1 in Figure 4.2, the *y*-direction curvature of the LIPCA-C2 actuators is noticeable in Figure 5.2. Of the actuators with the same thickness, *H*, the *y*-direction curvature for L_x/H = 100 is less pronounced than that for L_x/H = 200, despite the values of their *y*-direction curvatures being almost equal. This is because the actuator with L_x/H = 100 is half as wide in the *y*-direction as the one with L_x/H = 200. The *x*-direction curvatures are less noticeable since they are smaller to begin with and are suppressed by geometrically nonlinear effects. Figures 5.2 (b) and (c) also depict the comparison between room-temperature shapes predicted by the 23-term Rayleigh-Ritz and ABAQUS models. A good agreement can be seen from the comparison. Note that the manufactured shapes of the LIPCA-C2 actuators illustrated in Figure 5.2 may not be desirable in a practical sense, since the longer direction (the *x*-direction) is supposed to be exploited in an application and hence

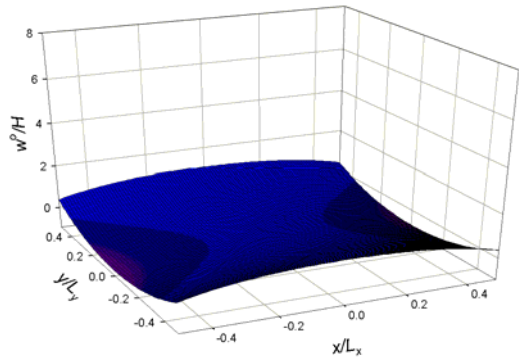

(a) 23-term Rayleigh-Ritz, L_x/H = 100

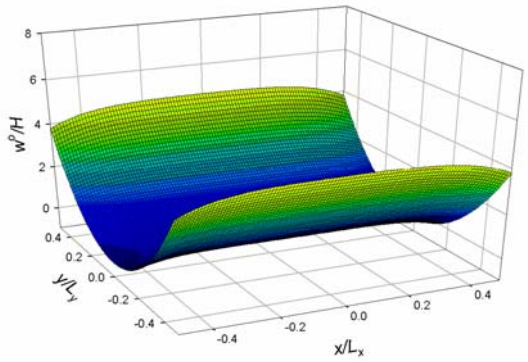

(b) 23-term Rayleigh-Ritz, L_x/H = 200

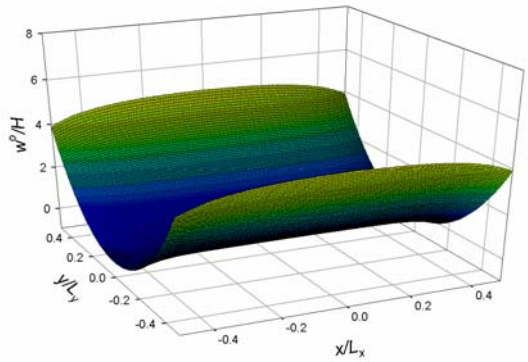

(c) ABAQUS, L_x/H = 200

Figure 5.2: Equilibrium Shapes of Rectangular LIPCA-C2 (L_y/L_x = 0.7, ΔT = -142 °C)

should have a larger room-temperature curvature. The shorter direction (the *y*-direction) should have a smaller room-temperature curvature so that attaching the actuators to a substrate on the *x*-edge(s) could be done easily.

For LIPCA-C2 actuators with an aspect ratio of 1, the relationships between the sidelength-to-thickness ratio and the average room-temperature curvature are illustrated in Figure 5.3. Overall, the relationships are very similar to the ones in Figure 5.1. However, it can be seen in Figure 5.3 that geometrically nonlinear effects are stronger than the case of aspect ratio 0.7. This is because the range of sidelength-to-thickness ratios within which the square LIPCA-C2 actuators behave linearly is smaller than the rectangular case, i.e.,

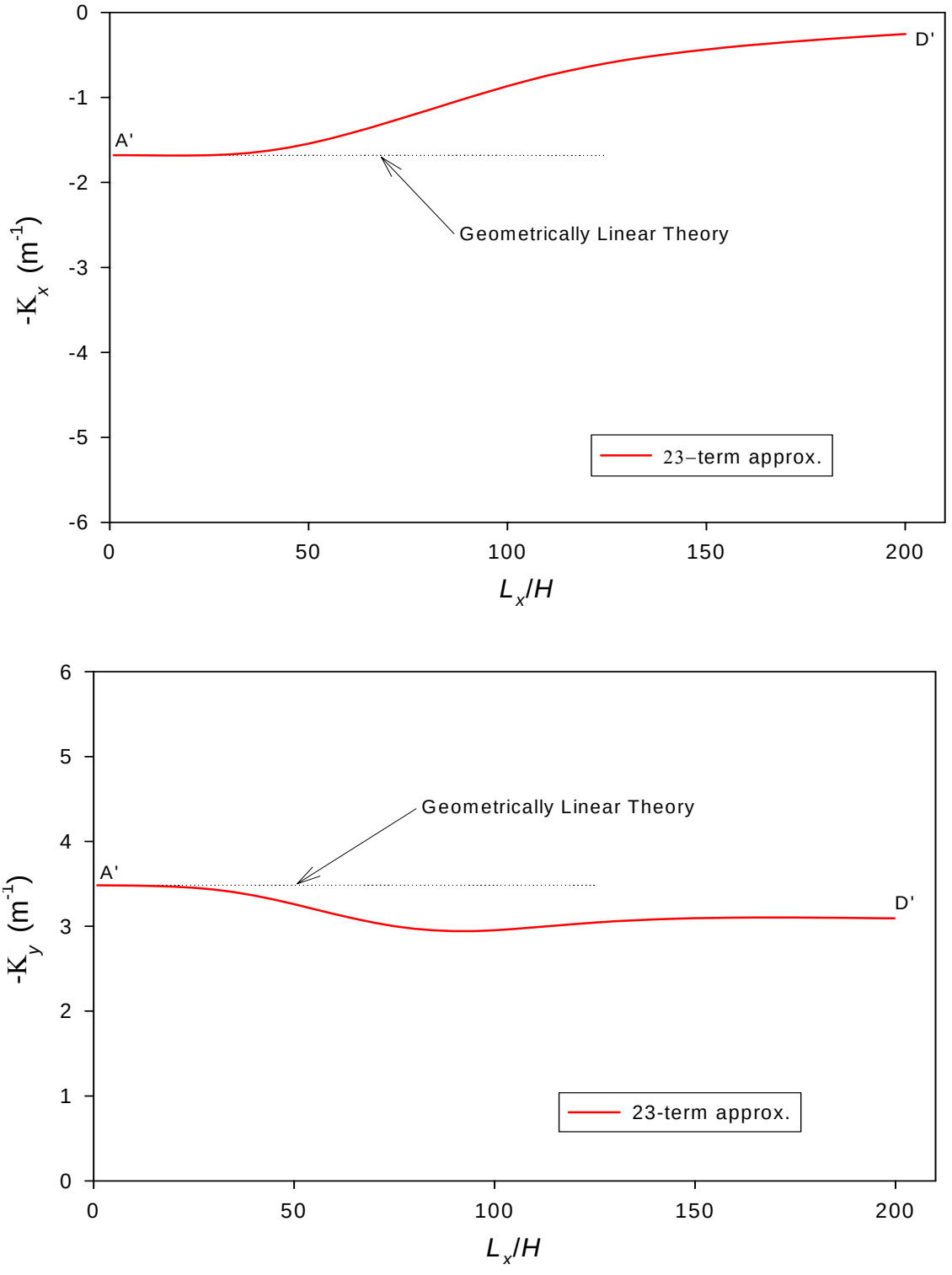

Figure 5.3: Sidelength-to-Thickness Ratio-Curvature Relations of Square LIPCA-C2 (ΔT = -142 °C)

$0 < L_x/H < 30$ for this case compared to $0 < L_x/H < 40$ for the rectangular case. In addition, the *y*-direction room-temperature curvature is suppressed about the same as the previous case when sidelength-to-thickness ratio increases. The *x*-direction curvature, on the other hand, is not affected much by the change of aspect ratio in general. The room-temperature shapes for square LIPCA-C2 actuators are analogous to Figure 5.2 and are not shown here. The same issue concerning the attachment of square LIPCA-C2 actuators to a substrate on the *x*-edge(s) can be made here, since the dimension in the *y*-direction is longer than that of the rectangular LIPCA-C2 actuators in the previous case and, therefore the curvatures in the *y*-direction are even more pronounced.

Finally, the influence of sidelength-to-thickness ratio on the room-temperature curvatures of a beam-like LIPCA-C2 actuator with an aspect ratio of 0.33 is illustrated in Figure 5.4. Like the beam-like aspect ratio considered for the LIPCA-C1 case, the value of 0.33 is chosen to represent the geometry of LIPCA-C2 actuators that was used by Yoon and coworkers [33] to perform their experiments. With L_y/L_x = 0.33, the geometry does not induce nonlinear effects as much compared to the cases with L_y/L_x = 0.7 and 1. As a result, the *x*-direction room-temperature curvature is suppressed less in magnitude when sidelength-to-thickness ratio increases. Interestingly, the *y*-direction curvature is influenced more than for the rectangular or square aspect ratios. The geometrical linear Rayleigh-Ritz model again predicts spatially uniform *x*- and *y*-direction curvatures (K_x = 1.68 m^{-1} and K_y = -3.48 m^{-1}), which are independent of sidelength-to-thickness and aspect ratios. Additionally, since the LIPCA-C2 actuators with L_y/L_x = 0.33 are beam-like, the *x*-direction curvature of the actuators can be computed from either a geometrically nonlinear or linear laminated beam model, as derived in Appendix B. Specifically, by using Equation (B.36) or (B.65), K_x = 1.86 m^{-1}, a constant over the range of sidelength-to-thickness ratios considered. This value is around 10% different from the *x*-direction room-temperature curvature predicted by the geometrically linear Rayleigh-Ritz model. The shapes at room-

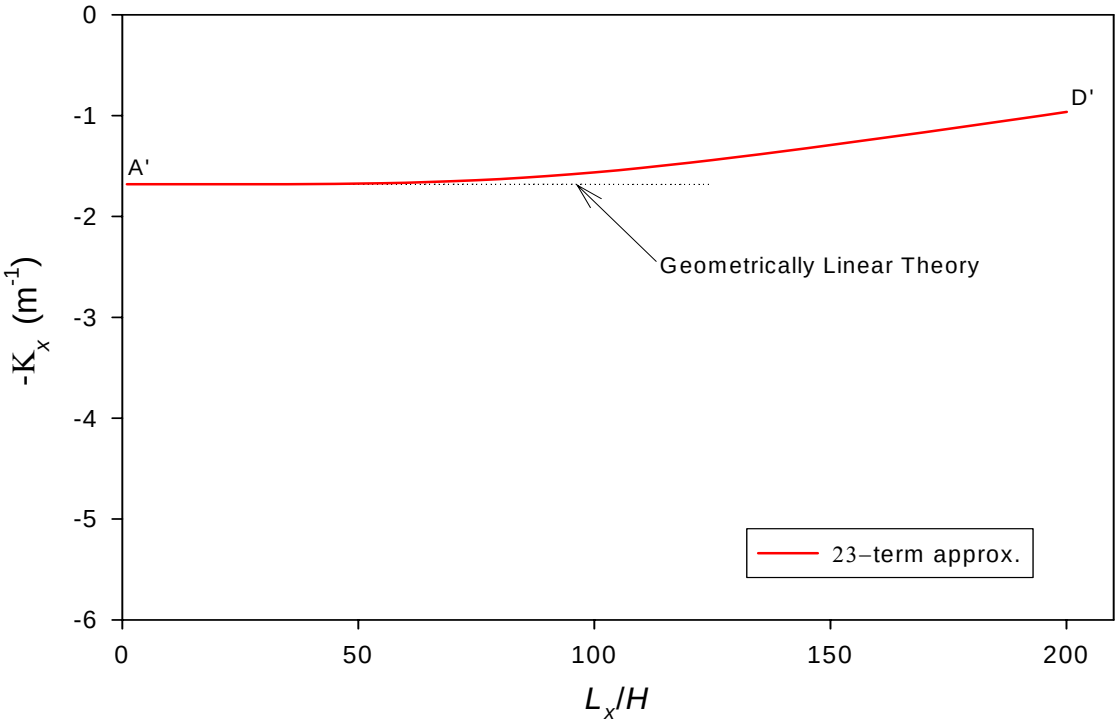

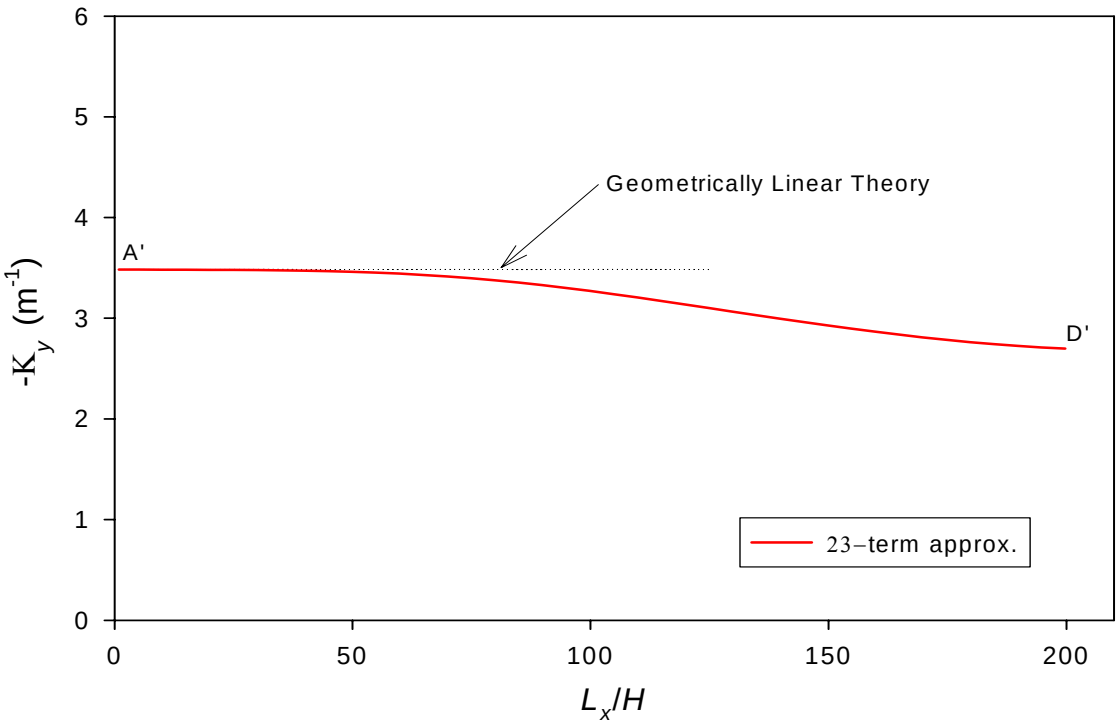

Figure 5.4: Sidelength-to-Thickness Ratio-Curvature Relations of Beam-Like LIPCA-C2 ($L_y / L_x = 0.33,\ \Delta T = -142\,^{\circ}\mathrm{C}$)

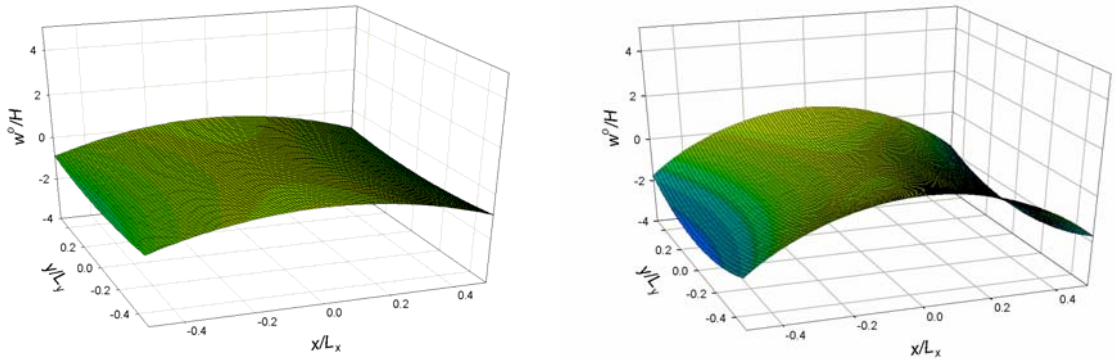

(a) 23-term Rayleigh-Ritz, L_x/H = 100 (b) 23-term Rayleigh-Ritz, L_x/H = 200

Figure 5.5: Equilibrium Shapes of Rectangular LIPCA-C2 (L_y/L_x = 0.33, ΔT = -142 °C)

Temperature for L_x/H = 100 and 200 in Figure 5.4 are shown in Figure 5.5. It should be mentioned that due to the beam-like geometry of the actuator, with the longer dimension in the *x*-direction, the *x*-direction curvature is more pronounced than the *y*-direction curvature despite the fact that the magnitude of the former curvature is smaller than the magnitude of the latter. Thus, these manufactured shapes seem to be more desirable than the ones with the aspect ratios of 0.7 and 1, since attachment on the *x*-edge(s) would be easier and have less adverse effect on the curvature in the *y*-direction.

5.2.2 Force and Moment Resultant and Stress Characteristics of LIPCA-C2 without Tabs

Generated during the cooling process of LIPCA-C2 actuators, thermal-induced residual stresses are present in the actuators at room-temperature, just like the other actuators discussed in the previous two chapters. Thus, it is of interest to examine the residual stresses and residual force and moment resultants, as defined in Equation (2.9). First, consider the force and moment resultants of a LIPCA-C2 actuator resulting from the ABAQUS calculation and illustrated in Figure 5.6. The actuator has an aspect ratio of 0.7 and a sidelength-to-thickness ratio of 200 and is in the configuration shown in Figure 5.2 (c). Thus, it has relatively small curvature in the *x*-direction and large curvature in the *y*-

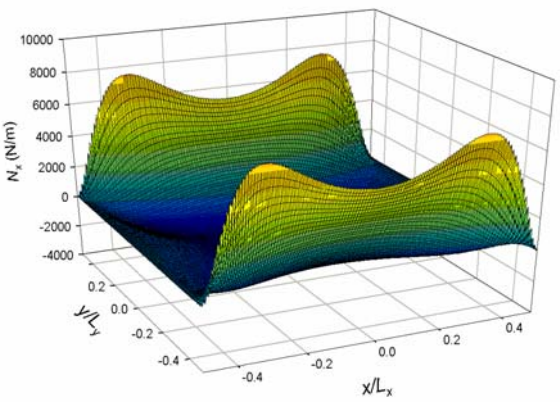

(a) Force Resultant N_x

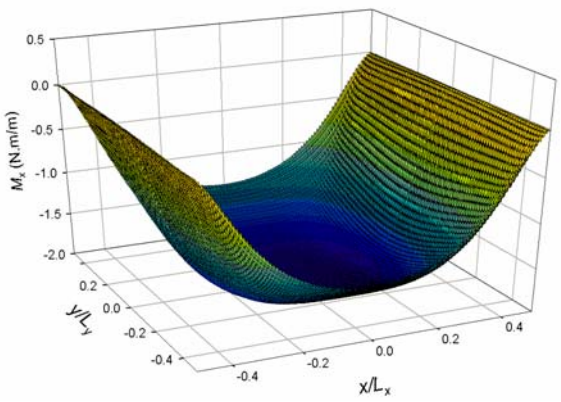

(b) Moment Resultant M_x

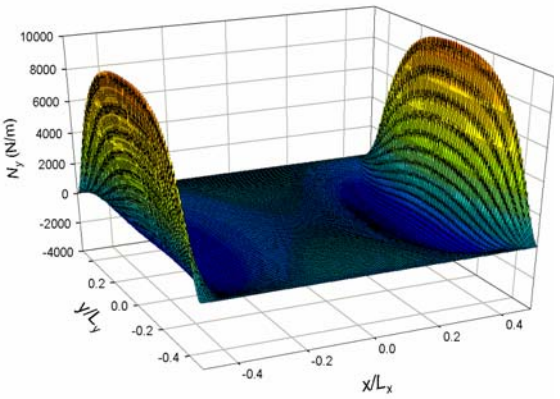

(c) Force Resultant N_y

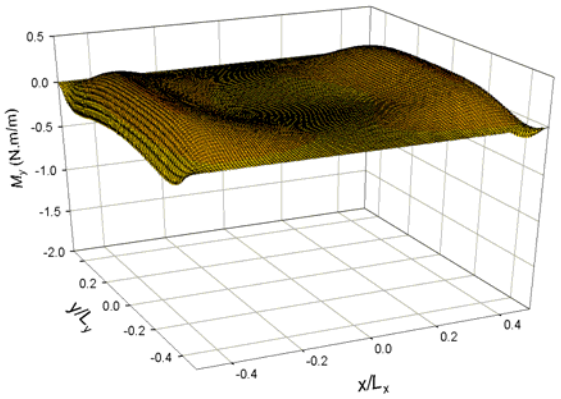

(b) Moment Resultant M_y

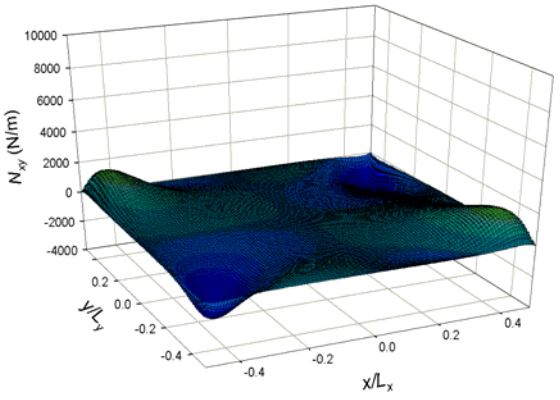

(e) Force Resultant N_{xy}

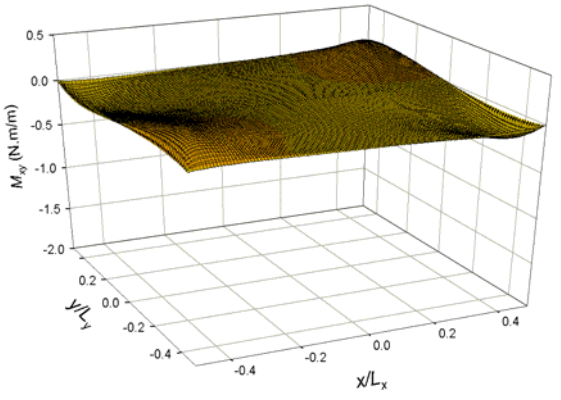

(f) Moment Resultant M_{xy}

Figure 5.6: Force and Moment Resultants in Rectangular LIPCA-C2 (L_y/L_x = 0.7, L_x/H = 200, ΔT = -142 °C)

direction. Since the boundaries of the actuator are traction free, specific force and moment resultants are zero on the boundaries, as seen in Figure 5.6. Also apparent in Figure 5.6, as in Figures 3.10 and 4.5 for THUNDER and LIPCA-C1 actuators, respectively, extreme values of the force and moment resultants occur in narrow regions along the edges of the LIPCA-C2 actuator. These force and moment resultants build in magnitude quite rapidly as the edges are approached from the central portion. Away from the edges, the magnitudes of the force and moment resultants are more uniform, and in some cases quite small. In addition, by considering Figure 5.6 along with Figures 3.10, 3.11, 4.5 and 4.6, it is interesting to summarize that in the direction that the curvature is being suppressed compared to the geometrical linear prediction, the associated bending moment resultant in that direction always has a noticeable 'well-like' distribution in the central portion of actuators. Furthermore, the well-like distribution represents negative bending moment resultants. Negative bending moment resultants are indeed the key reason for the suppression phenomenon, since they will reduce the magnitude of the positive-valued room-temperature curvatures and, as a result, the curvatures are suppressed. On the other hand, in the direction that the curvature is unchanged or enhanced compared to the geometrical linear prediction, the bending moment resultant in that direction does not exhibit the well-like configuration. Instead, it has relatively large values at some edges and fairly small values in the middle portion. Geometrically nonlinear effects on the bending moment resultant in this direction are not as strong as in the suppression direction. For inplane normal force resultants, comparatively large values at the edges and rather uniform small values in the central portion seem to always be the character of the stress resultant distributions for THUNDER-type and LIPCA-type actuators. Furthermore, values of inplane shear force and twisting moment resultants will always be comparatively small and will be the largest in the actuator corners. All of these stress resultant characteristics are due to geometric

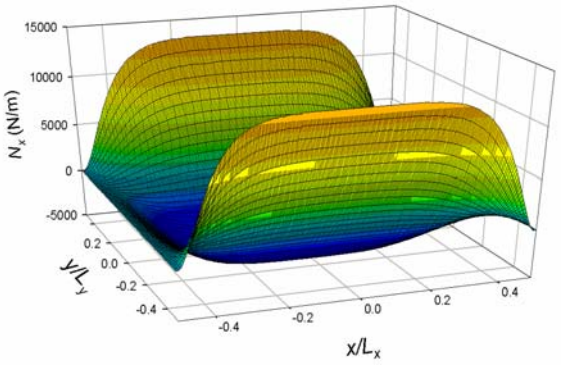

(a) Force Resultant N_x

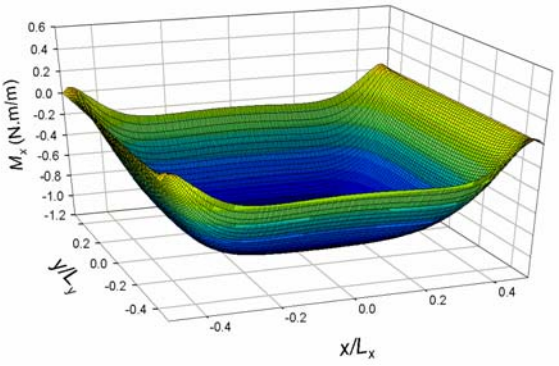

(b) Moment Resultant M_x

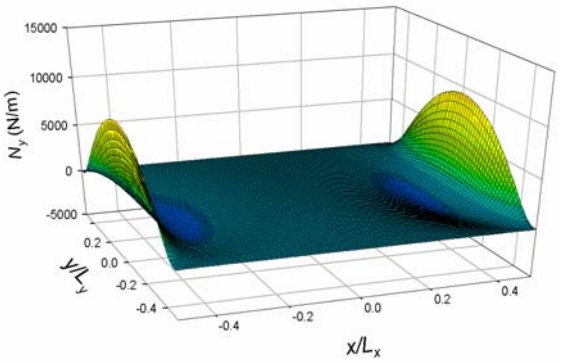

(c) Force Resultant N_y

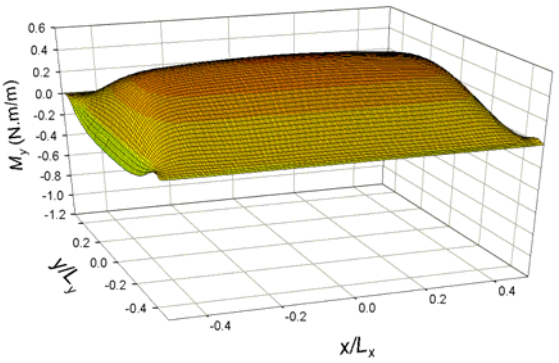

(d) Moment Resultant M_y

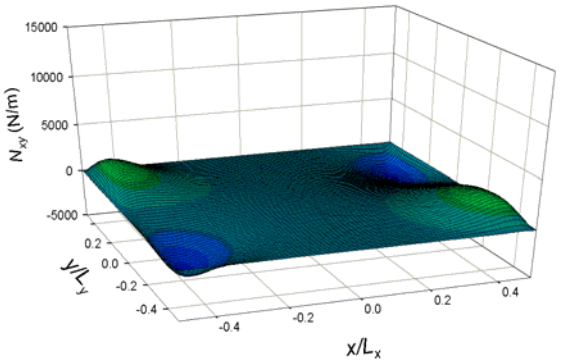

(e) Force Resultant N_{xy}

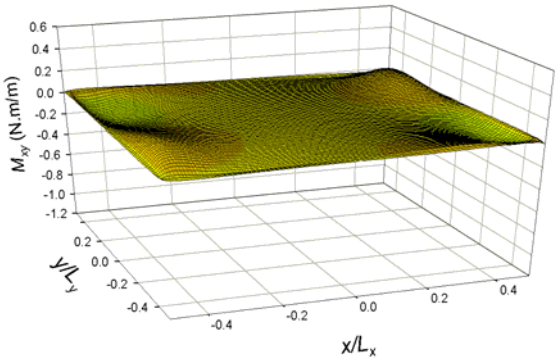

(f) Moment Resultant M_{xy}

Figure 5.7: Force and Moment Resultants in Beam-Like LIPCA-C2 (L_y/L_x = 0.33, L_x/H = 200, ΔT = -142 °C)

nonlinearities, because all force and moment resultants are exactly zero when calculated by the geometrically linear theory.

Also by employing the ABAQUS model, a similar picture emerges for the more beam-like actuator. Figure 5.7 shows the force and moment resultants for the actuator with an aspect ratio of 0.33 and sidelength-to-thickness ratio of 200. By comparison with Figure 5.7, it is observed that the magnitude of the force and moment resultants depends on the aspect ratio, to some degree, but the general character of the spatial distribution changes only slightly with aspect ratio. Note that the distribution of the *y*-direction bending moment resultant in Figure 5.7 (d) is similar to the distribution of the *x*-direction bending moment resultant in Figure 5.7 (b), the differences being the sign of the bending moment resultant in the central region and the edges along which the moment resultants are zero. As stated above, the well-like distribution of a bending moment resultant in a particular direction represents a curvature suppression characteristic in that direction. Accordingly, the beam-like LIPCA-C2 actuator at L_x/H = 200 with the well-like and 'inverted' well-like distributions of the bending moment resultants in the *x*- and *y*-directions, respectively, as illustrated in Figures 5.7 (b) and (d), has the curvatures being suppressed in the two directions at point D' in Figure 5.4. Additionally, though the two curvatures are being suppressed in magnitude at point D', the directions (signs) of the curvatures are opposite each other and this makes one of the wells 'inverted'.

A sample of the stresses that lead to the force and moment resultants N_x, N_y, M_x, and M_y illustrated in Figure 5.6 for the LIPCA-C2 actuator with an aspect ratio of 0.7 and a thickness ratio of 200 are illustrated in Figures 5.8 and 5.9 for four locations within the actuator. The through-thickness distributions of the inplane normal stresses near the center of the actuator $x \cong 0, y \cong 0$ are illustrated in Figure 5.8 (a), while the distributions near the midpoints near the longer edge $\left(x \cong 0, y \cong L_y/2\right)$ and near the shorter edge $\left(x \cong L_x/2, y \cong 0\right)$ are illustrated in Figures 5.8 (b), and 5.9 (a), respectively. The

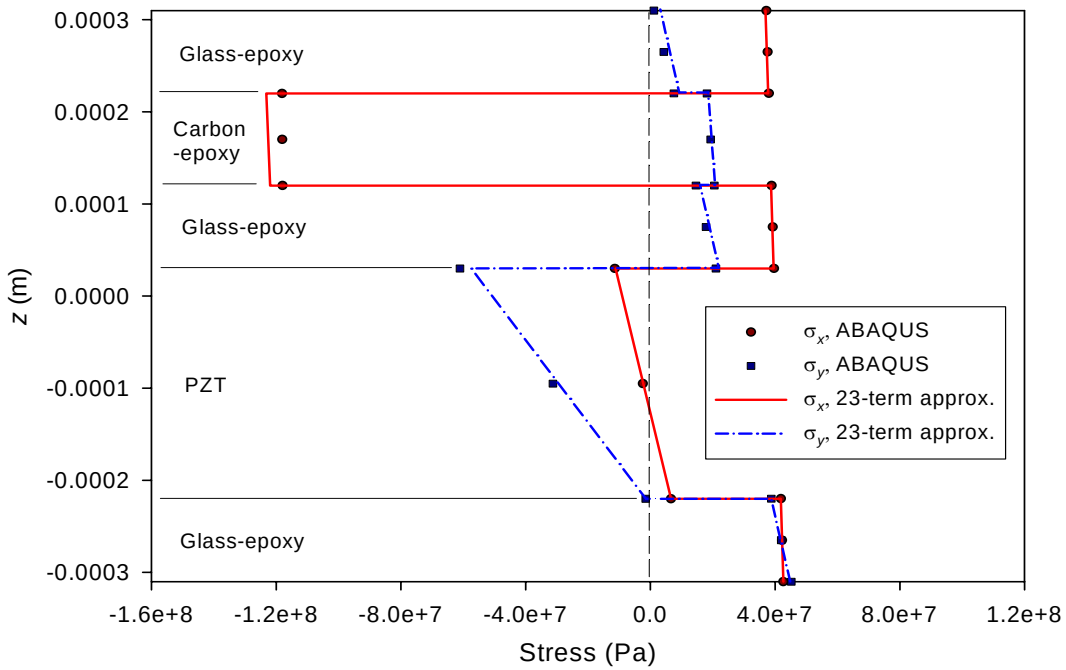

(a) Distribution of Normal Stresses at $x \cong 0,\ y \cong 0$

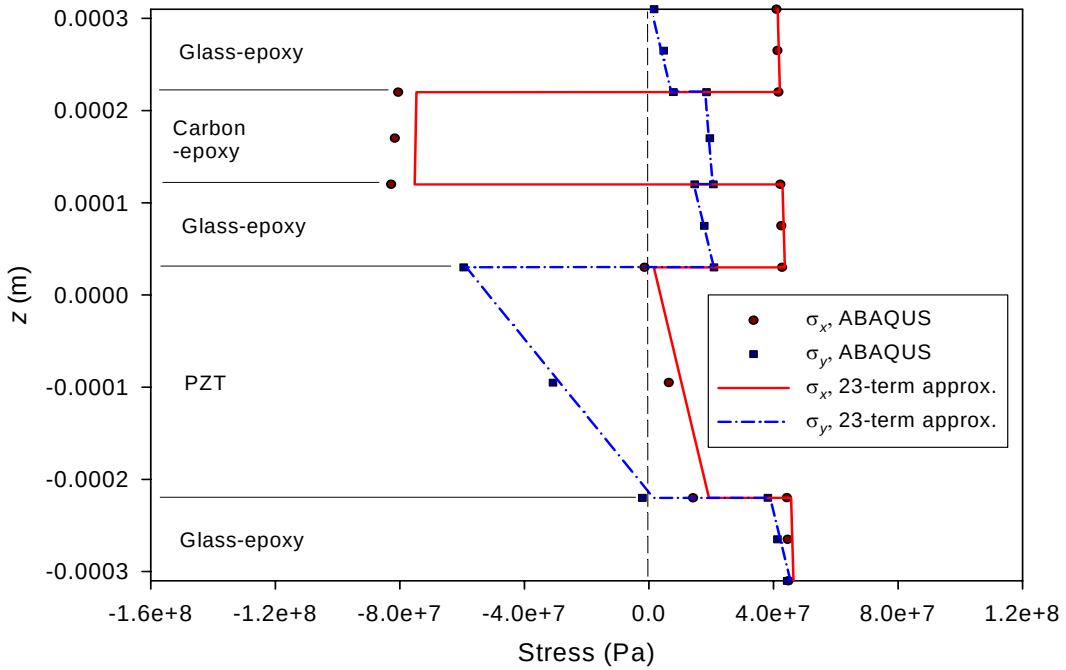

(b) Distribution of Normal Stresses at $x \cong 0,\ y \cong L_y/2$

Figure 5.8: Stress Distributions in LIPCA-C2 (L_y/L_x = 0.7, L_x/H = 200, ΔT = -142 °C) for Two Locations near Centerline x = 0

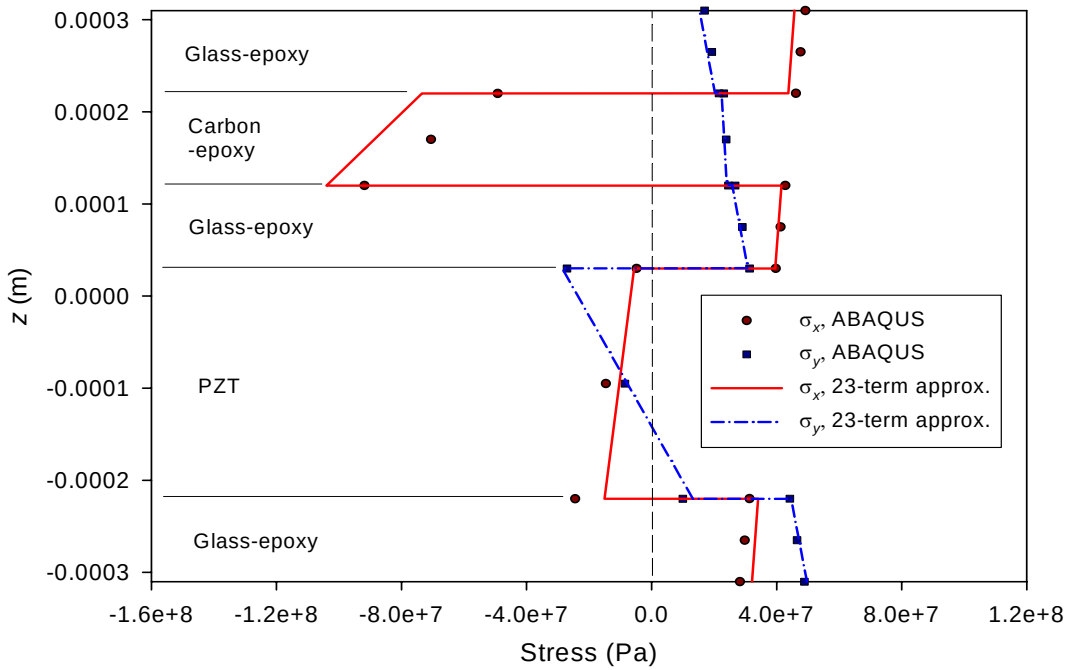

(a) Distribution of Normal Stresses at $x \cong L_x/2,\ y \cong 0$

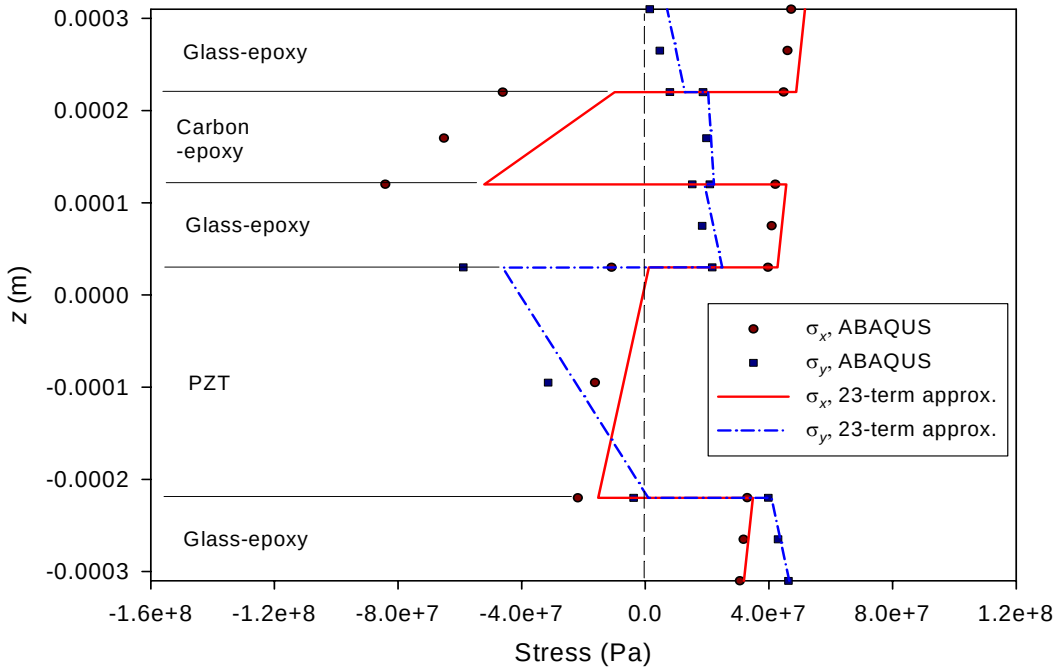

(b) Distribution of Normal Stresses at $x \cong L_x/2,\ y \cong L_y/2$

Figure 5.9: Stress Distributions in LIPCA-C2 (L_y/L_x = 0.7, L_x/H = 200, ΔT = -142 °C) for Two Locations near Boundary $x = L_x/2$

distributions near a corner $\left(x \cong L_x/2, y \cong L_y/2\right)$ are displayed in Figure 5.9 (b). The comparisons of the through-thickness stress distributions between the 23-term Rayleigh-Ritz and the ABAQUS models are also given in Figures 5.8 and 5.9. Since the stress calculations resulting from the ABAQUS model are expected to be more accurate than from the 23-term Rayleigh-Ritz approach, the following discussions about the stress distributions are based on the finite-element results.

As seen in Figures 5.8 and 5.9, the magnitudes of the room-temperature stresses for the LIPCA-C2 actuator are lower than for the THUNDER actuator illustrated in Figures 3.12 and 3.13, but are on the same order as for the LIPCA-C1 actuator shown in Figures 4.7 and 4.8. This is principally due to the lower cure temperature for the epoxy in the carbon-epoxy and glass-epoxy layers in the LIPCA-C2 actuators than for the polyimide adhesive in the THUNDER actuators. Despite the fact that the cure temperature for the LIPCA-C2 actuators is the same as for the LIPCA-C1 actuators, the magnitude of the inplane normal stress in the *x*-direction in the carbon-epoxy layer is the largest stress encountered in the two composite actuators and the layer is in compression in this direction at all four locations considered. However, the magnitude of the inplane normal stress in the *y*-direction in the carbon-epoxy layer are trivial and the layer is instead in tension in the *y*-direction. This is evidently caused by the inplane orthotropy of the carbon-epoxy layer, which possesses a high elastic modulus and a negative coefficient of thermal expansion in the *x*-direction, and a low elastic modulus and a positive coefficient of thermal expansion in the *y*-direction. The sign of the stress in the piezoceramic layer varies with thickness location and stress component. Note that even though the piezoceramic layer is subjected to a tensile stress, which is undesirable for a piezoceramic material due to its brittleness, the magnitude of the stress is not detrimentally large and should not be a concern. Like the LIPCA-C1 actuator, the residual normal stresses in the glass-epoxy layers in the LIPCA-C2 actuator are relatively small due to their comparatively low modulus of elasticity. In addition, the

increased or decreased magnitudes of some force and moment resultants on the specific edges can be explained from the stress distributions in Figures 5.8 and 5.9. For example, for the force resultant N_x shown in Figure 5.6 (a), when comparing Figure 5.8 (a) with Figure 5.8 (b) it can be seen that the main contribution to the large positive value of N_x on the *y*-edges comes from the value of σ_x in the carbon-epoxy and piezoceramic layers. The magnitude of the negative value of σ_x decreases going from the center to the edges. This leads to a positive value of N_x at the edges compared to the center. The glass-epoxy layers also have a contribution to the stress resultant behavior, but the magnitude of increase of the positive stress component σ_x is small. This is quite different from that of the LIPCA-C1 actuator presented in Section 4.2.2. The contribution to the large magnitude of resultant N_x on the *y*-edges for the LIPCA-C1 actuator in Figure 4.5 (a) is attributable to a change in stress components σ_x in all layers of the actuators at the edges compared to the center (Figure 4.7 (b) compared to Figure 4.7 (a)). Similarly, the large magnitudes of the force resultant N_y on the *x*-edges in Figure 5.6 (c) for the LIPCA-C2 actuator can also be studied. In contrast to those of the force resultant N_x in Figure 5.6 (a), the large magnitudes of the force resultant N_y at the midpoint of one of the *x*-edges $\left(x = L_x/2, y = 0\right)$ compared to the central point $\left(x = 0, y = 0\right)$ result from an increase of the stress components σ_y in all layers, as seen in Figure 5.9 (a) compared to Figure 5.8 (a). Moreover, because the increase in the stress component σ_y is nearly the same in all layers, large magnitudes of the moment resultant M_y on the *x*-edges do not noticeably develop. Finally, the comparison between the predictions of the stress distributions by 23-term Rayleigh-Ritz and ABAQUS models in Figure 5.8 shows a fairly good agreement. A small discrepancy between both predictions can be seen in the carbon-epoxy layer and the piezoceramic layer. However, the comparison of stress distributions in Figure 5.9 between the two models reveals a larger discrepancy in each layer than the comparison in Figure 5.8, especially in the carbon-epoxy layer in the *x*-direction. The reason for this is that the carbon-epoxy layer has a high modulus of elasticity

in the *x*-direction, and thus the normal stress in this direction is highly sensitive to the strains computed by using the assumed displacement field of Equation (2.26).

5.3 Numerical Results of Actuated Shapes

5.3.1 Deformation Characteristics of LIPCA-C2 subjected to Applied Electric Field

The relationships between the sidelength-to-thickness ratio and the actuation-induced curvatures at ±2 MV/m for rectangular LIPCA-C2 actuators with an aspect ratio of 0.7 are illustrated in Figure 5.10. Also, the room-temperature manufactured curvature vs. sidelength-to-thickness ratio relations, which were shown in Figure 5.1, are repeated in Figure 5.10 for reference. The characteristics of the actuation-induced curvature for the LIPCA-C2 design are quite interesting, and much different than the THUNDER and LIPCA-C1 actuators discussed. There is considerable enhancement of the actuated curvature change in the *x*- and *y*- directions for large sidelength-to-thickness ratios when a positive electric field is applied. However, suppression of the actuated curvature change in the *x*-direction and some degree of enhancement in the *y*-direction appear when the actuators are subjected to a negative applied electric field. It is interesting to note that the actuated curvature changes in the *x*-direction for positive and negative fields are different by more than a factor of five for large sidelength-to-thickness ratios. For a harmonically applied voltage, the dynamic response of the actuator could be quite undesirable. The unusual curvature changes for large sidelength-to-thickness ratios for positive and negative electric fields is confirmed with finite-element calculations for the case of L_x/H = 200 at points D^{P2} and D^{N2}, respectively. The sign of the changes in curvature owing to an applied electric field is consistent with the physical interpretation of actuator deformations based on the stacking sequence of the LIPCA-C2 actuators. Due to the comparatively high modulus of elasticity of the carbon-epoxy layer and more glass-epoxy layers stacked above the piezoceramic layer than below the layer, the effective extensional stiffness of all layers on the top of the

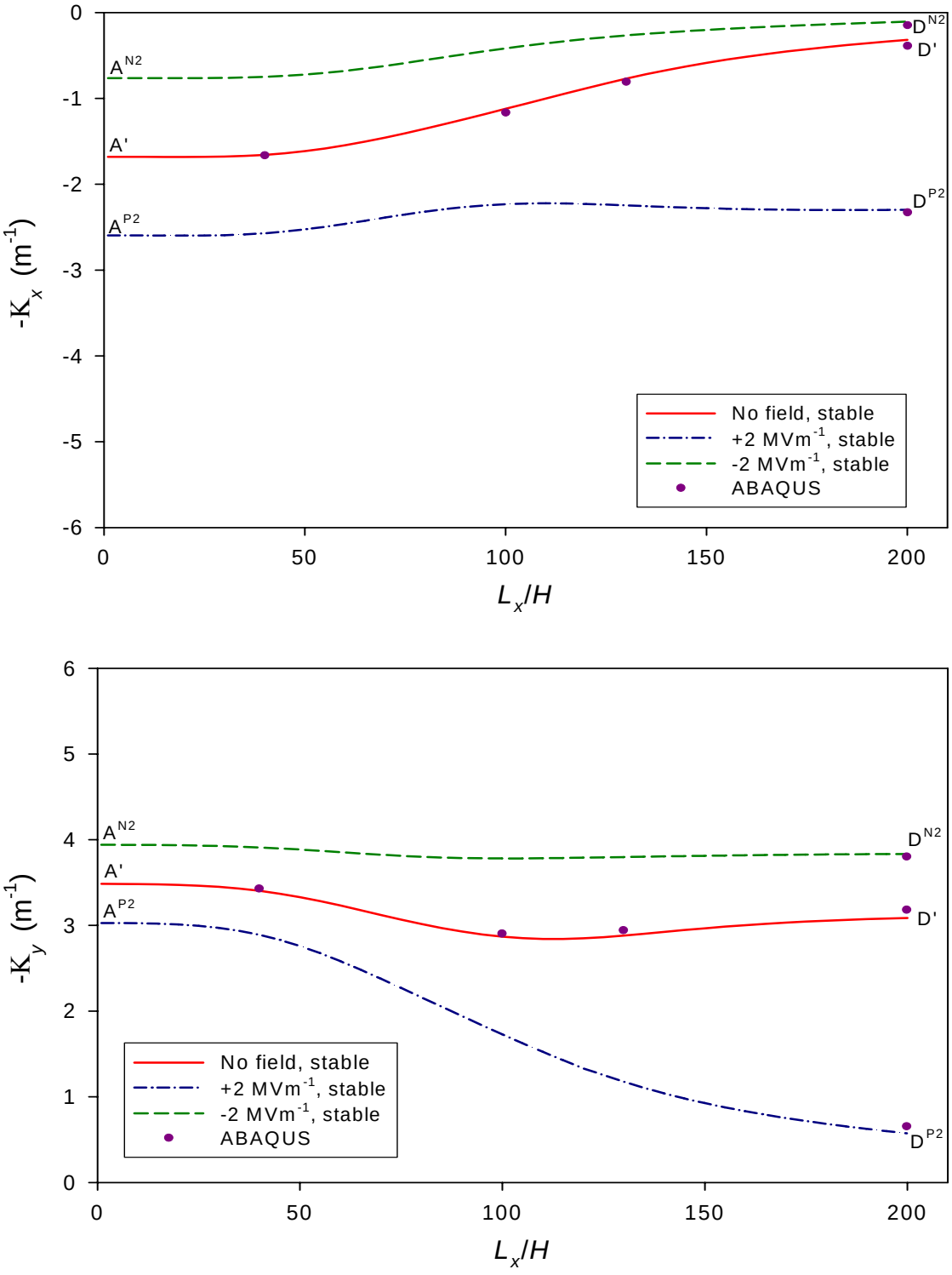

Figure 5.10: Influence of Actuation on the Change of Curvatures of Rectangular LIPCA-C2 (L_y/L_x = 0.7, ΔT = -142 °C)

piezoceramic layer is higher than that of the single glass-epoxy layer below the piezoceramic layer. As a result, the layers on the top, taken together, act as the backbone of the LIPCA-C2 actuator in both *x*- and *y*-directions. Thus, when a negative field is applied, as an example, the negative room-temperature curvature in the *x*-direction is reduced in magnitude, whereas the positive room-temperature curvature in the *y*-direction is increased in magnitude. The corresponding shapes of the LIPCA-C2 actuator at L_x/H =200 with +2 MV/m and -2 MV/m applied electric field strengths, as computed by employing the 23-term Rayleigh-Ritz model, are compared in Figure 5.11. In addition, the shape of the actuator without an applied electric field, which was shown in Figure 5.2 (b), are illustrated in Figure 5.11 for comparison. Note that the shape of the actuator with +2 MV/m applied in Figure 5.11 (c) is totally different than the shape of the actuator without an applied electric field in Figure 5.11 (b) and with -2 MV/m applied in Figure 5.11 (a). Therefore, it will be of interest and value to study the transition of the shape characteristic from the state with no application of electric field to the state with an application of the positive electric field. This will be discussed more subsequently in this section.

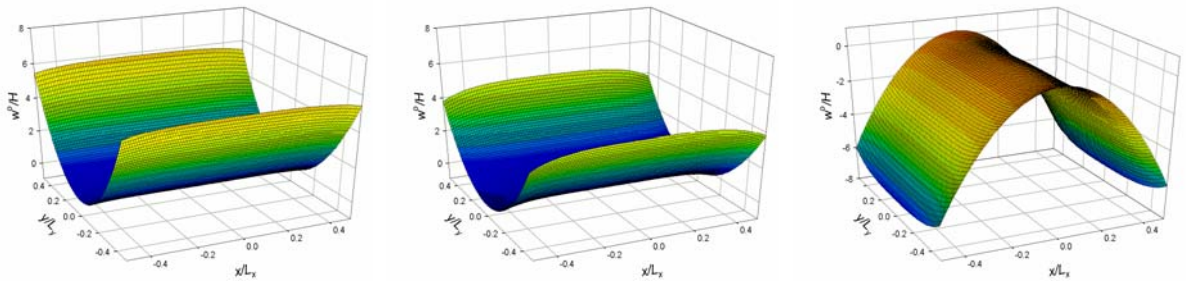

(a) With -2 MV/m field (on branch $A^{N2}D^{N2}$)

b) Without electrical field (on branch $A'D'$)

(c) With +2 MV/m field (on branch $A^{P2}D^{P2}$)

Figure 5.11: Out-of-Plane Shapes of LIPCA-C2 under Electrical Voltage Actuation (L_x/H = 200, L_y/L_x = 0.7, ΔT = -142 °C)

Figure 5.12 illustrates the average curvature of square LIPCA-C2 actuators due to an application of ±2 MV/m electric fields vs. sidelength-to-thickness ratio. As can be seen, the enhancement and suppression of the changes in actuated curvatures in this figure, as compared to those in Figure 5.10, are more pronounced because of the stronger geometrically nonlinear effects of the wider actuator. Overall, the behaviors of the LIPCA-C2 actuators with an aspect ratio of 0.7 and 1 as a function of sidelength-to-thickness ratio when subjected to an applied electric field are quite similar.

The influence of sidelength-to-thickness ratio on actuated curvatures of LIPCA-C2 actuators with an aspect ratio of 0.33 is illustrated in Figure 5.13. For this beam-like aspect ratio, geometrically nonlinear effects are weaker than for the aspect ratios of 0.7 and 1 discussed previously. However, the actuation-induced curvature changes in the *x*- and *y*-direction of the beam-like actuators due to a positive voltage increase somewhat in magnitude as sidelength-to-thickness ratio increases. On the other hand, compared to the rectangular and square actuators, the curvature changes due to a negative voltage are large in magnitude. Finally, for these beam-like actuators, it is of value to compare the *x*-direction curvature due to the applied electric field strengths as predicted by the geometrically linear Rayleigh-Ritz predictions with the predictions of the beam theories developed in Appendix B. By employing Equation (B.42) or (B.68), for +2 and -2 MV/m, $K_x = 2.74\ m^{-1}$ and $0.98\ m^{-1}$, respectively. The curvatures calculated from the beam theories are uniform over the range-of-sidelength-to-thickness ratios considered. Their values are fairly close to $K_x = 2.60\ m^{-1}$ and $0.76\ m^{-1}$, the values of the *x*-direction actuated curvatures predicted by the geometrically linear Rayleigh-Rtiz approach.

Viewed differently, the actuation-induced average curvature changes as a function of electric field strength can be considered. For example, LIPCA-C2 actuators with two different actuator sidelength-to-thickness ratios are investigated in Figure 5.14, L_x/H = 200 in Figure 5.14 (a) and L_x/H = 100 in Figure 5.14 (b). Note that only the aspect ratios of

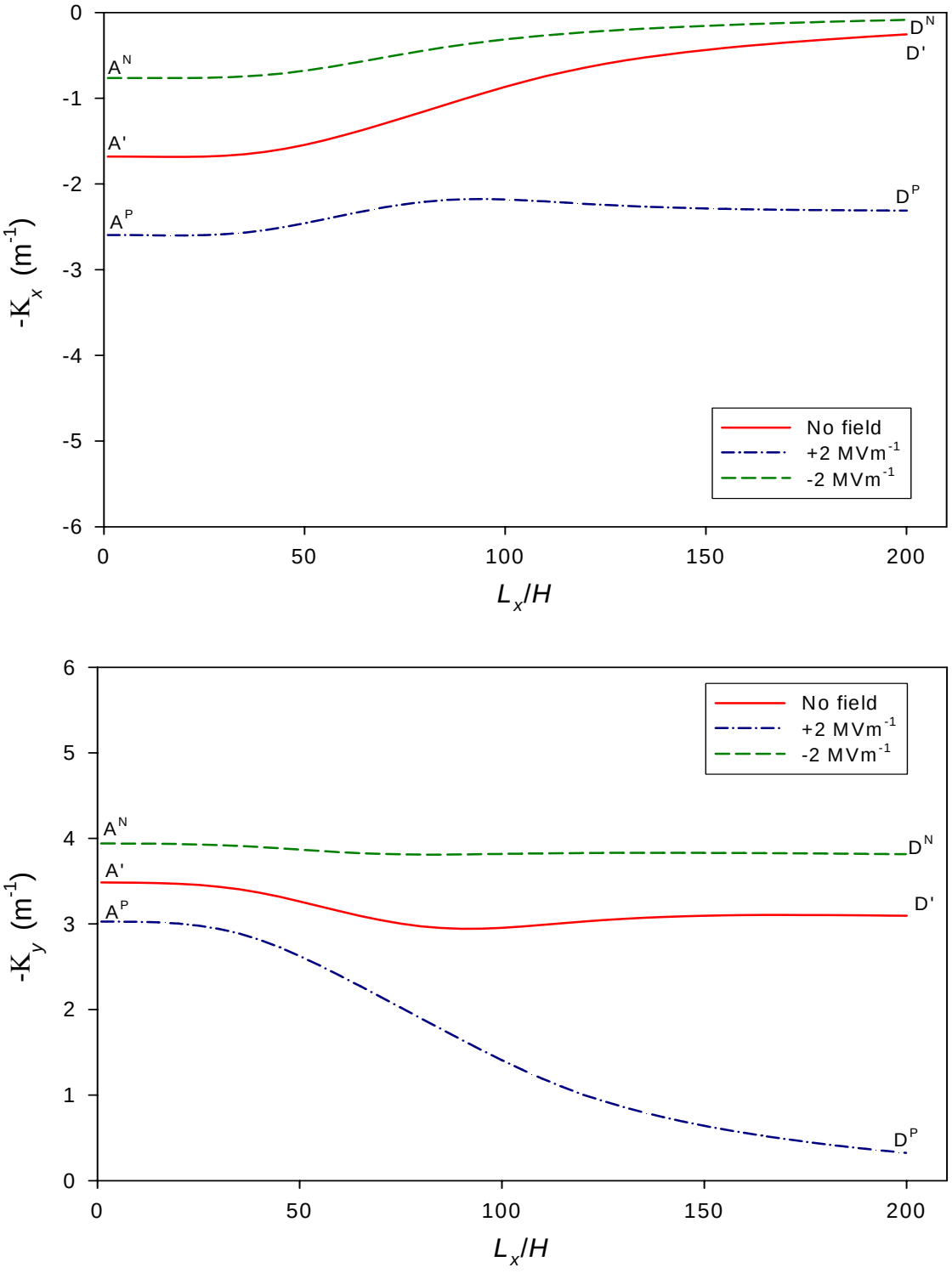

Figure 5.12: Influence of Actuation on the Change of Curvatures of Square LIPCA-C2 (ΔT = -142 °C)

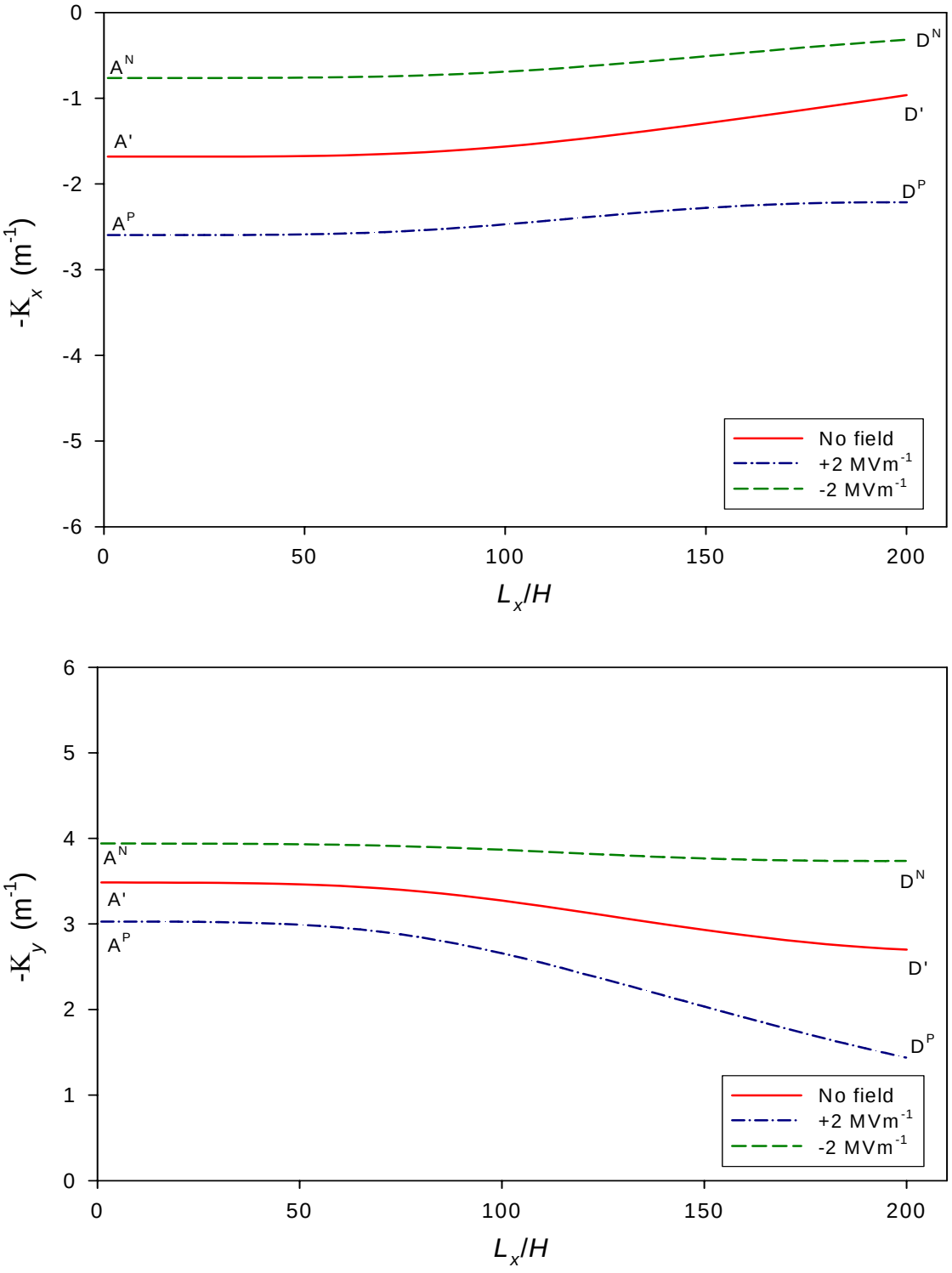

Figure 5.13: Influence of Actuation on the Change of Curvatures of Beam-Like LIPCA-C2 (L_y/L_x = 0.33, ΔT = -142 °C)

0.7 and 0.33 are taken into account in the figure because the actuated curvature vs. sidelength-to-thickness ratio relations at L_y/L_x =1 in Figure 5.12 are very similar to those at L_y/L_x = 0.7 in Figure 5.10. As a result, it is anticipated that the actuation-induced average curvature changes vs. electric field strength relations for the two aspect ratios are also very similar. Furthermore, without the relations for L_y/L_x =1, the plots in Figure 5.14 are less cluttered and it is easier to study the behavior of the LIPCA-C2 actuators as a function of electric field strength. Firstly, referring to Figure 5.10, the large difference in the change of curvature for positive voltages compared to negative voltages for large sidelength-to-thickness ratios for the LIPCA-C2 design can be explained by considering Figure 5.14 (a). For the case of the actuator with aspect ratio 0.7 and positive field strength, the relationships for both the *x*- and *y*-direction curvatures exhibit unusual behavior. Specifically, when the field strength reaches about +1.3 MV/m, rather than the curvature changing smoothly and monotonically with increasing field strength, the curvature changes abruptly. This occurs because the actuator suddenly changes configuration by way of a snap-through phenomenon. This is a dynamic event, and the snapped configuration has curvatures of larger and smaller magnitude, respectively, in the *x*- and *y*-directions than the configuration just before snapping. This snap-through phenomenon is the reason why the actuated shape of the LIPCA-C2 actuator with +2 MV/m illustrated in Figure 5.11 (c) is very different from the room-temperature shape without any electric field applied in Figure 5.11 (b). Also, the phenomenon is much like the change in configuration of THUNDER actuators that can be observed by applying moments along the edges of the actuator to induce snap through back and forth between branch $A'D'$ and branch $B'C'$ in Figure 3.8, as discussed in Section 3.2.3 for an actuator with L_x/H = 200. However, the snap-through phenomenon in Figure 5.14 (a) is induced by an applied electric field instead of a mechanical moment. For the beam-like LIPCA-C2 actuator, L_y/L_x = 0.33, the snap-through phenomenon does not occur, though the curvature change relationships are nonlinear with applied voltage. Note that according to

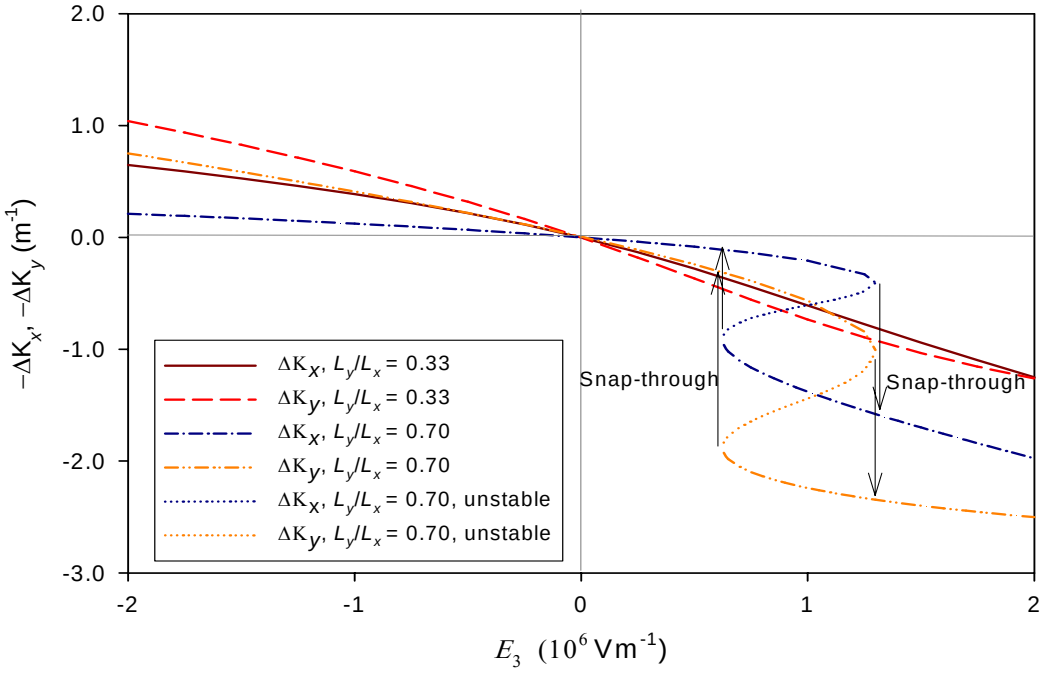

(a) L_x/H = 200

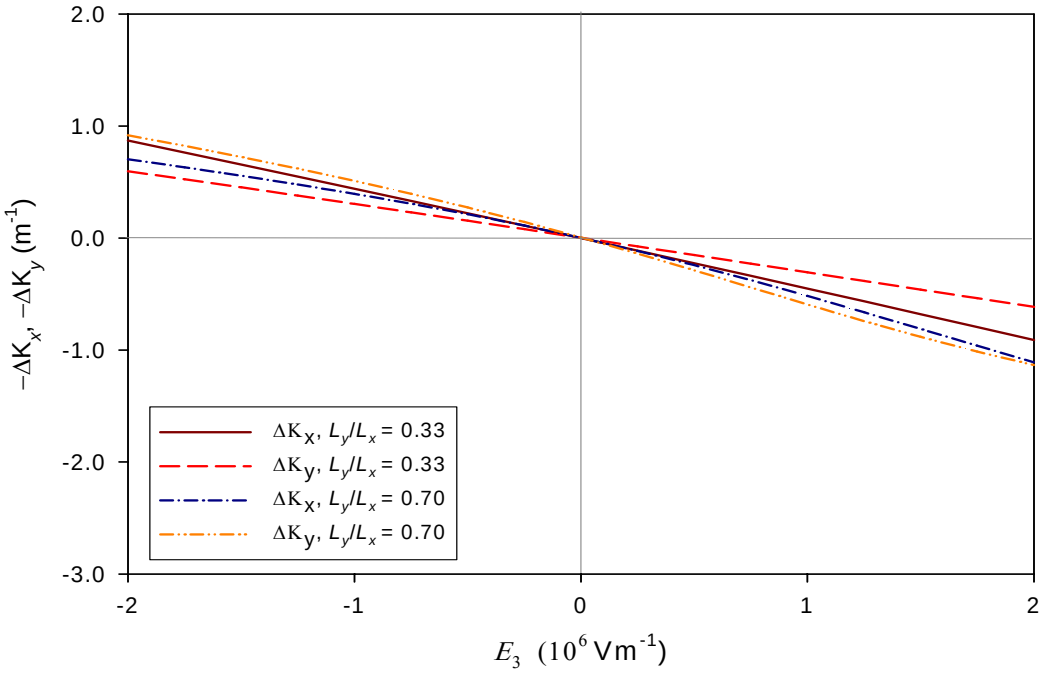

(b) L_x/H = 100

Figure 5.14: Influence of Actuation on the Change of Curvatures of LIPCA-C2 (ΔT = -142 °C)

Figure 5.14 (a), the change in the *y*-direction curvature due to an applied electric field is always larger than the change in the *x*-direction curvature. This is, in a way, not desirable, since based on the design intention, the functionality of the LIPCA-C2 actuators are utilized along the *x*-direction, not the *y*-direction. Thus, more authority should be expected from the *x*-direction free actuation response. However, this is not the case.

For the case of sidelength-to-thickness ratio L_x/H = 100, illustrated in Figure 5.14 (b), the snap-through phenomenon does not occur for either aspect ratio considered, though, as can be seen, the curvature change vs. field strength relation is slightly nonlinear for the rectangular actuator with the aspect ratio of 0.7. Also, for the rectangular actuator the change in the *y*-direction curvature due to an applied electric field is larger than that in the *x*-direction curvature. However, for the beam-like actuator with L_y/L_x = 0.33, the change in the *y*-direction curvature is smaller than in the *x*-direction. Therefore, this beam-like LIPCA-C2 actuator is superior to the others in Figure 5.14 in terms of the larger actuated curvature occurring in the preferred direction.

Before closing this section, it is of value to study the snap-through phenomenon induced by an applied electric field for a LIPCA-C2 actuator in more detail. The phenomenon can be explained further by considering Figure 5.15. The figure is similar to Figure 5.10, but considers only positive voltage levels. The legends are also different. The figure is complicated, but it explains the snap-through phenomenon illustrated in Figure 5.14 (a). Figure 5.15 illustrates the *x*- and *y*-direction curvatures as a function of sidelength-to-thickness ratio for several levels of increasing electric field strengths, starting with the no-field level and including +0.7 MV/m, +1 MV/m, +1.2 MV/m, +1.3 MV/m, and +2 MV/m. Considering the case L_x/H = 200, for no electric field, the *x*- and *y*-direction curvatures are about 0.3 m^{-1} and 3.1 m^{-1}, respectively, as given by branch A′D′. As the field strength is increased, the curvatures are determined by moving downward on a vertical line constructed at L_x/H = 200. As can be seen, for a field strength of +0.7 MV/m, there are three possible

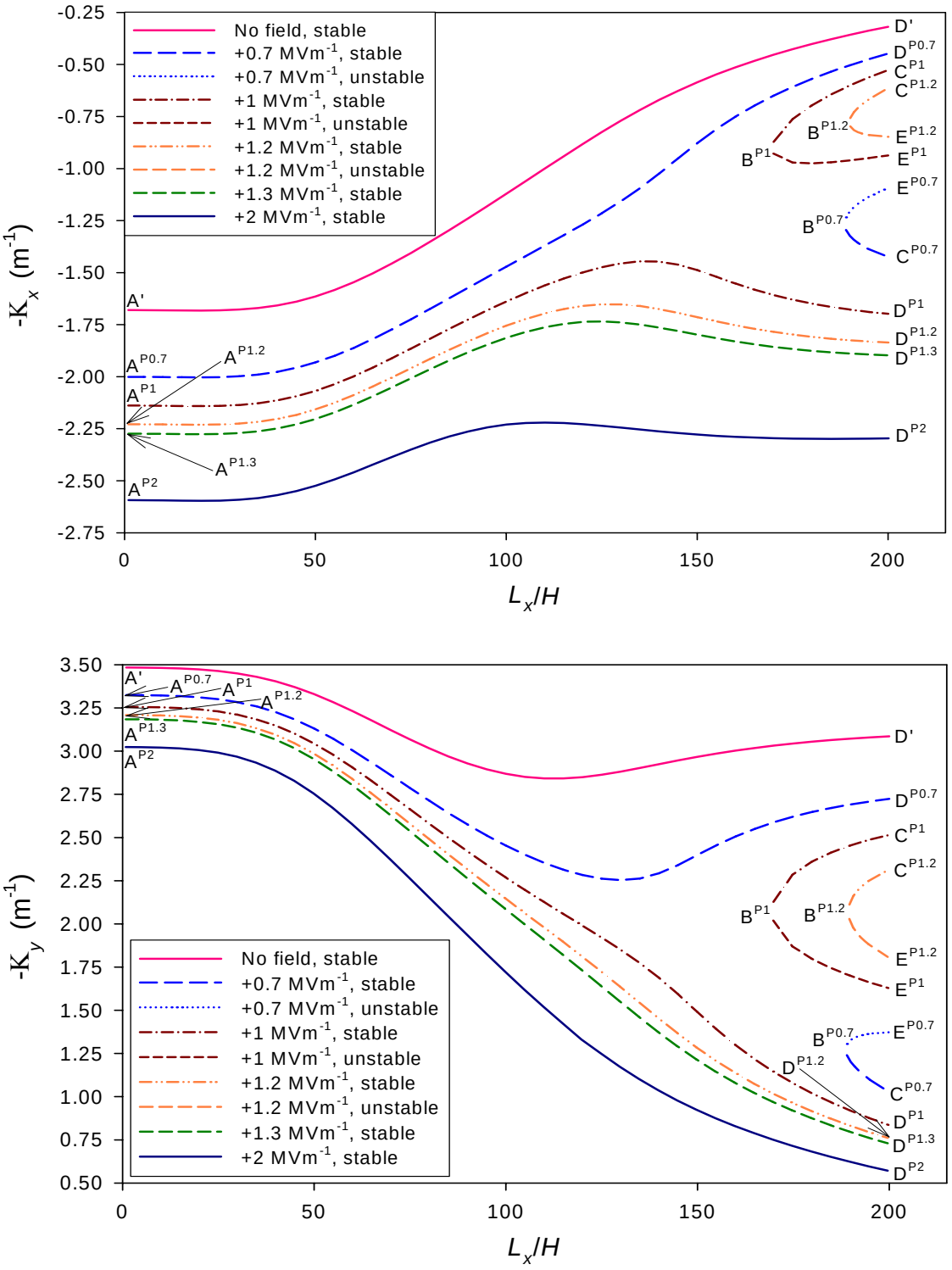

Figure 5.15: Curvature vs. Sidelength-to-Thickness Ratio Relations for Rectangular LIPCA-C2 actuators, L_y/L_x = 0.7, various positive field strengths

curvatures in each direction. These are given by branches $A^{P0.7}D^{P0.7}$, $B^{P0.7}E^{P0.7}$, and $B^{P0.7}C^{P0.7}$. Branch $B^{P0.7}E^{P0.7}$ represents unstable configurations, but when the field strength is gradually increased from zero, the curvatures change smoothly from branch $A'D'$ to branch $A^{P0.7}D^{P0.7}$, so the existence of branch $B^{P0.7}E^{P0.7}$ is not an issue. For a field strength of +1 MV/m, there are also multiple branches that are appropriately labeled. The curvatures move smoothly to branch $B^{P1}C^{P1}$ and then to branch $B^{P1.2}C^{P1.2}$ for a field strength of +1.2 MV/m. Notice that for increasing field strength, the U-shaped branches denoted by C, B, and E are moving to the right. For a field strength less than +1.3 MV/m, there are multiple curvature levels, two associated with the U-shaped branches and one with the other branch. For a field strength of +1.3 MV/m, there is no U-shaped branch on the figure. The U-shaped branch has move to the right, off the figure. There is thus only a single solution branch, and that solution branch is much further down the vertical line at L_x/H = 200, i.e., the solution has to jump because the U-shaped branch has moved out of contention. This is the snap through shown in Figure 5.14 (a) at +1.3 MV/m. A reverse jump also occurs at around +0.6 MV/m when the field strength is decreased from +2 MV/m to zero, as indicated in Figure 5.14 (a). Consequently, during the decrease of the electric field strength less than +2 MV/m but more than +0.6 MV/m, the curvatures changes smoothly. For example, as the field strength is decreased from +2 MV/m to +0.7 MV/m, the curvatures move from branch $A^{P2}D^{P2}$ to branch $B^{P0.7}C^{P0.7}$ without a snap-through occurring, smoothly passing branches $A^{P1.3}D^{P1.3}$, $A^{P1.2}D^{P1.2}$, and $A^{P1}D^{P1}$. However, when the electric field strength is decreased to be lower than +0.6 MV/m, the actuated curvatures jump, or snap, to a branch that lies between the branch $A'D'$ and $A^{P0.7}D^{P0.7}$, and finally back to branch $A'D'$ when the field is reduced to be zero. Additionally, as can be seen, for values of L_x/H less than 200, there are other values of field strength for which U-shaped branch is too far to the right for a smooth curvature increase with increasing field strength, so the snap-through phenomenon occurs. It can be concluded that for every actuator design, there could be a range of geometries and

field strengths where this phenomenon occurs and it needs to be investigated for particular actuator designs.

5.3.2 Stress Characteristics of LIPCA-C2 subjected to Applied Electric Field

The through-the-thickness stress distributions of the LIPCA-C2 actuator with L_y/L_x = 0.7 and L_x/H = 200 subjected to ±2 MV/m applied electric field are illustrated in Figures 5.16 and 5.17. The former figure shows the stress distributions at the location near the center (x = 0, y = 0) and the latter figure shows the stress distributions near the midpoint of the longer edge (x = 0, $y = L_y/2$). The room-temperature stress-distributions caused by the elevated temperature manufacturing process, as shown in Figure 5.8, are also included in the figures as references for no-electric field condition. As seen in the figures, and as was discussed before, there is some tensile residual stress in the x-direction at room temperature in the piezoceramic layer, and the stress changes sign with the applied electric field. The sign changes in the stress in the piezoceramic layer could be detrimental to the fatigue life of the actuator. The sign of the stress in the y-direction in the piezoceramic layer does not change sign, nor are there sign changes in the composite layers. The sign changes of the stress are a direct function of the magnitude of the applied voltage. Note that at a particular thickness location, the change in stress component σ_x in the carbon-epoxy layer is generally larger than the change in stress component σ_y in the same layer. This is because the layer is very stiff in the x-direction, so the changes in σ_x in the layer due to actuation are significant. On the other hand, the layer is very soft in the y-direction and thus the changes in σ_y are much less affected. These behaviors are like that of the LIPCA-C1 actuator illustrated in Figures 4.13 and 4.14 because the both actuators share the same types of materials used, despite different stacking sequences. The changes in the stress in the LIPCA-C2 actuator are more significant than for the THUNDER and LIPCA-C1 actuators because of the change in actuator configuration that accompanies the snap-through phenomenon for positive field strengths. In actuality, by merely looking at Figures 5.16 and 5.17 it is obvious that the

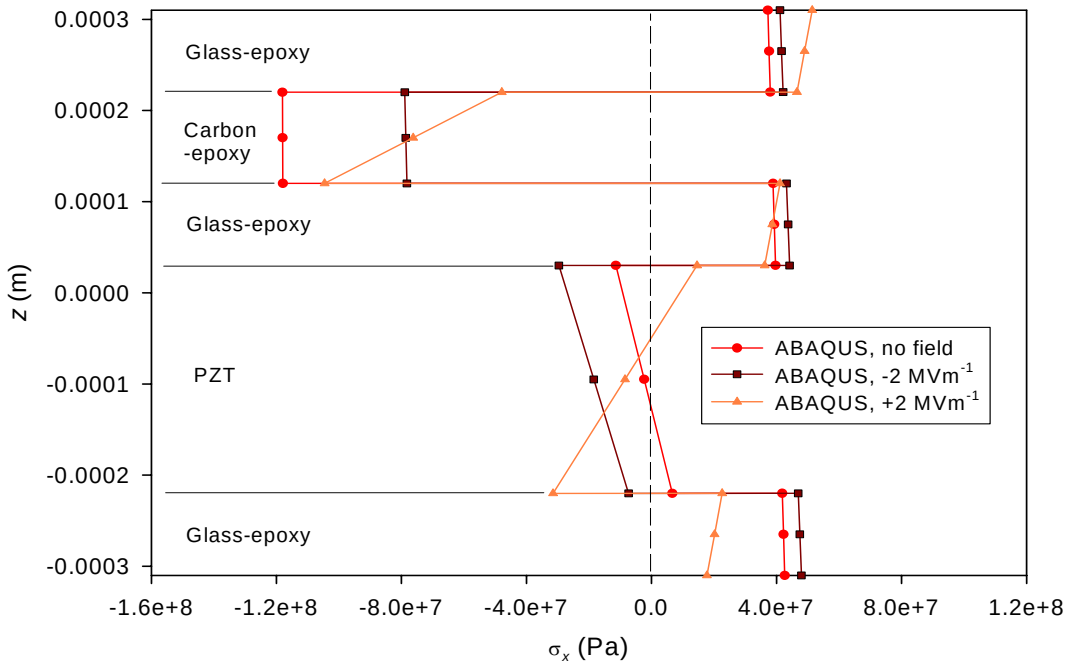

(a) Distribution of Normal Stress in the *x*-direction near Center, $x \cong 0, y \cong 0$

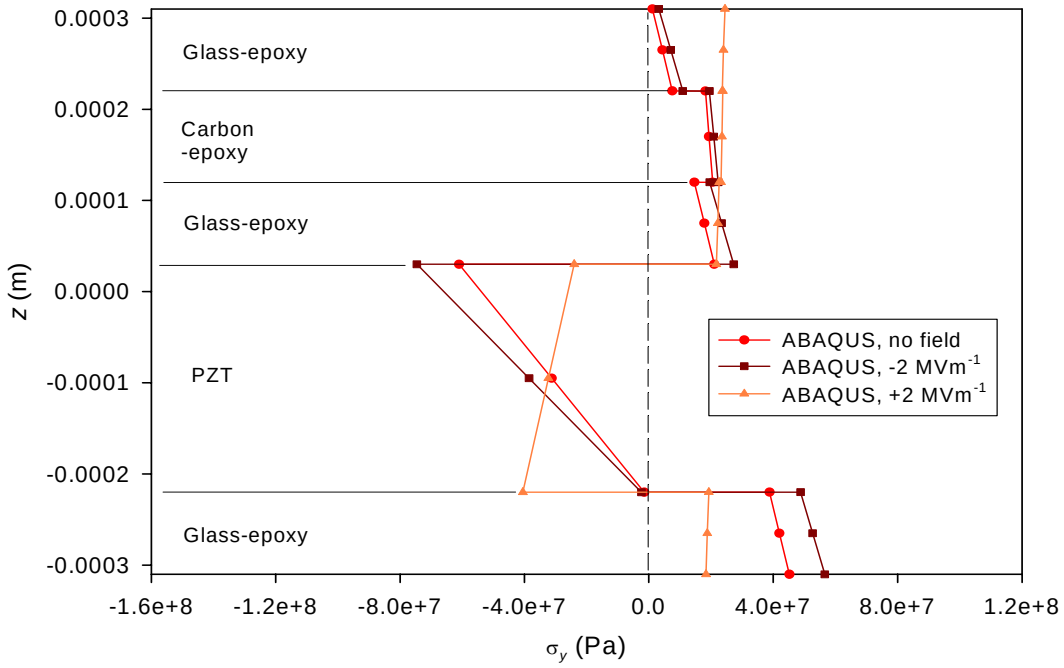

(b) Distribution of Normal Stress in the *y*-direction near Center, $x \cong 0, y \cong 0$

Figure 5.16: Stress distributions in rectangular LIPCA-C2 near center when subjected to applied electric fields, $L_y/L_x = 0.7$, $L_x/H = 200$

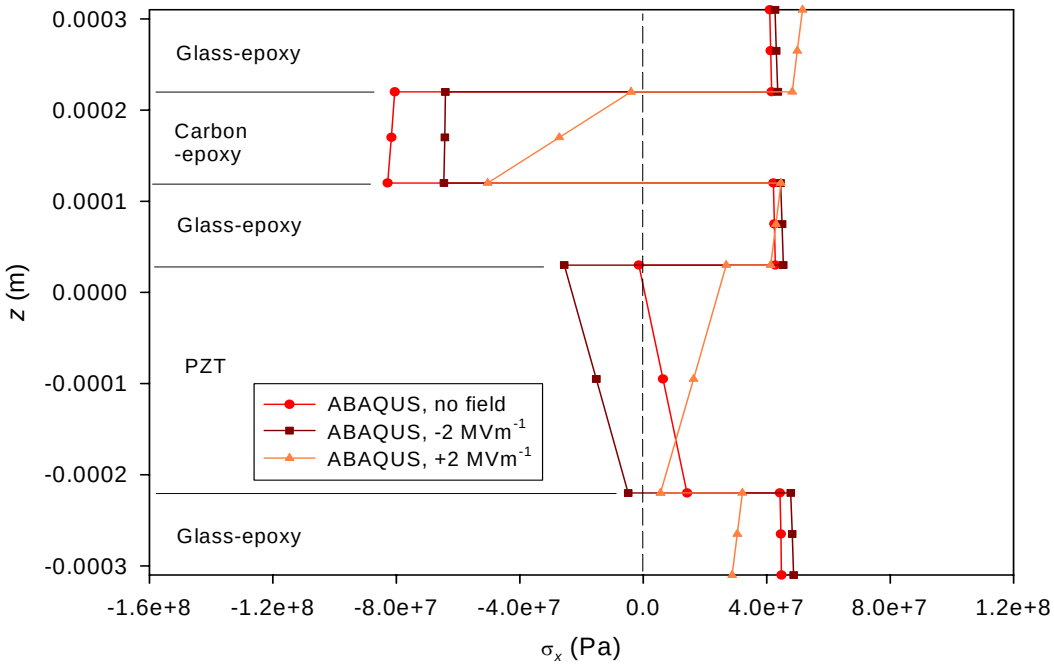

(a) Distribution of Normal Stress in the *x*-direction near Edge, $x \cong 0, y \cong L_y/2$

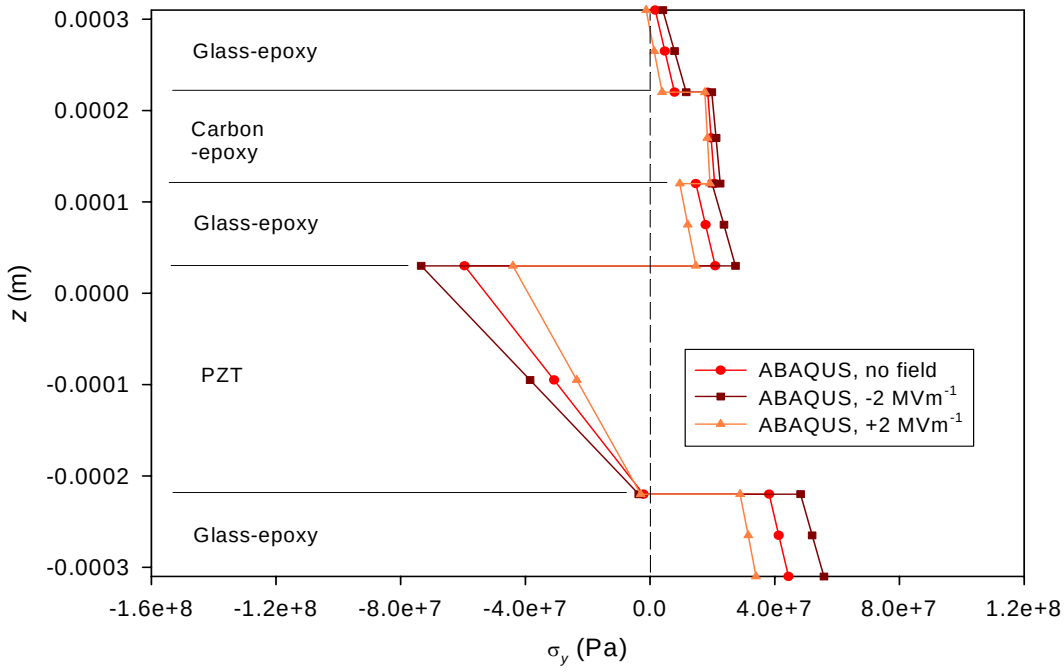

(b) Distribution of Normal Stress in the *y*-direction near Edge, $x \cong 0, y \cong L_y/2$

Figure 5.17: Stress distributions in rectangular LIPCA-C2 near midpoint of longer edge when subjected to applied electric fields, $L_y/L_x = 0.7$, $L_x/H = 200$

curvatures of the LIPCA-C2 actuator change sign after snap-through phenomenon, which is induced by the positive field strengths. This is because the gradients of the stress distributions in all layers change sign between the no-field or negative-field state and the positive-field state. The only exception is seen in Figure 5.17 (b), in which the gradient of stress distributions does not change sign for +2 MV/m. This is a local behavior of stress component σ_y due to edge effects and does not represent the overall change in curvature in the *y*-direction. Unlike for THUNDER actuators, for which the piezoceramic materials are in biaxial compression within the range ±2 MV/m, it appears there will always be a small volume of piezoceramic material in LIPCA-C2 actuators that changes sign with changing electric field, no matter how small the magnitude of the applied field.

5.4 Numerical Results for Blocking Forces

5.4.1 Blocking Forces of LIPCA-C2 as a Function of Electric Field Strength

Consider LIPCA-C2 actuators with an aspect ratio L_y/L_x = 0.7 and sidelength-to thickness ratios of 100 and 200 with shapes given by Figure 5.1 or 5.10. Figure 5.18 shows relations between the blocking forces and applied electric field E_3. The blocking forces of the LIPCA-C2 actuators with pinned-roller and pinned-pinned supports are illustrated in the figure. Like LIPCA-C1 actuators of Figure 4.15, the blocking force P_{bl} for the pinned-pinned case is of opposite sign to the blocking force P_{bl} for the pinned-roller case, which is not the case for THUNDER actuators of Figure 3.26. It is seen from Figure 5.18 that the blocking force relations for the pinned-roller and pinned-pinned cases for L_x/H = 100 can be approximated as linear functions of applied electric field strength over the range ±2 MV/m. However, blocking force relations for the two support cases for L_x/H = 200 vary nonlinearly with electric field strength. First, consider the pinned-roller case. The magnitude of force P_{bl} for L_x/H = 100 is lower than that for L_x/H = 200 over the range ±2 MV/m. For applied negative voltages, the blocking force relation for L_x/H = 200 is curved toward the blocking

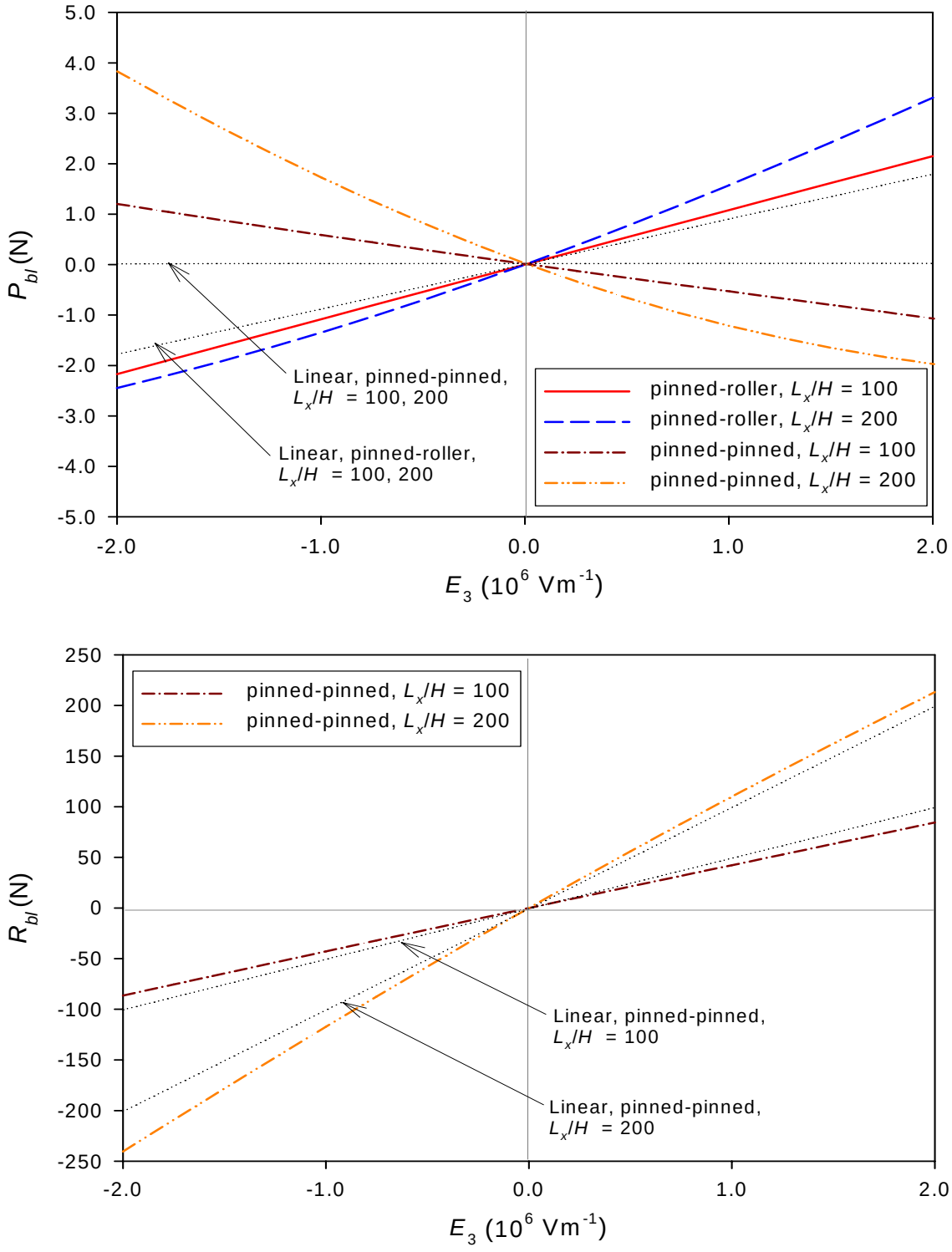

Figure 5.18: Blocking Force vs. Electric Field Relations of Rectangular LIPCA-C2 (L_y/L_x = 0.7)

force relation for L_x/H = 100 or, equivalently, the rate of change of P_{bl} vs. applied electric field is decreased. This is because the actuated curvature in the *x*-direction for L_x/H = 200 and a negative field is suppressed compared to the linear prediction, as illustrated in Figure 5.10. On the other hand, for a positive field, the blocking force relation for L_x/H = 200 deviates from that for L_x/H = 100 or, in the other words, the rate of change of P_{bl} vs. applied electric field increases, since the actuated curvature in the *x*-direction for L_x/H = 200 is enhanced. Note that the relationship between blocking force P_{bl} and applied electric field strength for L_x/H = 100 is close to the geometrically linear prediction, which is computed to be identical for the two sidelength-to-thickness ratio considered. For the pinned-pinned case, as mentioned, as compared to the pinned-roller case, a blocking force P_{bl} of opposite sign is obtained at a given electric field strength. At L_x/H = 100, the magnitude of force P_{bl} is smaller than that for the pinned-roller case by a factor of two. However, when the value of sidelength-to-thickness ratio is doubled, the magnitude of force P_{bl} is around one and a half times larger than that for the pinned-roller case for negative fields. This inconsistent behavior occurs due to very strong nonlinear effects as the actuator size is increased. Sidelength-to-thickness ratio effects also have an influence on force R_{bl}, since the magnitude of force R_{bl} for L_x/H = 200 compared to L_x/H = 100 is approximately three times greater for negative fields, despite being only two times greater based on the predictions of the geometrically linear theory. Like the pinned-roller case, the linear theory predictions of force P_{bl} for the pinned-pinned case are independent of sidelength-to-thickness ratio. However, the linear theory predictions for R_{bl} are dependent on sidelength-to-thickness ratio and the force and sidelength-to-thickness ratio are linearly proportional. Finally, it should be noted that the values of P_{bl} resulting from the linear theory for the pinned-pinned support case are very small and seen as a nearly horizontal dotted line on the upper portion of Figure 5.18.

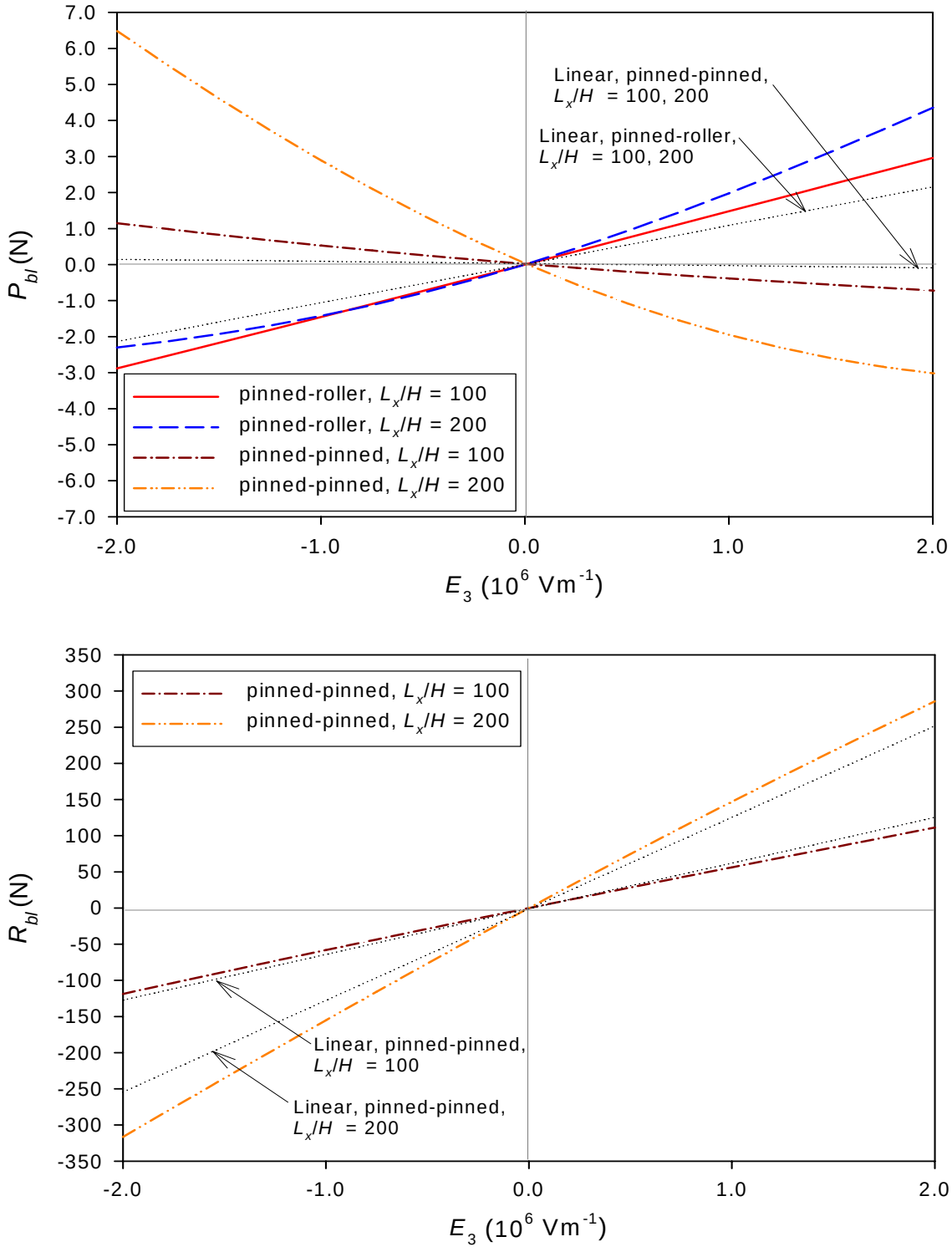

Figure 5.19: Blocking Force vs. Electric Field Relations of Square LIPCA-C2

The relations between blocking forces and electric field strength for square LIPCA-C2 actuators with L_x/H = 100 and 200 with shapes given by Figures 5.3 and 5.12 are illustrated in Figure 5.19. Effects of geometrical nonlinearities on the relations can be noticed more easily when the sidelength-to-thickness ratio is increased from 0.7 to 1, since most of the relations shown in Figure 5.19 cannot be approximated as linear functions of applied electric field within the range ±2 MV/m. For the pinned-roller case, as compared to Figure 5.18, the value of blocking force P_{bl} for L_x/H = 100 is larger over the entire range of electric field strength considered. The value of blocking force P_{bl} for L_x/H = 200 is larger over the entire range of applied voltage, except for large negative electric field strength. This is because the significant suppression of change in the *x*-direction curvature due to the negative-field actuation for L_x/H = 200 in Figure 5.12. For the pinned-pinned case, the value of blocking force P_{bl} for L_x/H = 100 is slightly smaller than that for L_x/H = 100 in Figure 5.18. Nevertheless, the opposite behavior can be observed for L_x/H = 200 because the blocking force P_{bl} is larger than that in Figure 5.18. The value of force P_{bl} for L_x/H = 200 is also considerably larger than that for L_x/H = 100. In addition, as can be seen, at any applied electric field strength, the square LIPCA-C2 actuators always have a higher blocking force R_{bl} than the rectangular one previously discussed.

Lastly, the relations between blocking forces and electric field strength for beam-like LIPCA-C2 actuators with L_y/L_x = 0.33 and L_x/H = 100 and 200 are illustrated in Figure 5.20. In general, as seen in the figure, the relations between blocking forces and electric field strength are similar to those in Figure 5.18 and 5.19. However, to all intents and purposes, all of the blocking force relations vary linearly with applied electric field strength due to the beam-like configuration of the actuators. Note that even though the relations are approximately linear relative to an applied electric field, the geometrically linear theory still cannot predict the relations accurately in some cases, particularly the pinned-pinned case. For the pinned-roller case, the blocking force relation for L_x/H = 100 is

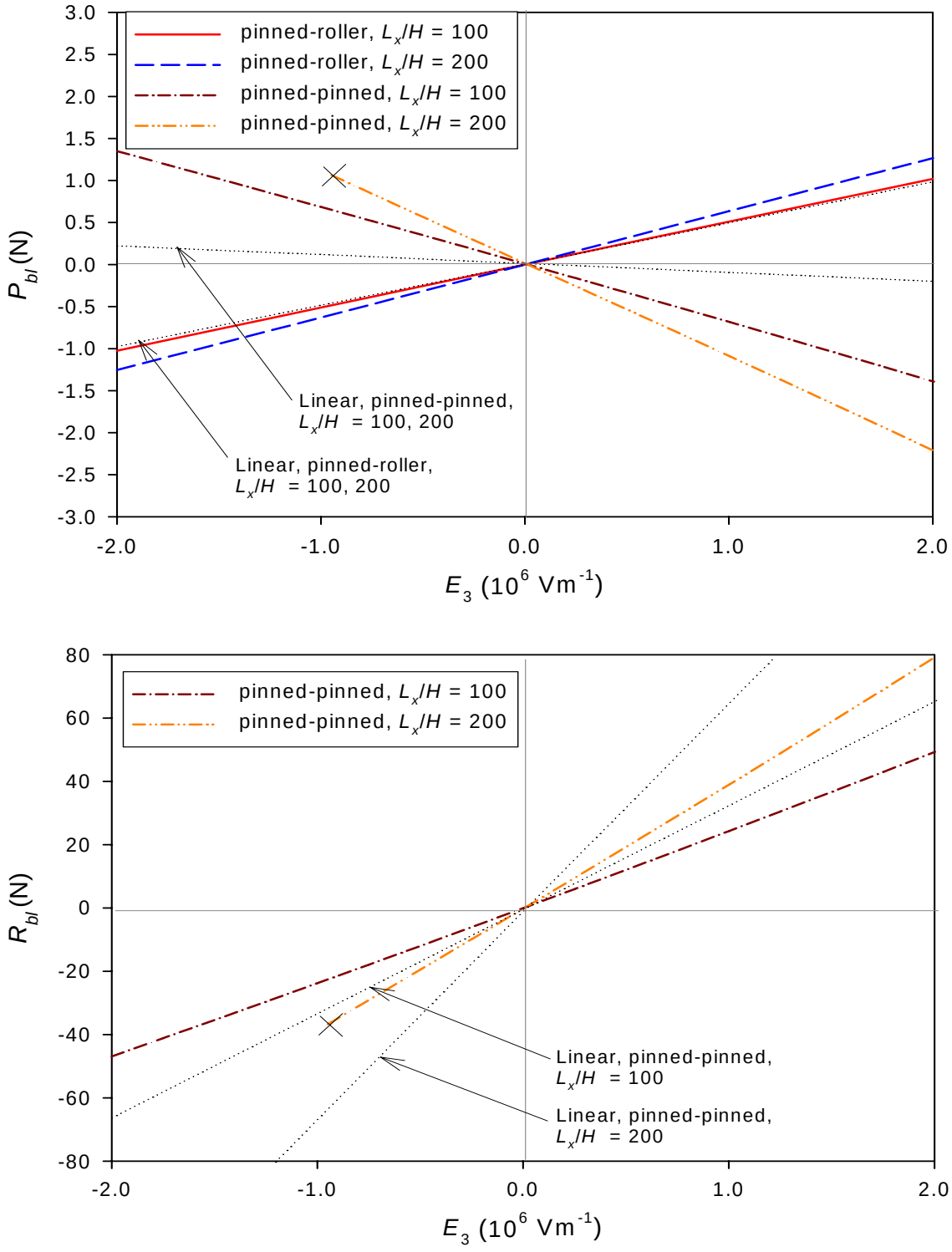

Figure 5.20: Blocking Force vs. Electric Field Relations of Beam-Like LIPCA-C2 (L_y/L_x = 0.33)

very close to the linear prediction, while the relation for L_x/H = 200 is around 25% higher in magnitude than the prediction from the linear theory. The magnitudes of force P_{bl} for both L_x/H = 100 and 200 are lower than the corresponding ones for aspect ratios of 0.7 and 1 illustrated in Figure 5.18 and 5.19, respectively. For the pinned-pinned case, the magnitude of blocking force P_{bl} for L_x/H = 100 is larger than that of the pinned-roller supported actuator with the same sidelength-to-thickness ratio. It is also larger than the magnitude of force P_{bl} for L_x/H = 100 for the two larger aspect ratios considered because of geometrically nonlinear effects with the larger aspect ratios. As the sidelength-to-thickness ratio is doubled, the magnitude of force P_{bl} is increased by approximately 70% compared to that for L_x/H = 100. The magnitudes of force R_{bl} for L_x/H = 100 and 200 are lower than the corresponding ones for aspect ratios of 0.7 and 1. Finally, it should be noted that for the value of sidelength-to-thickness ratio of 200, there exists a region where the algorithm presented in Section 2.4.3 fails to converge and, thus the associated blocking forces P_{bl} and R_{bl} cannot be solved for. The mark '×' represents the terminated point where the algorithm begins to have convergence failure when the magnitude of the negative electric field strength is increased. It is believed that the convergence failure is due to a change in the configuration or snap-through phenomenon of the actuator induced by the blocking forces P_{bl} and R_{bl}. Such a phenomenon cannot be captured by the blocking force analysis here.

5.4.2 Blocking Forces of LIPCA-C2 as a Function of Sidelength-to-Thickness Ratio: Pinned-Roller Case

As with THUNDER and LIPCA-C1 actuators, in addition to studying the relationships between blocking forces and electric field strength, it is also of value to study the dependency of blocking forces on the sidelength-to-thickness ratio when LIPCA-C2 actuators are subjected to applied voltages of ±2 MV/m. Analogous to the blocking force analyses for pinned-roller supported THUNDER and LIPCA-C1 actuators presented in Sections 3.4.2 and 4.4.2, respectively, the blocking force vs. electric field strength relations

for pinned-roller LIPCA-C2 actuators will be computed and analyzed for three aspect ratios, i.e., L_y/L_x = 0.7, 1, and 0.33.

First, consider Figure 5.21. The figure illustrates the relations between blocking force P_{bl} and sidelength-to-thickness ratio for pinned-roller supported LIPCA-C2 actuators with an aspect ratio of 0.7. As before, for both the +2 MV/m and -2 MV/m field strengths, the ordinate axis is normalized by a blocking force of a LIPCA-C2 actuator with L_x/H approaching zero, the result for the geometrically linear theory. Therefore, at very small values of sidelength-to-thickness ratio, $0 < L_x/H < 40$, the normalized values of the force P_{bl} for ±2 MV/m are approximately equal to one. When L_x/H increases, the values of force P_{bl} gradually increase. In the range of $40 < L_x/H < 120$, the relations for ±2 MV/m nearly coincide. Beyond $L_x/H = 120$, the values of normalized P_{bl} separate from each other. For +2 MV/m the value of normalized P_{bl} still increases monotonically. In contrast, the value of

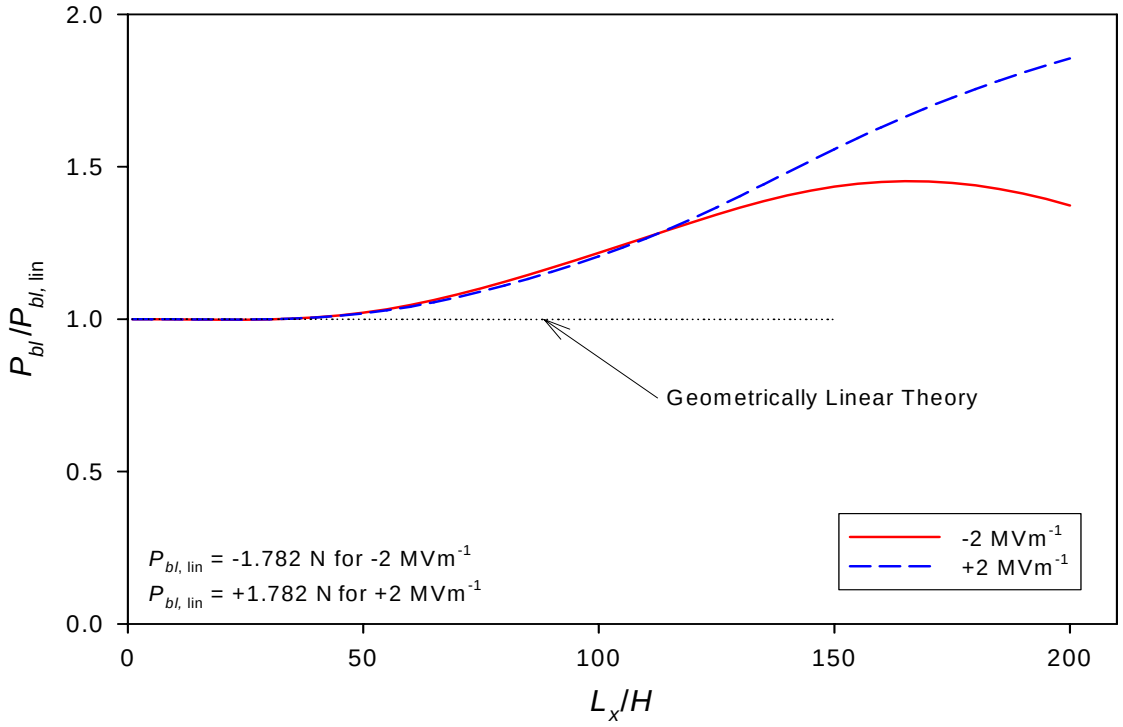

Figure 5.21: Blocking Force vs. Sidelength-to-Thickness Ratio Relations of Pinned-Roller Supported Rectangular LIPCA-C2 (L_y/L_x = 0.7)

normalized P_{bl} for -2 MV/m increases and then decreases as sidelength-to-thickness ratio increases beyond 170. According to the figure, an enhancement of blocking force P_{bl} can be observed in the range of $40 < L_x/H < 200$. Additionally, it should be noted that when compared to the changes in curvatures due to actuation as shown in Figure 5.10, the blocking force P_{bl} is not proportional to the changes in the *x*-direction curvature, particularly for negative field strengths, but are somewhat proportional to curvature changes in the *y*-direction. This is because the curvature suppression in the *x*-direction, when the electric field strength of -2 MV/m is applied, should not produce enhancement of the corresponding blocking force P_{bl}. There must be a contribution from the enhancement of the change in the *y*-direction curvature. In fact, this hypothesis is believed to support the cases of THUNDER and LIPCA-C1 actuators as well. However, the contribution from the changes in the *y*-direction curvature for those actuators is not as obvious as the LIPCA-C2 actuators because the changes in the *y*-direction curvature are strongly suppressed for the THUNDER and LIPCA-C1 actuators. The blocking forces predicted by the geometrically linear theory, $P_{bl,lin}$, are also illustrated in the figure. The prediction exhibits constant blocking forces for ±2 MV/m (±1.782 N, respectively) regardless of sidelength-to-thickness ratio values and therefore are drawn as coincident horizontal lines with values equal to one. Finally, it is essential to note that in accordance with Figure 5.21, designing a pinned-roller supported LIPCA-C2 actuator in the region of $40 < L_x/H < 200$ to carry a transverse load has an advantage from geometrically nonlinear effects. When compared to pinned-roller supported THUNDER and LIPCA-C1 actuators presented in Figure 3.29 and 4.18, respectively, a pinned-roller supported LIPCA-C2 actuator has a higher load-carrying capability. Like the LIPCA-C1 actuator and unlike the THUNDER actuator, for the sidelength-to-thickness ratios considered, there is enhancement. However, unlike the LIPCA-C1 actuators, the difference between positive and negative electric field strengths could be considered a disadvantage.

Analogous to Figure 5.21, Figure 5.22 illustrates the relations between the blocking force and sidelength-to-thickness ratio for pinned-roller supported LIPCA-C2 actuators with an aspect ratio of 1 subjected to ±2 MV/m. Generally, the relations in the figures are very similar to the case of aspect ratio 0.7 just discussed. A linear behavior of the relations takes place when L_x/H is small, but the linear range is shorter than that of the LIPCA-C2 actuators with an aspect ratio of 0.7 because it only covers the range $0 < L_x/H < 35$ as opposed to $0 < L_x/H < 40$. When $L_x/H > 35$, the normalized blocking forces increases with increasing L_x/H. Below L_x/H = 90, the blocking forces for ±2 MV/m roughly coincide. Beyond this sidelength-to-thickness ratio, the two blocking force relations gradually separate from each other. The value of normalized force P_{bl} for the positive field strength increases, while that for the negative field strength increases slightly and then decreases. The separation gap between the normalized relations for blocking force P_{bl} for +2

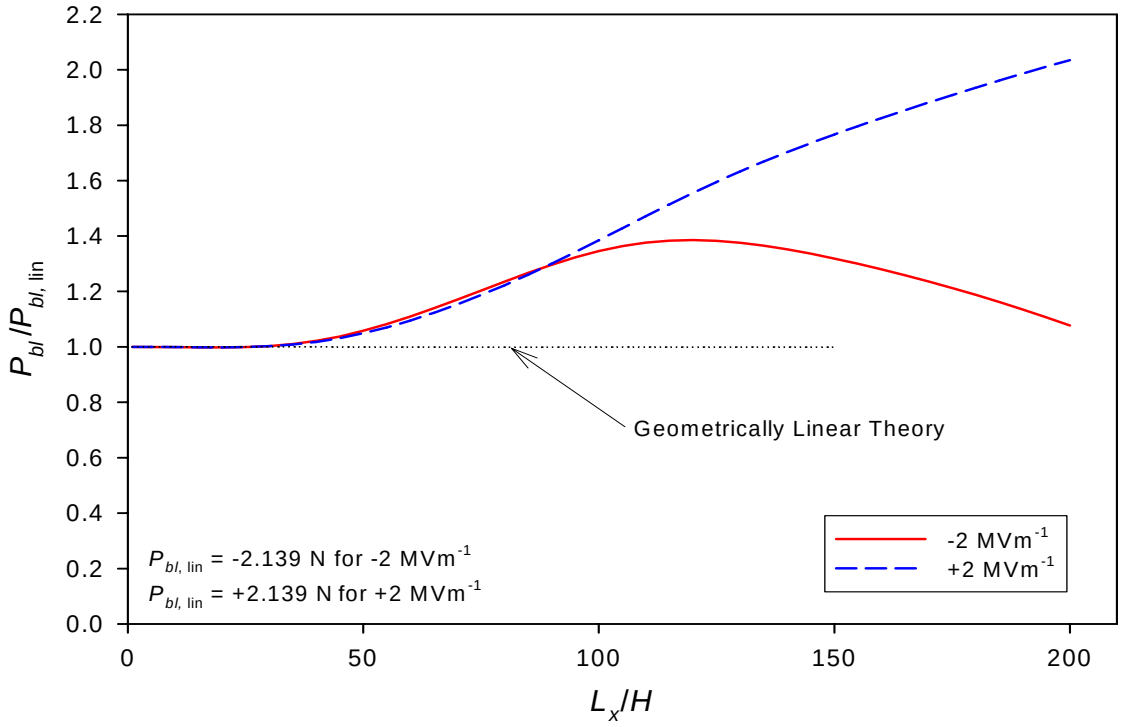

Figure 5.22: Blocking Force vs. Sidelength-to-Thickness Ratio Relations of Pinned-Roller Supported Square LIPCA-C2

MV/ m and -2 MV/m at large sidelength-to- thickness ratios is much larger than that of the actuator with aspect ratio 0.7. The blocking force predicted by the linear theory, $P_{bl,lin}$ is independent of the actuator sidelength-to-thickness ratio and is represented by straight horizontal lines with the unit value. The force $P_{bl,lin}$ of a square LIPCA-C1 actuator is equal to ±2.139 N for ±2 MV/m, respectively. Compared with the pinned-roller supported LIPCA-C2 actuators with L_y/L_x = 0.7, the pinned-roller supported square ones have 20.0% higher blocking force based on the linear theory, and they are 42.9% larger in terms of size.

Considering pinned-roller supported LIPCA-C2 actuators subjected to ±2 MV/m field strength with an aspect ratio of 0.33, shown in Figure 5.23 are relations between the normalized blocking forces and sidelength-to-thickness ratio. When L_x/H < 60, the relations can be approximated by the geometrically linear theory very well. This linear region is the largest of the three aspect ratios considered because the geometric nonlinearity associated

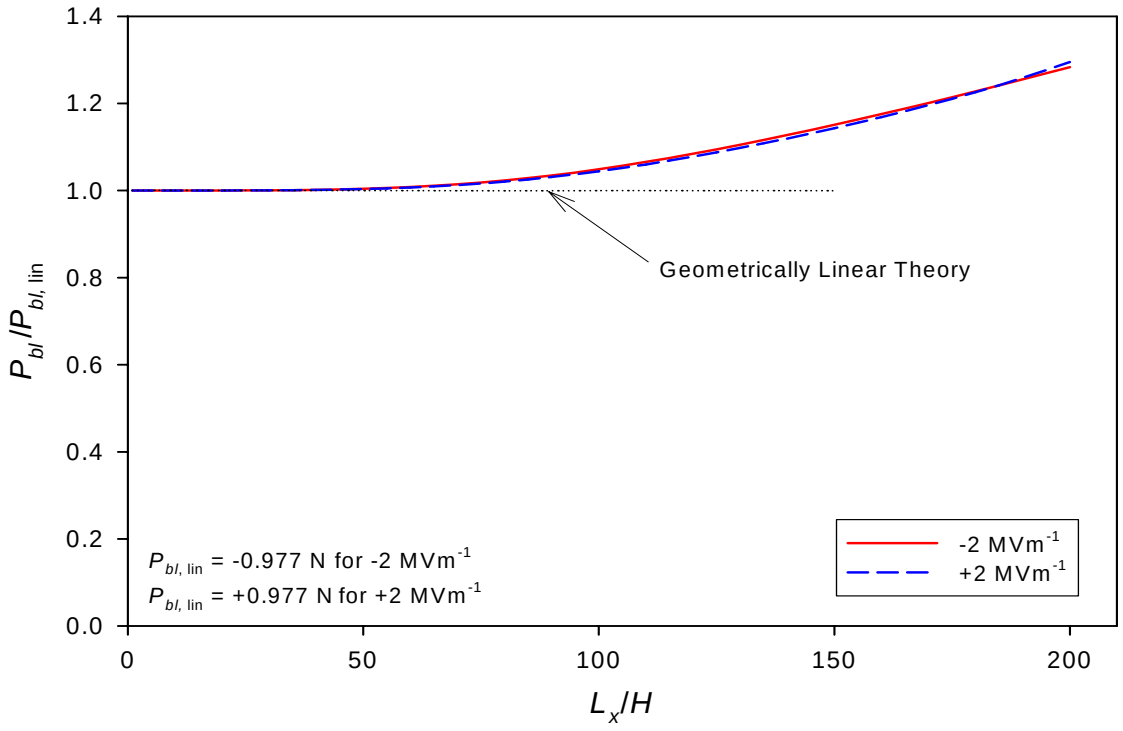

Figure 5.23: Blocking Force vs. Sidelength-to-Thickness Ratio Relations of Pinned-Roller Supported Beam-Like LIPCA-C2 (L_y/L_x = 0.33)

with the beam-like configuration is the weakest among the three aspect ratios. As L_x/H increases beyond 60, the normalized blocking force increases gradually. Unlike the previous two cases of aspect ratios of 0.7 and 1, the normalized relations for blocking force P_{bl} for ±2 MV/m in this case approximately coincide over the entire range of sidelength-to-thickness ratio considered. Thus, to all intents and purposes, there is no apparent separation between the blocking force relations. Also, no decrease in blocking force P_{bl} with increasing L_x/H is observed in the figure, as it was for negative field strengths with the other two aspect ratios. There are similarities with the previous two aspect ratios. Specifically, excluding the linear region for small sidelength-to-thickness ratios, the enhancement of the blocking force P_{bl} is observable over the entire range of sidelength-to-thickness ratio considered ($60 < L_x/H < 200$ for the beam-like aspect ratio). However, the degree of enhancement is smaller than those of the two larger aspect ratios. The linear theory predicts $P_{bl,lin}$ to be ±0.977 N for ±2 MV/m field strength, respectively. The values of $P_{bl,lin}$ in this case are lower than the linear values for an aspect ratio of 0.7 by 45.2%, while the active area of the beam-like actuator is less than that of the rectangular one by 52.9%. Additionally, it can be noted that because of the comparatively small aspect ratio, it is interesting to compare the blocking forces in Figure 5.23 with the ones computed from the nonlinear and linear beam theories developed in Appendix B. By employing Equation (B.41) and (B.67), and setting the relative transverse deflection, w^0, at $x = \pm L_x/2$ due to ±2 MV/m field strength to be zero, the blocking force predictions based on the beam theories can be solved for and found to be ±0.941 N for ±2 MV/m, respectively. These blocking forces are independent of the sidelength-to-thickness ratio, like those predicted from the geometrically linear theory, illustrated as the dotted line in Figure 5.23. Finally, in comparing beam-like THUNDER, LIPCA-C1 and LIPCA-C2 actuators, the blocking force performance of LIPCA-C2 actuator is superior.

5.4.3 Blocking Forces of LIPCA-C2 as a Function of Sidelength-to-Thickness Ratio: Pinned-Pinned Case

In this section, blocking forces of a LIPCA-C2 actuator with pinned-pinned supports as a function of sidelength-to-thickness ratio are taken into consideration. Illustrated in Figure 5.24 are relations for blocking forces P_{bl} and R_{bl} for ±2 MV/m for a LIPCA-C2 actuator with an aspect ratio of 0.7. Again, like the case of THUNDER and LIPCA-C1 actuators, the influence of restraining the motion in the *x*-direction at the support positions is obviously very strong because the normalized P_{bl} relations shown in Figure 5.24 are significantly different from those shown in Figure 5.21. Unlike THUNDER and LIPCA-C1 actuators, the magnitudes of both the normalized forces P_{bl} and R_{bl} generally increase with increasing L_x/H. Also, it should be noted that the sign of force P_{bl} (or the direction of the force P_{bl}) at a particular sidelength-to-thickness ratio and applied electric field strength for the pinned-pinned case in Figure 5.24 is opposite to that for the same sidelength-to-thickness ratio and applied electric field strength for the pinned-roller case in Figure 5.21. This behavior is similar to that of LIPCA-C1 actuator. As can be seen, the range of L_x/H for which the blocking force P_{bl} relations are approximately equal to the linear predictions is very short. As the sidelength-to-thickness ratio increases, the normalized values of P_{bl} deviate from the linear predictions and increase moderately in magnitude, while values of R_{bl} are still in agreement with the linear predictions and also increase considerably in magnitude. Like the similar phenomenon that occurs with THUNDER and LIPCA-C1 actuators discussed in Sections 3.4.3 and 4.4.3, the deviation of P_{bl} from the linear predictions originates at a small value of L_x/H because the magnitude of the associated R_{bl} is relatively large and this changes the structural stiffness of the actuator through geometrically nonlinear effects. However, the deviation of P_{bl} from the linear theory, in turn, does not affect the force R_{bl} as much due to the comparatively small magnitude of P_{bl}. The relations for blocking forces P_{bl} and R_{bl} for ±2 MV/m coincide up to L_x/H = 80 and 100, respectively. Beyond these values of sidelength-to-thickness ratio, the relations separate from each other,

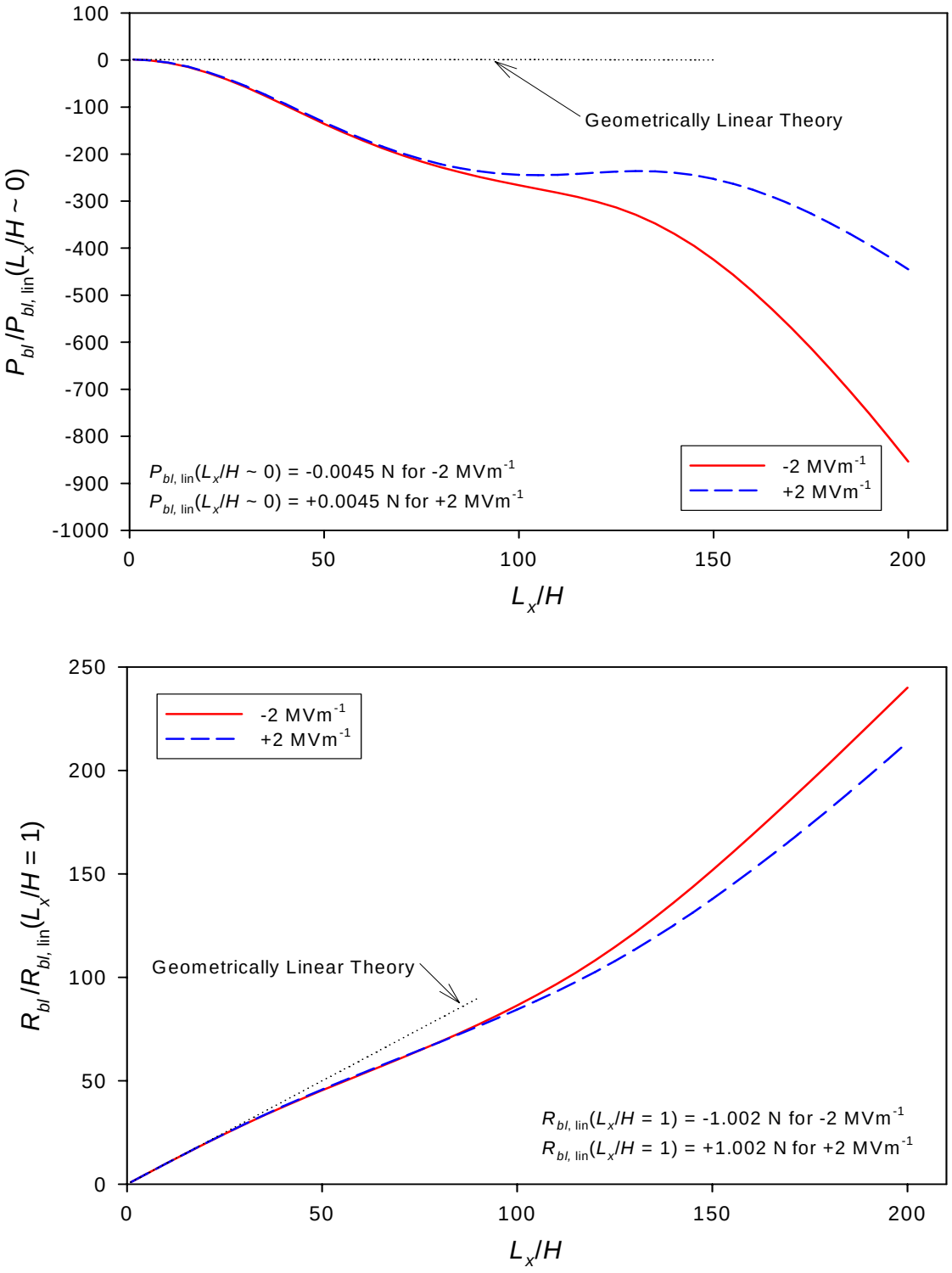

Figure 5.24: Blocking Force vs. Sidelength-to-Thickness Ratio Relations of Pinned-Pinned Supported Rectangular LIPCA-C2 (L_y/L_x = 0.7)

with more separation for larger values of sidelength-to-thickness ratio. According to Figure 5.24 and 5.21, in general the magnitude of force P_{bl} of the pinned-pinned supported actuators is smaller than that of the pinned-roller supported actuators with the same sidelength-to-thickness ratio and subjected to the same electric field strength. The only exception is for large sidelength-to-thickness ratios and the negative field strength applied, for which the blocking force P_{bl} for -2 MV/m is enhanced in magnitude appreciably. Thus, the existence of R_{bl} can weaken the transverse load-carrying capability of the LIPCA-C2 actuators. However, the comparison among Figures 5.24, 4.21, and 3.32 shows that the magnitude of blocking force R_{bl} for the pinned-pinned supported LIPCA-C2 actuator is the largest of all three actuator-types studied. In addition, the prediction of force $P_{bl,lin}$ from the linear theory again reveal values independent of sidelength-to-thickness ratio, i.e., ±0.0045 N for ±2 MV/m, respectively. Note that the value predicted from the linear theory is quite small. The values of $R_{bl,lin}$ for ±2 MV/m electric field strengths vary with sidelength-to-thickness ratio in a linear fashion with slopes of ±1.002 N, respectively.

The influence of the aspect ratio on blocking forces of LIPCA-C2 actuators with pinned-pinned supports will be examined in Figures 5.25 and 5.26. The figures illustrate the relations between blocking forces and sidelength-to-thickness ratio for the actuators with aspect ratios of 1 and 0.33. Considering Figure 5.25, the overall relations are similar to the ones in the previous figure for aspect ratio 0.7. However, qualitatively, the relations of the normalized blocking force P_{bl} are roughly a mirror image around the abscissa axis of those in the upper portion of Figure 5.24, since the normalization factors $P_{bl,lin}$ for the cases of the aspect ratio of 1 and 0.7 have opposite signs for a given electric field strength. In addition, when compared to the blocking force P_{bl} in Figure 5.24, it can be seen that the value of the force P_{bl} of the square actuators is larger only when sidelength-to-thickness ratio is greater than a certain value (around 150 for +2 MV/m, and 110 for -2 MV/m). Nevertheless, the value of blocking force R_{bl} of the square actuators is always larger than that of the

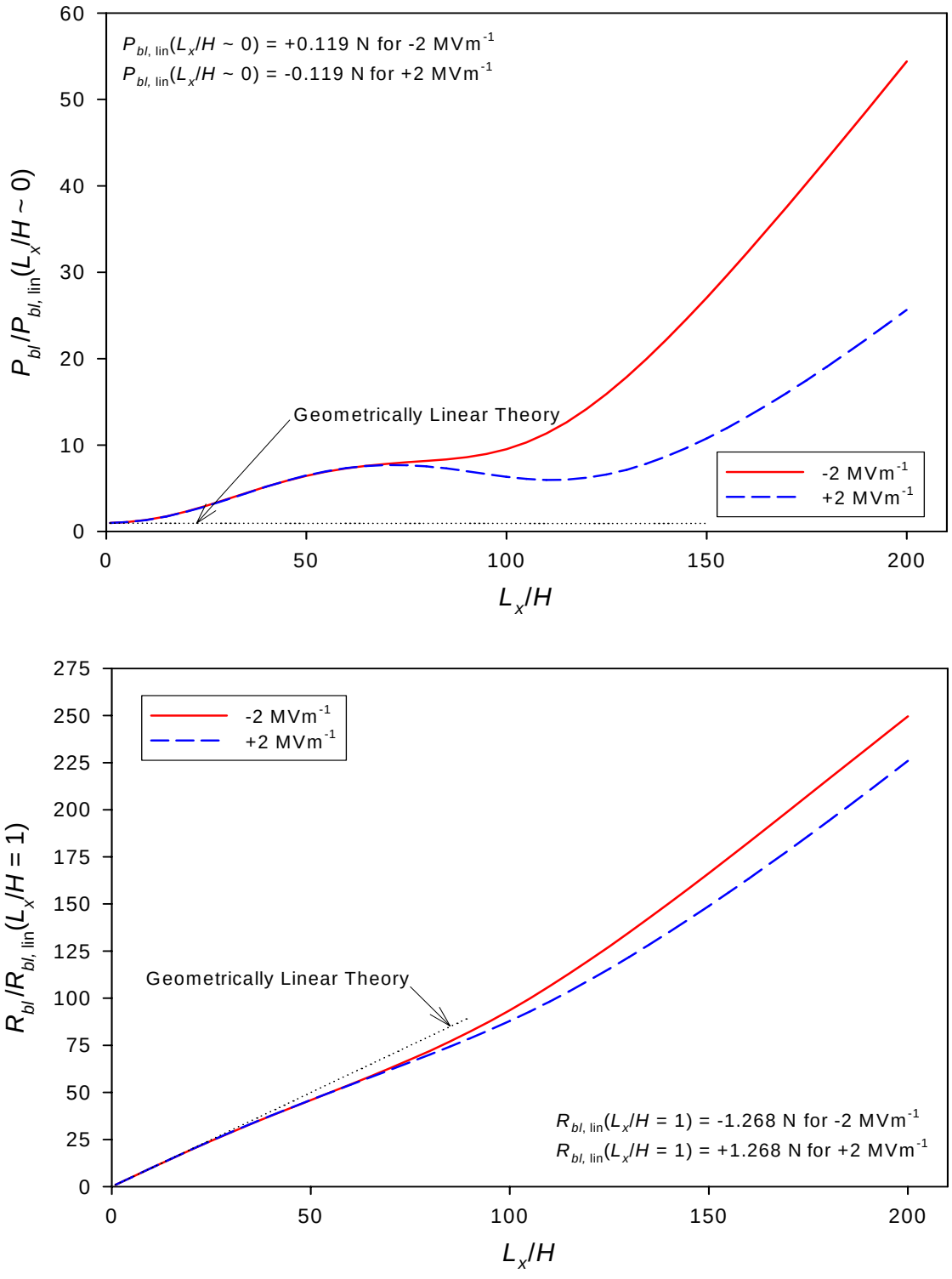

Figure 5.25: Blocking Force vs. Sidelength-to-Thickness Ratio Relations of Pinned-Pinned Supported Square LIPCA-C2

rectangular actuators with the same value of L_x/H. Additionally, similar to the case of aspect ratio 0.7, the magnitude of force P_{bl} of the pinned-pinned supported actuators is in general lower than that of the pinned-roller supported actuators with the same sidelength-to-thickness ratio and subjected to the same electric field strength. The exception is for large sidelength-to-thickness ratios and a negative field strength. The separation is larger for the square actuator due to stronger geometrically nonlinear effects. The geometrically linear theory predicts the force $P_{bl,lin}$ to be constant over the considered sidelength-to-thickness ratio, i.e., ∓ 0.119 N for ±2 MV/m, respectively. On the other hand, the force $R_{bl,lin}$ for ±2 MV/m is predicted to be a linear function of sidelength-to-thickness ratio with slopes of ±1.268 N, respectively.

Finally, the relations between blocking forces and sidelength-to-thickness ratio for pinned-pinned supported beam-like LIPCA-C2 actuators with an aspect ratio of 0.33 are illustrated in Figure 5.26. Overall, the blocking force relations are similar to those in Figures 5.24 and 5.25. The normalized value of P_{bl} is in good agreement with the linear predictions for small sidelength-to-thickness ratios. The normalized value of R_{bl} also agree well with the normalized values of $R_{bl,lin}$ predicted by the linear theory, over a limited range of sidelength-to-thickness ratios. Unlike the case of the LIPCA-C1 actuators, the value of blocking force P_{bl} of the beam-like LIPCA-C2 actuators is not always smaller than those of the actuators with aspect ratios of 0.7 and 1. However, the value of blocking force R_{bl} is always smaller than those of the actuators with the larger aspect ratios considered. This inconsistency of the blocking forces relative to the aspect ratios is due to strong geometrically nonlinear effects. Both the forces P_{bl} and R_{bl} increase monotonically with increasing L_x/H. However, it should be noted that when the value of L_x/H is beyond 120, the blocking forces for -2 MV/m field strength cannot be solved for due to the convergence failure of the algorithm presented in Chapter 2. Again, this failure is believed to occur because the LIPCA-C2 actuators snap through to another configuration. The geometrically linear theory predicts the values of $P_{bl,lin}$

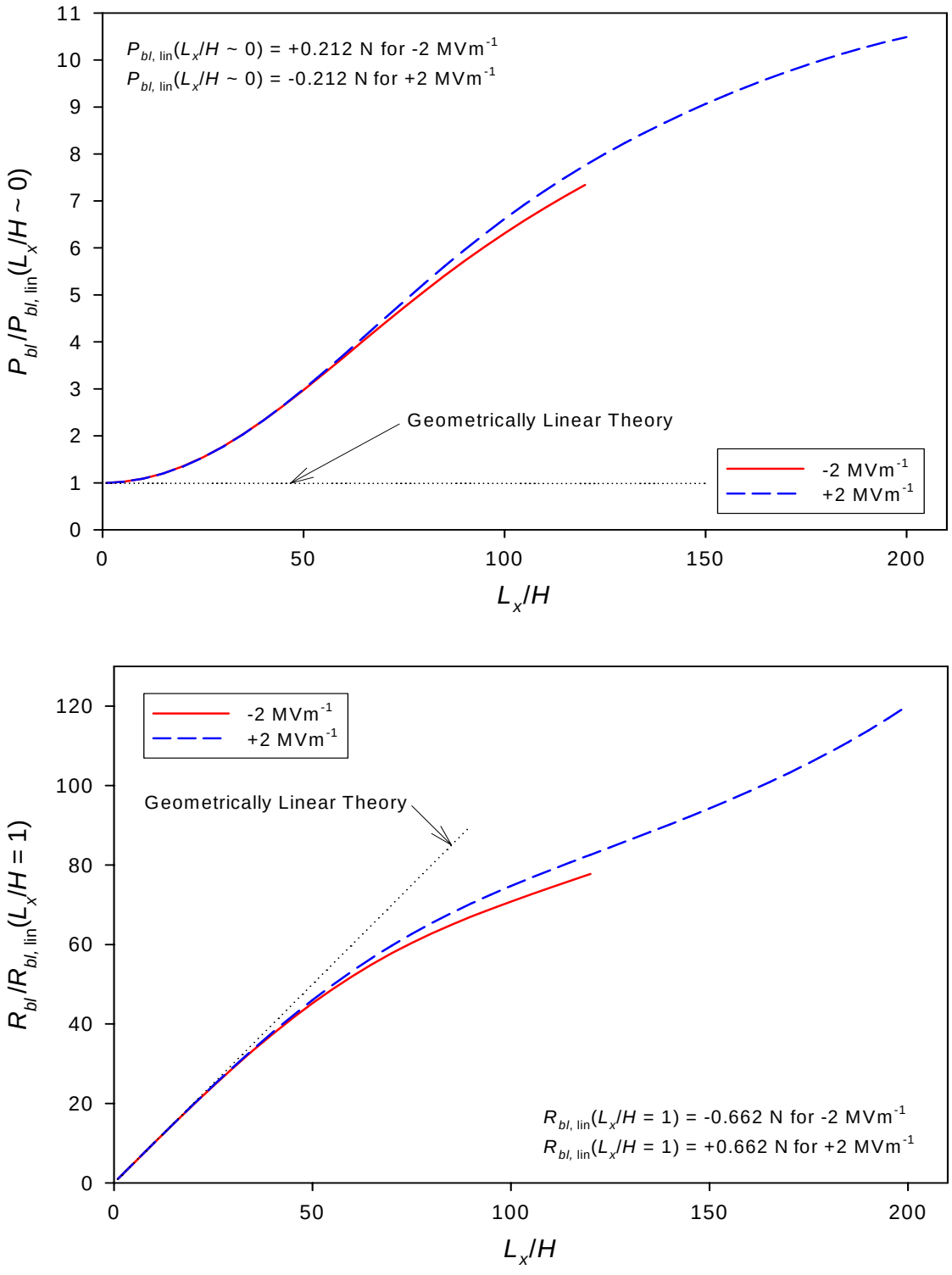

Figure 5.26: Blocking Force vs. Sidelength-to-Thickness Ratio Relations of Pinned-Pinned Supported Beam-Like LIPCA-C2 (L_y/L_x = 0.33)

to be ∓ 0.212 N for ± 2 MV/m, respectively. In addition, the slope of the relations between normalized R_{bl} and sidelength-to-thickness ratio is 0.662.

5.5 Chapter Summary

In this chapter, the numerical results for manufactured shapes of LIPCA-C2 actuators were presented. Similar to LIPCA-C1 actuators, the predicted shapes are single-valued at room temperature in the range of parameters considered. All manufactured shapes are stable and are saddle-like, with a positive smaller curvature in the *x*-direction and a negative larger curvature in the *y*-direction. Analogous to the LIPCA-C1 actuators, the 23-term Rayleigh-Ritz model with an incorporation of composite material constitutive equations for LIPCA-C2 actuators was shown to have a good agreement with the finite-element results obtained using ABAQUS for the selected cases compared. The results indicate that the predicted manufactured shapes for LIPCA-C2 actuators depend on sidelength-to-thickness ratio because of geometrically nonlinear effects. Generally, the *x*-direction room-temperature curvature is suppressed with increasing sidelength-to-thickness ratio, while the *y*-direction room-temperature curvature is, by comparison, unchanged. This is, in fact, very interesting Because the LIPCA-C2 actuators are much stiffer in the *x*-direction than the *y*-direction due to the carbon fibers in the carbon-epoxy layer, it would be expected that the *x*-direction curvature should not be sensitive to the change in geometry. However, this is certainly not the case and accordingly, it can be concluded that nonlinear effects are more influential than material stiffnesses on the room-temperature manufactured shapes.

In addition, the results of extension of the Rayleigh-Ritz model to predict the actuation response at room temperature of LIPCA-C2 actuators were presented. Interestingly, the average changes in curvature in each direction caused by positive and negative field strengths have different behavior with increasing L_x/H, and with aspect ratio.

The average curvature change in the *x*-direction is enhanced when a +2 MV/m field strength is applied, while it is suppressed when being subjected to a -2 MV/m field strength. On the other hand, when +2 and -2 MV/m field strengths are applied, the curvature change in the *y*-direction is enhanced considerably and slightly, respectively. Indeed, the considerable curvature enhancement in both the *x*- and *y*-directions of the LIPCA-C2 actuator with aspect ratios of 0.7 and 1 for +2 MV/m is due to a snap-through phenomenon of the actuator configuration. The actuation responses as a function of applied electric field were also discussed. The snap-through phenomenon of the actuator with L_x/H = 200 and L_y/L_x = 0.7 can obviously be seen as a function of applied electric field. Except for this phenomenon, the changes in the actuated curvatures vary with applied electric field in a moderately nonlinear fashion. Note that according to the change in curvatures vs. applied electric field strength relations, the beam-like LIPCA-C2 actuator with L_x/H =100 is superior to the rest of the LIPCA-C2 actuators considered in terms of the larger actuated curvature obtained for both positive and negative field strengths in the operational *x*-direction than the unexploited *y*-direction.

Finally, the blocking force predictions from the extension of the 23-term Rayleigh-Ritz model used to predict actuated shapes of LIPCA-C2 actuators were presented. For pinned-roller supported LIPCA-C2 actuators, blocking force P_{bl} is usually higher than force $P_{bl,lin}$, namely that predicted by the geometrical linear theory. For the aspect ratios of 0.7 and 1, the value of blocking force P_{bl} for +2 MV/m is larger than that for -2 MV/m for large sidelength-to-thickness ratios. This is due to the considerable enhancement of change in actuation-induced curvature for +2 MV/m. For pinned-pinned supported LIPCA-C2 actuators, the existence of force R_{bl} strongly influences the characters of blocking force P_{bl} because the comparatively large magnitude of force R_{bl} alters the structural stiffness of the actuators. For the same aspect ratio, the magnitude of force P_{bl} increases with increasing L_x/H. Also, the direction of force P_{bl} changes due to the presence of R_{bl}. The relations

between blocking forces and applied electric field strength were also presented. Generally speaking, the blocking force P_{bl} vs. electric field strength relations are linear for $L_x/H = 100$, but rather strongly nonlinear for $L_x/H = 200$. The blocking force R_{bl} vs. electric field strength relations are slightly nonlinear. Consequently, in order to design a LIPCA-C2 actuator to carry a transverse load or an inplane normal load, a careful analysis of actuator performance should be conducted, since its room-temperature shape and support type have very strong effects on the actuator capability.

In the next chapter, conclusions regarding the present study are made and recommendations for future work are specified.

Chapter 6

CONCLUSIONS AND RECOMMENDATIONS

6.1 Conclusions

In this work, a number of predictive analyses were developed to determine the deformation characteristics of the manufactured and actuated shapes of rectangular THUNDER, LIPCA-C1, and LIPCA-C2 actuators. The key modeling of these analyses, as presented in Chapter 2, was based on developing approximate displacement responses that minimize the total potential energy of these layered actuators. This was accomplished through the use of variational methods along with the 23-term Rayleigh-Ritz approximation to the displacement fields. All analyses were based on classical layered plate theory and assumed the various layers exhibited linear elastic, temperature-independent behavior. Since the out-of-plane deformations of these actuators when cooled from the manufacturing temperature to room temperature are several times the thickness of the actuators, geometric nonlinearities were important and were included in the strain-displacement relations. The presence of geometric nonlinearities implies the possibility of having more than one room-temperature shape predicted for a given set of parameters. For that purpose, an examination of the stability of the predicted shapes was considered. This was achieved by examining the second variation of the total potential energy. In addition to this, finite-element models by employing ABAQUS version 6.3 were also developed to compare with the predicted room-temperature and actuated shapes resulting from the 23-term Rayleigh-Ritz model. Nine-node shell elements with the geometrically nonlinear kinematics were used in ABAQUS. Multiple equilibrium shapes in ABAQUS could be obtained by an aid of the Rayleigh-Ritz

solutions. Blocking forces of the actuators were also determined. Two types of blocking forces were investigated, i.e., the force that restrained the *z*-direction motion of the midpoint of two edges of an actuator (equivalent to the force at pinned-roller support) and the forces that restrained both the *x*- and *z*-direction motions of the same points (equivalent to the forces at pinned-pinned support). The Rayleigh-Ritz models were modified to calculate the blocking forces by adding a work term due to the forces in the total potential energy. Supplementary iterative algorithms were developed and employed to solve for the blocking forces.

The numerical results for square and rectangular THUNDER actuators were presented in Chapter 3. As indicated in the chapter, THUNDER actuators could exhibit multiple room-temperature shapes for the geometrical and manufacturing parameters considered. This would especially occur for actuators with aspect ratios L_y/L_x = 0.7 and 1 when the inplane dimensions of the actuator's relative to thickness and temperature decrement were sufficiently large (larger than critical values of sidelength-to-thickness ratios and lower than critical values of temperature). The critical points of the curvature vs. temperature or curvature vs. sidelength-to-thickness ratio relations of the actuators with aspect ratios of 0.7 and 1 were limit and bifurcation points, respectively. However, when tabs were included in the analysis, the relations for actuators with a square active region exhibited limit point behavior rather than bifurcation behavior. This was due to geometric or structural orthotropy of the square actuators with tabs. The existence of these critical points suggests that care should be taken when designing THUNDER actuators. Indeed, if two THUNDER actuators are manufactured with a geometry that is very close to the critical value, they may behave quite differently. Specifically, manufacturing irregularities such as small variations in material properties, variations in layer thickness, or nonuniform cooling may result in different effective sidelength-to-thickness ratio. Hence, two 'identical' THUNDER actuators will not behave exactly the same way. Also, actuation responses of

THUNDER actuators strongly depended on sidelength-to-thickness and aspect ratios. The changes in curvatures in the *x*- and *y*-directions due to an actuation were not equal because of geometrically nonlinear effects. On a branch of stable room-temperature shapes, an enhancement of free actuation responses in the *x*-direction could be observed for actuators with aspect ratios of 0.7 and 1, and large values of sidelength-to-thickness ratio, while the suppression in free actuation responses in the associated *y*-direction was noticed. However, on the other stable room temperature shape branch, the opposite behavior of free actuation responses occurred in the *x*- and *y*-directions. The suppression in free actuation responses for THUNDER actuators with aspect ratios of 0.7 and 1 in mid-range of sidelength-to-thickness ratio and for beam-like actuators with an aspect ratio of 0.3 over the sidelength-to-thickness ratio considered could also be observed. As a result, it must be noted that not all THUNDER actuators exhibited enhancement of free actuation responses due to the curved shape characteristic. For the geometrical configurations that exhibit the suppression in free actuation responses, the counterpart flat actuator made from the same material, stacking sequence, and dimensions could have larger actuation-induced deflections than THUNDER actuators. However, in THUNDER actuator design, the piezoceramic layer always remained in compression even when subjected to high electric field strengths. This bodes well for there being little potential for tension cracking in the piezoceramic, a characteristic of a brittle material. The load-carrying capability of THUNDER actuators was evaluated by computing blocking forces, utilizing the blocking force algorithms presented in Chapter 2. Generally, transverse blocking forces (P_{bl}) of THUNDER actuators for the equivalent pinned-roller support case were lower in value than those of the counterpart flat actuators, except for actuators with aspect ratios of 0.7 and 1, and large values of sidelength-to-thickness ratio. With additional motion restraint in the *x*-direction, transverse blocking forces (P_{bl}) for equivalent pinned-pinned support case behaved oppositely and were higher in value than those of the counterpart flat actuators for mid-range sidelength-to-thickness

ratios. The magnitudes of the associated inplane blocking forces (R_{bl}) were considerably larger compare to those of P_{bl} for the pinned-pinned case. However, the inplane blocking forces were less than those predicted by the geometrically linear theory. Therefore, in order to design a THUNDER actuator to carry a transverse load or an inplane normal load, a careful analysis of actuator performance should be conducted, since its geometrical parameters and support conditions have very strong influences on the actuator load-carrying capability.

The numerical results for square and rectangular LIPCA-C1 actuators were presented in Chapter 4. Unlike THUNDER actuators, LIPCA-C1 actuators exhibited only one room-temperature shape for the entire range of all geometrical parameters considered. However, LIPCA-C1 actuators with the beam-like aspect ratio had a similar room-temperature curvature characteristic to beam-like THUNDER actuators, except the THUNDER actuators exhibited suppression of the manufactured curvature in the *x*-direction with increasing L_x/H, whereas the LIPCA-C1 actuators did not. Indeed, for all of the aspect ratios considered, the room-temperature curvature in the *x*-direction of LIPCA-C1 actuators was insensitive to sidelength-to-thickness ratio, while the *y*-direction room-temperature curvature was noticeably suppressed with increasing sidelength-to-thickness ratio. This was principally due to the orthotropic material properties of the carbon-epoxy layer in the LIPCA-C1 actuators (fibers running in the *x*-direction or the operational direction) and the specific stacking sequence of the LIPCA-C1 actuators. Compared to those of THUNDER actuators, the residual cooling stresses in LIPCA-C1 actuators were lower in magnitude due mainly to the lower cure temperature for the epoxy in carbon-epoxy and glass-epoxy layers than for the polyimide adhesive in the THUNDER actuators. In addition, when subjected to applied electric field strengths, there would be a possibility that stresses in the piezoceramic layer of the LIPCA-C1 actuators would change sign, especially in the *x*-direction. This could be detrimental to the piezoceramic layer owing to both tensile stresses, and a reversing stress

fatigue condition under an application of alternating electric field. The stresses in LIPCA-C1 actuators changed more in relation to the residual values when actuated than in THUNDER actuators. Analogous to the case of THUNDER actuators, blocking forces of LIPCA-C1 actuators were evaluated to analyze their load-carrying capability. The results showed that nonlinear effects enhance the transverse blocking force P_{bl} for the pinned-roller case, but the degree of enhancement was not significant for the three aspect ratios considered. However, for the pinned-pinned case, nonlinear effects enhanced blocking force P_{bl} remarkably. Additionally, the magnitude of the associated inplane blocking force R_{bl} was much higher than that of P_{bl}. However, geometrically nonlinear effects suppressed the value of R_{bl} relative to the prediction of the linear theory. In conclusion, a thorough analysis of LIPCA-C1 actuator performances should be conducted when a LIPCA-C1 actuator is designed for a specific task, since its performances change with geometrical parameters and support conditions.

The numerical results for square and rectangular LIPCA-C2 actuators were presented in Chapter 5. Similar to the LIPCA-C1 actuator case, there was only one room-temperature manufactured shape for a given set of geometrical parameters and temperature change during cooling. Unlike the other two actuator designs considered, the room-temperature curvature in the *y*-direction was of opposite sign to the *x*-direction curvature. Furthermore, the magnitude of the *y*-direction room-temperature curvature was larger than that of the *x*-direction curvature by at least a factor of two. This might not be favorable because it could be difficult to attach LIPCA-C2 actuators to a structure along the *x*-edges without adversely affecting the characteristic of the actuator manufactured shape. The room-temperature curvature in both directions was suppressed with increasing sidelength-to-thickness ratio, the *x*-direction curvature being more suppressed than the *y*-direction curvature. These effects were more pronounced for aspect ratios of 0.7 and 1 than for a beam-like aspect ratio of 0.33. For large sidelength-to-thickness ratios and aspect ratios of

0.7 and 1, the changes in the actuated curvature in the *x*-direction (operational direction) were appreciably enhanced for a +2 MV/m field strength and appreciably suppressed for a -2 MV/m field strength. This unusual actuation-induced behavior occurred because the LIPCA-C2 actuators snapped to another stable configuration when the applied positive electric field was sufficiently high. This behavior was not the case for THUNDER and LIPCA-C1 actuators and should be circumvented in designing a LIPCA-C2 actuator to prevent peizoceramic cracking due to stresses abruptly changing during snap-through. Additionally, this phenomenon would provide an undesirable non-harmonic response when the LIPCA-C2 actuators were subjected to a harmonic voltage. However, if large, sudden actuation is required, this behavior could be an advantage. For beam-like LIPCA-C2 actuators, free actuation responses were more balanced in the *x*- and *y*-directions, but the performance was not outstanding. The through-thickness stress distributions accompanying the free actuation responses were also determined. Like LIPCA-C1 actuators, there would always be a sign change in the normal stress σ_x in the piezoceramic layer regardless of strength of an electric field. This again could cause a fatigue problem for the PZT layer in LIPCA-C2 actuators. Blocking forces of LIPCA-C2 actuators were also evaluated to measure the actuator load-carrying capability. It was shown that for all geometries considered, blocking force P_{bl} for the pinned-roller case was enhanced compared to blocking force $P_{bl,lin}$ computed by the geometrically linear theory. Corresponding to the enhancement of the change in the actuated curvature caused by snap-through for LIPCA-C2 actuators with aspect ratios 0.7 and 1 when a +2 MV/m field strength was applied, the value of force P_{bl} for +2 MV/m was higher than that for -2 MV/m for large sidelength-to-thickness ratios. For the pinned-pinned case, the transverse blocking force P_{bl} was also enhanced by nonlinear effects. Note that unlike LIPCA-C1 actuators, the blocking force P_{bl} for the pinned-pinned case was not always larger than the blocking force P_{bl} for the pinned-roller case of the same dimensions. The magnitude of the associated inplane blocking force R_{bl} for LIPCA-C2

actuators was considerably larger than that of force P_{bl}, similar to THUNDER and LIPCA-C1 actuators. Nonetheless, force R_{bl}, in general, was slightly suppressed in relation to that predicted by the geometrically linear theory, except for LIPCA-C2 actuators with aspect ratios of 0.7 and 1 and large sidelength-to-thickness ratios, for which force R_{bl} was enhanced by nonlinear effects.

Finally, the comparisons among the major characteristics of THUNDER, LIPCA-C1 and LIPCA-C2 actuators in this study can be summarized as a quick reference in Table 6.1. Note that the term 'plate-like' in the table refers to the aspect ratios, L_y/L_x, of 0.7 and 1. The term 'beam-like', as defined before, refers to the aspect ratio of 0.3 or 0.33 for THUNDER and LIPCA-type actuators, respectively. All enhancement and suppression of performance characteristics of these actuators presented in the table are relative to the counterpart characteristics predicted by the geometrically linear Rayleigh-Ritz model.

Table 6.1: Summary Table for Characteristics of Laminated Piezoelectric Actuators Studied

Actuator Type	THUNDER	LIPCA-C1	LIPCA-C2
Multiple Room-Temperature Shapes	Plate-like*: Yes (bifurcation point for L_y/L_x = 1 , limit point for L_y/L_x = 0.7) Beam-like**: No	No	No
Room-Temperature Curvatures (on A′D′)	Plate-like: K_x moderately suppressed in mid-range of L_x/H and moderately enhanced when L_x/H is large, K_y greatly suppressed Beam-like: K_x moderately suppressed, K_y moderately suppressed	Plate-like: K_x no effect, K_y greatly suppressed Beam-like: K_x no effect, K_y moderately suppressed	Plate-like: K_x greatly suppressed, K_y moderately suppressed Beam-like: K_x moderately suppressed, K_y moderately suppressed
Residual PZT Stresses	Biaxial compression	Some tension in the *x*-direction, compression in the *y*-direction	Some tension in the *x*-direction, mostly compression in the *y*-direction
Change in Curvatures due to Actuation	Plate-like: ΔK_x moderately suppressed in mid-range of L_x/H and moderately enhanced when L_x/H is large, ΔK_y greatly suppressed Beam-like: ΔK_x moderately suppressed, ΔK_y moderately suppressed	Plate-like: ΔK_x no effect except for little enhancement in mid-range of L_x/H, ΔK_y greatly suppressed Beam-like: ΔK_x no effect, ΔK_y moderately suppressed	Plate-like: ΔK_x greatly suppressed for -2 MV/m but greatly enhanced for +2 MV/m , ΔK_y moderately enhanced for -2 MV/m and greatly enhanced for +2 MV/m Beam-like: ΔK_x moderately suppressed for -2 MV/m and moderately enhanced for +2 MV/m, ΔK_y moderately enhanced for ±2 MV/m
Stress due to Actuation	Biaxial compression, no reversal	Reversal in the *x*-direction, mostly compression in the *y*-direction	Reversal in the *x*-direction, mostly compression in the *y*-direction, gradient change for +2 MV/m
Blocking Forces, pinned-roller	Plate-like: P_{bl} greatly suppressed in mid-range of L_x/H and enhanced when L_x/H is large Beam-like: P_{bl} moderately suppressed	P_{bl} slightly enhanced for both plate-like and beam-like	Plate-like: P_{bl} slightly enhanced – for +2 MV/m larger than for -2 MV/m when L_x/H is large Beam-like: slightly enhanced
Blocking Forces, pinned-pinned	Plate-like: P_{bl} slightly enhanced in mid-range of L_x/H and suppressed when L_x/H is large, R_{bl} suppressed Beam-like: P_{bl} enhanced, R_{bl} suppressed	P_{bl} enhanced and R_{bl} suppressed for both plate like and beam-like	Plate-like: P_{bl} enhanced –for +2 MV/m smaller than for -2 MV/m, R_{bl} suppress in mid-range of L_x/H and enhanced for large L_x/H Beam-like: P_{bl} enhanced, R_{bl} slightly suppressed
Unusual Characteristics	Snap through with sufficiently high moment applied on edges for plate-like	None	Snap through with sufficiently high positive field for plate-like

* plate-like: L_y/L_x = 0.7 or 1, ** beam-like: L_y/L_x = 0.3 or 0.33

6.2 Actuator Design Recommendations

All of the results presented in Chapters 3-5 demonstrated that geometrically nonlinear effects can be important in determining the manufactured shapes, actuation responses, and blocking forces of curved laminated piezoelectric actuators. Performance analyses must be meticulously conducted in detail by employing the geometrically nonlinear theory in the actuator selection process to meet their functional requirements. Furthermore, according to the results obtained in this work, a vital conclusion of a curved laminated actuator's characteristics is deducible. This conclusion can be stated that "upon cooling, or with cooling plus actuating, for a curved laminated actuator with a specific aspect ratio, the curvature in the direction in which the magnitude of the average curvature is the least will be significantly suppressed compared to the linear prediction as actuator sidelength-to-thickness ratio increases, while the curvature in the direction in which the magnitude of the average curvature is the most will be only slightly suppressed or perhaps slightly enhanced compared to the linear prediction". This behavior is completely due to geometrically nonlinear effects and believed to be universal for any curved laminated piezoelectric actuator. Therefore, the behavior can be exploited to preliminarily design a new curved laminated piezoelectric actuator. As suggested by the behavior stated above, assuming the curvature changes in the *x*-direction are to be utilized rather than changes in the *y*-direction curvature, referring to Figure 6.1, these preliminary design criteria read as follows:

$$\left|\mathrm{K}^{T}_{x,lin}\right| > \left|\mathrm{K}^{T}_{y,lin}\right| \tag{6.1}$$

$$\textit{if } \left|\mathrm{K}^{T+E}_{y,lin}\right| > \left|\mathrm{K}^{T}_{y,lin}\right|, \textit{ then} \left|\mathrm{K}^{T+E}_{x,lin}\right| > \left|\mathrm{K}^{T+E}_{y,lin}\right| \tag{6.2}$$

$$\textit{if } \left|\mathrm{K}^{T+E'}_{y,lin}\right| < \left|\mathrm{K}^{T}_{y,lin}\right|, \textit{ then either} \left|\mathrm{K}^{T+E'}_{x,lin}\right| \geq \left|\mathrm{K}^{T+E'}_{y,lin}\right| \textit{ or } \left|\mathrm{K}^{T+E'}_{x,lin}\right| < \left|\mathrm{K}^{T+E'}_{y,lin}\right| \tag{6.3}$$

$$\left|\mathrm{K}_{x,lin}^{T+E}-\mathrm{K}_{x,lin}^{T}\right|>\left|\mathrm{K}_{y,lin}^{T+E}-\mathrm{K}_{y,lin}^{T}\right| \text{ or} \tag{6.4}$$

$$\left|\mathrm{K}_{x,lin}^{T+E'}-\mathrm{K}_{x,lin}^{T}\right|>\left|\mathrm{K}_{y,lin}^{T+E'}-\mathrm{K}_{y,lin}^{T}\right|$$

where $\mathrm{K}_{x,lin}^{T}$ and $\mathrm{K}_{y,lin}^{T}$ are the thermally-induced curvatures due to cooling process in the *x*- and *y*-directions, respectively. $\mathrm{K}_{x,lin}^{T+E}$ and $\mathrm{K}_{y,lin}^{T+E}$ are the thermally- plus piezoelectrically-induced curvatures. Like superscript $+E$, superscript $+E'$ also represents an additional inclusion of piezoelectric effects in the thermally-induced curvatures, but the corresponding electric field strength is the negative of the field strength associated with superscript $+E$. Symbol $|\ldots|$ represents the absolute value of the quantity inside the symbol. Also, as denoted by subscript *lin* after subscripts *x* and *y* used to indicate the direction of the curvatures, all curvatures evaluated in the design criteria are the values predicted by the geometrically linear plate theory in Appendix A, or by the 23-term linear Rayleigh-Ritz model, or by the 23-term nonlinear Rayleigh-Ritz model when the value of L_x/H approaches zero. This is done intentionally, since the nonlinear characteristic of the curvatures as L_x/H increases can be heuristically represented by knowing the linear values. The reasons behind the inequalities (6.1)-(6.4) in the criteria are given, respectively, as:

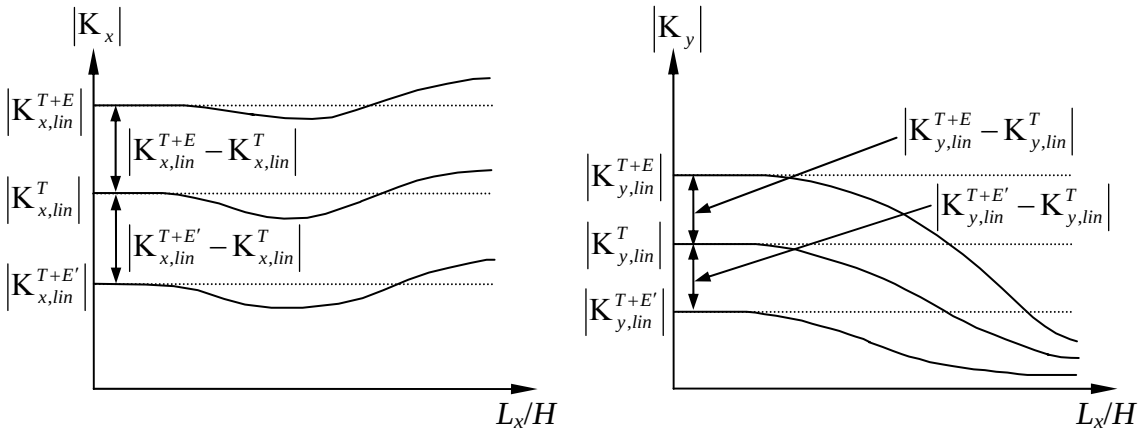

Figure 6.1: Schematic of Sidelength-to-Thickness ratio vs. Curvature Relations Based on Actuator Design Criteria

(6.1) to suppress the *y*-direction room-temperature curvature as illustrated in Figure 6.1 and, therefore, make it easier to attach the actuator to a structure or reduce undesirable effects from suppressing the anticlastic curvature when the actuator is attached on the *x*-edge(s), particularly when the dimension L_y is relatively large, since the *y*-direction curvature will be more pronounced. This inequality is not satisfied by THUNDER or LIPCA-C2 actuators. LIPCA-C2 actuators seriously violate the inequality, but since for THUNDER actuator $\left|\mathrm{K}_{x,lin}^{T}\right| = \left|\mathrm{K}_{y,lin}^{T}\right|$, the violation is not serious;

(6.2) to retain the *x*-direction actuated curvature, while suppressing the *y*-direction actuated curvature, so the change in the *x*-direction curvature due to actuation with electric field strength *E* is rather uniform with increasing L_x/H, but that in the *y*-direction is suppressed. The electrical input energy will be converted to mechanical output energy by changing curvature in the *x*-direction more than in the *y*-direction. This inequality is not satisfied by THUNDER or LIPCA-C2 actuators. The lack of satisfying this inequality does not penalize THUNDER actuators as much as LIPCA-C2 actuators because $\left|\mathrm{K}_{x,lin}^{T+E}\right| = \left|\mathrm{K}_{y,lin}^{T+E}\right|$ for THUNDER actuators;

(6.3) to complement the criterion (6.2) when the negative of electric field strength *E* (denoted as E') is applied. The actuated curvature in the *y*-direction will be restricted between the suppressed manufactured curvature and the horizontal axis in Figure 6.1 and thus will be suppressed automatically. The value of actuated curvature in the *x*-direction, therefore, has no restricted bound and can be either more or less than the actuated curvature in the *y*-direction. Note that the larger value of actuated curvature in the *x*-direction, however, may be more preferable to retain the uniformity of the change in the *x*-direction curvature due to the applied electric field strength E';

(6.4) to obtain larger change in the *x*-direction curvature than in the *y*-direction curvature due to actuation, as illustrated in Figure 6.1, because the *x*-direction of the actuator is mainly used as the operational direction. This inequality is not satisfied by THUNDER or LIPCA-C1 actuators.

It should be stated that the design criteria just presented provide twofold advantages for designing a new type of curved laminated actuator. Firstly, they reduce the trial and error process in the preliminary state, since the design parameters are confined into the desirable domains by inequalities (6.1)-(6.4). Secondly, without going through the geometrically nonlinear analysis every time whenever design parameters are changed, the consumption of computational time in design process is reduced considerably. After materials and stacking sequence are selected properly such that the resulting curvatures calculated from the geometrically linear theory fulfill the design criteria, the geometrically nonlinear analysis, however, must be performed to determine the actual characteristics of the actuator, including such effects as snap through.

6.3 Future Work

The development of these predictive analyses is expected to greatly aid many current and ongoing research efforts in the area of laminated piezoelectric actuators. The high promise of these analyses suggests the following future activities:

(1) Evaluate performances of THUNDER, LIPCA-C1, and LIPCA-C2 actuators by utilizing the 23-term Rayleigh-Ritz model as a function of thicknesses of steel and aluminum layers in THUNDER actuators and thicknesses of glass-epoxy and carbon-epoxy layers in LIPCA-C1 and LIPCA-C2 actuators, and then search for the optimal thicknesses that provide the maximum performances.

(2) Design a new type of curved laminated piezoelectric actuator by employing the design criteria proposed in Section 6.2 and analyze its performances as a comparison to the existing curved laminated piezoelectric actuators.

(3) Modify the 23-term Rayleigh-Ritz model by including material nonlinearities in the piezoceramic material.

(4) Extend the 23-term Rayleigh-Ritz model by employing Hamilton's principle in order to evaluate the dynamic behavior of curved laminated piezoelectric actuators.

Appendix A

ANALYTICAL SOLUTIONS FOR LAMINATED PLATES SUBJECTED TO A TEMPERATURE CHANGE: GEOMETRICALLY LINEAR MODEL

A.1 Modeling of Cross-Ply Laminated Plates

Consider an initially flat rectangular laminated plate with traction-free conditions on all four edges, as illustrated in Figure A.1. The plate is located in an $x-y-z$ Cartesian coordinate system. The dimensions of the plate before it is subjected to temperature increment ΔT are L_x by L_y. The total thickness of the plate is *H* and the total numbers of layers are assumed to be *N*. The location $z=0$ is the geometric midsurface of the plate, here taken to be the reference surface for the analysis. The lower and upper boundaries of layer 1, or the bottom layer, are located at $z=z_0=-H/2$ and $z=z_1$, the boundaries of layer 2 at z_1 and z_2, and in general, the boundaries of the k^{th} layer at z_{k-1} and z_k. The upper boundary of layer *N* is given by $z=z_N=+H/2$.

The plate is assumed to obey classical lamination theory, in which the Kirchhoff hypothesis and a plane-stress state are assumed to prevail. Linear kinematic relationships and linear elastic orthotropic temperature-independent material properties are assumed. Additionally, the temperature change ΔT is considered to be spatially uniform.

The equilibrium equations of a geometrically linear plate subjected to a spatially uniform temperature change can be written as follows:

$$N_{x,x}+N_{xy,y}=0 \tag{A.1}$$

$$N_{xy,x}+N_{y,y}=0 \tag{A.2}$$

$$M_{x,xx}+2M_{xy,xy}+M_{y,yy}=0 \tag{A.3}$$

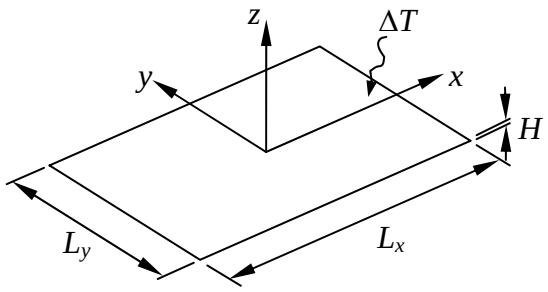

Figure A.1: Laminated Plate Subjected to Thermal Load

In the above, N_x, N_y, and N_{xy} are inplane normal force resultants in the *x*- and *y*-directions, and inplane shear force resultant, respectively, and M_x, M_y, and M_{xy} the bending moment resultants in the *x*- and *y*- directions, and twisting moment resultant, respectively. The comma means partial differentiation with respect to the ensuing variable.

Here, a cross-ply laminated plate is considered, and hence the constitutive equations simplify to become

$$\begin{Bmatrix} N_x \\ N_y \\ M_x \\ M_y \end{Bmatrix} = \begin{bmatrix} A_{11} & A_{12} & B_{11} & B_{12} \\ A_{12} & A_{22} & B_{12} & B_{22} \\ B_{11} & B_{12} & D_{11} & D_{12} \\ B_{12} & B_{22} & D_{12} & D_{22} \end{bmatrix} \begin{Bmatrix} \varepsilon_x^0 \\ \varepsilon_y^0 \\ \kappa_x^0 \\ \kappa_y^0 \end{Bmatrix} - \Delta T \begin{Bmatrix} \hat{N}_x^T \\ \hat{N}_y^T \\ \hat{M}_x^T \\ \hat{M}_y^T \end{Bmatrix} \tag{A.4}$$

$$\begin{Bmatrix} N_{xy} \\ M_{xy} \end{Bmatrix} = \begin{bmatrix} A_{66} & B_{66} \\ B_{66} & D_{66} \end{bmatrix} \begin{Bmatrix} \gamma_{xy}^0 \\ \kappa_{xy}^0 \end{Bmatrix} \tag{A.5}$$

where A_{ij}, B_{ij}, and D_{ij} are laminate stiffnesses.

The geometrically linear inplane strain-displacement and curvature-displacement relations are given by

$$\begin{aligned} \varepsilon_x^0 &= u_{,x}^0 \\ \varepsilon_y^0 &= v_{,y}^0 \\ \gamma_{xy}^0 &= u_{,y}^0 + v_{,x}^0 \end{aligned} \tag{A.6}$$

$$\kappa_x^0 = -w_{,xx}^0$$
$$\kappa_y^0 = -w_{,yy}^0 \tag{A.7}$$
$$\kappa_{xy}^0 = -2w_{,xy}^0$$

in the above, ε_x^0, ε_y^0, and γ_{xy}^0 are inplane extensional strains in the *x*- and *y*- directions, and inplane shear strain, respectively, and κ_x^0, κ_y^0, and κ_{xy}^0 are bending curvatures in the *x*- and *y*-directions, and twisting curvature, respectively. Given in Equations (A.6) and (A.7), u^0, v^0, and w^0 are the displacements of a point on reference surface in the *x*, *y*, and *z* directions, respectively.

Substituting Equations (A.6) and (A.7) into (A.4) and (A.5), and then employing Equations (A.4) and (A.5) in equilibrium equations (A.1)-(A.3) yields

$$A_{11}u_{,xx}^0 + \left(A_{12} + A_{66}\right)v_{,xy}^0 + A_{66}u_{,yy}^0 - B_{11}w_{,xxx}^0 - \left(B_{12} + 2B_{66}\right)w_{,xyy}^0 = 0 \tag{A.8}$$

$$A_{22}v_{,yy}^0 + \left(A_{12} + A_{66}\right)u_{,xy}^0 + A_{66}v_{,xx}^0 - B_{22}w_{,yyy}^0 - \left(B_{12} + 2B_{66}\right)w_{,xxy}^0 = 0 \tag{A.9}$$

$$B_{11}u_{,xxx}^0 + \left(B_{12} + 2B_{66}\right)\left(v_{,xxy}^0 + u_{,xyy}^0\right) + B_{22}v_{,yyy}^0 - D_{11}w_{,xxxx}^0 - 2\left(D_{12} + 2D_{66}\right)w_{,xxyy}^0 - D_{22}w_{,yyyy}^0 = 0 \tag{A.10}$$

As all four edges of the plate are traction-free, the boundary conditions are given as follows:

at $x = \pm L_x/2$,

$$N_x = 0 \tag{A.11}$$

$$N_{xy} = 0 \tag{A.12}$$

$$M_x = 0 \tag{A.13}$$

$$V_x = M_{x,x} + 2M_{xy,y} = 0 \tag{A.14}$$

where V_x is Kirchhoff shear force resultant defined on the *x*-edges,

at $y = \pm L_y/2$,

$$N_y = 0 \tag{A.15}$$

$$N_{xy} = 0 \tag{A.16}$$

$$M_y = 0 \tag{A.17}$$

$$V_y = M_{y,y} + 2M_{xy,x} = 0 \tag{A.18}$$

where V_y is Kirchhoff shear force resultant defined on the *y*-edges. Additionally, since all edges of the plate are traction-free, conditions must be imposed on the plate to stop rigid body motion, i.e., rigid body translations in the *x*-, *y*- and *z*-directions, and rigid body rotations around the *x*-, *y*- and *z*-axes. These conditions can be specified at the origin point, $x = y = z = 0$, as

$$u^0 = 0 \tag{A.19}$$

$$v^0 = 0 \tag{A.20}$$

$$w^0 = 0 \tag{A.21}$$

$$w^0_{,x} = 0 \tag{A.22}$$

$$w^0_{,y} = 0 \tag{A.23}$$

$$u^0_{,y} - v^0_{,x} = 0 \tag{A.24}$$

Equations (A.19)-(A.21) are for preventing rigid body translations in the *x*-, *y*- and *z*-directions, respectively. Equations (A.22)-(A.24) are for preventing rigid body rotations around the *x*-, *y*- and *z*-axes, respectively.

Assuming an analytical solution of this problem to be of the form

$$u^0 = U(x) \tag{A.25}$$

$$v^0 = V(y) \tag{A.26}$$

$$w^0 = W_1(x) + W_2(y) \tag{A.27}$$

and substituting the assumed u^0, v^0, and w^0 functions from Equations (A.25)-(A.27) into Equations (A.8)-(A.10), it can be shown that

$$A_{11}U_{,xx} - B_{11}W_{1,xxx} = 0 \tag{A.28}$$

$$A_{22}V_{,yy} - B_{22}W_{2,yyy} = 0 \tag{A.29}$$

$$B_{11}U_{,xxx} + B_{22}V_{,yyy} - D_{11}W_{1,xxxx} - D_{22}W_{2,yyyy} = 0 \tag{A.30}$$

Additionally, the conditions in Equations (A.11)-(A.24), respectively, become:
at $x = \pm L_x / 2$,

$$A_{11}U_{,x} + A_{12}V_{,y} - B_{11}W_{1,xx} - B_{12}W_{2,yy} - \hat{N}_x^T \Delta T = 0 \tag{A.31}$$

$$A_{66} \times 0 + B_{66} \times 0 = 0 \tag{A.32}$$

$$B_{11}U_{,x} + B_{12}V_{,y} - D_{11}W_{1,xx} - D_{12}W_{2,yy} - \hat{M}_x^T \Delta T = 0 \tag{A.33}$$

$$B_{11}U_{,xx} - D_{11}W_{1,xxx} = 0 \tag{A.34}$$

at $y = \pm L_y / 2$,

$$A_{12}U_{,x} + A_{22}V_{,y} - B_{12}W_{1,xx} - B_{22}W_{2,yy} - \hat{N}_y^T \Delta T = 0 \tag{A.35}$$

$$A_{66} \times 0 + B_{66} \times 0 = 0 \tag{A.36}$$

$$B_{12}U_{,x} + B_{22}V_{,y} - D_{12}W_{1,xx} - D_{22}W_{2,yy} - \hat{M}_y^T \Delta T = 0 \tag{A.37}$$

$$B_{22}V_{,yy} - D_{22}W_{2,yyy} = 0 \tag{A.38}$$

and

$$U(0) = 0 \tag{A.39}$$

$$V(0) = 0 \tag{A.40}$$

$$W_1(0) + W_2(0) = 0 \tag{A.41}$$

$$W_{1,x}(0) = 0 \tag{A.42}$$

$$W_{2,y}(0) = 0 \tag{A.43}$$

$$0 - 0 = 0 \tag{A.44}$$

Note that Equations (A.32), (A.36), and (A.44) are automatically satisfied.

Rearranging Equations (A.28) and (A.29) and differentiating them with respect to *x* and *y*, respectively, yields

$$U_{,xxx} = \frac{B_{11}}{A_{11}} W_{1,xxxx} \tag{A.45}$$

$$V_{,yyy} = \frac{B_{22}}{A_{22}} W_{2,yyyy} \tag{A.46}$$

After employing Equations (A.45) and (A.46), Equation (A.30) can be written as

$$\left(\frac{B_{11}^2}{A_{11}} - D_{11} \right) W_{1,xxxx} + \left(\frac{B_{22}^2}{A_{22}} - D_{22} \right) W_{2,yyyy} = 0 \tag{A.47}$$

It is clear that the first term on the left hand side of the above equation is a function of *x* only, and the second term is a function of *y* only. Therefore, both the terms must be equal to constants which are opposite in magnitude, or, stated explicitly,

$$\left(\frac{B_{11}^2}{A_{11}} - D_{11} \right) W_{1,xxxx} = C_1 \tag{A.48}$$

$$\left(\frac{B_{22}^2}{A_{22}} - D_{22} \right) W_{2,yyyy} = -C_1 \tag{A.49}$$

Equations (A.48) and (A.49) can be solved for W_1 and W_2, which can be expressed as

$$W_1 = \frac{C_1 A_{11}}{24\left(B_{11}^2 - A_{11} D_{11} \right)} x^4 + C_2 x^3 + C_3 x^2 + C_4 x + C_5 \tag{A.50}$$

$$W_2 = \frac{-C_1 A_{22}}{24\left(B_{22}^2 - A_{22} D_{22} \right)} y^4 + C_6 y^3 + C_7 y^2 + C_8 y + C_9 \tag{A.51}$$

After differentiating Equations (A.50) and (A.51) three times with respect to *x* and *y*, respectively, and substituting them into Equations (A.28) and (A.29), it can be shown that

$$U = \int \left[\int \frac{B_{11}}{A_{11}} \left\{ \frac{C_1 A_{11}}{\left(B_{11}^2 - A_{11} D_{11} \right)} x + 6C_2 \right\} dx \right] dx$$

$$= \frac{B_{11}}{A_{11}} \left\{ \frac{C_1 A_{11}}{6\left(B_{11}^2 - A_{11} D_{11} \right)} x^3 + 3C_2 x^2 + C_{10} x + C_{11} \right\} \tag{A.52}$$

and

$$V = \int \left[\int \frac{B_{22}}{A_{22}} \left\{ \frac{-C_1 A_{22}}{\left(B_{22}^2 - A_{22} D_{22} \right)} y + 6C_6 \right\} dy \right] dy$$

$$= \frac{B_{22}}{A_{22}} \left\{ \frac{-C_1 A_{22}}{6\left(B_{22}^2 - A_{22} D_{22} \right)} y^3 + 3C_6 y^2 + C_{12} y + C_{13} \right\} \tag{A.53}$$

Applying Equations (A.39) and (A.40) to Equations (A.52) and (A.53) yields

$$C_{11} = 0 \tag{A.54}$$

$$C_{13} = 0 \tag{A.55}$$

By inserting Equations (A.50)-(A.53), boundary condition (A.31) can be rewritten as

$$B_{11} \left\{ \frac{C_1 A_{11}}{2\left(B_{11}^2 - A_{11} D_{11} \right)} x^2 + 6C_2 x + C_{10} \right\} + \frac{A_{12} B_{22}}{A_{22}} \left\{ \frac{-C_1 A_{22}}{2\left(B_{22}^2 - A_{22} D_{22} \right)} y^2 + 6C_6 y + C_{12} \right\} -$$
$$B_{11} \left\{ \frac{C_1 A_{11}}{2\left(B_{11}^2 - A_{11} D_{11} \right)} x^2 + 6C_2 x + 2C_3 \right\} - B_{12} \left\{ \frac{-C_1 A_{22}}{2\left(B_{22}^2 - A_{22} D_{22} \right)} y^2 + 6C_6 y + 2C_7 \right\} - \hat{N}_x^T \Delta T = 0 \tag{A.56}$$

at $x = \pm L_x / 2$, or

$$B_{11}\left(C_{10} - 2C_3 \right) + \left(\frac{A_{12} B_{22}}{A_{22}} - B_{12} \right) \left\{ \frac{-C_1 A_{22}}{2\left(B_{22}^2 - A_{22} D_{22} \right)} y^2 + 6C_6 y \right\} +$$
$$\left(\frac{A_{12} B_{22}}{A_{22}} C_{12} - 2B_{12} C_7 \right) - \hat{N}_x^T \Delta T = 0 \tag{A.57}$$

at $x = \pm L_x / 2$. This statement must be valid for any value of *y* on the *x*-edges. Therefore, the terms in the brace must be zero. As a result,

$$C_1 = 0 \tag{A.58}$$

$$C_6 = 0 \tag{A.59}$$

and Equation (A.57) becomes

$$-2B_{11}C_3 - 2B_{12}C_7 + B_{11}C_{10} + \frac{A_{12}B_{22}}{A_{22}}C_{12} = \hat{N}_x^T \Delta T \tag{A.60}$$

Analogously, by inserting Equations (A.50)-(A.53), boundary condition (A.35) can be rewritten as

$$\begin{aligned} &\frac{A_{12}B_{11}}{A_{11}}\left(6C_2 x + C_{10}\right) + B_{22}C_{12} - \\ &B_{12}\left(6C_2 x + 2C_3\right) - 2B_{22}C_7 - \hat{N}_y^T \Delta T = 0 \end{aligned} \tag{A.61}$$

at $y = \pm L_y / 2$. Equation (A.61) must be valid at any value of *x* on the *y* edges. Thus,

$$C_2 = 0 \tag{A.62}$$

and Equation (A.61) becomes

$$-2B_{12}C_3 - 2B_{22}C_7 + \frac{A_{12}B_{11}}{A_{11}}C_{10} + B_{22}C_{12} = \hat{N}_y^T \Delta T \tag{A.63}$$

Additionally, after applying (A.50)-(A.53) to boundary conditions (A.33) and (A.37), it can be shown that, respectively,

$$-2D_{11}C_3 - 2D_{12}C_7 + \frac{B_{11}^2}{A_{11}}C_{10} + \frac{B_{12}B_{22}}{A_{22}}C_{12} = \hat{M}_x^T \Delta T \tag{A.64}$$

at $x = \pm L_x / 2$, and

$$-2D_{12}C_3 - 2D_{22}C_7 + \frac{B_{11}B_{12}}{A_{11}}C_{10} + \frac{B_{22}^2}{A_{22}}C_{12} = \hat{M}_y^T \Delta T \tag{A.65}$$

at $y = \pm L_y / 2$.

At this point, the deformation field simplifies to

$$w^0 = C_3 x^2 + C_4 x + C_7 y^2 + C_8 y + C_5 + C_9 \tag{A.66}$$

$$u^0 = \frac{B_{11}}{A_{11}} C_{10} x \tag{A.67}$$

$$v^0 = \frac{B_{22}}{A_{22}} C_{12} y \tag{A.68}$$

By applying the conditions (A.41)-(A.43) in order to prevent rigid body motions, Equation (A.66) is simplified to be

$$w^0 = C_3 x^2 + C_7 y^2 \tag{A.69}$$

Lastly, the deformation fields (A.67)-(A.69) must satisfy the last two boundary conditions Equations (A.34) and (A.38). It can be shown that they automatically fulfill these Kirchhoff shear boundary conditions on all four edges. Consequently, the deformation fields expressed in Equations (A.67)-(A.69) are the analytical solution of this problem with unknown coefficients C_3, C_7, C_{10}, and C_{12} determined by the set of algebraic equations (A.60), (A.63), (A.64), and (A.65), or in the matrix form,

$$\begin{bmatrix} -2B_{11} & -2B_{12} & B_{11} & \frac{A_{12}B_{22}}{A_{22}} \\ -2B_{12} & -2B_{22} & \frac{A_{12}B_{11}}{A_{11}} & B_{22} \\ -2D_{11} & -2D_{12} & \frac{B_{11}^2}{A_{11}} & \frac{B_{12}B_{22}}{A_{22}} \\ -2D_{12} & -2D_{22} & \frac{B_{11}B_{12}}{A_{11}} & \frac{B_{22}^2}{A_{22}} \end{bmatrix} \begin{Bmatrix} C_3 \\ C_7 \\ C_{10} \\ C_{12} \end{Bmatrix} = \Delta T \begin{Bmatrix} \hat{N}_x^T \\ \hat{N}_y^T \\ \hat{M}_x^T \\ \hat{M}_y^T \end{Bmatrix} \tag{A.70}$$

It should be noted that C_3, C_7, C_{10}, and C_{12} do not involve the lengths of the laminate so they are independent of the inplane dimensions of the laminate. This also indicates that the curvatures in the *x*- and *y*-direction of a laminate determined by using Equation (A.7) are uniform throughout the laminated plate, and the twist curvature is identically zero.

A.2 Special Case for Isotropic Laminated Plates

An isotropic laminate, which is a special case of a cross-ply laminate, is considered in this section. Due to the material isotropy in each layer, laminate stiffnesses are simplified as indicated below:

$$A_{11} = A_{22} = A = \sum_{k=1}^{N} \frac{E_k}{1-\nu_k^2}\left(z_k - z_{k-1}\right) \tag{A.71}$$

$$A_{12} = A_{\nu} = \sum_{k=1}^{N} \frac{\nu_k E_k}{1-\nu_k^2}\left(z_k - z_{k-1}\right) \tag{A.72}$$

$$A_{16} = A_{11} - A_{12} = A - A_{\nu} \tag{A.73}$$

$$B_{11} = B_{22} = B = \frac{1}{2}\sum_{k=1}^{N} \frac{E_k}{1-\nu_k^2}\left(z_k^2 - z_{k-1}^2\right) \tag{A.74}$$

$$B_{12} = B_{\nu} = \frac{1}{2}\sum_{k=1}^{N} \frac{\nu_k E_k}{1-\nu_k^2}\left(z_k^2 - z_{k-1}^2\right) \tag{A.75}$$

$$B_{16} = B_{11} - B_{12} = B - B_{\nu} \tag{A.76}$$

$$D_{11} = D_{22} = D = \frac{1}{3}\sum_{k=1}^{N} \frac{E_k}{1-\nu_k^2}\left(z_k^3 - z_{k-1}^3\right) \tag{A.77}$$

$$D_{12} = D_{\nu} = \frac{1}{3}\sum_{k=1}^{N} \frac{\nu_k E_k}{1-\nu_k^2}\left(z_k^3 - z_{k-1}^3\right) \tag{A.78}$$

$$D_{16} = D_{11} - D_{12} = D - D_{\nu} \tag{A.79}$$

where E is the extensional modulus of the material and ν is the Poisson ratio. The subscripts k on the material properties merely identify the material properties with the k^{th} layer. In addition, the effective inplane force resultants $\left(\hat{N}_x^T, \hat{N}_y^T\right)$, and the effective bending moment resultants $\left(\hat{M}_x^T, \hat{M}_y^T\right)$ due to a unit temperature change are simplified to become

$$\hat{N}_x^T = \hat{N}_y^T = \hat{N}^T = \sum_{k=1}^{N} \frac{E_k \alpha_k}{1-\nu_k}\left(z_k - z_{k-1}\right) \tag{A.80}$$

$$\hat{M}_x^T = \hat{M}_y^T = \hat{M}^T = \frac{1}{2}\sum_{k=1}^{N} \frac{E_k \alpha_k}{1-\nu_k}\left(z_k^2 - z_{k-1}^2\right) \tag{A.81}$$

where α is coefficient of thermal expansion of the material. As a result, Equation (A.70) can be written as

$$\begin{bmatrix} -2B & -2B_\nu & B & \frac{A_\nu B}{A} \\ -2B_\nu & -2B & \frac{A_\nu B}{A} & B \\ -2D & -2D_\nu & \frac{B^2}{A} & \frac{B_\nu B}{A} \\ -2D_\nu & -2D & \frac{B_\nu B}{A} & \frac{B^2}{A} \end{bmatrix} \begin{Bmatrix} C_3 \\ C_7 \\ C_{10} \\ C_{12} \end{Bmatrix} = \Delta T \begin{Bmatrix} \hat{N}^T \\ \hat{N}^T \\ \hat{M}^T \\ \hat{M}^T \end{Bmatrix} \tag{A.82}$$

from which it can be proven that

$$C_3 = C_7 = C_O \tag{A.83}$$

$$C_{10} = C_{12} = C_I \tag{A.84}$$

In the above, C_O and C_I are the coefficients of the displacement fields, which are now expressed as

$$w^0 = C_O\left(x^2 + y^2\right) \tag{A.85}$$

$$u^0 = \frac{B}{A} C_I x \tag{A.86}$$

$$v^0 = \frac{B}{A} C_I y \tag{A.87}$$

Thus, Equation (A.82) is reduced to

$$\begin{bmatrix} -2B\left(1+\frac{B_\nu}{B}\right) & B\left(1+\frac{A_\nu}{A}\right) \\ -2D\left(1+\frac{D_\nu}{D}\right) & \frac{B^2}{A}\left(1+\frac{B_\nu}{B}\right) \end{bmatrix} \begin{Bmatrix} C_O \\ C_I \end{Bmatrix} = \Delta T \begin{Bmatrix} \hat{N}^T \\ \hat{M}^T \end{Bmatrix} \tag{A.88}$$

Accordingly, C_O and C_I can be solved for as

$$C_O = \frac{A\Delta T}{2AD\left(1+\frac{A_\nu}{A}\right)\left(1+\frac{D_\nu}{D}\right)-2B^2\left(1+\frac{B_\nu}{B}\right)^2}\left\{\frac{B}{A}\left(1+\frac{B_\nu}{B}\right)\hat{N}^T-\left(1+\frac{A_\nu}{A}\right)\hat{M}^T\right\} \quad \text{(A.89)}$$

$$C_I = \frac{2A\Delta T}{2AD\left(1+\frac{A_\nu}{A}\right)\left(1+\frac{D_\nu}{D}\right)-2B^2\left(1+\frac{B_\nu}{B}\right)^2}\left\{\frac{D}{B}\left(1+\frac{D_\nu}{D}\right)\hat{N}^T-\left(1+\frac{B_\nu}{B}\right)\hat{M}^T\right\} \quad \text{(A.90)}$$

Appendix B

ANALYTICAL SOLUTIONS FOR LAMINATED BEAMS SUBJECTED TO A TEMPERATURE CHANGE, PIEZOELECTRICAL ACTUATION, AND FORCES

B.1 Geometrically Nonlinear Beam Theory for Pinned-Roller Supports

B.1.1 Mathematical Formulation and Solution Procedures

Consider a laminated beam with simply-supported boundary conditions at each end subjected to a thermal load with temperature change, ΔT, and a force, $2P$ acting at the middle of the beam, illustrated in Figure B.1. Assume one end of the beam is pinned and the other end is on rollers i.e., pinned-roller conditions. A Cartesian coordinate system x-z is located at the center of the beam. The length and total thickness of the beam are denoted as L_x and H, respectively. The number of layers in the beam is assumed to be N. The location $z = 0$ is the geometric midline, here taken to be the reference line of the analysis. The lower and upper boundaries of layer 1, or the bottom layer, are situated at $z = z_0 = -H/2$ and $z = z_1$, the boundaries of layer 2 at z_1 and z_2, and in general, the boundaries of the k^{th} layer at z_{k-1} and z_k.

The equilibrium equations for the laminated beam, including a geometrically nonlinear term, are written as

$$N_{x,x} = 0 \tag{B.1}$$

$$M_{x,xx} + N_x w^0_{,xx} = 0 \tag{B.2}$$

where N_x and M_x are force and moment resultants in the x-direction, and w^0 is the deflection of the beam in the z-direction. The ensuing comma and subscript x represents the derivative with respect to x variable. Equations (B.1) and (B.2) represent force equilibrium in the x-

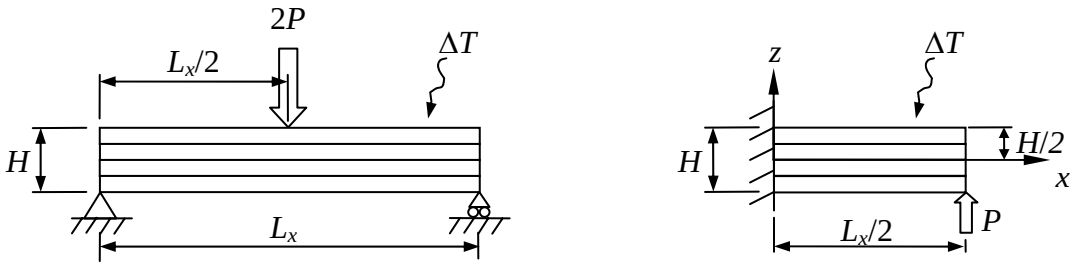

(a) Full laminated beam (b) Half model

Figure B.1: Pinned-Roller Simply-Supported Laminated Beam Subjected to Thermal Load and Vertical Force

and *z*-directions, respectively. The second term on the left hand side of Equation (B.2) is the geometrically nonlinear term necessary to account for moderate rotations in the *x*-*z* plane.

The constitutive equations for the linear elastic laminated beam are given by

$$N_x = A_{11}\varepsilon_x^0 + B_{11}\kappa_x^0 - \hat{N}_x^T \Delta T \tag{B.3}$$

$$M_x = B_{11}\varepsilon_x^0 + D_{11}\kappa_x^0 - \hat{M}_x^T \Delta T \tag{B.4}$$

In the above, A_{11}, B_{11}, and D_{11} are extensional or stretching stiffness, bending-stretching coupling stiffness, and bending stiffness, respectively, which are defined as

$$\begin{aligned} A_{11} &= \sum_{k=1}^{N} E_{xk}\left(z_k - z_{k-1}\right) \\ B_{11} &= \frac{1}{2}\sum_{k=1}^{N} E_{xk}\left(z_k^2 - z_{k-1}^2\right) \\ D_{11} &= \frac{1}{3}\sum_{k=1}^{N} E_{xk}\left(z_k^3 - z_{k-1}^3\right) \end{aligned} \tag{B.5}$$

Additionally, $\hat{N}_x^T$ and $\hat{M}_x^T$ are equivalent thermal force and moment resultants and are defined as

$$\hat{N}_x^T = \sum_{k=1}^{N} E_{xk}\alpha_{xk}\left(z_k - z_{k-1}\right) \tag{B.6}$$

$$\hat{M}_x^T = \frac{1}{2}\sum_{k=1}^{N} E_{xk}\alpha_{xk}\left(z_k^2 - z_{k-1}^2\right) \tag{B.7}$$

where E_{xk} and α_{xk} are extensional modulus of elasticity and coefficient of thermal expansion in the *x*-direction of the k^{th} layer, respectively. In addition, the extensional strain ε_x^0, reflecting moderate rotations, and bending curvature κ_x^0 are given by

$$\varepsilon_x^0 = \frac{du^0}{dx} + \frac{1}{2}\left(\frac{dw^0}{dx}\right)^2 \tag{B.8}$$

$$\kappa_x^0 = -\frac{d^2 w^0}{dx^2} \tag{B.9}$$

where u^0 is the *x*-direction deformation on the reference line.

The boundary conditions imposed on the half model, which can be employed because of symmetry conditions, illustrated in Figure B.1 (b) are as follows:

at $x = 0$,

$$u^0 = 0 \tag{B.10}$$

$$w^0 = 0 \tag{B.11}$$

$$\frac{dw^0}{dx} = 0 \tag{B.12}$$

at $x = L_x/2$,

$$N_x = 0 \tag{B.13}$$

$$Q_x = P \tag{B.14}$$

$$M_x = 0 \tag{B.15}$$

where Q_x is the transverse shear stress resultant defined as

$$\begin{aligned} Q_x &= M_{x,x} + N_x w_{,x}^0 \\ &= B_{11}u_{,xx}^0 - D_{11}w_{,xxx}^0 + B_{11}w_{,x}^0 w_{,xx}^0 + N_x w_{,x}^0 \end{aligned} \tag{B.16}$$

From Equations (B.1) and (B.13), it can be concluded that

$$N_x = 0 \tag{B.17}$$

Thus,

$$A_{11}\varepsilon_x^0 + B_{11}\kappa_x^0 - \hat{N}_x^T \Delta T = 0 \tag{B.18}$$

By inserting Equations (B.8) and (B.9) into Equation (B.18), rearrangement yields

$$u_{,x}^0 = \frac{B_{11}}{A_{11}} w_{,xx}^0 - \frac{1}{2}\left(w_{,x}^0\right)^2 + \frac{\hat{N}_x^T \Delta T}{A_{11}} \tag{B.19}$$

After substituting Equations (B.4), and then (B.8) and (B.9), into Equation (B.2) and using Equation (B.17), Equation (B.2) is rewritten as

$$B_{11}\left(u_{,xxx}^0 + w_{,x}^0 w_{,xxx}^0 + \left(w_{,xx}^0\right)^2\right) - D_{11} w_{,xxxx}^0 = 0 \tag{B.20}$$

By taking second derivative of Equation (B.19) with respect to *x* and inserting the result into Equation (B.20), the following expression is obtained.

$$\left(\frac{B_{11}^2}{A_{11}} - D_{11}\right) w_{,xxxx}^0 = 0 \tag{B.21}$$

The term in the parenthesis in Equation (B.21) is a function of material properties and thickness of the consisting layers, so it is generally not equal to zero. Therefore, the fourth derivative of the out of plane deflection w^0 must vanish. As a result, w^0 is of the form

$$w^0 = Ax^3 + Bx^2 + Cx + D \tag{B.22}$$

By applying the boundary conditions in Equations (B.11) and (B.12),

$$\begin{aligned} C &= 0 \\ D &= 0 \end{aligned} \tag{B.23}$$

and w^0 becomes

$$w^0 = Ax^3 + Bx^2 \tag{B.24}$$

By using Equations (B.8), (B.9), (B.19), and (B.24), and applying the boundary condition of Equation (B.14) with the aid of Equation (B.16), it can be shown that

$$6\left(\frac{B_{11}^2}{A_{11}} - D_{11}\right) A = P \tag{B.25}$$

or
$$A = \frac{-A_{11}P}{6\left(D_{11}A_{11} - B_{11}^2\right)} \tag{B.26}$$

To determine coefficient B in Equation (B.24), the boundary condition in Equation (B.15) must be employed in conjunction with Equations (B.4), (B.8), (B.9), and (B.19). Thus, B is given by

$$B = \frac{A_{11}}{2\left(D_{11}A_{11} - B_{11}^2\right)}\left(\frac{B_{11}}{A_{11}}\hat{N}_x^T\Delta T - \hat{M}_x^T\Delta T + \frac{PL_x}{2}\right) \tag{B.27}$$

Finally, the deflection w^0 is expressed as

$$w^0 = \frac{-A_{11}P}{6\left(D_{11}A_{11} - B_{11}^2\right)}x^3 + \frac{A_{11}}{2\left(D_{11}A_{11} - B_{11}^2\right)}\left(\frac{B_{11}}{A_{11}}\hat{N}_x^T\Delta T - \hat{M}_x^T\Delta T + \frac{PL_x}{2}\right)x^2 \tag{B.28}$$

and the curvature in the x-direction, defined in Equation (B.9), is given by

$$\kappa_x^0 = \frac{A_{11}}{\left(D_{11}A_{11} - B_{11}^2\right)}\left\{P\left(x - \frac{L_x}{2}\right) - \frac{B_{11}}{A_{11}}\hat{N}_x^T\Delta T + \hat{M}_x^T\Delta T\right\} \tag{B.29}$$

Substituting (B.24) into (B.19), and then, integrating Equation (B.19) with respect to x results in

$$u^0 = -\frac{9}{10}A^2x^5 - \frac{6}{4}ABx^4 - \frac{2}{3}B^2x^3 + \frac{3B_{11}}{A_{11}}Ax^2 + \left(\frac{2B_{11}}{A_{11}}B + \frac{\hat{N}_x^T\Delta T}{A_{11}}\right)x + F \tag{B.30}$$

After applying Equation (B.10) to Equation (B.30), it is shown that

$$F = 0 \tag{B.31}$$

Therefore, Equation (B.30) becomes

$$u^0 = -\frac{9}{10}A^2x^5 - \frac{6}{4}ABx^4 - \frac{2}{3}B^2x^3 + \frac{3B_{11}}{A_{11}}Ax^2 + \left(\frac{2B_{11}}{A_{11}}B + \frac{\hat{N}_x^T\Delta T}{A_{11}}\right)x \tag{B.32}$$

Interestingly, even though the present beam theory is geometrically nonlinear, it can be seen that w^0 in Equation (B.28) and κ_x^0 in Equation (B.29) are linear functions of the thermal and mechanical loads, i.e., $\hat{N}_x^T\Delta T$, $\hat{M}_x^T\Delta T$, and P. However, u^0 is a nonlinear (quadratic)

function of the thermal and mechanical loads because of the presence of A^2, AB, and B^2 in Equation (B.32). Thus, the nonlinear effect plays a role in the longitudinal deformation, but not in the transverse deformation for the geometrically nonlinear laminated beam theory with the pinned-roller simply-supported boundary condition. Additionally, it is evident that for this case the theory does not provide multiple solutions despite being a geometrically nonlinear.

In a special case when $P = 0$,

$$A = 0 \tag{B.33}$$

$$B = \frac{A_{11}}{2\left(D_{11}A_{11} - B_{11}^2\right)}\left(\frac{B_{11}}{A_{11}}\hat{N}_x^T\Delta T - \hat{M}_x^T\Delta T\right) \tag{B.34}$$

and Equations (B.28), (B.29) and (B.32) are simplified to become

$$w^0 = \frac{A_{11}}{2\left(D_{11}A_{11} - B_{11}^2\right)}\left(\frac{B_{11}}{A_{11}}\hat{N}_x^T\Delta T - \hat{M}_x^T\Delta T\right)x^2 \tag{B.35}$$

$$\kappa_x^0 = \frac{A_{11}}{\left(D_{11}A_{11} - B_{11}^2\right)}\left(-\frac{B_{11}}{A_{11}}\hat{N}_x^T\Delta T + \hat{M}_x^T\Delta T\right) \tag{B.36}$$

$$u^0 = -\frac{2}{3}B^2x^3 + \left(\frac{2B_{11}}{A_{11}}B + \frac{\hat{N}_x^T\Delta T}{A_{11}}\right)x \tag{B.37}$$

It should be noted that the without the applied load P, w^0 and u^0 are an even and odd functions of beam coordinate x, respectively. In addition, κ_x^0 depends only on the material properties and the thickness of each lamina and is uniform throughout the length of the beam.

B.1.2 Problem Extension to Include Piezoelectrically-Induced Deformations

The analytical solutions of the geometrically nonlinear laminated beam subjected to a thermal load and a transverse force established in the previous section can be modified to include the piezoelectrically-induced deformation if some of the layers in the

laminated beam have piezoelectric properties. The piezoelectrically-induced strain caused by the transverse converse piezoelectric effect (d_{31} effect) can be modeled in the same way as the thermally-induced strain. As a result, analogous to the equivalent thermal force and moment resultants, $\hat{N}_x^T$ and $\hat{M}_x^T$, equivalent piezoelectrical force and moment resultants for the beam are defined as

$$\hat{N}_x^E = \sum_{k=1}^{N} E_{xk} d_{31k} \left(z_k - z_{k-1} \right) \tag{B.38}$$

$$\hat{M}_x^E = \frac{1}{2} \sum_{k=1}^{N} E_{xk} d_{31k} \left(z_k^2 - z_{k-1}^2 \right) \tag{B.39}$$

Thus, including the piezoelectric effect, Equations (B.27), (B.28), (B.29) and (B.32) are modified to become

$$B = \frac{A_{11}}{2\left(D_{11} A_{11} - B_{11}^2 \right)} \left\{ \frac{B_{11}}{A_{11}} \left(\hat{N}_x^T \Delta T + \hat{N}_x^E E_3 \right) - \left(\hat{M}_x^T \Delta T + \hat{M}_x^E E_3 \right) + \frac{P L_x}{2} \right\} \tag{B.40}$$

$$w^0 = \frac{-A_{11} P}{6\left(D_{11} A_{11} - B_{11}^2 \right)} x^3 + B x^2 \tag{B.41}$$

$$\kappa_x^0 = \frac{A_{11}}{\left(D_{11} A_{11} - B_{11}^2 \right)} \left\{ P\left(x - \frac{L_x}{2} \right) - \frac{B_{11}}{A_{11}} \left(\hat{N}_x^T \Delta T + \hat{N}_x^E E_3 \right) + \left(\hat{M}_x^T \Delta T + \hat{M}_x^E E_3 \right) \right\} \tag{B.42}$$

$$u^0 = -\frac{9}{10} A^2 x^5 - \frac{6}{4} A B x^4 - \frac{2}{3} B^2 x^3 + \frac{3 B_{11}}{A_{11}} A x^2 + \left(\frac{2 B_{11}}{A_{11}} B + \frac{\hat{N}_x^T \Delta T + \hat{N}_x^E E_3}{A_{11}} \right) x \tag{B.43}$$

B.2 Geometrically Linear Beam Theory for Pinned-Roller Supports

Consider the same laminated beam illustrated in Figure B.1. Geometrically linear laminated beam theory will now be investigated. Equilibrium of forces in the *x*- and *z*-directions is given respectively by

$$N_{x,x} = 0 \tag{B.44}$$

$$M_{x,xx} = 0 \tag{B.45}$$

Note that the nonlinear term $N_x w^0_{,xx}$ in Equation (B.2) disappears. The constitutive relations used here are the same as Equation (B.3)-(B.7) except for the transverse shear stress resultant Q_x, which, for the linear theory, is defined as

$$\begin{aligned} Q_x &= M_{x,x} \\ &= B_{11}u^0_{,xx} - D_{11}w^0_{,xxx} \end{aligned} \tag{B.46}$$

The strain-displacement relations are different, as the rotational term in the longitudinal strain in the x-direction is not included for the geometrically linear theory. As a result,

$$\varepsilon^0_x = \frac{du^0}{dx} \tag{B.47}$$

$$\kappa^0_x = -\frac{d^2w^0}{dx^2} \tag{B.48}$$

The boundary conditions imposed here are pinned-roller simply-supported, which are identical to those given in Equations (B.10)-(B.15). By following the solution procedure presented in Section B.1, the extensional force resultant can be obtained as

$$N_x = 0 \tag{B.49}$$

Using constitutive equation (B.3) and strain-displacement relations (B.47)-(B.48) in Equation (B.49), and rearranging terms, results in

$$u^0_{,x} = \frac{B_{11}}{A_{11}} w^0_{,xx} + \frac{\hat{N}^T_x \Delta T}{A_{11}} \tag{B.50}$$

After substituting Equation (B.4), and then Equations (B.47) and (B.48) into Equation (B.45), Equation (B.45) is rewritten as

$$B_{11}u^0_{,xxx} - D_{11}w^0_{,xxxx} = 0 \tag{B.51}$$

By taking two derivatives of Equation (B.50) with respect to x, and inserting the result into Equation (B.51), the following expression is obtained:

$$\left(\frac{B_{11}^2}{A_{11}} - D_{11}\right) w^0_{,xxxx} = 0 \tag{B.52}$$

Again, $w^0_{,xxxx}$ must be zero since the term in the parenthesis is functions of the structural stiffnesses and not equal to zero in general. Therefore, the deflection w^0 can be solved for and given by

$$w^0 = Ax^3 + Bx^2 + Cx + D \tag{B.53}$$

By applying the boundary conditions in Equations (B.11) and (B.12),

$$\begin{aligned} C &= 0 \\ D &= 0 \end{aligned} \tag{B.54}$$

and w^0 becomes

$$w^0 = Ax^3 + Bx^2 \tag{B.55}$$

By using Equations (B.47), (B.48), (B.50), and (B.53), and applying Equation (B.14) with the aid of Equation (B.46), it can be shown that

$$6\left(\frac{B_{11}^2}{A_{11}} - D_{11}\right) A = P \tag{B.56}$$

or

$$A = \frac{-A_{11}P}{6\left(D_{11}A_{11} - B_{11}^2\right)} \tag{B.57}$$

To determine coefficient *B* in Equation (B.55), the boundary condition in Equation (B.15) must be employed in conjunction with Equations (B.4), (B.47), (B.48), and (B.50). Thus, *B* can be solved to be

$$B = \frac{A_{11}}{2\left(D_{11}A_{11} - B_{11}^2\right)}\left(\frac{B_{11}}{A_{11}}\hat{N}_x^T\Delta T - \hat{M}_x^T\Delta T + \frac{PL_x}{2}\right) \tag{B.58}$$

Finally, the transverse deflection w^0 is expressed as

$$w^0 = \frac{-A_{11}P}{6\left(D_{11}A_{11} - B_{11}^2\right)}x^3 + \frac{A_{11}}{2\left(D_{11}A_{11} - B_{11}^2\right)}\left(\frac{B_{11}}{A_{11}}\hat{N}_x^T\Delta T - \hat{M}_x^T\Delta T + \frac{PL_x}{2}\right)x^2 \tag{B.59}$$

and the curvature in the *x*-direction defined in Equation (B.48) is given by

$$\kappa_x^0 = \frac{A_{11}}{\left(D_{11}A_{11} - B_{11}^2\right)}\left\{P\left(x - \frac{L_x}{2}\right) - \frac{B_{11}}{A_{11}}\hat{N}_x^T\Delta T + \hat{M}_x^T\Delta T\right\} \tag{B.60}$$

Note that the expressions for the transverse deflection and the *x*-direction curvature of geometrically linear laminated beam in Equations (B.59) and (B.60), respectively, are exactly the same as those of geometrically nonlinear laminated beam in Equations (B.28) and (B.29). This makes sense since the transverse deflection w^0 and the *x*-direction curvature κ_x^0 resulted from the geometrically nonlinear beam theory do not reveal the nonlinear relationships with the applied loads.

The inplane deformation is obtained by integrating Equation (B.50) once with respect to *x*. The result is expressed as

$$u^0 = \frac{3B_{11}}{A_{11}}Ax^2 + \left(\frac{2B_{11}}{A_{11}}B + \frac{\hat{N}_x^T\Delta T}{A_{11}}\right)x + F \tag{B.61}$$

After applying Equation (B.10) to Equation (B.61), it is shown that

$$F = 0 \tag{B.62}$$

Therefore, Equation (B.61) becomes

$$u^0 = \frac{3B_{11}}{A_{11}}Ax^2 + \left(\frac{2B_{11}}{A_{11}}B + \frac{\hat{N}_x^T\Delta T}{A_{11}}\right)x \tag{B.63}$$

Unlike the deflection w^0, u^0 in Equation (B.63) is, however, partially different from the counterpart in Equation (B.32). Specifically what is different is lack of the quantities *x* raised to the third, fourth, and fifth powers in Equation (B.63) compared to Equation (B.32). This is because the coefficients of these high degree monomials of *x* contain the nonlinear functions of the applied loads, i.e., A^2, AB, and B^2. Thus, the corresponding monomials $\left(x^3,\ x^4,\ x^5\right)$ must vanish for the linear case.

A special case when $P = 0$ (or $A = 0$) can be obtained for w^0, κ_x^0, and u^0 in Equations (B.59), (B.60) and (B.63). In this case the deformations are written as

$$w^0 = \frac{A_{11}}{2\left(D_{11}A_{11} - B_{11}^2\right)}\left(\frac{B_{11}}{A_{11}}\hat{N}_x^T\Delta T - \hat{M}_x^T\Delta T\right)x^2 \tag{B.64}$$

$$\kappa_x^0 = \frac{-A_{11}}{\left(D_{11}A_{11} - B_{11}^2\right)}\left(\frac{B_{11}}{A_{11}}\hat{N}_x^T\Delta T - \hat{M}_x^T\Delta T\right) \tag{B.65}$$

$$u^0 = \left(\frac{2B_{11}}{A_{11}}B + \frac{\hat{N}_x^T\Delta T}{A_{11}}\right)x \tag{B.66}$$

In the above, w^0 and u^0 are quadratic and linear functions of *x*, respectively.

B.2.1 Problem Extension to Include Piezoelectrically-Induced Deformations

Like the discussion in Section B.1.2, the extension of the geometrically linear laminated beam problem to include piezoelectrically-induced deformations can also be obtained. Employing the same equivalent piezoelectrical force and moment resultants defined in Equations (B.38) and (B.39), the beam deformations with inclusion of the transverse converse piezoelectric effect are written as

$$w^0 = \frac{-A_{11}P}{6\left(D_{11}A_{11} - B_{11}^2\right)}x^3 + Bx^2 \tag{B.67}$$

$$\kappa_x^0 = \frac{A_{11}}{\left(D_{11}A_{11} - B_{11}^2\right)}\left\{P\left(x - \frac{L_x}{2}\right) - \frac{B_{11}}{A_{11}}\left(\hat{N}_x^T\Delta T + \hat{N}_x^E E_3\right) + \left(\hat{M}_x^T\Delta T + \hat{M}_x^E E_3\right)\right\} \tag{B.68}$$

$$u^0 = \frac{3B_{11}}{A_{11}}Ax^2 + \left(\frac{2B_{11}}{A_{11}}B + \frac{\hat{N}_x^T\Delta T + \hat{N}_x^E E_3}{A_{11}}\right)x \tag{B.69}$$

where *B* is given by Equation (B.40).

REFERENCES

[1] W.B. Spillman Jr, J.S. Sirkis, and P.T. Gardiner, "Smart Materials and Structures: What are They?," *Smart Materials and Structures*, 5, 247-254, 1996.

[2] C. Shakeri, M.N. Noori, and Z. Hou, "Smart Materials and Structures A Review," http://me.wpi.edu/~cirrus/Publications/SmartMaterials/SmartMaterialExtension.html.

[3] R.E. Newnham, and Gregory R. Ruschau, "Smart Electroceramics," *Journal of American Ceramic Society*, 74 (3), 463-80, 1991.

[4] S.L. Swartz, "Topics in Electronic Ceramics," *IEEE Transactions on Electrical Insulation*, 25(5), 935-987, 1990.

[5] Morgan Matroc, Inc., http://www.morganelectroceramics.com.

[6] Face International Corporation, "Application Notes", http://www.faceco.com.

[7] V.Z. Parton, and B.A. Kudryavtsev, "Electromagnetoelasticity," Gordon and Breach Science Publishers, 1988.

[8] D.J. Inman, and H.H. Cudney, "Structural and Machine Design Using Piezoceramic Materails: A Guide for Structural Design Engineers," Final Report to NASA Langley Research Center, 2000.

[9] T. Bailey, and J.E. Hubbard, "Distributed Piezoelectric-Polymer Active Vibration Control of a Cantilever Beam," *Journal of Guidance, Control, and Dynamics*, 8(5), 605-611, 1985.

[10] E.F. Crawley, and J. de Luis, "Use of Piezoelectric Actuators as Elements of Intelligent Structures," *AIAA Journal*, 25(10), 1373-1385, 1987.

[11] Z. Chaudhry, and C.A. Rogers, "The Pin-Force Model Revisited," *Journal of Intelligent Material Systems and Structures*, 5, 347-354, 1994.

[12] E.F. Crawley, and E. H. Anderson, "Detailed Models of Piezoceramic Actuation of Beams," *Journal of Intelligent Material Systems and Structures*, 1, 4-25, 1990.

[13] E.F. Crawley, and K.B. Lazarus, "Induced Strain Actuation of Isotropic and Anisotropic Plates," *AIAA Journal*, 29(6), 944-951, 1989.

[14] J.G. Smits and Wai-shing Choi, "The Constituent Equations of Piezoelectric Heterogeneous Bimorphs," *IEEE Transactions on Ultrasonics, Ferroelectrics, and Frequency Control*, 38(3), 256-270, 1991.

[15] J.G. Smits, S. I. Dalke, and T.K. Cooney, "The Constituent Equations of Piezoelectric Bimorphs," *Sensor and Actuators A*, 28, 41-61, 1991.

[16] Q.M. Wang, and L. E. Cross, "Performance Analysis of Piezoelectric Cantilever Bending Actuators," *Ferroelectrics*, 215, 187-213, 1998.

[17] E. Furman, G. Li, and G.H. Haertling, "An Investigation of the Resonance of Properties of RAINBOW Devices," *Ferroelectrics*, 160, 357-369, 1994.

[18] E. Furman, G. Li, and G.H. Haertling, "Electromechanical Properties of RAINBOW devices," Proceedings of the 9th IEEE International Symposium on Applications of Ferroelectrics, 146-149, 1995.

[19] G.H. Haertling, "Reduction/oxidation Effects in PLZT Ceramics," Proceedings of 4th International SAMPE Electronics Conference, Albuquerque, NM, 699-711, 1990.

[20] G.H. Haertling, "RAINBOW Ceramics – A New Type of Ultra-high-displacement Actuator," *American Ceramic Society Bulletin*, 73(1), 93-96, 1994.

[21] G.H. Haertling, "Chemically Reduced PLZT Ceramics for Ultra-high-displacement Actuators," *Ferroelectric*, 154, 101-106, 1994.

[22] G. Li, E. Furman, and G.H. Haertling, "Stress-Enhanced Displacements in PLZT Rainbow Actuators," *Journal of American Ceramic Society*, 80(6), 1382-1388, 1997.

[23] Q.M. Wang and L.E. Cross, "Tip Deflection and Blocking Force of Soft PZT-Based Cantilever RAINBOW Actuators," *Journal of American Ceramic Society*, 82(1), 103-110, 1999.

[24] R. Hellbaum, R.G. Bryant, and R.L. Fox, "Thin Layer Composite Unimorph Ferroelectric Driver and Sensor," United States Patent No. 5,6632,841. 1997.

[25] Face International Corporation, 427 W 35th Street, Norfolk, VA 23508, USA. http://www.faceco.com.

[26] K.M. Mossi, G.V. Selby, and R.G. Bryant, "Thin-layer composite unimorph ferroelectric driver and sensor properties," *Materials Letters*, 35, 39-49, 1998.

[27] K.M. Mossi, and R. P. Bishop, "Characterization of Different Types of High Performance THUNDER Actuators," Proceedings of SPIE - the International Society for Optical Engineering, 3675, 43-52, 1999.

[28] K.M. Mossi, R.P. Bishop, R.C. Smith, H T. Banks, “Evaluation criteria for THUNDER actuators,” Proceedings of SPIE - the International Society for Optical Engineering, 3667, 738-743, 1999.

[29] M. Capozzoli, J. Gopalakrishnan, K. Hogan, J. Massad, T. Tokarchik, S. Wilmarth, H. T. Banks, K. M. Mossi, R.C. Smith, “Modeling aspects concerning THUNDER actuators,” Proceedings of SPIE - the International Society for Optical Engineering, 3667, 719-727, 1999.

[30] K.J. Yoon, S. Shin, J. Kim, H.C. Park, M.K. Kwak, “Development of Lightweight THUNDER with fiber composite layers,” Proceedings of SPIE - the International Society for Optical Engineering, 3992, 57-64, 2000.

[31] K.J. Yoon, J.H. Chung, N.S. Goo, and H.C. Park, “Thermal Deformation and Residual Stress Analysis of Lightweight Piezo-composite Curved Actuator Device,” Proceedings of SPIE - the International Society for Optical Engineering, 4333, 418-425, 2001.

[32] K.J. Yoon, S. Shin, H.C. Park, and N.S. Goo, “Design and Manufacture of a Lightweight Piezo-Composite Curved Actuator,” *Smart Materials and Structures*, 11(1), 163-168.

[33] K.J. Yoon, K.H. Park, H.C. Park, D. Perreux, “Thermal deformation analysis of curved actuator LIPCA with a piezoelectric ceramic layer and fiber composite layers,” *Composites Science & Technology*, 63, 501-506, 2003.

[34] R.M. Barrett, and R.S. Gross, “Recent Advances in Adaptive Aerostructures: Designing for Flight Control,” Proceedings, 4th European Conference on Smart Structures and Materials (ESSM) and 2nd International Conference on Micromechanics, Intelligent Materials and Robotics (MIMR), Harrogate, 17-24, 1998.

[35] A.B. Jilani, “Deformations of Piezoceramic-Composite Actuators,” Ph.D. Disseration, Virginia Polytechnic Institute and State University, 1999.

[36] M.W. Hyer, and A.B. Jilani, “Manufactured Shapes of Rectangular RAINBOW Actuators,” 42nd AIAA/ASME/ASCE/ASH/ASC Structures, Structural Dynamics, and Materials Conference and Exhibit, Seattle, April, 2001.

[37] M.W. Hyer and A.B. Jilani, “Deformation Characteristics of Circular RAINBOW Actuators,” *Smart Materials and Structures*, 11, 175-195, 2002.

[38] M.W. Hyer and A. Jilani, “Predicting the Deformation Characteristics of Rectangular Unsymmetrically Laminated Piezoelectric Materials,” *Smart Materials and Structures*, 7, 784-791, 1998.

[39] M.W. Hyer, “Stress Analysis of Fiber-Reinforced Composite Materials,” WCB McGraw-Hill, New York, 1998.

[40] Wolfram Research, Inc. http://www.wolfram.com.

[41] C. Elissalde, and L.E. Cross, "Dynamic Characteristics of RAINBOW Ceramics," *Journal of American Ceramic Society*, 78(8), 2233-2236, 1995.

[42] S. Chandran, V.D. Kugel, and L.E. Cross, "Characterization of the Linear and Non-Linear Dynamic Performance of Rainbow Actuator," Proceedings of the Tenth IEEE International Symposium on Applications of Ferroelectrics, 1996.

[43] Z. Ounaies, K. Mossi, R. Smith, and J. Bernd, "Low-field and High-field Characterization of THUNDER actuators," Proceedings of SPIE, Smart Structures and Materials: Active Materials: Behavior and Mechanics, Vol. 4333, 2001.

[44] C. Shakeri, C.M. Bordonaro, M.N. Noori, and R. Champagne, "Experimental Study of THUNDER: A New Generation of Piezoelectric Actuators," Proceeding of SPIE, Smart Material Technology, Vol. 3675, 1999.

[45] J. Mulling, T. Usher, B. Dessent, J. Palmer, P. Franzon, E. Grant, and A. Kingon, "Load Characterization of High Displacement Piezoelectric Actuators with Various End Conditions," *Sensors and Actuators A*, 94, 19-24, 2001.

[46] R.W. Schwartz, and M. Narayanan, "Development of High Performance Stress-Biased Actuators through the Incorporation of Mechanical Pre-loads," *Sensors and Actuators A*, 101, 322-331, 2002.

[47] K.M. Mossi, Z. Ounaies, R. Smith, and B. Ball, "Pre-stressed Curved Actuators: Characterization and Modeling of their Piezoelectric Behavior," Proceedings of SPIE, Active Materials: Behavior and Mechanics, Vol. 5053, 2003.

[48] K.J. Yoon, K.H. Park, S.K. Lee, N.S. Goo, and H.C. Park, "Analytical design model for a piezo-composite unimorph actuator and its verification using lightweight piezo-composite curved actuators," *Smart Materials and Structures*, 13, 459-467, 2004.

[49] B.K. Taleghani, J.F. Campbell, "Non-linear finite element modeling of THUNDER piezoceramic actuators," NASA TM-1999-209322, 1999.

VITA

Sontipee Aimmanee was born in Bangkok, Thailand. He attended King Mongkut's University of Technology Thonburi (KMUTT, which was formerly named as King Mongkut's Institute of Technology Thonburi) in Bangkok during 1992-1996 and received a Bachelor of Engineering degree with first class honors in Mechanical Engineering. Right after the graduation, he spent two years as a lecturer at the Department of Mechanical Engineering at the same university. Then, he was granted a teaching assistantship from the University of Delaware to study a Master degree in Mechanical Engineering Department. Under the supervision of Prof. Jack R. Vinson, he carried out graduate research work in the field of mechanics of sandwich structures and earned a Master of Science in Mechanical Engineering in 2000. In the same year, he was awarded a scholarship from the Royal Thai Government to further his postgraduate study. He enrolled at Virginia Polytechnic Instituted and State University as a doctoral student of Engineering Mechanics, working toward his Ph.D. degree in the area of mechanics of actuators under the supervision of Prof. Michael W. Hyer. He received the degree of Doctor of Philosophy of Engineering Mechanics in 2004.